Quantum Magnetism at High Resolution

Sergey Shinkevich

Thesis submitted for the degree of
Philosophiae Doctor

Department of Physics
University of Oslo

August 2013

Series of dissertations submitted to the
Faculty of Mathematics and Natural Sciences, University of Oslo
No. 1433

ISSN 1501-7710

Cover: Inger Sandved Anfinsen.
Printed in Norway: AIT Oslo AS.

Produced in co-operation with Akademika Publishing.
The thesis is produced by Akademika Publishing merely in connection with the
thesis defence. Kindly direct all inquiries regarding the thesis to the copyright
holder or the unit which grants the doctorate.

Preface

The topic of this thesis is the study of low-dimensional quantum magnets and the investigation of their static and dynamic properties on very fine scales.

The main results of this work were published in the attached articles, and presented and discussed in international conferences, schools and symposiums: NordForsk network meeting in NTNU, Trondheim (November 3–5, 2008) and in Å, Lofoten, Norway (August 3–8, 2009); European School on Magnetism (ESM-2009) in Timişoara, Romania (September 1–10, 2009); Moscow International Symposium on Magnetism (MISM-2011) in MSU, Moscow, Russia (August 21–25, 2011) [1]; the 19th International Conference on Magnetism with Strongly Correlated Electron Systems (ICM2012 with SCES) in Busan, Republic of Korea (July 8–13, 2012) [2].

Thesis structure

The thesis is organized in two parts. The first part contains an introduction to the dissertation topic as well as calculations omitted in the published papers.

The second part consists of a list of my contributions to the papers and the published papers themselves.

Acknowledgements

I am greatly thankful to my supervisor Olav F. Syljuåsen for excellent fruitful collaboration, wise supervision and warm all-out support during my study at the University of Oslo. Actually he has become for me as the second father in Norway. I would like also to thank all members of the Theoretical Group for great hospitality, close friendship and exceptionally warm atmosphere at the Department of Physics.

In addition, I would like to thank my family for the shown patience and the heartfelt support.

List of papers

Paper I: Sergey Shinkevich and Olav F. Syljuåsen,

Spectral signatures of magnetic Bloch oscillations in one-dimensional easy-axis ferromagnets,

Phys. Rev. B **85**, 104408 (2012)

Paper II: Sergey Shinkevich and Olav F. Syljuåsen,

Numerical simulations of laser-excited magnetic Bloch oscillations,

Phys. Rev. B **87**, 060401 (2013)

Paper III: Sergey Shinkevich, Olav F. Syljuåsen, and Sebastian Eggert,

Spin-wave calculation of the field-dependent magnetization pattern around an impurity in Heisenberg antiferromagnets,

Phys. Rev. B **83**, 054423 (2011)

Contents

Part I

Introduction

Chapter 1

Introduction

Towards the end of the XIX-th century many physicists believed that all physical problems were almost solved. The famous British scientist William Thomson (well-known as Lord Kelvin) gave a lecture entitled "Nineteenth-Century Clouds over the Dynamical Theory of Heat and Light" [3] in 1900, where he said

> *The beauty and clearness of the dynamical theory, which asserts heat and light to be modes of motion, is at present obscured by two clouds.*

These Kelvin's "clouds" were two unexplained phenomena: the Michelson-Morley experiment [4] and a black-body radiation effect known as the ultraviolet catastrophe [5], which were indicated as the final steps to a complete understanding of the universe, explained in terms of classical motion of particles. The two "clouds" on the horizon represented new challenges and fundamental limits to the classical approach. In fact, they meant totally new and unanticipated physics, now known as *relativity theory* and *quantum mechanics*.

In 1900 Max Karl Ernst Ludwig Planck originated the quantum theory when he suggested the first quantum hypothesis that any energy radiating from an atomic system can be divided into a number of discrete "energy elements" (*energy quantums*)[1] [7, 8]. The term "quantum mechanics" itself was first used in 1925 by Max Born [9], and a keystone to the quantum theory was laid the same year by Erwin Schrödinger who developed and formulated the wave equation [10] that describes the behaviour of a quantum mechanical system. In the following years the quantum mechanical framework were applied to atomic and nuclear physics, chemical structure and bonding.

In solid state physics quantum mechanics was used to improve predictions of the classical theory and to explain electrical and thermal properties of crystalline materials. In particular Arnold Sommerfeld combined the classical Drude model [11, 12] with quantum mechanics in the free electron model (also known as the Drude-Sommerfeld model) [13], where electrons are modelled as a gas of particles which obey the quantum mechanical Fermi-Dirac statistics [14, 15].

---

[1] The word **"quantum"** (plural: **quanta**) comes from the Latin "*quantus*" which can be translated "*how much*". The quantum in general was well-known also before era of the quantum mechanics. Physicians often used this word, such as the term "quantum satis" (*the amount which is needed*). Historically at that time many scientists were physicians as well as physicists (e.g. Hermann von Helmholtz graduated from Charité - Universitätsmedizin Berlin where he defended the thesis in physiology "De fabrica systematis nervosi evertebratorum" in 1842 [6]).

This period was also the beginning of the quantum theory of magnetism. The theory of magnetism was initially focused on explaining order-disorder phase transitions in ferromagnets. Wilhelm Lenz proposed a model of interacting magnetic moments (known as the Lenz-Ising model) [16] and gave it as a problem to his student, Ernst Ising, who solved it in one dimension in 1925 without finding any phase transitions [17]. The same model, but in higher dimensions, was used to explain the phase transition between ferromagnetic and paramagnetic states in subsequent studies by Rudolf Peierls, Hendrik Kramers, Gregory Wannier and Lars Onsager, see the history review [18].

While the Ising model is a purely classical model, its quantum counterpart was introduced by Werner Heisenberg in 1928 [19] by using the Pauli exclusion principle [20]. In 1931 the one dimensional version of the Heisenberg model was solved by Hans Bethe [21] using a new method, Bethe ansatz, for finding exact eigenvalues and eigenvectors. This model is, with small modifications, used extensively to describe properties of several magnetic insulators [22].

Quantum mechanics has come a long way since its beginnings, and is now established as the framework for explaining all microscopic phenomena, including magnetism. The effects of quantum mechanics are getting more and more important as experiments are moving towards the atomic scale. Experimental techniques are now approaching, and have in some cases even reached, a spatial and temporal resolution corresponding to the atomic scale. In particular scanning tunneling microscopy (STM), transmission electron microscopy (TEM) and atomic force microscopy (AFM) can now spatially resolve atoms and can provide detailed information of physical phenomena on the single-atom scale, see [23–26]. Also infrared lasers probe very well the energy levels at the meV-scale [27, 28] and allow to access timescales of a picosecond [29–31] that is the typical energy and time scale of quantum magnetic phenomena. There is no reason to expect these advances to halt, and so there will also be need for quantitative theoretical predictions in these regimes.

The aim of the works presented in this thesis has been to carry out detailed quantitative predictions of quantum magnetic phenomena that might be within the reach of probes with high spatial or temporal resolution in the near future. In particular, the main focus of this thesis is on magnetic Bloch oscillations in the cobalt chloride dihydrate ($\mathrm{CoCl_2 \cdot 2H_2O}$). These are very fast magnetization oscillations and will require high frequency magnetization detection equipment in the hundreds of GHz-range, see our Article I [32]. Yet indirect signals, such as the energy spectrum corresponding to these oscillations, can in principle be observed in todays neutron scattering experiments [33].

To complement this with a magnetic phenomena requiring high spatial resolution we also discuss the magnetization pattern around a general impurity in a Heisenberg antiferromagnet. Such a pattern can only be observed with a magnetization probe that has atomic spatial resolution such as for instance magnetic force microscopy (MFM) [34] or spin-polarized scanning tunnelling microscopy (SP-STM) [35].

It is a hope that the results calculated here can be experimentally observed in the near future.

Chapter 2

Bloch Oscillations

Bloch oscillations (BOs) [36] were predicted in the first age of quantum mechanics in 1928. This phenomenon which is oscillatory motion of a particle in a periodic potential in a uniform constant field is rather counterintuitive from the standpoint of classical mechanics. Initially it was predicted for an electron in a crystal subject to an external static electric field by Bloch and Zener [36, 37]. Electron Bloch oscillations are however extremely hard to observe experimentally in metals due to electron scattering off impurities and phonons. So while the phenomenon was predicted theoretically long ago, BOs have only recently been demonstrated [38] in very clean artificial materials with a periodic layer structure known as semiconductor superlattices [39].

Subsequently the same oscillatory motion of a particle in an external field have been observed in many different physical systems. The Bloch oscillations were experimentally demonstrated in ultracold atoms in a periodical optical potential [40, 41] and in Bose-Einstein condensates [42, 43]. Bloch oscillations of light were theoretically predicted [44–46] and shown in an experiment with optical superlattices [47]. Also acoustic Bloch oscillations were recently observed in ultrasonic superlattices [48], artificial 2D-structures on water (a phononic crystal) [49] and grating structures on solid substrates [50]. In this thesis we will discuss theoretically the possibility of observing Bloch oscillations in *magnetic* systems. This possibility was suggested by Jordan Kyriakidis and Daniel Loss [51] in 1998. Such magnetic BOs have not been observed experimentally yet. Before we treat the details of magnetic BOs, we will discuss Bloch oscillations from a general point of view.

2.1 Theory of Bloch oscillations

In general the phenomenon of the Bloch oscillations is based on the following properties of a particle in a periodic potential and an external field [52]:

- the energy spectrum has a band structure and the energy is a periodic function in the reciprocal lattice,

- the interaction of the particle with the external field can be described by classical equations.

In order to simplify calculations without loss of generality we can consider a particle in one-dimensional system.

2.1.1 Semiclassical approach

If one makes these assumptions, then the equation of motion for a particle under the influence of an external force is

$$\frac{dp}{dt} = F_{ext}, \tag{2.1}$$

where momentum p is proportional to wave vector (*crystal momentum* or *quasi-momentum*): $p = \hbar k$, see [53], and the external force F_{ext} depends on the nature of the particle and the applied field. The evolution equation can be rewritten as

$$\hbar \frac{dk}{dt} = F_{ext}, \tag{2.2}$$

which is the so-called "acceleration theorem" [54, 55]. It has the following solution

$$k(t) = k(0) + \frac{F_{ext}}{\hbar} t. \tag{2.3}$$

In a crystal with a periodic potential the energy spectrum has a band structure. In the simplest case, e.g. the tight-binding approximation (or linear combinations of atomic orbitals approximation) [56], the particle energy for a given energy band in the one-dimensional crystal is

$$\mathcal{E}(k) = A \cos ak, \tag{2.4}$$

where a is the lattice parameter and the constant A corresponds to a half of the bandwidth, see [57, 58]. In the semiclassical approximation the velocity of the particle is given by

$$v(k) = \frac{1}{\hbar} \frac{d\mathcal{E}}{dk} = -\frac{Aa}{\hbar} \sin ak. \tag{2.5}$$

Therefore the particle position is

$$x(t) = \int v(k(t)) dt = x_0 + \frac{A}{F_{ext}} \cos\left(\frac{aF_{ext}}{\hbar} t\right), \tag{2.6}$$

and so the particle undergoes oscillatory motion with the Bloch angular frequency

$$\omega_B = \frac{aF_{ext}}{\hbar} \tag{2.7}$$

and the amplitude of the Bloch oscillations is given by

$$x_B = \frac{A}{F_{ext}}. \tag{2.8}$$

In particular, in the case of a charged particle in a constant electric field E the electric force is $F_{ext} = eE$, where the e is charge of the particle.

It is important to note that the Bloch frequency ω_B is proportional to the lattice spacing of the crystal and to the force acting on the particle while the magnitude of the oscillations x_B in Eq. (2.8) is proportional to the bandwidth but inversely proportional to the external force.

2.1.2 Wave-packets approach

We can make the above semiclassical description of BOs more "quantum" by identifying the particle as a wave-packet of Bloch waves. Bloch's theorem [36] states that the solution of the Schrödinger equation of a non-relativistic particle in a periodic potential, in the one-dimensional case, can be written as *Bloch waves*:

$$\psi_{n,k}(x) = e^{ikx} u_{n,k}(x), \tag{2.9}$$

where e^{ikx} is a plane wave envelope function, n indicates the energy band $\mathcal{E}_n(k)$, and $u_{n,k}(x)$ is the periodic (Bloch) function with the same periodicity as the crystalline potential $u_{n,k}(x) = u_{n,k}(x+a)$ when a is the period of the lattice.

A particle subject to an external static force is described by the Hamiltonian

$$\hat{H} = -\frac{\hbar^2}{2m}\frac{d^2}{dx^2} + U(x) + xF_{ext}, \tag{2.10}$$

where $U(x+a) = U(x)$ is the periodic potential of the crystal lattice. In the presence of the applied external field the particle wave function can be considered as a *wave-packet* built from the Bloch waves characterized by momentum distributions $g_n(k,t)$ for each individual band n

$$\psi(x,t) = \sum_{n=1}^{\infty} \int dk\, g_n(k,t)\, \psi_{n,k}(x). \tag{2.11}$$

In the case when only a single band n_0 is occupied initially at $t = t_0$, so that the momentum distributions are $g_n(k,t_0) = 0$ for the band indices $n \neq n_0$ and if the distribution $g_{n0}(k,t_0)$ is a smooth function and well localized around some value k_0 within a single Brillouin zone (it implies that characteristic width Δk of the momentum distribution is small compared with the Brillouin zone width $2\pi/a$, so in real space the wave-packet extends over a few lattice spacings) and couplings to other bands are weak (so we can neglect transitions to these bands $n \neq n_0$), then the mentioned semiclassical "acceleration theorem" (2.2) becomes valid and the Schrödinger equation corresponding to the Hamiltonian (2.10) can be written [37, 59] as

$$\frac{\partial}{\partial t}|g_{n_0}(k,t)|^2 = \frac{F_{ext}}{\hbar}\frac{\partial}{\partial k}|g_{n_0}(k,t)|^2, \tag{2.12}$$

which has the following solution

$$|g_{n_0}(k,t)|^2 = G\left(k + \frac{F_{ext}}{\hbar}t\right), \tag{2.13}$$

where G is a smooth function of its argument. It means that the momentum distribution of the wave-packet propagates at a constant speed in momentum space, while the shape of the distribution does not change, see [59,60]. This physical phenomenon corresponds to *dynamical localization* of a particle in a uniform external field.

The argument of the function G in Eq. (2.13) indicates that the wave-packet center moves with constant speed $F_{ext}/\hbar$ through the Brillouin zone. When it reaches the boundary of the Bloch band in momentum space it experiences Bragg reflection by the crystal (in the considered approximation of "Bloch particle" within the single band model the interband transitions or Zener tunneling were neglected), e.g. see [60,61]. The period of the oscillatory motion is then size of the Brillouin zone, $2\pi/a$, divided by the effective constant speed $F_{ext}/\hbar$ that gives the angular frequency of the Bloch oscillations

$$\omega_B = \frac{aF_{ext}}{\hbar} = \frac{eaE}{\hbar} \tag{2.14}$$

in the uniform electric field E.

2.1.3 Wannier-Stark description

The semiclassical approach in the previous sections treated the periodic potential and external force differently. First the wave-packet is formed from Bloch states and then the only role of the external force is to move the wave-packet. A proper quantum theory of the Bloch oscillations solves the eigenvalue problem in the presence of both factors: the periodic potential and the external force. The result of this is a spectrum with equidistant energy levels known as the Wannier-Stark ladder (WSL) [62].

We will now show how the WSL can be obtained in a simple approach where we first neglect the periodic potential and treat the particle in the external force field quantum mechanically. Then we impose the periodic potential as a boundary condition which leads to the appearance of the WSL. The Bloch oscillations can then be obtained from consideration of time evolution of this quantum system with an equidistant energy spectrum (WSL) and the oscillations here are sometimes termed Wannier-Bloch oscillations [63].

The dynamics of a single particle in an external potential of a constant force without the periodic potential is described by the Hamiltonian

$$\hat{H} = -\frac{\hbar^2}{2m}\nabla^2 + \hat{V}(x), \qquad \hat{V}(x) = xF_{ext}. \tag{2.15}$$

The corresponding time-independent Schrödinger equation for the particle is

$$\mathcal{E}\psi = -\frac{\hbar^2}{2m}\frac{d^2\psi}{dx^2} + xF_{ext}\,\psi, \tag{2.16}$$

which corresponds to the description of a particle in a linear potential (e.g. free fall in gravitational field near the Earth surface [64]). This equation can be written in the following form

$$\frac{d^2\psi}{d\xi} - \xi\psi = 0, \qquad \xi = \frac{x}{l} - \lambda, \tag{2.17}$$

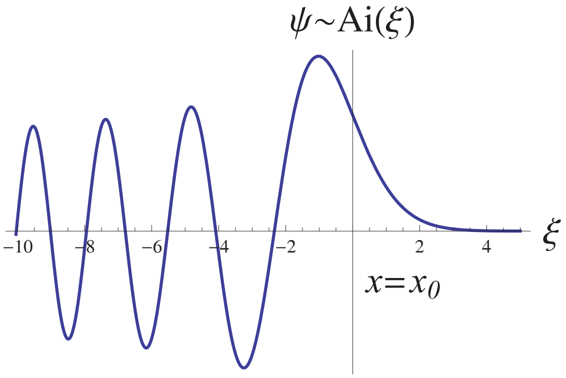

Figure 2.1: Solution of the Schrödinger equation for a particle with energy $\mathcal{E}$ in a linear potential described by the Hamiltonian (2.15). The zero argument $\xi = 0$ corresponds to the turning point at $x = x_0 = \mathcal{E}/F_{ext}$ when the particle energy is equal to potential energy of the external force field $\mathcal{E} = V(x_0)$.

where the new variables are introduced

$$l = \sqrt[3]{\frac{\hbar^2}{2mF_{ext}}}, \qquad \lambda = \frac{2m\mathcal{E}}{\hbar^2}\, l^2 = \frac{2m\mathcal{E}}{\hbar^2}\left(\frac{\hbar^2}{2mF_{ext}}\right)^{2/3}. \tag{2.18}$$

The parameter l is a characteristic length.

The general solution of the second order differential equation (2.17) is Airy functions of the first and second types which are related to Bessel functions and modified Bessel functions of the $1/3$-order [65]. Only the Airy functions of the first type $\mathrm{Ai}(x)$ are physical, as the other ones of the second type $\mathrm{Bi}(x)$ diverge exponentially at large positive argument and are not normalizable. Therefore the wave function of the particle is

$$\psi \sim \mathrm{Ai}(\xi) = \mathrm{Ai}\left(\frac{x}{l} - \lambda\right) \tag{2.19}$$

and its characteristic behaviour is shown in Fig. 2.1. The zero argument $\xi = 0$ corresponds to the turning point at $x_0 = \mathcal{E}/F_{ext}$ when the particle energy is equal to the potential energy of the external field $\mathcal{E} = V(x_0) = x_0 F_{ext}$.

For positive argument ξ (when $x > x_0$) the Airy function $\mathrm{Ai}(\xi)$ is a positive and concave function, and decreases exponentially to zero in the following way

$$\mathrm{Ai}(\xi) \sim \frac{\xi^{-1/4}}{2\sqrt{\pi}}\, e^{-\frac{2}{3}\xi^{3/2}}. \tag{2.20}$$

This corresponds to under-barrier tunneling for which the particle wave function $\psi(x > x_0)$ decays exponentially and the particle kinetic energy is negative $\mathcal{E} < V(x)$.

When the argument is negative the Airy function oscillates around zero with ever-increasing frequency and ever-decreasing amplitude which is given by the asymptotic formula [66]

$$\mathrm{Ai}(-\xi) \sim \frac{\xi^{-1/4}}{\sqrt{\pi}} \sin\left(\frac{2}{3}\xi^{3/2} + \frac{\pi}{4}\right). \tag{2.21}$$

For negative argument ξ (when $x < x_0$) the particle is above the potential barrier ($\mathcal{E} > V(x)$) and its quasi-momentum k is *real-valued* and depends on the spatial coordinate x.

If the particle is also subject to a periodic potential, then its velocity goes to zero at the boundary of the Brillouin zone, so effectively the particle is reflected from the Brillouin zone boundary. It means that magnitude of the particle wave function $\psi(x)$ decreases with increasing the deviation from the turning point $x_0 = \mathcal{E}/F_{ext}$ (see Fig. 2.1) and the wave function is non-zero only in the region near $x = x_0$. Therefore the electron becomes localised around the turning point that corresponds to the phenomenon of the dynamical localization of a particle.

The energy spectrum can be found from the wave function boundary condition that the localization points, where the Airy function argument becomes zero ($\xi = 0$), are to be invariant under the translations of an integer number of lattice spacings due to the periodic crystal structure

$$x_n = x_0 + a\,n, \qquad n = 0, \pm 1, \pm 2, \ldots, \tag{2.22}$$

that implies

$$\lambda_n = \frac{x_0}{l} + \frac{a}{l}n. \tag{2.23}$$

The energy of the states in Eq. (2.18) becomes then

$$\mathcal{E}_n = \frac{\hbar^2}{2ml^2}\lambda_n = \mathcal{E}_0 + aF_{ext}\,n. \tag{2.24}$$

Therefore the energy spectrum of the localized states is equidistant. It is called the Wannier-Stark ladder (WSL) [62]

$$\mathcal{E}_n = \mathcal{E}_0 + \hbar\omega_B\,n, \qquad n = 0, \pm 1, \pm 2, \ldots, \tag{2.25}$$

where the index n describes the energy levels and the localization points of the particle wave function $x_n = x_0 + \frac{\hbar\omega_B}{F_{ext}}n$, see [52]. The distance between the nearest energy levels in the equidistant spectrum of WSL defines the frequency ω_B of the Bloch oscillations

$$\omega_B = \frac{aF_{ext}}{\hbar} = \frac{aeE}{\hbar} \tag{2.26}$$

and agrees with what is found in the wave packet approach in Eq. (2.14).

2.1.4 Experimental observation of BOs

Electron Bloch oscillations were controversial and interesting mostly from a theoretical point of view for along time. In the idealized case even a weak electric field should be sufficient to excite BOs at low Bloch frequency with long oscillation period $T_B = 2\pi\hbar/(aeE)$ which must be smaller than a characteristic relaxation time τ in a crystal in order to complete the entire oscillation cycle before the electron gets scattered. At the same time the amplitude of

BOs depends linearly on bandwidth $\Delta = 2A$ and varies inversely to the external field by $x_B = A/eE$, so the oscillation magnitude should also not exceed the electron scattering length.

This means that in real natural crystals the Bloch oscillations are extremely hard to observe because of scattering processes due to lattice defects, impurities, phonons, etc. For example the metal copper has a face-centered cubic (fcc) crystal structure with lattice parameter $a = 3.6$ Å and Fermi energy $\mathrm{E}_F = 7.0$ eV [67]. In a moderate electric field $E = 100$ kV/m it gives the following estimates: the Bloch period is $T_B = 0.1$ ns and the amplitude of BOs is $x_B = 70\ \mu\mathrm{m}$ while the typical electron mean free path at room temperature is just $l_e = 40$ nm [58, 68] corresponding to an extremely short mean time between collisions $\tau = 25$ fs.

For a typical semiconductor with a lattice constant $a = 5$ Å and a presumably conduction bandwidth of $\Delta = 1$ eV [69, 70] in the same electric field an electron should oscillate with amplitude $x_B = 5\ \mu\mathrm{m}$ and Bloch period $T_B = 80$ ps while a typical inelastic scattering time scale is $\tau = 0.1$–10 ps and decreases with electric field strength [71]. So the Bloch period could coincide with the scattering time at an electric field of about $E_\tau = 2\pi\hbar/(ae\tau) \approx$ 10–100 MV/m. This magnitude is of the order of the dielectric breakdown field strength of most dielectric materials [70].

Therefore in these situations the period of a single Bloch oscillation exceeds significantly the characteristic relaxation time ($T_B \gg \tau$). This prevents the experimental observation of the electron BOs in ordinary metals and semiconductors at room temperature. Experimental evidence of Bloch oscillations of electrons was obtained only in synthetic artificial semiconductor superlattices, where the typical bandwidth is in the range $\Delta = 10$–100 meV and the lattice constant is about $a \approx 100$ Å [69, 72]. This gives a Bloch period of $T_B = 4$ ps and amplitude $x_B = 50$ nm for the electric field $E = 100$ kV/m.

The first experimental observation of Bloch oscillations in a GaAS–GaAlAs superlattice with lattice constant $a = 65$ Å and bandwidth $\Delta = 30$ meV was seen in an electric field $E = 2$ MV/m [38] that gives the Bloch period $T_B = 0.3$ ps and the amplitude of BOs $x_B =$ 8 nm. The typical damping time of the Bloch oscillations in the semiconductor superlattices is $\tau_B = 1$–2 ps [73, 74] and originates from non-equidistant energy spectrum and electron scattering at the interfaces of junctions in the superlattices, see [75].

Chapter 3

Magnetic Bloch Oscillations

Theoretically one can ask the following question: "Can the same phenomenon of Bloch oscillations also exist in magnetic systems?" This possibility was first discussed by Kyriakidis and Loss [51] in 1998. They considered a spin chain where the particle is a propagating single domain-wall excitation, and concluded that magnetic BOs should indeed exist. In particular, the blue crystalline material $\mathrm{CoCl_2} \cdot 2\mathrm{H_2O}$ which can be modeled as an easy-axis quasi one-dimensional ferromagnet was proposed as a promising candidate to observe the magnetic Bloch oscillations at low temperature.

3.1 Theory of magnetic Bloch oscillations

We consider this proposal in further details. In our study of a quantum ferromagnetic spin-$\frac{1}{2}$ chain we assume that

- The spin chain has a strong easy-axis (Ising) character ($J_z \gg J_x, J_y$) in order to suppress the proliferation of domain-walls.

- There is no interband tunneling (Zener transitions). This requires the energy of the oscillation to be small which restricts the magnitude of static magnetic field ($h_z \ll J_z$).

- Inelastic scattering processes, which destroy the phase coherent motion, are neglected. It implies that there are no phonon emissions or absorptions, and the density of excitations (domain-wall separating regions of overturned spins) is quite small so that we can neglect local interaction between them.

- The quantum system is at low temperature ($T \ll J_z$).

3.2 Hamiltonian

Specifically we consider a spin-$\frac{1}{2}$ XYZ ferromagnetic Hamiltonian for a chain with next nearest neighbour coupling in a magnetic field

$$\hat{H} = -\sum_i \left(J_x \hat{S}_i^x \hat{S}_{i+1}^x + J_y \hat{S}_i^y \hat{S}_{i+1}^y + J_z \hat{S}_i^z \hat{S}_{i+1}^z \right) + \sum_i J_B \hat{S}_i^z \hat{S}_{i+2}^z - \sum_i \left(h_x \hat{S}_i^x + h_z \hat{S}_i^z \right), \quad (3.1)$$

which can be written as

$$\hat{H} = \hat{H}_z + \hat{H}_a + \hat{H}_\perp + \hat{H}_x + \hat{H}_B, \quad (3.2)$$

where

$$\begin{aligned}
\hat{H}_z &= -J_z \sum_i \hat{S}_i^z \hat{S}_{i+1}^z - h_z \sum_i \hat{S}_i^z, \\
\hat{H}_a &= -J_a \sum_i \left(\hat{S}_i^+ \hat{S}_{i+1}^+ + \hat{S}_i^- \hat{S}_{i+1}^- \right), & J_a &= (J_x - J_y)/4, \\
\hat{H}_\perp &= -J_\perp \sum_i \left(\hat{S}_i^+ \hat{S}_{i+1}^- + \hat{S}_i^- \hat{S}_{i+1}^+ \right), & J_\perp &= (J_x + J_y)/4, \\
\hat{H}_x &= -h_\perp \sum_i \left(\hat{S}_i^+ + \hat{S}_i^- \right), & h_\perp &= h_x/2, \\
\hat{H}_B &= J_B \sum_i \hat{S}_i^z \hat{S}_{i+2}^z
\end{aligned} \quad (3.3)$$

with the redefined coupling constants J_a and $J_\perp$, and $\hat{S}_i^\pm = \hat{S}_i^x \pm i\hat{S}_i^y$ are the usual spin-$\frac{1}{2}$ raising and lowering operators. The parameter $h_\perp = h_x/2$ corresponds to an effective transverse magnetic field which can either be an external field or it can arise due to crystal field effects and interchain coupling in real materials. The coupling constant J_B describes a next-nearest-neighbor interaction in the chain, which might arise for example due to a zigzag structure (see Figure 3.1). In the case of a magnet with strong anisotropy with $J_z > 0$ as the largest coupling the system has an easy-axis and behaves roughly like an Ising ferromagnet.

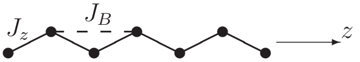

Figure 3.1: A chain with a zigzag structure where the next-nearest-neighbor interaction couples z-components of spins with the parameter J_B. The constant J_z describes their nearest-neighbor coupling.

This Hamiltonian can also be mapped to an antiferromagnetic one-dimensional system, where every second spin is rotated an angle $180°$ about the x-axis. Then the Hamiltonian in Eq. (3.1) is mapped to a spin-$\frac{1}{2}$ antiferromagnet in a staggered longitudinal field $h_{st}^z = (-1)^i h_z$ and a uniform transverse h_x magnetic field, see [76]. In a real crystal the staggered field can be caused by Dzyaloshinskii-Moriya interactions (antisymmetric exchange) [77,78].

$\uparrow\uparrow\uparrow\uparrow\uparrow\uparrow\downarrow\downarrow\downarrow\downarrow\downarrow\downarrow$ (a)

$\uparrow\uparrow\downarrow\downarrow\uparrow\uparrow\uparrow\uparrow\downarrow\uparrow\uparrow\uparrow$ (b)

Figure 3.2: (a) A spin state with a single domain wall. (b) Two bound states, where each state consists of a domain and an anti-domain wall.

We consider a ferromagnet where the ferromagnetic coupling ($J_z > 0$) causes alignment of z-components of neighboring spins. With $J_z \gg J_x, J_y$ the energy of an excited state depends mainly on the number of pairs of anti-aligned spin neighbours, or *domain walls* (see Figure 3.2). Each domain wall costs an energy of $J_z/2$, thus we can divide the energy states into sectors which are specified by the number of domain walls N_{dw}. An external magnetic field h_z imposes a penalty having a spin anti-aligned with the h_z-field. At low temperature the ground state favors having a large number of spins aligned with the static magnetic field h_z.

In the absence of other couplings the first excited state corresponds to a single domain wall excitation ($N_{dw} = 1$) in the system, see Figure 3.2(a). Acting on this state the $\hat{H}_a$ term of the Hamiltonian (3.3) can shift the position of the domain wall which makes its dynamic. This mode of a single domain wall propagating along the magnetic chain was first predicted by Villain [79] in 1975 and has been observed in various neutron scattering experiments [80–82].

Natural examples of spin-$\frac{1}{2}$ systems described by the Hamiltonian (3.1) are quasi one-dimensional magnetic materials at low temperature with Co^{2+}-ions as magnetic centers, e.g. the cobalt salts $\mathrm{CsCoBr_3}$, $\mathrm{KCoF_3}$, $\mathrm{CsCoCl_3}$, $\mathrm{CoCl_2} \cdot 2\mathrm{H_2O}$ and $\mathrm{CoNb_2O_6}$. In particular, the quasi 1D ferromagnet $\mathrm{CoNb_2O_6}$ has the zigzag chain structure of the magnetic ions [83, 84] that gives the nonzero next-neighbours coupling J_B. Magnetic properties of the Co^{2+} magnetic centers are discussed below.

3.2.1 Properties of Co^{2+} ions

Cobalt is a transition element with atomic number $Z = 27$ which is in the d-block of the periodic table. It means that the atomic d-orbital subshell of the second outermost shell is not filled and the atom has the electron configuration $1s^2\ 2s^2\,2p^6\ 3s^2\,3p^6\,\underline{3d^7\ 4s^2}$. The labels $s, p, d, f, \ldots$ correspond to the orbital angular momentum quantum numbers $l = 0, 1, 2, 3, \ldots$[1]

In the cobalt ion Co^{2+} the two electrons from the outermost $4s$-shell are removed and its electron configuration for the last subshell is $3d^7$ in the ground state. Using Hund's rules [86,87] the ground state configuration corresponds to the term ^4F with total spin $S = 3/2$ and total angular momentum $L = 3$. The detailed diagram of the electron configuration in the ground state is shown in Figure 3.3. There are three unpaired electrons on the d-subshell (with $l = 2$) so the total spin of the cobalt ion is $S_{ion} = 3 \times \frac{1}{2}$.

Examples of quasi one-dimensional magnetic materials at low temperature with Co^{2+}-ions as magnetic centers are the cobalt salts $\mathrm{CsCoBr_3}$, $\mathrm{KCoF_3}$, $\mathrm{CsCoCl_3}$, $\mathrm{CoCl_2} \cdot 2\mathrm{H_2O}$ and $\mathrm{CoNb_2O_6}$. The total spin momentum of cobalt ion is $S = \frac{3}{2}$ but due to spin-orbit coupling and

---

[1] Historically, letters of the orbital labels s, p, d, f came to quantum mechanics from spectroscopy and describe properties of the spectral series observed in alkali metals as "**s**harp", "**p**rincipal", "**d**iffuse" and "**f**undamental" [85] while letters for subsequent values of orbital momentum l were assigned in alphabetical order, omitting the letter "j".

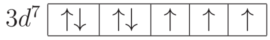

Figure 3.3: Electron configuration of Co^{2+} ion for the outer $3d$-subshell in the ground state. The ground state term is ^4F with total spin $S = \frac{3}{2}$ and total angular momentum $L = 3$.

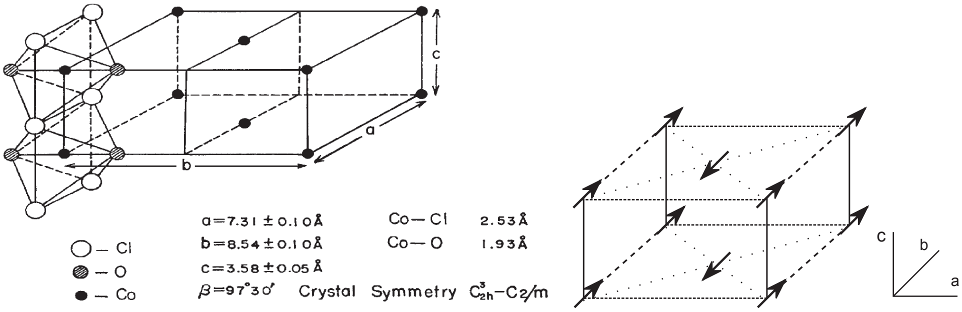

(a) (b)

Figure 3.4: (a) Crystal structure of the cobalt chloride dihydrate ($\mathrm{CoCl_2 \cdot 2H_2O}$) from Ref. [96]. (b) Magnetic unit cell of this material. The strong ferromagnetic J_z couples spins along the c axis in $\mathrm{CoCl_2 \cdot 2H_2O}$. The spin z-axis corresponds to the crystallographic b axis. Neighbour spin chains are coupled weakly antiferromagnetically.

slight distortion in the materials at low temperature the molecular field causes exchange mixing of single-ion levels that results in a spectrum of doublets, thus the effective spin is $S_0 = \frac{1}{2}$ with a relatively large g-factor (for details see [88–91]). Therefore the quasi one-dimensional magnetic materials can be described by an effective spin-$\frac{1}{2}$ Hamiltonian.

In our study we will focus mainly on magnetic properties of $\mathrm{CoCl_2 \cdot 2H_2O}$ as a candidate material for observing magnetic Bloch oscillations in purely Ising-like magnetic systems [51]. The crystal structure of the cobalt chloride dihydrate ($\mathrm{CoCl_2 \cdot 2H_2O}$) was first deduced using electron diffraction techniques [92] and refined later by x-ray diffraction techniques [93]. The magnetic structure of the material was investigated by using proton nuclear magnetic resonance (NMR) measurements [94]. The lattice parameters, crystal structure and magnetic properties of $\mathrm{CoCl_2 \cdot 2H_2O}$ are given in the Ref. [95, 96]. In this material strong chemical bonds result in polymeric $\mathrm{CoCl_2}$-chains along the crystallographic c axis which are relatively weakly bonded by hydrogen bonds between chlorine ions of a neighboring polymeric chain and the oxygen atom of the water molecule completing the almost octahedral structure about the Co^{2+}-ion. The exchange spin interaction between cobalt ions within the same chain is ferromagnetic and much stronger than the weak antiferromagnetic interaction between different chains. These neighbour magnetic spin chains become antiferromagnetically ordered below the Néel temperature $T_N \approx 17.2$ K [97] with chain magnetizations directed parallel to the crystallographic b axis. Crystal structure and magnetic unit cell of $\mathrm{CoCl_2 \cdot 2H_2O}$ at low temperature ($T \ll T_N$) are shown in Figure 3.4. The magnetic excitation spectrum of $\mathrm{CoCl_2 \cdot 2H_2O}$ at low temperature was observed experimentally in far-infrared transmission measurements [88, 98] and analytically studied in a series of papers [99–101].

3.2.2 Two domain wall approximation

In Ref. [51] Kyriakidis and Loss focused on the study of a single domain wall and how it undergoes Bloch oscillations when subject to a magnetic field. In the presence of a magnetic field however, the states with an odd number of domain walls are heavily suppressed as they cost an energy of the order of the system size unless the domain walls are close to the chain ends [102]. Therefore neglecting boundary effects the single domain wall state is not part of the low energy spectrum in a finite magnetic field. Assuming a large energy cost to create domain walls we therefore investigate low energy excitations involving only a few even number of domain walls N_{dw}.

In the simplest approximation, the two-domain wall approximation ($N_{dw} \leq 2$), where a domain and an anti-domain wall create a cluster (or simply a *domain*) of overturned spins, each state can be described in the following way

$$|j,l\rangle = |\ldots \uparrow\uparrow \underbrace{\overset{j}{\downarrow}\downarrow \ldots \downarrow}_{l} \uparrow\uparrow \ldots\rangle, \tag{3.4}$$

where the index $j = 1, 2, \ldots, N$ gives the starting position of the down-spin cluster (domain) and $l = 1, 2, \ldots, N$ describes its length, N is the total number of spins in the chain which can be a macroscopic number ($N \gg 1$), and $\uparrow$ is a spin-up along the z-axis. Using periodic boundary conditions there are no boundary effects. Extending this representation to $l = 0$ the ferromagnetic state is $|0,0\rangle = |\uparrow\uparrow \ldots \uparrow\uparrow\rangle$ with all overturned spins along the magnetic field and belongs to the zero domain wall sector, which is independent of site number j. Neglecting contribution from higher number of domain walls we consider below the action of the spin-$\frac{1}{2}$ Hamiltonian terms in Eq. (3.3) on the state (3.4) and retain only terms with $N_{dw} \leq 2$.

H_z-term

Since the $\hat{S}^z$-operator does not change the state and J_z is the largest coupling, the first term of the Hamiltonian has a diagonal matrix form and gives, as a result, the leading contribution to the energy levels

$$\hat{H}_z|j,l\rangle = \begin{cases} -(J_z + h_z l)|j,l\rangle, & l \neq 0, \\ 0, & l = 0, \end{cases} \tag{3.5}$$

where the energy of the fully polarized ferromagnetic state was chosen equal to zero.

H_B-term

The next-nearest-neighbour interaction gives an additional contribution to the Hamiltonian diagonal elements that lowers the energy of a single overturned spin (one spin domain $l = 1$) in comparison with the energy of domains with several overturned spins

$$\hat{H}_B|j,l\rangle = \begin{cases} 2J_B|j,l\rangle, & l \geq 2, \\ J_B|j,l\rangle, & l = 1, \\ 0, & l = 0. \end{cases} \tag{3.6}$$

H_x-term

Acting on the state (3.4) the raising and lowering spin operators $\hat{S}^+$ and $\hat{S}^-$ can change the length of the domain by one site, create an extra domain with $l = 1$ (just one overturned spin) or annihilate one. The rising operator acts in the following manner

$$\hat{S}_i^+|j,l\rangle = \begin{cases} 0 & l=0, \\ |0,0\rangle, & i=j, \quad l=1, \\ |j+1,l-1\rangle, & i=j, \quad l>1, \\ |j,l-1\rangle, & i=j+l-1, \\ 0, & \text{otherwise,} \end{cases} \tag{3.7}$$

where we neglect transition to higher number domain wall states ($N_{dw} \leq 2$). The action of the lowering operator is similarly

$$\hat{S}_i^-|j,l\rangle = \begin{cases} |i,1\rangle, & l=0, \\ |j-1,l+1\rangle, & i=j-1, \\ |j,l+1\rangle, & i=j+l, \\ 0, & \text{otherwise.} \end{cases} \tag{3.8}$$

That gives the following $\hat{H}_x$-contribution to the Hamiltonian

$$\hat{H}_x|j,l\rangle = -h_\perp(1-\delta_{l,0})\Big[(|j,l+1\rangle + |j-1,l+1\rangle) \\ + (|j,l-1\rangle + |j+1,l-1\rangle)(1-\delta_{l,1})\Big] - h_\perp \sum_{i=1}^{N}(|i,1\rangle\delta_{l,0} + |0,0\rangle\delta_{l,1}). \tag{3.9}$$

The first term describes the change of a domain length of a state in the $N_{dw} = 2$ sector while the second term corresponds to transitions between $N_{dw} = 2$ and $N_{dw} = 0$ sectors. This transition between the ferromagnetic state and two-domain wall state depends on the system size, as there are N places to insert the new domain with a single overturned spin.

$H_\perp$-term

The $\hat{H}_\perp$ term involves spin operators $\hat{S}_i^+\hat{S}_{i+1}^-$ which can change position of a single overturned spin (or domain with $l = 1$) by one site or create a new additional domain in a higher domain wall sector. Restricting to $N_{dw} \leq 2$ the spin operators act as

$$\hat{S}_i^+\hat{S}_{i+1}^-|j,l\rangle = \begin{cases} |j+1,1\rangle, & i=j, \quad l=1, \\ 0, & \text{otherwise,} \end{cases}$$
$$\hat{S}_i^-\hat{S}_{i+1}^+|j,l\rangle = \begin{cases} |j-1,1\rangle, & i=j-1, \quad l=1, \\ 0, & \text{otherwise,} \end{cases} \tag{3.10}$$

$$\begin{array}{cccc|cccc} & \hat{H}_\perp & & & & \hat{H}_a & & \\ \uparrow\uparrow\uparrow\uparrow\uparrow\uparrow & \rightarrow & 0 & & \uparrow\uparrow\uparrow\uparrow\uparrow\uparrow & \rightarrow & \uparrow\uparrow\downarrow\downarrow\uparrow\uparrow & ,+2 \\ \uparrow\downarrow\downarrow\uparrow\uparrow\uparrow & \rightarrow & \uparrow\downarrow\uparrow\downarrow\uparrow\uparrow & ,+2 & \uparrow\downarrow\downarrow\uparrow\uparrow\uparrow & \rightarrow & \uparrow\downarrow\downarrow\downarrow\downarrow\uparrow & ,0 \\ \uparrow\uparrow\downarrow\uparrow\uparrow\uparrow & \rightarrow & \uparrow\uparrow\uparrow\downarrow\uparrow\uparrow & ,0 & \uparrow\uparrow\downarrow\uparrow\uparrow\uparrow & \rightarrow & \uparrow\uparrow\downarrow\downarrow\downarrow\uparrow & ,0 \end{array}$$

Figure 3.5: Examples of the actions of $\hat{H}_\perp$ and $\hat{H}_a$ terms on particular states from the zero and two domain wall sectors. Only cases that yield the minimal amount of increase in domain walls are shown. Operating with $\hat{H}_\perp$ are shown on the left, while the right hand side shows the effects of operating with $\hat{H}_a$. The increase in the number of domain walls is indicated to the right of each process. Note that $\hat{H}_a$ has the ability to move domain walls without increasing their number when acting on a state with one or more domain walls (right side, the two lowest processes), while $\hat{H}_\perp$ lacks this ability with the exception that it can move a single overturned spin without creating new domain walls (left side, the bottom line).

which can be summed up as

$$\hat{H}_\perp|j,l\rangle = -J_\perp(|j+1,1\rangle + |j-1,1\rangle)\delta_{l,1}. \tag{3.11}$$

In fact, the $\hat{H}_\perp$ term only affects the odd l sector since $\hat{H}_\perp$ is only non-zero when it acts on the state with a single overturned spin (i.e. the minimal bound state of two domain walls separated by one site, see Figure 3.2(b) right), while its action on all other states produces more domain walls, see Fig. 3.5. When the term $\hat{H}_\perp$ acts on the state with a single overturned spin ($l = 1$), it can move this whole bound state without creating extra domain walls. This minimal bound state of two domains walls (or domain with length $l = 1$) plays role of the "kinetic bound state" which was observed in the neutron scattering experiment [103] in $\mathrm{CoNb_2O_6}$.

H_a-term

The corresponding sum of the operators $\hat{S}_i^+\hat{S}_{i+1}^+$ and $\hat{S}_i^-\hat{S}_{i+1}^-$ in the $\hat{H}_a$ term can create/annihilate an extra domain with $l = 2$ or change the size of a domain by two sites

$$\hat{S}_i^+\hat{S}_{i+1}^+|j,l\rangle = \begin{cases} 0, & l = 0,1, \\ |0,0\rangle, & i = j, \quad l = 2, \\ |j+2,1-2\rangle, & i = j, \quad l > 2, \\ |j,1-2\rangle, & i = j+l-2, \quad l > 2, \\ 0, & \text{otherwise} \end{cases} \tag{3.12}$$

and

$$\hat{S}_i^-\hat{S}_{i+1}^-|j,l\rangle = \begin{cases} |j,2\rangle, & l = 0, \\ |j-2,l+2\rangle, & i = j-2, \quad l > 0, \\ |j,l+2\rangle, & i = j+l, \quad l > 0, \\ 0, & \text{otherwise}, \end{cases} \tag{3.13}$$

where again contribution from higher domain wall sectors was neglected. Thus in the two domain wall approximation ($N_{dw} \leq 2$) the term $\hat{H}_a$ acts as

$$\begin{aligned}\hat{H}_a|j,l\rangle = &- J_a(1-\delta_{l,0})\Big[(|j,l+2\rangle + |j-2,l+2\rangle) \\ &+ (|j,l-2\rangle + |j+2,l-2\rangle)(1-\delta_{l,2})(1-\delta_{l,1})\Big] - J_a\sum_{i=1}^{N}(|j,2\rangle\delta_{l,0} + |0,0\rangle\delta_{l,2}),\end{aligned} \tag{3.14}$$

where the sum is performed over all next nearest neighbour pairs.The first term changes the domain length of state by two sites while the second term describes transitions between two and zero domain wall sectors, see Figure 3.5.

The action of the full Hamiltonian on the state in the two domain wall approximation $N_{dw} \leq 2$ becomes

$$\begin{aligned}\hat{H}|j,l\rangle = &(1-\delta_{l,0})\Big\{J|j,l\rangle + h_z l|j,l\rangle - J_a\Big[(|j,l+2\rangle + |j-2,l+2\rangle) \\ &+ (|j,l-2\rangle + |j+2,l-2\rangle)(1-\delta_{l,2})(1-\delta_{l,1})\Big] - h_\perp\Big[(|j,l+1\rangle + |j-1,l+1\rangle) \\ &+ (|j,l-1\rangle + |j+1,l-1\rangle)\,(1-\delta_{l,1})\Big]\Big\} + \Big[J_B|j,1\rangle - J_\perp(|j+1,1\rangle + |j-1,1\rangle)\Big]\delta_{l,1} \\ &- J_a N(|j,2\rangle\delta_{l,0} + |0,0\rangle\delta_{l,2}) - h_\perp N(|i,1\rangle\delta_{l,0} + |0,0\rangle\delta_{l,1}),\end{aligned} \tag{3.15}$$

where we defined the new coupling coefficient

$$J = J_z - 2J_B. \tag{3.16}$$

We consider a system with periodic boundary conditions which does not allow of an odd number of domain walls. This permits to express the Hamiltonian in momentum basis

$$|p,l\rangle = e^{-ip\frac{l}{2}}\frac{1}{\sqrt{N}}\sum_j e^{-ipr_j}|j,l\rangle, \tag{3.17}$$

where p corresponds to the total momentum of the bound state and $r_j = a \times j$ with the lattice spacing constant $a = 1$ in the system of units chosen here. Due to translation invariance the ferromagnetic state has zero momentum $|p = 0, 0\rangle$. In this momentum basis the Hamiltonian is diagonal in terms of the momentum p and acts as follows

$$\begin{aligned}\hat{H}|p,l\rangle = &(1-\delta_{l,0})\Big\{\Big[J + h_z l + \Big(J_B - 2J_\perp\cos\frac{p}{2}\Big)\,\delta_{l,1}\Big]|p,l\rangle - 2J_a\cos p\,\Big[|p,l+2\rangle \\ &+ |p,l-2\rangle(1-\delta_{l,2})(1-\delta_{l,1})\Big] - 2h_\perp\cos\frac{p}{2}\,\Big[|p,l+1\rangle + |p,l-1\rangle(1-\delta_{l,1})\Big]\Big\} \\ &- \Big[J_a\sqrt{N}(|p,2\rangle\delta_{l,0} + |p,0\rangle\delta_{l,2}) + h_\perp\sqrt{N}(|p,1\rangle\delta_{l,0} + |p,0\rangle\delta_{l,1})\Big]\delta_{p,0}.\end{aligned} \tag{3.18}$$

The zero domain wall sector consists of just two states, all spins pointing either up or down along the z-axis. We can see from Eq. (3.18) that the $N_{dw} = 0$ sector couples to states with odd domain length $l = 1$ through only the $h_\perp$ parameter describing the $\hat{H}_x$-term. In absence of the transverse field $h_\perp = 0$ when the Hamiltonian $\hat{H}$ acts on either of the ferromagnetic states it can create states in the two domain wall sector with two overturned spins. We note that since $\hat{H}_a$ flips two spins, while the terms $\hat{H}_\perp$ and $\hat{H}_z$ keep the number of up spins unchanged, the parity of the number of up-spins will be conserved, meaning that we can diagonalize the Hamiltonian in the sectors with an even and odd number of overturned spins (i.e. the domain length l) separately. In addition, the zero domain wall sector states carry zero momentum $p = 0$ and the Hamiltonian is translational invariant, thus the states in the zero domain wall sector couple only to states with zero momentum.

3.2.3 Contribution from $N_{dw} > 2$ sectors

We can see from Eq. (3.18) in the two domain wall approximation $N_{dw} \leq 2$ that the matrix elements corresponding to transitions between the ferromagnetic zero domain wall state and the state with a single overturned spin (or a spin pair) depend on the system size N as $\sqrt{N}$. This causes the energy gap between the ground state and any excited state to depend on the chain length. This is an artifact of the two domain wall approximation. This can be understood by considering the perturbative energy corrections to the ferromagnetic state from processes which involve creation and annihilation of an additional state belong to a sector with higher number of domain walls. Since there are roughly N places to insert the new extra domain, the energy correction becomes proportional to N.

Therefore the sector with higher number of domain walls always gives this length dependent correction to states in the nearest lower sector. When we are restricting to $N_{dw} \leq 2$ the energy of the ferromagnetic state in the zero domain wall sector receives this correction proportional to the system size N, but not the states with $N_{dw} = 2$, because their corrections come from the excluded higher domain walls sector $N_{dw} = 4$.

Simple model: contribution from $N_{dw} = 4$ sector

Let us elaborate on the size dependence of the gap by applying perturbation theory to the simplest model with only the J_z and J_a couplings for a chain in the external magnetic field along the z-axis. In this case the unperturbed Hamiltonian is diagonal and acts as

$$\hat{H}_0 |p, l\rangle = (1 - \delta_{l,0})(J_z + h_z l)|p, l\rangle, \tag{3.19}$$

that corresponds to eigenstates $|p, l = n\rangle$ with eigenenergies $E_n^{(0)} = J_z + h_z n$. The unperturbed ground state is the fully polarized ferromagnetic state $|0, 0\rangle$ with zero ground state energy $E_0^{(0)} = 0$. Considering the J_a coupling as a perturbation, $\hat{V} = \hat{H}_a$, we assume that the perturbation parameter $J_a\sqrt{N} \ll 1$. The transition matrix elements between low-energy states in different N_{dw} sectors are given by the relations

$$\begin{gathered}\langle 0, l|\hat{V}|0, 0\rangle = J_a\sqrt{N}\delta_{l,2}, \\ (\langle 0, l_1 = 2| \otimes \langle 0, l_2 = 2|)\hat{V}|0, l = 2\rangle = J_a\sqrt{2(N - 1 - l_1 - l_2)},\end{gathered} \tag{3.20}$$

where the two-domain state with domain lengths $l_1 = l_2 = 2$ is expressed as tensor product of two one-domain states in the $N_{dw} = 4$ sector, that gives the following transition matrix elements

$$V_{01} = J_a\sqrt{N}, \qquad V_{12} = J_a\sqrt{2(N-5)} \tag{3.21}$$

with the indices describing the number of domains in the coupled sectors. The unperturbed energy of the lowest excited state with a single domain ($l = 2$) in the $N_{dw} = 2$ sector and the state of two domains with the same minimal length ($l_1 = l_2 = 2$) in the $N_{dw} = 4$ sector are

$$E_1^{(0)} = J_z + 2h_z, \qquad E_2^{(0)} = 2(J_z + 2h_z). \tag{3.22}$$

In accordance to perturbation theory [86] the energy levels have the following corrections up to second-order

$$E_n \approx E_n^{(0)} + \langle n|\hat{V}|n\rangle + \sum_{m\neq n} \frac{|\langle m|\hat{V}|n\rangle|^2}{E_n^{(0)} - E_m^{(0)}}, \tag{3.23}$$

where $|n\rangle$ are the unperturbed states. The ground state energy becomes

$$E_0 = E_0^{(0)} + V_{00} + \frac{|V_{10}|^2}{E_0^{(0)} - E_1^{(0)}} = -\frac{|V_{01}|^2}{E_1^{(0)}}. \tag{3.24}$$

Note that the correction to the ground state in Eq. (3.24) is negative and proportional to the system size N. The energy correction to the first excited state is

$$E_1 = E_1^{(0)} + V_{11} + \frac{|V_{01}|^2}{E_1^{(0)} - E_0^{(0)}} + \frac{|V_{21}|^2}{E_1^{(0)} - E_2^{(0)}} = E_1^{(0)} + \frac{|V_{01}|^2}{E_1^{(0)}} - \frac{|V_{12}|^2}{E_2^{(0)} - E_1^{(0)}}. \tag{3.25}$$

We can see that the corrections shift *both* energies of the ground and first excited states but only the energy difference (or gap) between the states has a physical meaning. The gap to the first excited state behaves as

$$\Delta E = E_1 - E_0 = E_1^{(0)} + 2\frac{|V_{01}|^2}{E_1^{(0)}} - \frac{|V_{12}|^2}{E_2^{(0)} - E_1^{(0)}}, \tag{3.26}$$

which becomes

$$\Delta E = J_z + 2h_z + \frac{2NJ_a^2}{J_z + 2h_z} - \frac{(2N-10)J_a^2}{J_z + 2h_z} = J_z + 2h_z + \frac{10J_a^2}{J_z + 2h_z}. \tag{3.27}$$

So taking into account the contribution from the sector with higher number of domain walls gives a positive contribution to the gap which cancels the dependence on the system size N of the correction to the ground state.

The analytic treatment of higher sectors with $N_{dw} > 2$ is very difficult while the $N_{dw} \leq 2$ case can be solved analytically. In order to avoid the nonphysical dependence on the system size N while still working with $N_{dw} \leq 2$ states exclusively we redefine the coupling between the ferromagnetic state and the states with $l = 1, 2$ in the two domain wall sector by dividing it by a factor $\sqrt{N}$. This procedure makes the energy correction to the ferromagnetic state independent of the system size. Note that this redefined coupling only has consequences for the zero momentum states $p = 0$. Another way of viewing this is that we redefine the ferromagnetic state as set of independent localized non-excited "particles" (or single non-overturned spins)

$$|p = 0, l = 0\rangle = \frac{1}{\sqrt{N}} \sum_i |i, 0\rangle, \tag{3.28}$$

where the states $|i, 0\rangle$ with zero domain length are independent and orthogonal $\langle i, 0|j, 0\rangle = \delta_{i,j}$. This approach can be viewed to some extent as the independent particle approximation. In this case the redefined Hamiltonian is

$$\begin{aligned} \hat{H}_{red}|p, l\rangle = (1 - \delta_{l,0}) \Big\{ \Big[J + h_z l + \Big(J_B - 2J_\perp \cos\frac{p}{2} \Big) \delta_{l,1} \Big] |p, l\rangle - 2J_a \cos p \Big[|p, l + 2\rangle \\ + |p, l - 2\rangle (1 - \delta_{l,2})(1 - \delta_{l,1}) \Big] - 2h_\perp \cos\frac{p}{2} \Big[|p, l + 1\rangle + |p, l - 1\rangle (1 - \delta_{l,1}) \Big] \Big\} \\ - \Big[J_a (|p, 2\rangle \delta_{l,0} + |p, 0\rangle \delta_{l,2}) + h_\perp (|p, 1\rangle \delta_{l,0} + |p, 0\rangle \delta_{l,1}) \Big] \delta_{p,0}, \end{aligned} \tag{3.29}$$

where the last term describes the coupling between the ferromagnetic and the two domain wall states.

The redefined Hamiltonian can be solved analytically and for some coupling parameters its solution can be given in exact and closed form.

3.3 Eigenvalues and eigenvectors

Before we diagonalize the redefined Hamiltonian we want to see also numerically how an upper limit on the number of domain walls affects the eigenvalues of the Hamiltonian. For a finite system size the Hamiltonian can be diagonalized numerically but the number of states increases dramatically with N_{dw} and the system size N. In further numerical calculations in this section we focus on $\mathrm{CoCl_2 \cdot 2H_2O}$ which has the following coupling parameters

$$J_z = 36.5 \text{ K}, \quad J_a = 3.8 \text{ K}, \quad J_\perp = 5.43 \text{ K}, \quad J_B = 0, \tag{3.30}$$

which have been obtained from far-infrared absorption spectroscopy [88] and spin wave analysis of neutron scattering experiments [104–106]. It is convenient for further consideration to use system of units in terms of the leading J_z coupling that gives

$$J = J_z = 1, \quad J_a = 0.1041J, \quad J_\perp = 0.149J, \tag{3.31}$$

since the coupling coefficient $J = J_z - 2J_B$ is given by Eq. (3.16).

The external uniform magnetic field was chosen at $h_z = 0.05J$. An important consequence of interchain coupling in $\mathrm{CoCl_2 \cdot 2H_2O}$ is that it causes the ferromagnetic spin chains to order antiferromagnetically with respect to each other below $T_N = 17.3\,\text{K}$, see [95, 96]. This implies that in the antiferromagnetic phase below T_N the magnetic field h_z used here should be interpreted as a sum of the external applied magnetic field and an internal field, which arises due to the magnetic moments of neighboring chains [88].

3.3.1 Suitable parameters for numerical calculation

The Hamiltonian (3.2) can be diagonalized numerically but the number of allowed states rises exponentially fast with system size like $\sim 2^N$. The number of states can be reduced by using periodic boundary conditions, that allows only states with even number of domain walls $N_{dw} = 0, 2, 4, \ldots$ We also impose a maximal N_{dw} since J_z is the largest coupling and we study low-energy excitations at low temperature. In addition we use translational and reflection symmetries of the Hamiltonian that also reduces the number of allowed states.

In the case of $\mathrm{CoCl_2 \cdot 2H_2O}$ in the absence of a transversal magnetic field ($h_\perp = 0$) and no next-nearest-neighbour coupling ($J_B = 0$) the states with even and odd domain lengths l are decoupled. These sectors can therefore be separately diagonalized.

The low energy spectrum as a function of system size for a chain described by the parameters (3.31) for $\mathrm{CoCl_2 \cdot 2H_2O}$ is shown in Figure 3.6 for different maximal N_{dw} of sectors included in the numerical diagonalization. The correction from $N_{dw} = 2$ states shifts the ground state energy towards negative energies and the shift depends on the system size N. This dependence of the ground state energy shift is linear in N in accordance with the perturbation theory in Eq. (3.24). We can see in Figure 3.6(a) that for the $N_{dw} \leq 2$ diagonalization the excited levels depend very weakly on the system size, except for the lowest excited state which energy increases linearly with N. This is the ferromagnetic state where all spins are anti-aligned with the magnetic field h_z. Its energy descends into the low-energy spectrum only in a relatively weak field for a small system. This finite system-size effect on the energy of the anti-aligned ferromagnetic state does not depend on the N_{dw}-approximation and is also visible in Figure 3.6(b).

As can be seen from the $N_{dw} \leq 6$ diagonalization, Figure 3.6(b), the contribution from higher $N_{dw} > 2$ sectors gives corrections to the excited states also that results in a negative shift of these energy levels which depends also on the chain length and acts as to compensate the ground state energy correction. Therefore the energy gap between excited states and the ground state does not depend on the system size when one includes the high N_{dw} states.

The maximal number of domain walls in a finite chain is equal to the system size N that corresponds to the antiferromagnetic state with opposite aligned neighbour spins. Certainly it is not possible to include into consideration all domain wall sectors even for a relatively small chain due to computational restriction, so we need to find a suitable maximal N_{dw} for a reasonably large system size N. In order to do this for low energy excitations we can consider the behaviour of the gap between the first excited state and the ground state as a function of the system size N and pick a value of $N_{dw,max}$ so that the energy gap no longer depends significantly on system size.

Using the parameters (3.31) the energy gap between the first excited and the ground state behaves as shown in Figure 3.7. We can conclude that for this parameters a reasonably good value is $N_{dw,max} = 6$ for a chain with length $N = 34$ sites while the better approximation with maximum 8 domain walls ($N_{dw} \leq 8$) is out of reach due to computer performance for this system size. In addition, we see that the redefined effective coupling in the Hamiltonian in Eq. (3.29) gives a quite good agreement with the approximation $N_{dw} \leq 6$ for the energy gap for the finite system size $N = 34$. However, the true gap value for a large system size N is more likely to be lower than this as is indicated by extrapolating the $N_{dw} \leq 8$ curve in Figure 3.7.

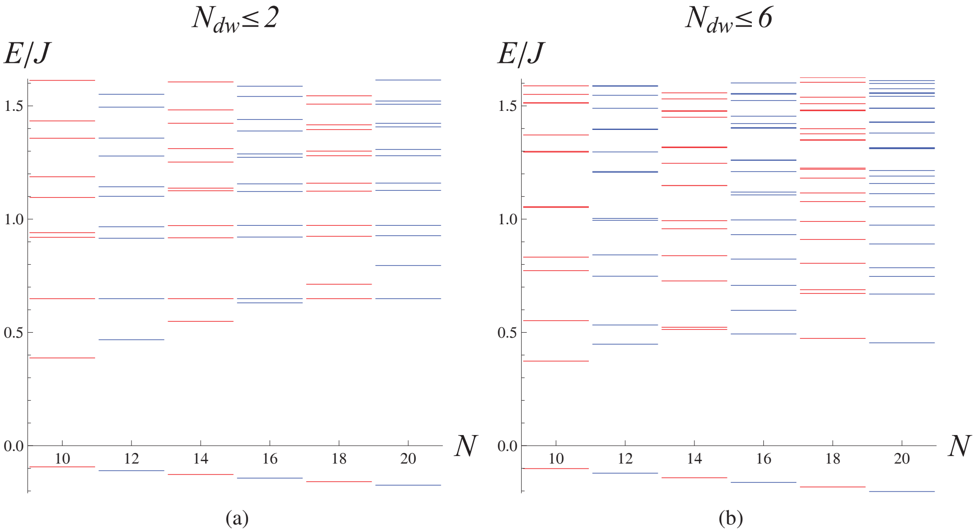

(a)

(b)

Figure 3.6: Energy levels of zero momentum eigenstates for a chain with parameters of $\mathrm{CoCl_2 \cdot 2H_2O}$ as function of the system size N. The plots differs by having different maximal number of domain walls, $N_{dw} \leq 2$ (a) and $N_{dw} \leq 6$ (b). Including high N_{dw} sectors gives a negative shift of excited levels that compensate the negative shift of the ground state energy. Due to finite system-size effect in relatively weak magnetic field h_z the first excited state for small N corresponds to the ferromagnetic state of all spins anti-aligned with the magnetic field h_z which energy increases linearly with the system size N.

3.4 Analytic diagonalization of the redefined Hamiltonian

We now return to the redefined Hamiltonian in Eq. (3.29) for $N_{dw} \leq 2$ which can be diagonalized analytically. In order to solve the eigenvalue problem the eigenstate $|n,p\rangle$ with energy E_n can be expressed in the basis of two domain wall states in Eq. (3.4) as

$$|n,p\rangle = \sum_{l=0}^{\infty} \psi_{n,l}(p)|p,l\rangle, \tag{3.32}$$

where $\psi_{n,l}(p)$ are coefficients which are complex-valued in general. Normalizing the eigenstates results in

$$\sum_{l=0} \psi^{*}_{n',l}(p')\, \psi_{n,l}(p) = \delta_{n,n'}\delta_{p,p'}, \tag{3.33}$$

where the asterisk $*$ corresponds to complex conjugation.

The eigenvalue equation for the $\hat{H}_{red}$ operator is given by the action of the redefined Hamil-

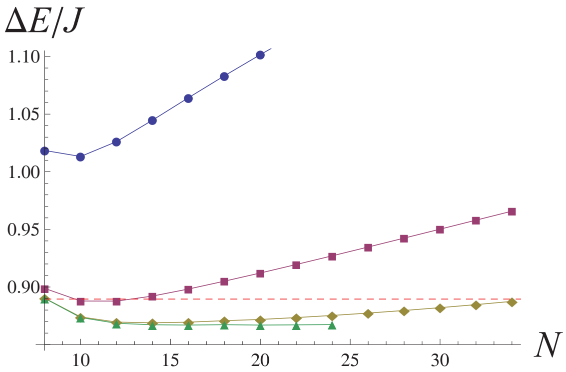

Figure 3.7: Energy gap between the ground state and the first excited state in the even sector for different N_{dw} as a function of the system size N. The color symbols specify the maximum N_{dw} included in the diagonalization: blue solid circles ($N_{dw} = 2$), magenta squares ($N_{dw} = 4$), brown diamonds ($N_{dw} = 6$) and green triangles ($N_{dw} = 8$). The dashed red line shows the energy gap obtained analytically for $N_{dw} \leq 2$ with the $1/\sqrt{N}$ redefinition of the coupling to the ferromagnetic state.

tonian in Eq. (3.29) that can be written in the form of an equation set

$$\begin{cases} -(h_\perp \psi_{n,1} + J_a \psi_{n,2})\delta_{p,0} = E_n \psi_{n,0}\delta_{p,0}, \\ [J + h_z + (J_B - 2J_\perp \cos p)]\psi_{n,1} - h_\perp \cos(p/2)(2\psi_{n,2} + \psi_{n,0}\delta_{p,0}) - 2J_a \cos p\, \psi_{n,3} = E_n \psi_{n,1}, \\ [J + 2h_z]\psi_{n,2} - 2h_\perp \cos(p/2)(\psi_{n,3} + \psi_{n,1}) - J_a \cos p\,(2\psi_{n,4} + \psi_{n,0}\delta_{p,0}) = E_n \psi_{n,2}, \\ [J + 3h_z]\psi_{n,3} - 2h_\perp \cos(p/2)(\psi_{n,4} + \psi_{n,2}) - 2J_a \cos p(\psi_{n,5} + \psi_{n,1}) = E_n \psi_{n,3}, \\ \quad\vdots \\ [J + l h_z]\psi_{n,l} - 2h_\perp \cos(p/2)(\psi_{n,l+1} + \psi_{n,l-1}) - 2J_a \cos p(\psi_{n,l+2} + \psi_{n,l-2}) = E_n \psi_{n,l}, \\ \quad\vdots \end{cases} \tag{3.34}$$

The first equation in the set corresponds to the coupling between the ferromagnetic state with the coefficient $\psi_{n,l=0}(p = 0)$ and the zero-momentum excited states with a single ($l = 1$) or two overturned spins ($l = 2$).

The equation set in Eq. (3.34) describes the infinite system size limit ($N \to \infty$). In the case of a finite spin chain there are modification to the high-energy states as they are coupled to the ferromagnetic state where all spins are opposite to the h_z field. Since we are interested in low-energy excitations at low temperature for a macroscopic chain, the coupling to the high-energy ferromagnetic state can be neglected.

In the general case when all coupling parameters are present, the equation set in Eq. (3.34) has a complicated solution which is hard to analyze analytically. We consider therefore two limits. One where the coupling $J_a = 0$ and another where the effective transversal field $h_\perp = 0$. In both these cases the solution can easily be analyzed in analytical form.

Vanishing coupling $J_a = 0$: The equation set becomes

$$\begin{cases} (h_\perp \psi_{n,1} + E_n \psi_{n,0})\delta_{p,0} = 0, \\ [J + h_z + (J_B - 2J_\perp \cos p) - E_n]\psi_{n,1} - h_\perp \cos(p/2)(2\psi_{n,2} + \psi_{n,0}\delta_{p,0}) = 0, \\ [J + 2h_z - E_n]\psi_{n,2} - 2h_\perp \cos(p/2)(\psi_{n,3} + \psi_{n,1}) = 0, \\ \quad \vdots \\ [J + lh_z - E_n]\psi_{n,l} - 2h_\perp \cos(p/2)(\psi_{n,l+1} + \psi_{n,l-1}) = 0, \\ \quad \vdots \end{cases} \tag{3.35}$$

The equation for large $l \geq 2$ can be written in the form

$$\psi_{n,l} = \frac{2h_\perp \cos(p/2)}{J + lh_z - E_n}(\psi_{n,l+1} + \psi_{n,l-1}), \tag{3.36}$$

which is similar to a recurrent relation for Bessel functions [107] and indicates that the solution can be given in terms of a Bessel function of order dependent on l.

Vanishing transversal field $h_\perp = 0$: In this case states with even and odd domain lengths are decoupled and can be separated. The equation set for the states in the even domain length sector is

$$\begin{cases} (J_a \psi_{n,2} + E_n \psi_{n,0})\delta_{p,0} = 0, \\ [J + 2h_z - E_n]\psi_{n,2} - J_a \cos p\,(2\psi_{n,4} + \psi_{n,0}\delta_{p,0}) = 0, \\ \quad \vdots \\ [J + lh_z - E_n]\psi_{n,l} - 2J_a \cos p(\psi_{n,l+2} + \psi_{n,l-2}) = 0, \qquad l \in \text{even}, \\ \quad \vdots \end{cases} \tag{3.37}$$

For the states in odd sector we have the following relation

$$\begin{cases} [J + h_z + (J_B - 2J_\perp \cos p) - E_n]\psi_{n,1} - 2J_a \cos p\,\psi_{n,3} = 0, \\ [J + 3h_z - E_n]\psi_{n,3} - 2J_a \cos p(\psi_{n,5} + \psi_{n,1}) = 0, \\ \quad \vdots \\ [J + lh_z - E_n]\psi_{n,l} - 2J_a \cos p(\psi_{n,l+2} + \psi_{n,l-2}) = 0, \qquad l \in \text{odd}, \\ \quad \vdots \end{cases} \tag{3.38}$$

In the limit of large domain length l we get a recurrent relation similar to Eq. (3.36)

$$\psi_{n,l} = \frac{2J_a \cos p}{J + lh_z - E_n}(\psi_{n,l+2} + \psi_{n,l-2}), \tag{3.39}$$

which also has a Bessel function solution.

3.4.1 Spectrum in zero magnetic field

The eigenvalue problem of the redefined Hamiltonian (3.29) can be easily solved in the case of zero longitudinal magnetic field h_z. Using Fourier transform of the wave function coefficients

$$\phi_{n,k}(p) = \frac{1}{\sqrt{N}} \sum_l e^{-ikl} \psi_{n,l}(p), \tag{3.40}$$

the equation in the set (3.34) for large domain length $l \geq 2$ can be written as

$$\begin{aligned} J\phi_{n,k}(p) + ih_z \frac{\partial}{\partial k}\phi_{n,k}(p) - 4h_\perp \cos(p/2)\, \cos k\, \phi_{n,k}(p) \\ - 4J_a \cos p\, \cos(2k)\, \phi_{n,k}(p) = E_n \phi_{n,k}(p), \end{aligned} \tag{3.41}$$

where the following relation was used

$$\frac{\partial \phi_{n,k}(p)}{\partial k} = \frac{1}{\sqrt{N}} \sum_l \frac{\partial}{\partial k} e^{-ikl} \psi_{n,l}(p) = -i \frac{1}{\sqrt{N}} \sum_l e^{-ikl}\, l\, \psi_{n,l}(p). \tag{3.42}$$

For vanishing longitudinal field $h_z = 0$, the wave function coefficients $\phi_{n,k}(p)$ can be cancelled on both sides of Eq. (3.41) and the energy spectrum of the system becomes continuous. In this case the energy spectrum becomes

$$E_{cont}(k,p) = J - 4h_\perp \cos(p/2)\, \cos k - 4J_a \cos p\, \cos(2k), \tag{3.43}$$

where $0 \leq k \leq 2\pi$ and is shown in Figure 3.8 for $h_\perp = 0$.

States with short domain lengths give an additional contribution that describes a *"kinetic bound state"*. This kinetic mode can be calculated analytically for the vanishing coupling constant J_a or the vanishing transversal field $h_\perp$ by using the corresponding wave function ansatz in the following form

$$\psi_l(p)_{\text{kin}} = Az^l, \qquad J_a = 0 \tag{3.44}$$

$$\psi_l(p)_{\text{kin}} = A' z'^{l/2}, \qquad h_\perp = 0, \tag{3.45}$$

where A and A' are normalizing constants, and the new variables were introduced

$$z = \frac{2h_\perp \cos(p/2)}{2J_\perp \cos p - J_B}, \qquad z' = \frac{2J_a}{2J_\perp - J_B \sec p}, \tag{3.46}$$

with $\sec x$ being secant of argument x. Inserting these ansatze into Eq. (3.34) one finds

$$E_{kin}(p) = J + J_B - 2J_\perp \cos p - 2h_\perp z \cos(p/2), \qquad J_a = 0, \tag{3.47}$$

$$E'_{kin}(p) = J + J_B - 2J_\perp \cos p - 2J_a z' \cos p, \qquad h_\perp = 0. \tag{3.48}$$

We can see that the ansatz wave functions are normalizable only for $|z| < 1$ (or $|z'| < 1$), thus the bound state exists only for these values of z (or z'). This requirement implies that the

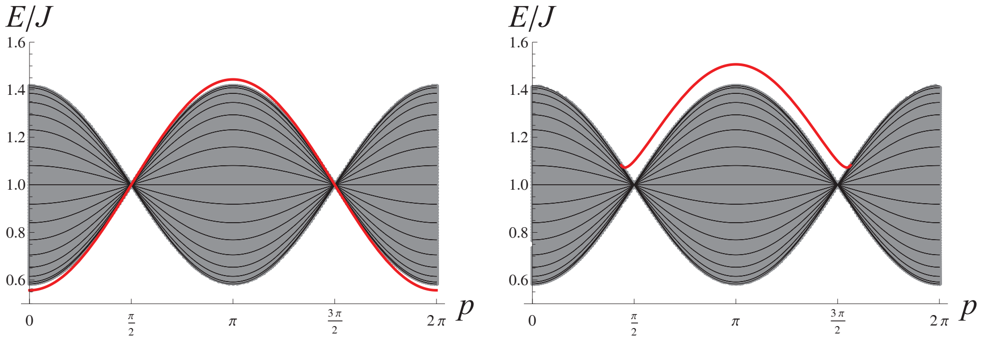

(a) (b)

Figure 3.8: Energy spectrum in zero magnetic fields $h_z = 0$ and $h_\perp = 0$ at low temperature for different values of the next-neighbor coupling: (a) $J_B = 0$ and (b) $J_B = 0.1J$. The red line corresponds to the bound state given by Eq. (3.48), the black lines describes analytically the continuous energy spectrum of the system for the same selected values of k in Eq. (3.43). The shaded gray region corresponds to energy solutions obtained by numerical diagonalizing the redefined Hamiltonian. The underlying gray line of numerical solution corresponding to the bound state coincides with the red line of analytical solution.

kinetic bound state exists when

$$\left|\cos\frac{p}{2}\right| < \frac{h_\perp}{2J_\perp}\sqrt{\frac{h_\perp^2 + 2J_\perp(2J_\perp + J_B) - h_\perp\sqrt{h_\perp^2 + 4J_\perp(2J_\perp + J_B)}}{8J_\perp^2}}, \qquad J_a = 0. \tag{3.49}$$

In the case of the vanishing transversal field $h_\perp$ the kinetic mode exists at

$$\cos p < \frac{J_B}{2(J_a + J_\perp)} \quad \cup \quad \cos p > \frac{-J_B}{2(J_a - J_\perp)}, \qquad h_\perp = 0. \tag{3.50}$$

The energy gap between the continuous spectrum and the kinetic bound state vanishes at the edges of these regions, see Figure 3.8(b).

Ground state

The ground state of the system is dominated by the zero domain wall state, but the coupling J_a (or $h_\perp$) mixes this with the two domain wall sector, that induces quantum fluctuations. The ground state energy is shifted slightly below zero (energy of the ferromagnetic state) by these fluctuations. For small parameters $h_\perp \ll J$ and $J_a \ll J$, the ground state energy is given by

$$E_0\big|_{h_z=0} \approx -h_\perp^2 \frac{1 + \frac{J}{2(J_B - 2J_\perp)}\left(1 - \sqrt{1 - \frac{12h_\perp^2}{J^2}}\right)}{J + J_B - 2J_\perp + \frac{3h_\perp^2}{J_B - 2J_\perp}} \approx -\frac{h_\perp^2}{J + J_B - 2J_\perp}, \qquad J_a = 0, \tag{3.51}$$

$$E_0'\big|_{h_z=0} = -\frac{J}{6}\left(1 - \sqrt{1 - 12\frac{J_a^2}{J^2}}\right) \approx -\frac{J_a^2}{J}, \qquad h_\perp = 0. \tag{3.52}$$

The corresponding wave function coefficients of the ground state are

$$\psi_{0,l}(p=0) = \begin{cases} -A_0 \frac{h_\perp}{E_0} z_0, & l=0, \\ A_0\, z_0^l, & l=1,2,3,\dots \end{cases} \qquad J_a = 0, \tag{3.53}$$

$$\psi'_{0,l}(p=0) = \begin{cases} 2A'_0, & l=0, \\ A'_0\, {z'_0}^{l/2}, & l=2,4,6,\dots \end{cases} \qquad h_\perp = 0, \tag{3.54}$$

where A_0 and $A'_0 = \sqrt{1-z'_0}/(2-z'_0)$ are normalizing constants, and the variables z_0 and z'_0 are

$$z_0 = \frac{-2h_\perp}{J_B - 2J_\perp + h_\perp^2/E_0} \approx 2\frac{h_\perp}{J}, \qquad z'_0 = -\frac{2E'_0}{J_a} \approx 2\frac{J_a}{J}. \tag{3.55}$$

This approximation is valid for small $h_\perp/J$ and J_a/J.

3.4.2 Spectrum in a finite magnetic field

Consider now the case of a finite longitudinal magnetic field h_z. First of all we will study excitations with large domain lengths, which correspond to the high energy spectrum of single domain states, for which the equations for $l > 2$ in the two limits of the vanishing parameters J_a and $h_\perp$ are given by Eqs. (3.36) and (3.39). Using new variables

$$\mu_n = \frac{E_n - J}{h_z}, \qquad x = \frac{4h_\perp \cos(p/2)}{h_z}, \tag{3.56}$$

$$\mu'_n = \frac{E_n - J}{2h_z}, \qquad x' = \frac{2J_a \cos p}{h_z}. \tag{3.57}$$

these equations can be transformed into the well-known form

$$\psi_{n,l} = \frac{x}{2(l-\mu_n)}(\psi_{n,l+1} + \psi_{n,l-1}), \qquad J_a = 0, \tag{3.58}$$

$$\psi_{n,l} = \frac{x'}{2(l/2-\mu'_n)}(\psi_{n,l+2} + \psi_{n,l-2}), \qquad h_\perp = 0, \tag{3.59}$$

which corresponds to a recurrent relation for Bessel functions. Therefore the equations (3.58) and (3.59) have the solution for the wave function coefficients in terms of Bessel functions of the first kind

$$\psi_{\mu_n,l}(p) = J_{l-\mu_n}(x), \qquad J_a = 0, \tag{3.60}$$

$$\psi_{\mu'_n,l}(p) = J_{l/2-\mu'_n}(x'), \qquad h_\perp = 0. \tag{3.61}$$

In general we can extend this definition also for negative values of l. Orthonormality of the wave function coefficients gives restriction which is used to define acceptable values of the variable

μ_n. Thus the special case of Neumann's addition theorem for Bessel function [65, 108]

$$\sum_{k=-\infty}^{\infty} J_k(x)\, J_{k+n}(x) = J_n(0) = \delta_{n,0}, \tag{3.62}$$

indicates that the solutions in Eqs. (3.60) and (3.61) are orthogonal and normalized to unity only when the order of the Bessel functions is an integer. The last statement gives that the parameters μ_n and μ'_n are integer

$$\mu_n = n, \qquad \mu'_n = 2n, \tag{3.63}$$

where n is an integer number. From the relations for μ_n and μ'_n in Eqs. (3.56) and (3.57) we obtain the energy levels corresponding to the equidistant energy spectrum

$$E_n(p) = J + h_z n, \tag{3.64}$$

which describes the Wannier-Zeeman ladder (WZL) [62].

In order to study low-energy excitations we have to take into account also states with short domain length $l \leq 2$ which contribution changes significantly the energy spectrum. Continuing by considering the two limits of the vanishing parameters J_a and $h_\perp$ separately we can solve the eigenvalue problem analytically.

Vanishing coupling $J_a = 0$: The equation set in Eq. (3.35) can be written

$$\begin{cases} \psi_{n,0} = -\dfrac{h_\perp}{E_n}\psi_{n,1}\delta_{p,0}, \\ [J + h_z + (J_B - 2J_\perp \cos p)] - E_n = 2h_\perp \cos(p/2)\dfrac{\psi_{n,2}}{\psi_{n,1}} - \dfrac{h_\perp^2}{E_n}\delta_{p,0}, \\ \quad\vdots \\ [J + lh_z] - E_n = 2h_\perp \cos(p/2)\dfrac{\psi_{n,l+1} + \psi_{n,l-1}}{\psi_{n,l}}, \qquad\qquad \text{for } l \geq 2 \end{cases} \tag{3.65}$$

where the first equation describes coupling to the ferromagnetic state and contributes only for zero-momentum states. This contribution defines the ground state of the spin system with the ground state energy E_0 and does not affect significantly any excited states since the ratio $h_\perp/E_n \ll 1$ for the single domain excitation energy E_n which is at least of the order of the strongest coupling J (each domain wall costs an energy of $J_z/2$). Therefore we consider first the energy spectrum of states with non-zero momentum p.

We are looking for solution of the wave function coefficients in terms of Bessel functions

$$\psi_{\nu_n,l}(p) = BJ_{l-\nu_n}(x), \tag{3.66}$$

where B is normalizing constant, the argument x is given in Eq. (3.56), and ν_n is to be determined by Eq. (3.65). Substituting the wave function coefficients (3.66) into the set (3.65) the energy eigenvalues become parameterized by ν_n as

$$E_n(p) = J + h_z\nu_n. \tag{3.67}$$

Inserting into the second equation in the set, $l = 1$, we have

$$J_B - 2J_\perp \cos p = -2h_\perp \cos(p/2) \left. \frac{J_{l-1-\nu_n}(x)}{J_{l-\nu_n}(x)} \right|_{l=1}, \tag{3.68}$$

which determines the parameter ν_n. Equation (3.68) can be written in the following form

$$\frac{J_{-\nu_n}(x)}{J_{1-\nu_n}(x)} = \frac{1}{z}, \qquad\qquad J_a = 0, \tag{3.69}$$

where the momentum dependent constant z is given by Eq. (3.46).

Vanishing transversal field $h_\perp = 0$**:** In this case states with even and odd domain lengths are decoupled and are described by Eqs. (3.37) and (3.38). For states with even domain length l the equation sets are

$$\begin{cases} \psi_{n,0} = -\dfrac{J_a}{E_n}\psi_{n,2}\delta_{p,0}, \\ [J + 2h_z] - E_n = J_a \cos p \, \dfrac{2\psi_{n,4} + \psi_{n,0}\delta_{p,0}}{\psi_{n,2}}, \\ \quad \vdots \\ [J + lh_z] - E_n = 2J_a \cos p \dfrac{\psi_{n,l+2} + \psi_{n,l-2}}{\psi_{n,l}}, \qquad l \in \text{even}, \end{cases} \tag{3.70}$$

and for states with odd length of domain

$$\begin{cases} [J + h_z + (J_B - 2J_\perp \cos p)] - E_n = 2J_a \cos p \, \dfrac{\psi_{n,3}}{\psi_{n,1}}, \\ \quad \vdots \\ [J + lh_z] - E_n = 2J_a \cos p \dfrac{\psi_{n,l+2} + \psi_{n,l-2}}{\psi_{n,l}}, \qquad l \in \text{odd}, \end{cases} \tag{3.71}$$

The states in even domain length sector are coupled to the ferromagnetic ground state by the first equation in the set in Eq. (3.70). This coupling plays an important role for the ground state while its contribution to excited states are vanishing small due to the small ratio $J_a/E_n \ll 1$ for the excitation energy E_n which is at least of the order of the strongest coupling J. In order to study the excitation spectrum we consider now non-zero momentum states when this coupling is absent.

In this case we are looking for a solution for the wave function coefficients in the form

$$\psi_{\nu'_n,l}(p) = B' J_{l/2-\nu'_n}(x'), \tag{3.72}$$

where $J_n(x')$ is the Bessel function of the first kind of order n with argument x' given by Eq. (3.57), B' is a normalizing constant. Substituting the relation (3.72) into the sets in Eqs. (3.70) and (3.71) we get the energy levels parameterized by the variable ν'_n as

$$E'_n(p) = J + 2h_z\nu'_n \tag{3.73}$$

in each domain length sector. The parameter ν'_n is determined by the equation sets in Eq. (3.70) and (3.71), the first equation corresponding to the shortest domain length ($l = 1$ and $l = 2$ for the odd and even sectors respectively) imposes a restriction and determines this parameter. Therefore ν'_n has two branches of solutions, one for odd and one fore even sectors of the domain length l. For even lengths

$$\frac{J_{-\nu'_n}(x')}{J_{1-\nu'_n}(x')} = 0, \qquad l \in \text{even}, \tag{3.74}$$

and for the states in the odd sector

$$\frac{J_{-1/2-\nu'_n}(x')}{J_{1/2-\nu'_n}(x')} = \frac{1}{z'}, \qquad l \in \text{odd}, \tag{3.75}$$

where the momentum dependent constant z' is given by Eq. (3.46).

We can summarize and conclude that a finite longitudinal magnetic field h_z splits the continuous energy spectrum in Eq. (3.43) into discrete levels

$$E_n(p) = J + h_z\nu_n, \qquad J_a = 0, \tag{3.76}$$

$$E'_n(p) = J + 2h_z\nu'_n, \qquad h_\perp = 0, \tag{3.77}$$

where $\nu_n,\ \nu'_n$ are determined by Eqs. (3.36) and (3.39). This determines the parameter ν_n to be a solution of the equation

$$\frac{J_{-\nu_n}(x)}{J_{1-\nu_n}(x)} = \frac{1}{z}, \qquad J_a = 0. \tag{3.78}$$

For vanishing transversal field $h_\perp = 0$, the parameter ν'_n obeys the relations

$$\frac{J_{-1/2-\nu'_n}(x')}{J_{1/2-\nu'_n}(x')} = \frac{1}{z'}, \qquad \text{for } \textit{odd} \text{ sector}, \tag{3.79}$$

$$\frac{J_{-\nu'_n}(x')}{J_{1-\nu'_n}(x')} = 0, \qquad \text{for } \textit{even} \text{ sector}, \tag{3.80}$$

with $J_n(x)$ being the Bessel function of the first kind of order n. The momentum dependent constants z and z' are given in Eq. (3.46), and the momentum dependent arguments of the Bessel functions are

$$x = \frac{4h_\perp \cos(p/2)}{h_z}, \qquad x' = \frac{2J_a \cos p}{h_z}. \tag{3.81}$$

The low-energy spectrum of the system in the field $h_z = 0.05J$ is shown in Figure 3.9.

The wave function coefficients are expressed in terms of Bessel functions and are given by the following relations

$$\psi_{\nu_n,l}(p) = BJ_{l-\nu_n}(x), \qquad J_a = 0, \tag{3.82}$$

$$\psi_{\nu'_n,l}(p) = B'J_{l/2-\nu'_n}(x'), \qquad h_\perp = 0, \tag{3.83}$$

where B and B' are normalization constants, which can be found by using the identity [108]

$$\sum_{l=l_0}^{\infty} J_{l-\nu}^2(x) = -\frac{x}{2} J_{l_0-\nu}^2(x) \frac{\partial}{\partial \nu} \left[\frac{J_{l_0-\nu-1}(x)}{J_{l_0-\nu}(x)} \right], \tag{3.84}$$

that gives the following expressions for the normalization constants

$$B = \sqrt{2 \left\{ x \frac{\partial}{\partial \nu} \left[\frac{J_\nu(x)}{J_{\nu+1}(x)} \right] \right\}^{-1}} \Bigg|_{\nu=-\nu_n}, \qquad J_a = 0, \tag{3.85}$$

$$B' = \sqrt{2 \left\{ x' \frac{\partial}{\partial \nu} \left[\frac{J_{\nu-1/2}(x')}{J_{\nu+1/2}(x')} \right] \right\}^{-1}} \Bigg|_{\nu=-\nu_n'}, \qquad h_\perp = 0, \tag{3.86}$$

Orthogonality of the wave functions in Eqs. (3.82) and (3.83) follows from the properties of product sum of Bessel functions [108]

$$\sum_{k=1}^{\infty} J_{k+\nu}(x) J_{k+\mu}(x) = \frac{x}{2} \frac{J_{1+\nu}(x) J_{1+\mu}(x)}{\nu - \mu} \left(\frac{J_\nu(x)}{J_{1+\nu}(x)} - \frac{J_\mu(x)}{J_{1+\mu}(x)} \right), \tag{3.87}$$

when the variable ν obeys the Eqs. (3.78)–(3.80).

The longitudinal h_z-field shifts the energy of the kinetic bound state by an amount which is given to linear order in h_z by the following expression

$$\begin{aligned} E_{kin}(p) =& E_{kin}\Big|_{h_z=0} + \frac{h_z}{1-z^2} \\ &= J + J_B - 2J_\perp \cos p - 2h_\perp z \cos(p/2) + \frac{h_z}{1-z^2}, \qquad J_a = 0, \end{aligned} \tag{3.88}$$

$$\begin{aligned} E_{kin}'(p) =& E_{kin}'\Big|_{h_z=0} + \frac{h_z}{1-z'^2} \\ &= J + J_B - 2J_\perp \cos p - 2J_a z' \cos p + \frac{h_z}{1-z'^2}, \qquad h_\perp = 0. \end{aligned} \tag{3.89}$$

For high energy excited states in the magnetic field we can expand the solutions and obtain the equidistant spectrum (for details see our Article II [109]) describing the Wannier-Zeeman ladder (WZL) [62]

$$E_n = J + h_z n, \tag{3.90}$$

where n is integer number corresponding to state with $n \gg 1$.

Zero momentum states: In the case of the momentum $p = 0$ the corresponding states contain also the zero domain wall sector giving additional coupling. Using the wave function coefficients in terms of Bessel functions in Eqs. (3.82) and (3.83) the second relation in Eqs. (3.65) and (3.70) can be written for the small domain length l as

$$J_B - 2J_\perp + \frac{h_\perp^2}{E_n} = -2h_\perp \frac{J_{l-1-\nu_n}(x_0)}{J_{l-\nu_n}(x_0)} \Bigg|_{l=1}, \qquad J_a = 0, \tag{3.91}$$

$$\frac{J_a^2}{E_n'} = -2J_a \frac{J_{l/2-1-\nu_n'}(x_0')}{J_{l/2-\nu_n'}(x_0')} \Bigg|_{l=2}, \qquad h_\perp = 0, \tag{3.92}$$

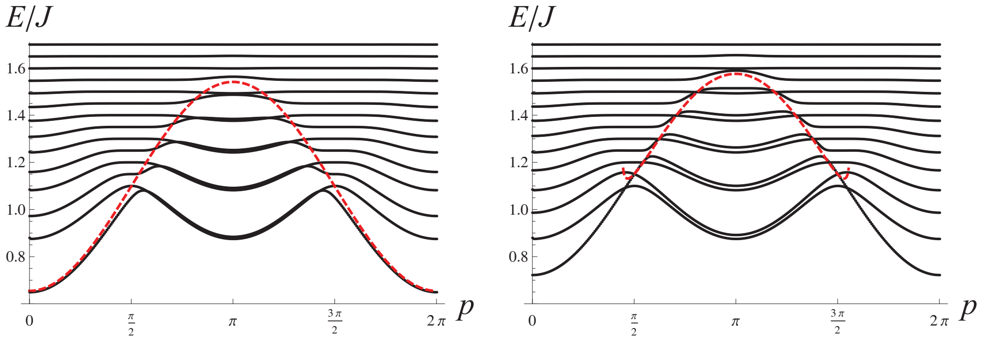

(a) (b)

Figure 3.9: Low-energy spectrum of the redefined Hamiltonian (3.29) in the longitudinal magnetic fields $h_z = 0.05J$ ($h_\perp = 0$) at low temperature for different values of the next-neighbor coupling: (a) $J_B = 0$ and (b) $J_B = 0.1J$. The dashed red line corresponds to the approximate analytical solution in Eq. (3.89) for the kinetic bound state.

where the energies are $E_n = J + h_z\nu_n$ and $E'_n = J + 2h_z\nu'_n$ given by Eqs. (3.76) and (3.77), and arguments of Bessel functions x_0 and x'_0 correspond to the zero momentum case and become

$$x_0 = x\big|_{p=0} = \frac{4h_\perp}{h_z}, \qquad\qquad x'_0 = x'\big|_{p=0} = \frac{2J_a}{h_z}. \tag{3.93}$$

That modifies finally Eqs. (3.78) and (3.80) defining ν_n to the form

$$\frac{J_{-\nu_n}(x_0)}{J_{1-\nu_n}(x_0)} = \frac{1}{z_n^0}, \qquad\qquad J_a = 0, \tag{3.94}$$

$$\frac{J_{-\nu'_n}(x'_0)}{J_{1-\nu'_n}(x'_0)} = \frac{1}{z_n'^0}, \qquad\qquad h_\perp = 0, \tag{3.95}$$

where the introduced parameters z_n^0 and $z_n'^0$ are similar to the constants z_0 and z'_0 in Eq. (3.55) and are given by

$$z_n^0 = \frac{-2h_\perp}{J_B - 2J_\perp + h_\perp^2/(J + h_z\nu_n)}, \qquad\qquad z_n'^0 = -2\frac{J + 2h_z\nu_n}{J_a}. \tag{3.96}$$

For simplifying further calculations it is convenient to use the following notations of the normalized wave function coefficients

$$C_l^n(p) = \frac{\psi_{\nu_n,l}(p)}{\sqrt{\sum_l |\psi_{\nu_n,l}(p)|^2}}, \tag{3.97}$$

where the index n describes the eigenstate with the eigenenergy E_n and l is the length of the domain.

Ground state

The lowest energy solutions ν_0 and ν'_0 of Eqs. (3.94) and (3.95) give the ground state energy which can be approximated analytically for the small parameter $h_\perp \ll J$ and $J_a = 0$ by the relation

$$E_0 \approx -h_\perp^2 \frac{1 + \frac{3h_\perp^2}{(J+h_z)(J_B-2J_\perp)}}{J + h_z + J_B - 2J_\perp + \frac{3h_\perp^2}{J_B-2J_\perp}} \approx \frac{-h_\perp^2}{J + h_z + J_B - 2J_\perp}. \tag{3.98}$$

Whereas in the case $h_\perp = 0$ and $J_a \ll J$ the ground state energy becomes

$$E'_0 \approx -\frac{J + 2h_z}{6}\left(1 - \sqrt{1 - \frac{12J_a^2}{(J+2h_z)^2}}\right) \approx -\frac{J_a^2}{J + 2h_z}. \tag{3.99}$$

The wave function coefficients corresponding to the zero domain wall sector are given by

$$\psi_{\nu_n,l=0}(p=0) = \frac{-h_\perp}{J + h_z\nu_n} B J_{1-\nu_n}(x_0), \qquad J_a = 0, \tag{3.100}$$

$$\psi_{\nu'_n,l=0}(p=0) = \frac{-J_a}{J + 2h_z\nu'_n} B' J_{1-\nu'_n}(x'_0), \qquad h_\perp = 0, \tag{3.101}$$

where B and B' are constants which can be found from the normalization condition.

For simplifying notation of further calculations it is convenient to redefine the wave function coefficients of the fluctuated ground state as

$$\phi_0(l) = \psi_{\nu_{min},l}(0), \tag{3.102}$$

where ν_{min} corresponds to the lowest energy solutions ν_0 and ν'_0.

Note that the zero domain-wall sector gives the biggest contribution only to the ground state. For excited zero-momentum states with energy $E_n \gg h_\perp$ and $E'_n \gg J_a$ its contribution becomes vanishing small, so we can work exclusively in the two domain wall sector $N_{dw} = 2$ to describe the excited low-energy spectrum.

3.4.3 Solution of the ratio of Bessel functions

We consider now briefly the low energy spectrum and its general behaviour for different coupling parameters. In order to define the single domain excitation we have to solve the general equation with the ratio of Bessel functions

$$\frac{J_{-\nu}(x)}{J_{1-\nu}(x)} = \gamma, \tag{3.103}$$

where γ is constant. Particular analytical solutions of this equation has been found in some limits [110]. An intuitive picture of the solutions of Eq. (3.103) can be gotten by plotting the left hand side of the equation as a function of ν for a fixed value of x. This is shown in Figure 3.10 for the argument $x = 1$ as the black solid curve.

In the case of $\gamma \to 0$ corresponding to the big z limit in Eqs. (3.78)–(3.79) and the even sector for $h_\perp = 0$ in Eq. (3.80) the solutions are gotten by the crossings of the curve with the x-axis in Figure 3.10. We see that these crossings occur almost exactly at positive integer values of ν, except for the first lowest solution which is slightly below unity. These values of ν as a function of x for the zero constant γ is shown in Figure 3.11(a). To a very good approximation the solution ν is a positive integer at $\nu \geq 1 + |x|$. This implies that in the case of vanishing transversal field $h_\perp$ the eigenstates in the even domain lengths sector are described by the solution ν'_n of Eq. (3.80) which is to a good approximation integers $\nu'_n = n$, where $n \in 1, 2, 3, \ldots$ when $n \geq |x'| + 1$. The eigenenergies of these even states in Eq. (3.76) become

$$E_n^{even} = J + 2h_z n, \qquad \nu'_n = n, \qquad n \in \mathbb{Z} \quad \cap \quad n \geq |x'| + 1, \qquad \begin{cases} h_\perp = 0, \\ l \in \text{even}. \end{cases} \tag{3.104}$$

For smaller values of n, the solution ν'_n is generally lower and depends on the argument x' of the Bessel functions. In the case of small γ, that corresponds to the big values of z in Eq. (3.78) and for the odd l sector in Eq. (3.79), the solutions are very similar to the case of $\gamma = 0$. This means that in the case of the vanishing $h_\perp$ the solutions for the odd states ν'_n correspond to half-integer numbers $\nu'_n = n - 1/2$, where $n \in 1, 2, 3, \ldots$ when $n \geq |x'| + 1$, that describes the energy levels of the odd states

$$E_n^{odd} = J + (2n-1)h_z, \quad \nu'_n = n - \frac{1}{2}, \quad n \in \mathbb{Z} \quad \cap \quad n \geq |x'| + 1, \quad \begin{cases} h_\perp = 0, \\ l \in \text{odd}. \end{cases} \tag{3.105}$$

In the case of $J_a = 0$ the solutions ν_n are integers $\nu_n = n$, where $n \in 1, 2, 3, \ldots$ for $n \geq |x| + 1$, and the eigenvalues E_n in Eq. (3.76) form the equidistant energy spectrum

$$E_n = J + h_z n, \qquad \nu_n = n, \qquad n \in \mathbb{Z} \quad \cap \quad n \geq |x| + 1, \qquad J_a = 0, \tag{3.106}$$

which describes the WZL.

A simple qualitative analysis of how the solution ν behaves with changing γ for a fixed argument x in Eq. (3.103) can be performed from Figure 3.10. While the big value solutions describing the higher-energy levels do not change substantially for this fixed value of x, the lowest solution ν_0 corresponding to the lowest-energy level decreases with increasing γ. The solutions ν of Eq. (3.103) as functions of x for a fixed value of the constant $\gamma = 2$ are shown in Figure 3.11(b). We see that for positive x the lowest energy solution ν_0 decreases with increasing argument x. The lowest solution behavior can be given analytically.

Using the relation for the first derivative of Bessel function

$$J'_\nu(z) = \frac{J_{\nu-1}(z) - J_{\nu+1}(z)}{2} \qquad (\nu \neq 0), \tag{3.107}$$

we get

$$x^\nu J_{1-\nu} = -\frac{d}{dx}\left(x^\nu J_{-\nu}\right) \tag{3.108}$$

that allows to modify the left hand side of the equation (3.103) as

$$\frac{J_{-\nu}(x)}{J_{1-\nu}(x)} = -\left\{\frac{\nu}{x} + \frac{d}{dx}\ln J_{-\nu}(x)\right\}^{-1}. \tag{3.109}$$

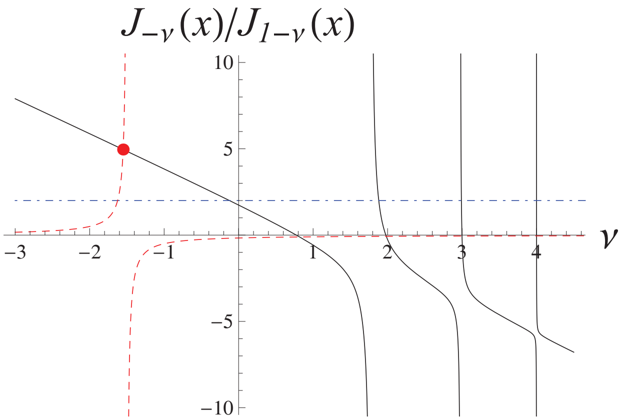

Figure 3.10: The behavior of the ratio of Bessel functions $J_{-\nu}(x)/J_{1-\nu}(x)$ for fixed argument $x = 1$ as a function of ν is plotted as the black solid curve. The blue dot-dashed line corresponds to $\gamma = 2$, while the red dashed curve shows the right hand side of Eq. (3.114) for fixed values of $x_0 = 1$, $y = 3/2$ and $b = 0$. The crossing point (the red solid circle) describes the lowest energy solution ν_0 of the zero momentum even sector, the ground state.

Now using the asymptotic expression [65] for Bessel function

$$J_{-\nu}(-\nu\xi) \approx \frac{\xi^{-\nu} e^{-\nu\sqrt{1-\xi^2}}}{\sqrt{-2\pi\nu}\,\sqrt[4]{1-\xi^2}\,\left(1+\sqrt{1-\xi^2}\right)^{-\nu}}, \qquad \nu \to \infty, \quad 0 < \xi < 1 \tag{3.110}$$

and taking the limit of large ν the ratio of the Bessel functions can be written in the form

$$\frac{J_{-\nu}(-\nu\xi)}{J_{1-\nu}(-\nu\xi)} = \frac{1+\sqrt{1-\xi^2}}{\xi} = \gamma, \qquad x = -\nu\xi, \tag{3.111}$$

that gives the following asymptote to the lowest energy solution

$$\nu_0 \approx -\frac{x}{2}\left(\gamma + \frac{1}{\gamma}\right). \tag{3.112}$$

The corresponding dot-dashed blue line with this slope $(\gamma + \gamma^{-1})/2$ for a fixed value of $\gamma = 2$ is shown in Figure 3.11(b).

The limit of large argument x (or x') given in Eq. (3.81) corresponds to the limit of vanishing magnetic field h_z. Therefore the lowest excitation energy in this case can be calculated by using the asymptotic result in Eq. (3.112) and the definitions of γ and x. In particular, in the case of the coupling parameters $J_B = 0$ (or $J = J_z$) and $h_\perp = 0$ the energy of the lowest excited state is

$$E = J + h_z(2\nu - 1) \approx J - 2J_\perp \left[1 + \left(\frac{J_a}{J_\perp}\right)^2\right] \cos p, \tag{3.113}$$

that corresponds to a spin wave excitation in the chain [111]. This result can also be obtained

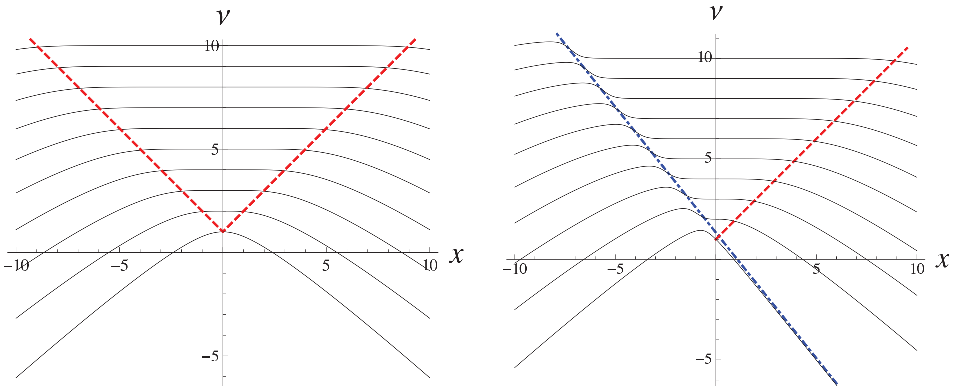

(a) (b)

Figure 3.11: (a) Solutions ν of Eq. (3.103) as a function of x for $\gamma = 0$. The red dashed line is the line $\nu = 1 + |x|$. (b) Solutions ν of this equation as a function of x for $\gamma = 2$. The dot-dashed blue line has slope $(\gamma + \gamma^{-1})/2$ while the red dashed line corresponds to the line $\nu = 1 + x$ for positive x.

by second-order perturbation theory in the limit of vanishing magnetic field h_z in the case of the coupling parameters $J_a \ll J_\perp \ll J$.

The asymptotic solution can be extended to negative x where it coincides with smooth step-like behaviors of the energy levels in Figure 3.11(b). These steps become sharper and higher for increasing γ and they become a step discontinuity of unit one for $\gamma \to \infty$. This characteristic behaviour of the solutions restricts the existence of the WZL to $n > (\gamma + \gamma^{-1})|x| + 1$ for $x < 0$ and $\gamma > 1$.

Consider now the zero momentum states which are coupled to the ferromagnetic state. In this case the relations defining ν_n in Eqs. (3.94) and (3.95) are modified and can be written in the general form

$$\frac{J_{-\nu_n}(x_0)}{J_{1-\nu}(x_0)} = \frac{2b}{x_0} - \frac{x_0}{4(y+\nu)}, \tag{3.114}$$

where constants b and y are given by

$$b = \frac{2J_\perp - J_B}{h_z}(1 - \delta_{h_\perp,0}), \qquad y = \frac{J}{h_z}, \tag{3.115}$$

and argument x_0 corresponds to the variables x_0 and x_0' given by Eqs. (3.93). The equation (3.114) has an additional negative solution $\nu_0 < 0$ which is well separated from the other positive solutions ν_n and describes the ground state energy. This solution appears due to the singular behavior of the right-hand side in the neighbourhood of $\nu = y$ while the first term gives a shift along the ordinate that is shown as the dashed red curve for a fixed value of $y = -3/2$ and $b = 0$ in Figure 3.10.

We can see that in the case of vanishing constant b due to the rapid changing of the Bessel function ratio on the left hand side around positive even integer values of ν, the right hand side of the relation (3.114) changes only slightly the high even integer solutions found for $p \neq 0$

from Eq. (3.103). However, there is a crucial difference for the lowest energy solution. Since the right hand side has a singularity at $\nu = -y$ and the left hand side is positive for $\nu < 0$ and increases as $\nu \to -\infty$, somewhere below this singularity a negative solution $\nu_0 \lesssim -y$ will occur, see the red dashed curve in Figure 3.10. This lowest solution corresponds to the ground state energy which will be negative because $E_0 = J + h_z \nu_0$ and $\nu_0 < -J/h_z$, since $y = J/h_z$.

In the case of non-zero b the shift of the right side of the equation (3.114) causes vertical shift of the red dashed curve in Figure 3.10. This shift modifies only slightly the lowest energy solution corresponding to the ground state due to its rapid variations around the singularity $\nu = -y$. In the case of a positive constant b only the second low energy solution is modified significantly. This solution describes the energy of the first excited state which corresponds to the kinetic bound state at zero momentum $p = 0$. For a negative b, corresponding to a negative vertical shift, a number of higher energy solutions are also affected. The number depends on the magnitude of the shift due to the kink-like behavior of the Bessel functions ratio, see Figure 3.10.

The energy levels $E_n(p)$ for the coupling parameters in Eq. (3.31) corresponding to $\mathrm{CoCl_2} \cdot 2\mathrm{H_2O}$ is shown in Figure 3.12. The energy spectrum is equidistant in the momentum region around $p = \pi/2$ and $p = 3\pi/2$ that is bounded by the red dashed and blue dot-dashed curves which correspond to the asymptotic color lines in Figure 3.11(b). The spectrum becomes the WZL for all momenta p in the region of energies where

$$E(p=0) > J_z + 2h_z + 4J_a, \tag{3.116}$$

$$E(p=\pi) > J_z + h_z + 2J_\perp \left[1 + \left(\frac{J_a}{J_\perp} \right)^2 \right], \tag{3.117}$$

that defines the lowest energy level of the WSL which is $E^0_{WSL} \approx 1.6J$ for the $\mathrm{CoCl_2} \cdot 2\mathrm{H_2O}$ parameters. We can see that in the region below this limit of WSL the even levels are symmetric around $\pi/2$ while the odd levels lack this property of symmetry. This is a consequence of the level asymmetry which can be seen in Figure 3.11(b).

3.5 Magnetization

A direct probe of the magnetic Bloch oscillations is the time-dependent total magnetization. We can consider time evolution of the magnetization both along and transverse to the uniform magnetic field. A general time-dependent state of the quantum system can be expressed in terms of the eigenstates as

$$|\chi(t)\rangle = \sum_n a_n(t)\, e^{-iE_n t} |n\rangle, \tag{3.118}$$

where the coefficient $a_n(t)$ describes the square root of the population of eigenstate $|n\rangle$ with energy E_n. The eigenstate is given by Eq. (3.32) in the two domain wall approximation for $N_{dw} \leq 2$.

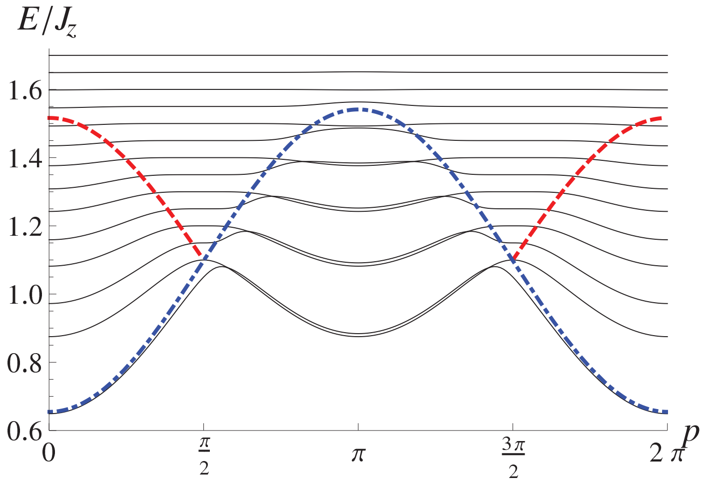

Figure 3.12: Energy levels as a function of momentum p computed with the parameters in Eq. (3.31) for a magnetic field $h_z = 0.05J$. The dot-dashed blue curve corresponds to the asymptotic dot-dashed line drawn in Figure 3.11(b) but with the constant $\gamma = 1.43$. The red dashed curve corresponds to the red dashed line in Figure 3.11(b).

3.5.1 Longitudinal magnetization

The total magnetization along the z-axis corresponds to the expectation value of the spin operator $\hat{S}^z_{q=0} = \sum_i \hat{S}^z_i$ that gives

$$M_z(t) = \langle \chi(t) | \hat{S}^z_{q=0} | \chi(t) \rangle = \int_0^{2\pi} \frac{dp}{2\pi} \sum_{m,n} a^*_m(t) a_n(t) \, \mathbf{S}^z_{mn}(p) \, e^{i[E_m(p) - E_n(p)]t}, \tag{3.119}$$

where $\mathbf{S}^z_{mn}$ is the matrix element of the spin operator which can be expressed as

$$\mathbf{S}^z_{mn}(p) = \langle m | \hat{S}^z_{q=0} | n \rangle = \frac{1}{N} \sum_l C^{m*}_l(p) \, C^n_l(p) \left(\frac{N}{2} - l \right), \tag{3.120}$$

where the notation of the wave function coefficients $C^n_l(p)$ are given in Eq. (3.97). The total magnetization along the z-axis becomes then

$$M_z(t) = \frac{1}{N} \int_0^{2\pi} \frac{dp}{2\pi} \sum_{m,n} a^*_m(t) a_n(t) \, e^{i[E_m(p) - E_n(p)]t} \sum_{l,l'} C^{m*}_{l'}(p) \, C^n_l(p) \left(\frac{N}{2} - l \right), \tag{3.121}$$

where the integration is performed over all momenta p in the Brillouin zone.

Let us consider case of high energy excited states (the limit of WZL) with zero momentum $p = 0$ when the energy spectrum becomes equidistant $E_n = J_z + h_z n$ and the coefficients correspond to the Bessel function of integer order $C^n_l(p = 0) = J_{(l-n)/2}(x'_0)$ in the case of $h_\perp = 0$, where the argument $x'_0 = 2J_a/h_z$ is given in Eq. (3.93). Using the properties of the

Bessel function (see Appendix B) the matrix element in Eq. (3.120) becomes

$$\mathbf{S}^z_{mn}\Big|_{p=0} = \left(\frac{N}{2} - n\right)\delta_{n,m} - x'_0\delta_{|n-m|,2}, \qquad \begin{cases} m, n \in even, \\ m, n \in odd, \end{cases} \tag{3.122}$$

where both indices m, n of the eigenstates are either both even or odd numbers since the operator $\hat{S}^z$ does not mix states in the even and odd domain length sectors. In this case the total magnetization becomes

$$M_z(t) = \frac{N}{2} - \sum_n |a_n(t)|^2 n - 2x'_0 \sum_n \Re\left(a^*_n(t)a_{n+2}(t)e^{-i\omega_B t}\right), \qquad \omega_B = 2h_z. \tag{3.123}$$

The Bloch oscillations can thus be observed directly as time-dependent oscillations in the magnetization. The last term in Eq. (3.123) describes the magnetic BOs and depends on the overlap between next-neighbouring states. The real part of the oscillating term can be written in the form

$$\sum_n \Re\left(a^*_n a_{n+2}e^{-i\omega_B t}\right) = \sum_n \rho_n \cos(\omega_B t - \phi_n), \tag{3.124}$$

where ρ_n and ϕ_n are absolute value and argument of the overlap respectively

$$\rho_n = |a^*_n a_{n+2}|, \qquad \phi_n = \arg(a^*_n a_{n+2}). \tag{3.125}$$

We can see that in order to get the magnetic BOs in a multilevel system at the Bloch frequency $\omega_B = 2h_z$ the phase shift ϕ_n of the population between next-neighbouring states n and $n+2$ should be constant. It means that population of the states should change coherently at least for levels which have the biggest overlap and give the biggest contribution to the magnetic Bloch oscillations.

The state giving maximal amplitude of the magnetic BOs consists of N coherently excited levels (so there are $N-1$ pairs of neighbours). Then the overlap is $\rho_n = 1/N$ with $a_n = 1/\sqrt{N}$ and the phase shift $\phi_n = 0$, and the amplitude of the oscillating magnetization becomes

$$A_B = 2x'_0 \sum_{n=1}^{N-1} \rho_n = 2x'_0 \sum_{n=1}^{N-1} \frac{1}{N} = 2x'_0\left(1 - \frac{1}{N}\right). \tag{3.126}$$

The maximal amplitude ${A_B}^{max} = 2x'_0 = 4J_a/h_z$ of corresponding magnetic BOs can be achieved at the WZL with a large number of coherently excited states. This is twice the amplitude x'_0 derived semiclassically which is natural because here we consider the motion of both a domain wall and an anti-domain wall together.

In the case of uniformly excited states for all momenta p the total magnetization becomes

$$M_z(t) = \frac{N}{2} - \sum_n |a_n(t)|^2 n - \int_0^{2\pi} \frac{dp}{2\pi} 2x' \sum_n \Re\left(a^*_n(t)a_{n+2}(t)e^{-i\omega_B t}\right), \tag{3.127}$$

where the argument $x' = 2J_a\cos(p)/h_z$ is given by Eq. (3.81) and the frequency is $\omega_B = 2h_z$. In this case the magnetic BOs disappear because the corresponding oscillating term in Eq. (3.127) vanishes due to the average $\int_0^{2\pi} dp\, \cos p = 0$.

3.5.2 Transverse magnetization

Consider now the total transverse magnetization along the x-axis

$$M_x(t) = \langle \chi(t)|\hat{S}^x_{q=0}|\chi(t)\rangle = \sum_{m,n} a^*_m(t)a_n(t)\mathbf{S}^x_{mn}e^{i(E_m-E_n)t}, \tag{3.128}$$

where $\mathbf{S}^x_{mn} = \langle m|\hat{S}^x_{q=0}|n\rangle$ is the matrix element of the $\hat{S}^x$-spin operator which can be written in terms of the standard $\hat{S}^+$ and $\hat{S}^-$ operators which act on a zero-momentum state as

$$\hat{S}^+_{q=0}|l\rangle = 2|l+1\rangle, \qquad \hat{S}^-_{q=0}|l\rangle = (2-\delta_{l,1})|l-1\rangle. \tag{3.129}$$

Their corresponding matrix elements are

$$\mathbf{S}^+_{mn} = (\mathbf{S}^-_{mn})^\dagger = \langle m|\hat{S}^+_{q=0}|n\rangle = C^{m*}_0 C^n_1 + 2\sum_{l>0} C^{m*}_l C^n_{l+1}, \tag{3.130}$$

where the notation $C^n_l = C^n_l(p=0)$ of the wave function coefficients was used. That gives the following matrix element of the spin operator along the x-axis

$$\mathbf{S}^x_{mn} = \frac{1}{2}\left(\mathbf{S}^+_{mn} + \mathbf{S}^-_{mn}\right) = \frac{1}{2}\left(C^{m*}_0 C^n_1 + C^n_0 C^{m*}_1 + 2\sum_{l>0}\left(C^{m*}_l C^n_{l+1} + C^n_l C^m_{l+1}{}^*\right)\right). \tag{3.131}$$

The expectation value of the total transverse magnetization is

$$\begin{aligned} M_x(t) &= \sum_{m,n} a^*_m(t)a_n(t)\,\mathbf{S}^x_{mn}\,e^{i(E_m-E_n)t} \\ &= \frac{1}{2}\sum_{m,n}(C^{m*}_0 C^n_1 + C^n_0 C^{m*}_1)a^*_m(t)a_n(t) + \sum_{m,n}\sum_{l>0}\left(C^{m*}_l C^n_{l+1} + C^n_l C^m_{l+1}{}^*\right)a^*_m(t)a_n(t). \end{aligned} \tag{3.132}$$

The first term in Eq. (3.132) gives contributions from transitions between the ground state and excited states (overlap between these states decays exponentially). The last term corresponds to the magnetic BOs in the system.

In the case of the WZL when the energy levels are equidistant and the wave coefficient are described by the Bessel function, using properties of the sum of Bessel function products we obtain

$$M_x(t) = 2\sum_n \Re\left(a^*_n(t)a_{n+1}(t)\,e^{i\omega_B t/2}\right) = 2\sum_n \rho^\perp_n \cos\left(\frac{\omega_B}{2}t - \phi^\perp_n\right), \qquad \omega_B = 2h_z, \tag{3.133}$$

where the sum is performed over all states including the odd and even sectors, the absolute value and argument of the overlap between neighbouring states are

$$\rho^\perp_n = |a^*_n a_{n+1}|, \qquad \phi^\perp_n = \arg(a^*_n a_{n+1}). \tag{3.134}$$

In order to get the magnetic Bloch oscillations in multilevel system the levels should be populated coherently. In the case of N uniformly excited states in the WZL with $a_n = 1/\sqrt{N}$ and the phase shift $\phi_n^{\perp} = 0$ the amplitude of the magnetic BOs becomes

$$A_0^{\perp} = 2\sum_{n=1}^{N-1} \rho_n = 2\left(1 - \frac{1}{N}\right). \tag{3.135}$$

We can see that the transverse magnetization M_x oscillates at half the Bloch frequency $\omega_{\perp} = \omega_B/2 = h_z$ since the separation between neighbour levels of different sectors is $E_{n+1} - E_n = h_z$. The maximal magnitude of these oscillations is $A_{max}^{\perp} = 2$ which does not dependent on the argument x_0' describing the domain length. It reflects the fact that the transverse magnetization in an Ising-like chain is only non-zero on the domain walls and is therefore independent of the size of domains.

3.6 Dynamical structure factor

An indirect way of studying the magnetic Bloch oscillations is to investigate the magnetic excitation spectrum. This can be achieved experimentally by inelastic neutron scattering. The magnetic neutron scattering cross section measured in experiment is related to the dynamic structure factor, or "scattering law" [112], which is defined as

$$S^{\alpha\beta}(q,\omega) = \int dt\, e^{-i\omega t} \frac{1}{N}\sum_{i,j} e^{iq(r_i - r_j)} \langle \hat{S}_i^{\alpha}(t)\hat{S}_j^{\beta}(0)\rangle = \int dt\, e^{-i\omega t} \langle \hat{S}_q^{\alpha}(t)\hat{S}_{-q}^{\beta}(0)\rangle, \tag{3.136}$$

where the expectation value is

$$\langle \hat{S}_q^{\alpha}(t)\hat{S}_{-q}^{\beta}(0)\rangle = \sum_n \frac{1}{Z} e^{-\beta_T E_n} \langle n|\hat{S}_q^{\alpha}(t)\hat{S}_{-q}^{\beta}(0)|n\rangle. \tag{3.137}$$

Here Z is the partition function and the thermodynamic β_T is the inverse temperature of the system

$$Z = \sum_n e^{-\beta_T E^n}, \qquad \beta_T = \frac{1}{k_B T}. \tag{3.138}$$

Since $|n\rangle$ are eigenstates of the Hamiltonian and they form a complete set

$$\sum_m |m\rangle\langle m| = 1, \tag{3.139}$$

the expectation value for a translationally invariant system can be written as

$$\begin{aligned}\langle \hat{S}_q^{\alpha}(t)\hat{S}_{-q}^{\beta}(0)\rangle =& \sum_n \frac{1}{Z} e^{-\beta_T E_n} \langle n|e^{i\hat{H}t}\hat{S}_q^{\alpha} e^{-i\hat{H}t} \sum_m |m\rangle\langle m|\hat{S}_{-q}^{\beta}|n\rangle \\ =& \sum_{n,m} \frac{1}{Z} e^{-\beta_T E_n} e^{i(E_n - E_m)t} \langle n|\hat{S}_q^{\alpha}|m\rangle\langle m|\hat{S}_{-q}^{\beta}|n\rangle. \end{aligned} \tag{3.140}$$

Substituting this into Eq. (3.136) and performing integration over time we obtain the dynamical structure factor at finite temperature

$$S^{\alpha\beta}(q,\omega) = \sum_{n,m} \frac{1}{Z} e^{-\beta_T E_n} \delta\big(\omega - (E_m - E_n)\big) \, \langle n|\hat{S}^{\alpha}_{q}|m\rangle\langle m|\hat{S}^{\beta}_{-q}|n\rangle. \tag{3.141}$$

We consider first the chain at low temperature when the main contribution is given by transitions out of the ground state. In this case the dynamical structure factor for a translationally invariant system becomes

$$S^{\alpha\beta}(q,\omega) = \sum_{m} \delta(\omega - E_m) \, \langle 0|\hat{S}^{\alpha}_{q}|m\rangle\langle m|\hat{S}^{\beta}_{-q}|0\rangle, \tag{3.142}$$

where $|0\rangle$ is the ground state and $|m\rangle$ corresponds to an excited state with energy E_m and momentum q. The dynamical structure factors measured in experiments can be cast into theoretically more transparent forms involving the spin rasing and lowering operators $\hat{S}^{\pm}$

$$\begin{aligned} S^{xx} &= \frac{1}{4}\left[(S^{+-} + S^{-+}) + (S^{--} + S^{++})\right], \\ S^{yy} &= \frac{1}{4}\left[(S^{+-} + S^{-+}) - (S^{--} + S^{++})\right]. \end{aligned}$$

At low temperatures the leading contribution is given by the ferromagnetic state when all spins are aligned along the magnetic field. Then only the dynamical structure factor $S^{+-}(q,\omega)$ has a leading non-zero contribution since only the spin lowering operator $\hat{S^-}$ can act on the ferromagnetic state with non-zero contribution by a creating state with a single overturned spin, see the first line in Eq. (3.8).

3.6.1 $S^{+-}(q,\omega)$

Approximating the ground state as the ferromagnetic spin state $|0,0\rangle$ gives the leading contribution. In this case the non-zero dynamical structure factor S^{+-} takes the form

$$S^{+-}(q,\omega) = \sum_{n}^{\infty} \delta(\omega - E_n(q)) \, I_n(q), \tag{3.143}$$

where I_n is the normalized relative intensity of the n-th mode with a single flipped spin

$$I_n(q) = |C^{n}_{l=1}(q)|^2 = \frac{|\psi_{n,l=1}(q)|^2}{\sum_l |\psi_{n,l}(q)|^2}. \tag{3.144}$$

In this approximation $S^{--} = S^{-+} = S^{++} = 0$ which implies $S^{xx} = S^{yy} = S^{+-}/4$. Using the relations (3.82, 3.83) for the wave function coefficients and the following identity of the Bessel functions [108]

$$\sum_{l=l_0}^{\infty} J^2_{l-\nu}(x) = -\frac{x}{2} J^2_{l_0-\nu}(x) \frac{\partial}{\partial\nu}\left[\frac{J_{l_0-\nu-1}(x)}{J_{l_0-\nu}(x)}\right], \tag{3.145}$$

the intensity can be expressed in the form

$$I_n(q) = 2\left\{ x\frac{\partial}{\partial\nu}\left[\frac{J_\nu(x)}{J_{\nu+1}(x)}\right]\right\}^{-1}\Bigg|_{\nu=-\nu_n}, \qquad J_a = 0, \tag{3.146}$$

$$I'_n(q) = 2\left\{ x'\frac{\partial}{\partial\nu}\left[\frac{J_{\nu-1/2}(x')}{J_{\nu+1/2}(x')}\right]\right\}^{-1}\Bigg|_{\nu=-\nu'_n}, \qquad h_\perp = 0, \tag{3.147}$$

where ν_n is the n-th solution of the equation (3.78) for $J_a = 0$, and ν'_n is the solution of the equation (3.79) for the odd domain length l in the case of $h_\perp = 0$.

For the vanishing longitudinal magnetic field ($h_z = 0$) the relation in Eq. (3.144) can be written in terms of contributions from the continuous and kinetic modes

$$S^{+-}(q,\omega) = I_{kin}\delta(\omega - E_{\text{kin}}) + \frac{1}{\pi}\int_0^{2\pi}\delta(\omega - E_{\text{cont}}(k))I(k)\,dk, \tag{3.148}$$

where the relative intensities for $J_a = 0$ are

$$I_{\text{kin}}(q) = (1 - z^2)\,\Theta(1 - |z|), \qquad J_a = 0, \tag{3.149}$$

$$I(k,q) = \frac{\sin^2 k}{1 - 2z^{-1}\cos k + z^{-2}}, \tag{3.150}$$

and $\Theta(x)$ is the Heaviside step function [113]. In the case of the vanishing field $h_\perp$ the intensities are given by

$$I'_{\text{kin}}(q) = (1 - z'^2)\,\Theta(1 - |z'|), \qquad h_\perp = 0, \tag{3.151}$$

$$I'(k,q) = \frac{\sin^2 k}{1 - 2z'^{-1}\cos k + z'^{-2}}. \tag{3.152}$$

When the parameter $J_B = 0$ and $J_a < J_\perp$ the kinetic mode exists in the full Brillouin zone and its intensity is uniform

$$I'_{\text{kin}} = \left(\frac{J_a}{J_\perp}\right)^2, \qquad J_B = 0. \tag{3.153}$$

The dynamical structure factor S^{+-} for coupling parameters in Eq. (3.31) relevant to $\mathrm{CoCl_2 \cdot 2H_2O}$ is shown in Fig. 3.13 for zero longitudinal and transversal magnetic fields ($h_z = 0$ and $h_\perp = 0$ together). We can see that the inclusion of the next-neighbor interaction leads to an increasing intensity of the kinetic bound state.

The external magnetic field h_z changes the dynamical structure factor by splitting the energy levels. While this is in accordance with Figure 3.14 the structure factor shows very low intensities in the regions where the energy levels are equidistant. Increasing of the next-neighbor coupling J_B causes the kinetic bound state to become more preferable and its corresponding line intensifies as shown in Figure 3.14.

We can go beyond approximating the ground state as the ferromagnetic state by including

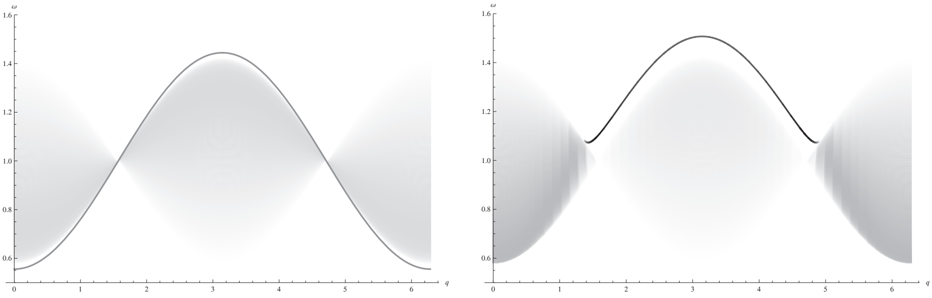

(a) (b)

Figure 3.13: Dynamical structure factor $S^{+-}(q,\omega)$ calculated by the analytic expression for zero magnetic fields $h_z = 0$ and $h_\perp = 0$ at low temperature for different values of the next-neighbor coupling: (a) $J_B = 0$ and (b) $J_B = 0.1J$. Other parameters as in Eq. (3.31).

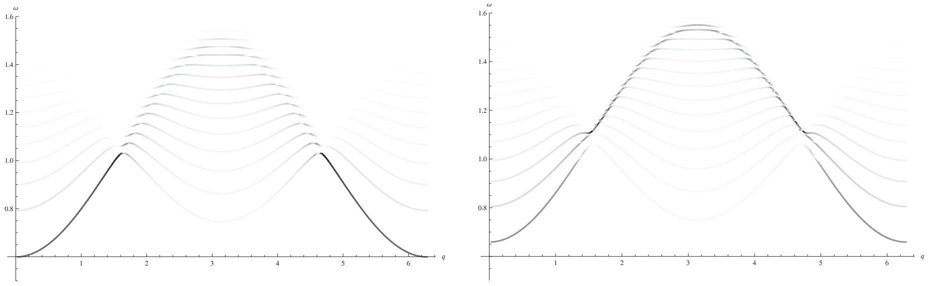

(a) (b)

Figure 3.14: Dynamical structure factor $S^{+-}(q,\omega)$ in the magnetic field $h_z = 0.02J$ and $h_\perp = 0$ at low temperature for different values of the next-neighbor coupling: (a) $J_B = 0$ and (b) $J_B = 0.1J$. Other parameters as in Eq. (3.31).

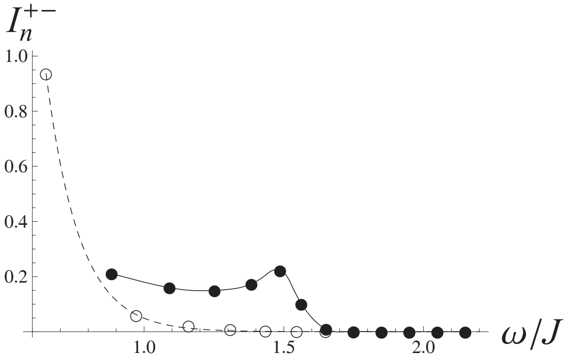

Figure 3.15: Intensities $I^{+-}(q)$ vs. ω at low temperature for the coupling parameters in Eq. (3.31) and magnetic field $h_z = 0.05J$. The results for two momenta are shown: $q = 0$ (open circles, dashed line) and $q = \pi$ (solid circles, solid line). The lines are guides to the eye.

the quantum fluctuations in the ground state. This can be formally written

$$I_n^{+-}(q) = \left(C_0 C_1^n(q) + 2 \sum_{l>0} C_l C_{l+1}^n(q) \cos(ql/2) \right)^2 , \tag{3.154}$$

where we have used the following notation for the normalized wave function coefficients

$$C_l = \frac{\phi_0(l)}{\sqrt{\sum_l |\phi_0(l)|^2}}, \qquad C_l^n(q) = \frac{\psi_{n,l}(q)}{\sqrt{\sum_l |\psi_{n,l}(q)|^2}} \tag{3.155}$$

corresponding to the ground state and n-th excited state in the chain respectively, $\phi_0(l)$ describes the wave function coefficients of the fluctuated ground state, see Eq. (3.102).

The leading terms of the intensity in Eq. (3.154) give the contribution

$$I_n^{+-}(q) \approx C_0^2 I_n(q) + 4 C_0 C_{l_0} C_1^n(q) C_{l_0+1}^n(q) \cos(q l_0/2), \tag{3.156}$$

where $l_0 = 1$ for $J_a = 0$ and $l_0 = 2$ in the case of $h_\perp = 0$. The change introduced by this correction is relatively small and hardly visible for the parameters used in Figure 3.14. Corresponding expressions for the intensities I^{-+}, I^{++} and I^{--} of the corresponding dynamical structure factors in this approximation are given in Appendix.

In Figure (3.15) we can see for the material parameters in Eq. (3.31) how the intensities I_n^{+-} changes for the different levels for two momenta $q = 0$ and $q = \pi$, open circles with dashed line and solid circles with solid line respectively. For zero momentum the intensities drop exponentially with frequency, while for $q = \pi$ the intensities decrease only slightly before their increase at the energy of the lowest WZL level, and then they drop rapidly. This behaviour also reflects the fact that the main contribution in Eq. (3.156) comes from transitions to the state with a single overturned spin $l = 1$.

3.6.2 $S^{zz}(q,\omega)$

At low temperature the dynamical structure factor S^{zz} characterizes the longitudinal magnetization squared which is mostly determined by fluctuations in the ground state carrying zero momentum. The wave function of the ground state can be expressed as a superposition of states $|p=0,l\rangle$ with the coefficients $\phi_0(l)$. Since the operator $\hat{S}^z$ acts on a two domain wall state by the formula

$$\hat{S}^z_q|p,l\rangle = \frac{1}{2}N|p,l\rangle\delta_{q,0} - \frac{1-e^{iql}}{1-e^{iq}}|p+q,l\rangle, \tag{3.157}$$

the dynamical structure factor S^{zz} at low temperature is given by

$$S^{zz}(q,\omega) = S^2\left[N - 2\frac{\sum_l l\phi_0^2(l)}{\sum_l \phi_0^2(l)}\right]^2 \delta(q)\delta(\omega) + 4S^2\sum_n \delta(\omega - E_n(q))\, I^{zz}_n(q), \tag{3.158}$$

where $S=1/2$ for the spin-$\frac{1}{2}$ chain of length N, and I^{zz}_n is the normalized relative intensity of the n-th mode given by

$$I^{zz}_n(q) = \frac{\left[\sum_{l=1}^N \phi_0(l)\psi_{n,l}(q)\sin(ql/2)\right]^2}{\sin^2(q/2)\sum_l \phi_0^2(l)\ \sum_l \psi^2_{n,l}(q)}. \tag{3.159}$$

The first term in Eq. (3.158) describes the leading order contribution from the squared total magnetization of the ferromagnetic state: $S^{zz}_{\text{FM}} = (NS)^2\delta(q)\delta(\omega)$. The correction to the SN-term is caused by quantum fluctuations which flips spins and gives finally the term $N/2 - \langle l\rangle$, where $\langle l\rangle$ is the average domain length in the ground state.

The intensity $I^{zz}_n(q)$ in Eq. (3.158) has the following leading behaviour

$$\begin{aligned}
I^{zz}_n(q) =& \frac{E_0^2}{h_\perp^2}\frac{|\psi_{n,l=1}(q)|^2}{\sum_l|\psi_{n,l}(q)|^2} \approx \frac{h_\perp^2}{(J+J_B-2J_\perp+2h_z)^2}\, I_n(q), && J_a = 0, && (3.160)\\
I'^{zz}_n(q) =& \frac{4E'^2_0}{J_a^2}\frac{|\psi_{n',l=2}(q)|^2}{\sum_l|\psi_{n',l}(q)|^2}\cos^2(q/2)\\
\approx&\ \frac{4J_a^2}{(J+2h_z)^2}\cos^2(q/2)\, I'^{\text{ev}}_n(q), && h_\perp = 0, && (3.161)
\end{aligned}$$

where the normalized relative intensity I_n is given by Eq. (3.146) for $J_a=0$, the introduced intensity I'^{ev}_n corresponds to contributions from states with even l for $h_\perp = 0$ and can be written as

$$I'^{\text{ev}}_n(q) = 2\left\{x'\frac{\partial}{\partial\nu}\left[\frac{J_\nu(x')}{J_{\nu+1}(x')}\right]\right\}^{-1}\Bigg|_{\nu=-\nu'_n}, \tag{3.162}$$

where ν'_n is the solution of the Eq. (3.80) for the even domain length l. The relative intensity I'^{ev}_n contribution to the dynamical structure factor in $\text{CoCl}_2\cdot 2\text{H}_2\text{O}$ can be seen in Figure 3.16. We can see that only excitations to even n level gives non-zero contribution which implies that S^{zz} is independent of the coupling $J_\perp$. However, the total spectral weight of $S^{zz}(q\neq 0)$ is much smaller than for S^{+-} since it is proportional to the probability to find two overturned spins in the ground state, which is reflected by the small factor $4J_a^2/(J+2h_z)^2$ in Eq. (3.161).

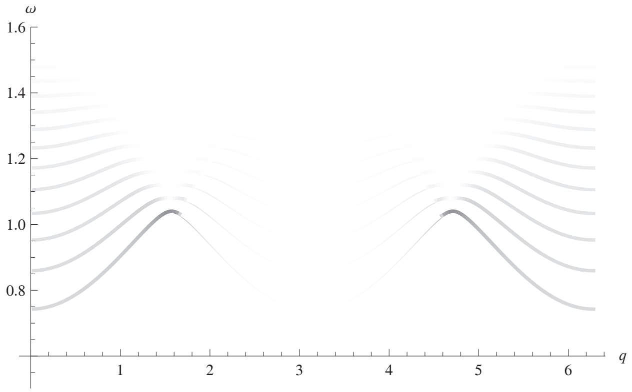

Figure 3.16: The dynamical structure factor $S^{zz}(q,\omega)$ at low temperature for a magnetic field $h_z = 0.02J$ and the coupling constants $h_\perp = 0,\ J_B = 0$. Other parameters as in Eq. (3.31). The intensity of the plot has been increased by a factor $(J+2h_z)^2/(4J_a^2) \approx 25$ in order to make it visible.

3.6.3 Dynamical structure factor at finite temperature

In a real experiment at finite temperature thermal effects have to be taken into account. The dynamical structure factor for a translationally invariant system at non-zero temperature is given by Eq. (3.141) and can be rewritten as

$$S^{\alpha\gamma}(q,\omega) = \sum_{m,n} \frac{1}{Z} e^{-\beta_T E_n} \langle n|\hat{S}^{\alpha}_{q}|m\rangle \langle m|\hat{S}^{\gamma}_{-q}|n\rangle\, \delta\big(\omega - (E_m - E_n)\big), \tag{3.163}$$

where $|n\rangle$ and $|m\rangle$ correspond to excited states with energy E_n and E_m respectively, Z is the partition function.

Since the operator $\hat{S}^z$ acts on a two domain wall state by the formula given in Eq. (3.157) the dynamical structure factor S^{zz} can be written as

$$S^{zz}(q,\omega) = \sum_{m,n} \int \frac{dp}{2\pi} \frac{e^{-\beta_T E^n(p)}}{Z} \mathbf{S}^{zz}_{mn}(p,q)\, \delta\left[\omega - (E^m(p+q) - E^n(p))\right], \tag{3.164}$$

where the integration is performed over p-momentum in the first Brillouin zone and $\mathbf{S}^{zz}_{mn}(p,q)$ is the matrix element of transition between the system states $|m\rangle$ and $|n\rangle$ which is given by

$$\begin{aligned}\mathbf{S}^{zz}_{mn}(p,q) = \frac{1}{4}\left(N \sum_l C^n_l(p) C^m_l(p) - 2\sum_l l C^n_l(p) C^m_l(p)\right)^2 \delta_{q,0} \\ + (1-\delta_{q,0}) \frac{1}{\sin^2 q/2} \left(\sum_l C^n_l(p) C^m_l(p+q) \sin\frac{ql}{2}\right)^2,\end{aligned} \tag{3.165}$$

where we use the notation of the wave function coefficients $C^n_l(p)$ given in Eq. (3.97). The first term of the transition matrix element in Eq. (3.165) describes the total bulk magnetization squared at $q = 0$.

Similarly the transverse dynamical structure factor is

$$S^{+-}(q,\omega) = \sum_{m,n} \int \frac{dp}{2\pi} \frac{e^{-\beta_T E^n(p)}}{Z} \mathbf{S}^{+-}_{mn}(p,q)\, \delta\left[\omega - (E^m(p+q) - E^n(p))\right], \tag{3.166}$$

where $\mathbf{S}^{+-}_{mn}(p,q)$ is the transition matrix element between the energy eigenstates $|m\rangle$ and $|n\rangle$, and is given by the expression

$$\mathbf{S}^{+-}_{mn}(p,q) = \left[C^n_0(0) C^m_1(q) \delta_{p,0} + 2 \sum_{l>0} C^n_l(p) C^m_{l+1}(p+q)\, \cos\left(\frac{ql - p}{2}\right) \right]^2. \tag{3.167}$$

3.7 Limit of WZL

While the expressions in Eqs. (3.164) and (3.166) can be calculated numerically it is possible to work out an analytic expression in the simplifying case when all energy levels are equidistant. We consider the case of zero transversal field $h_\perp = 0$ and vanishing coupling constant $J_B = 0$. The assumption of an equidistant energy spectrum describing the WZL leads to the following restrictions on the parameters

1. Argument x' of Bessel function should be small: $h_z \geq 2J_a$.

2. The parameter z' in Eq. (3.46) should be large: $J_\perp \ll h_\perp$.

These conditions allow to get the integer roots $\nu'_n = n$ of Eqs. (3.79) and (3.80) with the energy spectrum $E_n = J + h_z n$ where the even (odd) number n describes states in the even (odd) domain length sector, see Eqs. (3.104) and (3.105). The normalized wave functions Eq. (3.155) correspond then to Bessel function of integer order

$$C^n_l(p) = J_{\frac{l-n}{2}}(x'_0 \cos p) = J_{\frac{l-n}{2}}\left(\frac{2J_a \cos p}{h_z}\right), \tag{3.168}$$

where we extended the expression to all integer l (not necessarily positive). The normalization comes from the property of Bessel functions: $\sum_{k=-\infty}^{\infty} J^2_k(x) = 1$.

The partition function in the case of the equidistant energy spectrum becomes

$$Z = 1 + \sum_{n>0} e^{-\beta_T(J + h_z n)} = 1 + \frac{e^{-\beta_T J}}{e^{\beta_T h_z} - 1}, \tag{3.169}$$

where β_T is the inverse temperature of the system.

3.7.1 $S^{zz}(q,\omega)$

Substituting Eq. (3.168) into the expression for the matrix element $\mathbf{S}^{zz}_{mn}$ in Eq. (3.165), the second term with $q \neq 0$ becomes

$$\mathbf{S}^{zz}_{mn}\Big|_{q\neq 0} = \frac{1}{\sin^2(q/2)} \left(\sum_{l>0} J_{\frac{l-n}{2}}(x_0' \cos p)\, J_{\frac{l-m}{2}}\big(x_0' \cos(p+q)\big) \sin\frac{ql}{2} \right)^2 . \tag{3.170}$$

The Bessel functions in Eq. (3.170) have integer order because the variables l, n and m are even (or odd) simultaneously. Therefore, it is convenient to introduce a new integer-valued variable $t = (l-n)/2$ and rewrite the sum in the form

$$\begin{aligned}\sum_{t>1-\frac{n}{2}} J_t(x_0' \cos p)\, J_{t+\frac{n-m}{2}}\big(x_0' \cos(p+q)\big) \sin\left[q\Big(t+\frac{n}{2}\Big)\right] \\ = J_{\frac{n-m}{2}}(\zeta') \sin\left[\Big(p-\frac{\pi}{2}\Big)\frac{n-m}{2} + q\frac{n}{2}\right], \end{aligned} \tag{3.171}$$

where we introduced a new variable

$$\zeta' = x_0' |\sin q| = \frac{2J_a}{h_z} |\sin q|. \tag{3.172}$$

The sum over the product of Bessel functions was performed using Graf's addition theorem [65]

$$\sum_{k=-\infty}^{\infty} J_{k+\nu}(u)\, J_k(v) \overset{\sin}{\underset{\cos}{}}(k\phi) = J_\nu(w) \overset{\sin}{\underset{\cos}{}}(\nu\chi) \tag{3.173}$$

with the relations $w = \sqrt{u^2 + v^2 - 2uv\cos\phi}$, $w\cos\chi = u - v\cos\phi$, and $w \sin\chi = v \sin\phi$. With this the dynamical structure factor S^{zz} for $q \neq 0$ can be written in the form

$$\begin{aligned} S^{zz}(q,\omega)\Big|_{q\neq 0} =& \frac{1}{\sin^2 q/2} \sum_{m,n} \frac{e^{-\beta_T (J+h_z n)}}{Z} \delta(\omega - (m-n)) \\ & \times J^2_{\frac{n-m}{2}}(\zeta') \begin{cases} 1/2, & n \neq m, \\ \sin^2(q\frac{n}{2}), & n = m, \end{cases} \end{aligned} \tag{3.174}$$

where integration over momentum p was performed for integer values of n and m variables

$$\int_0^{2\pi} \frac{dp}{2\pi} \sin^2\left[\Big(p-\frac{\pi}{2}\Big)\frac{n-m}{2} + q\frac{n}{2}\right] = \begin{cases} 1/2, & n \neq m, \\ \sin^2(q\frac{n}{2}), & n = m. \end{cases} \tag{3.175}$$

Since there are not allowed transitions between the even and odd sectors the order of Bessel function is integer, so it is convenient to introduce a new integer variable $k = (m-n)/2$ which describes energy difference between states at the transitions.

We can reorder the double sum as

$$\sum_{m,n} = \left(\sum_{m\geq n} + \sum_{m<n}\right)\sum_{n} = \sum_{m\geq n}\sum_{n} + \sum_{m}\sum_{n>m} = \sum_{n}\sum_{k\geq 0} + \sum_{m}\sum_{k<0}, \tag{3.176}$$

that allows to rewrite the dynamical structure factor in the case of non-zero energy transitions, when $n \neq m$ and $k \neq 0$, in the following form

$$\begin{aligned} S^{zz}\Big|_{q,\omega\neq 0} =& \frac{1}{2\sin^2 q/2}\frac{e^{-\beta_T J}}{Z}\frac{1}{e^{\beta_T h_z}-1} \\ & \times \sum_{k\neq 0}\delta(\omega - 2h_z k) J_k^2(\zeta')\begin{cases} 1, & k>0, \\ e^{\beta_T 2h_z k}, & k<0, \end{cases} \end{aligned} \tag{3.177}$$

where we used the expression for the sum of the first N terms of a geometric series

$$\sum_{n=1}^{N} e^{-\beta_T h_z n} = e^{-\beta_T h_z}\frac{1-e^{-\beta_T h_z N}}{1-e^{-\beta_T h_z}} \approx \frac{1}{e^{\beta_T h_z}-1}. \tag{3.178}$$

For the zero mode, when $n = m$, in order to find the sum in Eq. (3.174) we can use the following identity

$$\sum_{n=1}^{\infty} \sin^2(an) e^{-bn} = \frac{1}{1-e^{-b}}\frac{\sin^2 a}{2}\frac{1+e^{-b}}{\cosh b - \cos 2a}, \tag{3.179}$$

which can be proved using Euler's formula and sum of terms of geometric series [113]. That gives the contribution of the zero-mode transitions

$$S^{zz}\Big|_{\substack{q\neq 0\\ \omega=0}} = \frac{e^{-\beta_T J}}{Z}\frac{1+e^{-\beta_T h_z}}{1-e^{-\beta_T h_z}}\frac{\delta(\omega)}{2}\frac{J_0^2(\zeta')}{\cosh(\beta_T h_z) - \cos q} \tag{3.180}$$

Finally, combining together Eqs. (3.177) and (3.180) we obtain the dynamical structure factor in the form

$$S^{zz}(q,\omega)\Big|_{q\neq 0} = \frac{e^{-\beta_T J}}{Z}\frac{e^{-\beta_T h_z}}{1-e^{-\beta_T h_z}}\sum_{k=-N}^{N} G_k(q)\,\delta(\omega - 2h_z k), \tag{3.181}$$

where the partition function Z is given by Eq. (3.169) and the contributions from each mode are

$$G_0 = \frac{J_0^2(\zeta')}{\cosh(\beta_T h_z) - \cos q}\frac{e^{\beta_T h_z}+1}{2}, \tag{3.182}$$

$$G_k = \frac{J_k^2(\zeta')}{2\sin^2(q/2)}\begin{cases} 1, & k>0, \\ e^{\beta_T 2h_z k}, & k<0, \end{cases} \tag{3.183}$$

and the argument of the Bessel function is $\zeta' = \frac{2J_a}{h_z}|\sin q|$. Analysing the expressions in Eqs. (3.182) and (3.183) for the dynamical structure factor S^{zz} the maximum intensity of the finite frequency WZL transitions occurs at $q = \pi/2$ when the argument ζ' of the Bessel functions is maximal.

If we introduce the Bloch frequency $\omega_B = 2h_z$ this gives the obtained result in Eq. (3.181)

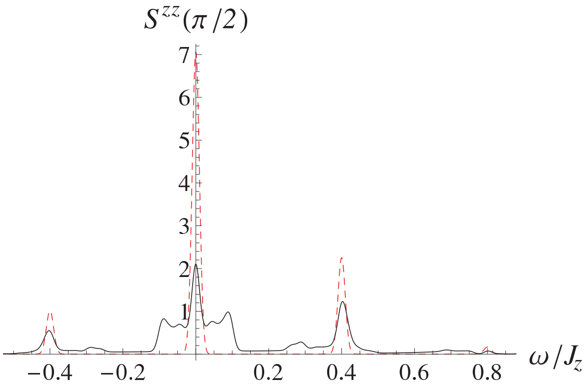

Figure 3.17: The structure factor $S^{zz}(q = \pi/2, \omega)$ as a function of ω for $T = J/2$ in the field $h_z = 0.2J$ and parameters from Eq. (3.31). The red dashed curve corresponds to the WZL result given in Eq. (3.181) using the same parameters. In order to generate the plot Dirac delta-functions were approximated by a Gaussian distributions with variance 10^{-4}.

similar to the expression in the article by Kyriakidis and Loss [51]. In contrast to that result, however, there are different coefficients and we get an additional factor $e^{-\beta_T J}$ which decreases dramatically the intensity at low temperature (compared to the coupling constant J). Therefore in order to see finite temperature signatures of the magnetic Bloch oscillations, a relatively high temperature is required to thermally occupy the energy levels. At the same time the magnetic field h_z leads to decreasing the weights of the finite frequency Bloch peaks in Eqs. (3.181)–(3.183) that weakens the signatures of the magnetic BOs.

Comparison of the general analytical result in Eq. (3.165) and the expression obtained in the limit of WZL in Eq. (3.181) for the $S^{zz}(q = \pi/2, \omega)$ in the magnetic field $h_z = 0.2J$ at the temperature $T = J/2 \approx 18.3\,\mathrm{K}$ is shown in Figure 3.17. We can see clear peaks separated by the Bloch frequency $\omega_B = 2h_z$ while the calculation in the WZL limit (the red dashed curve) gives an overestimated weight of these peaks. Nevertheless it captures their relative intensities. The peak broadening at the Bloch frequency and other additional peaks in the general case (the black solid line) are caused by the non-equidistance of the energy spectrum.

Let us consider now the zero momentum contribution ($q = 0$) to the dynamical structure factor S^{zz}. Then the transition matrix element $\mathbf{S}^{zz}_{mn}$ becomes

$$\mathbf{S}^{zz}_{mn}\Big|_{q=0} = \left(\sum_{l} \left(\frac{N}{2} - l \right) J_{\frac{l-n}{2}}(x'_0)\, J_{\frac{l-m}{2}}(x'_0) \right)^2 . \qquad (3.184)$$

Using Neumann's addition theorem and properties of sum of Bessel functions [108]

$$\sum_{k=-\infty}^{\infty} J_k(x)\, J_{k+n}(x) = J_n(0) = \delta_{n,0}, \qquad \sum_{k=-\infty}^{\infty} k J_k(x)\, J_{k+n}(x) = \frac{x}{2}\, \delta_{n,1}, \qquad (3.185)$$

we obtain the following relation

$$\mathbf{S}^{zz}_{mn}\Big|_{q=0} = \left(\left[\frac{N}{2}-n\right]\delta_{n,m} - x'_0\delta_{|n-m|,2}\right)^2 = \left(\frac{N}{2}-n\right)^2\delta_{n,m} + (x'_0)^2\delta_{|n-m|,2}. \qquad (3.186)$$

That gives an expression for the dynamical structure factor at zero momentum in the form

$$S^{zz}(q=0,\omega) = \frac{e^{-\beta_T J}}{Z}\frac{e^{-\beta_T h_z}}{1-e^{-\beta_T h_z}}\sum_{k=-1}^{1} G^0_k(q)\,\delta(\omega - 2h_z k),$$

where the contributions from each mode are

$$G^0_0 = \left(\frac{N}{2}\right)^2 - \frac{N}{1-e^{-\beta_T h_z}} + \frac{1}{2}\frac{e^{\beta_T h_z}+1}{\cosh(\beta_T h_z)-1}, \qquad (3.187)$$

$$G^0_k = \frac{1}{2}\left(\frac{2J_a}{h_z}\right)^2\begin{cases}1, & k=1,\\ e^{-\beta_T 2h_z}, & k=-1.\end{cases} \qquad (3.188)$$

We can see that the expression G^0_k corresponds to the limit of vanishing momentum ($q\to 0$) in the obtained relation for the dynamical structure factor $S^{zz}(q,\omega)$ above, Eq. (3.181) and Eq. (3.183), while the zero-coefficient G^0_0 has additional terms describing the squared total magnetization which are proportional to the chain length N and its squared value N^2, see Eq. (3.187).

3.7.2 $S^{+-}(q,\omega)$

At finite temperature the leading contribution to the transverse dynamical structure factor S^{+-} comes from transitions between states with non-zero momentum p. The matrix element in Eq. (3.167) becomes

$$\mathbf{S}^{+-}_{mn}(p,q) = 4\left[\sum_{l>0} J_{\frac{l-n}{2}}(x'_0\cos p)\, J_{\frac{l+1-m}{2}}\big(x'_0\cos(p+q)\big)\,\cos\left(\frac{ql-p}{2}\right)\right]^2. \qquad (3.189)$$

The order of the first Bessel function is integer (the second Bessel function has half-integer order), therefore it is convenient to introduce a new integer variable $t=(l-n)/2$. Using Graf's addition theorem the sum over the product of the Bessel functions is

$$\sum_{t>1-\frac{n}{2}} J_t(x'_0\cos p)\, J_{t+\frac{n-m+1}{2}}\big(x'_0\cos(p+q)\big)\cos\left[q\left(t+\frac{n}{2}\right)-\frac{p}{2}\right]$$
$$= J_{\frac{n-m+1}{2}}(\zeta')\,\sin\left[\left(p-\frac{\pi}{2}\right)\frac{n-m+1}{2}+\frac{p}{2}+q\frac{n}{2}\right], \qquad (3.190)$$

where we use the variable $\zeta' = \frac{2J_a}{h_z}|\sin q|$.

Since the transitions between the same (even or odd) sectors are not allowed it is convenient to introduce integer variable $k=(m-n-1)/2$. In this case the corresponding integral over

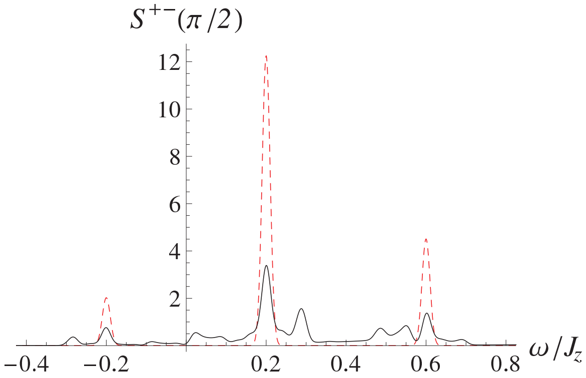

Figure 3.18: The structure factor $S^{+-}(q=\pi/2,\omega)$ as a function of ω using the same parameters as in Figure 3.17. The red dashed curve corresponds to the WZL result in Eq. (3.192) using the same parameters. Dirac delta-functions were approximated by a Gaussian distributions with variance 10^{-4}.

momentum p is

$$\int_0^{2\pi}\frac{dp}{2\pi}\cos^2\left[\left(\frac{\pi}{2}-p\right)k+\frac{p}{2}+q\frac{n}{2}\right]=\frac{1}{2}. \tag{3.191}$$

After reordering of the double sum we obtain finally

$$\begin{aligned} S^{+-}(q,\omega) =& \frac{e^{-\beta_T J}}{Z}\frac{1}{e^{\beta_T h_z}-1}\sum_k \delta\big(\omega-h_z(2k+1)\big) \\ & \times 2J_k^2(\zeta')\begin{cases}1, & k>1/2,\\ e^{\beta_T h_z(2k+1)}, & k<1/2,\end{cases}\end{aligned} \tag{3.192}$$

where $\zeta'=\frac{2J_a}{h_z}|\sin q|$ and k is integer variable which takes values in the domain $1-N\le k\le N-1$.

The dynamical structure factor $S^{+-}(q=\pi/2,\omega)$ is plotted in Figure 3.18 using the same parameters as in Figure 3.17. Peaks at frequencies corresponding to odd multiples of the magnetic field h_z (half the Bloch frequency $\omega_B=2h_z$) are clearly visible. Other additional peaks (the black solid line) come due to the dispersion of the lowest energy levels.

3.8 Beyond the $N_{dw}\le 2$ approximation

The restriction to $N_{dw}\le 2$ does not allow to discuss interactions between domains in the chain which play an important role in the high energy spectrum and may even destroy the magnetic Bloch oscillations. We will study contributions from the higher domain wall sectors numerically.

3.8.1 Single domain states

In order to make a connection between the analytical results for the $N_{dw} \leq 2$ restricted Hamiltonian and numerical results where also states with more domain walls are allowed we construct an approximate single domain creation operator in the following way

$$a_n^\dagger(p) = \frac{1}{\sqrt{N}} \sum_l e^{-ipl/2} \psi_{n,l}(p) \sum_j e^{-ipr_j} \prod_{k=j}^{j+l-1} \hat{S}_k^-, \tag{3.193}$$

where $\psi_{n,l}(p)$ are the wave function coefficients in the two domain wall approximation, see Eq. (3.4). When this operator, with zero momentum $p = 0$, acts on the ferromagnetic state $|\uparrow\uparrow\uparrow \ldots \uparrow\rangle$ it gives an energy eigenstate in the $N_{dw} \leq 2$ approximation[2].

The usefulness of this construction is that we can calculate overlaps of these single domain states with exact energy eigenstates from numerical calculations which also involve higher domain wall sectors. This lets us identify which states that are best characterized as a single domain excitation. For each value of the parameter n at zero momentum $p = 0$ we calculate the overlaps of this state with all the exact energy eigenstates obtained numerically with the restriction $N_{dw} \leq 6$. The energy eigenstate with the biggest overlap for each value of n can be said to correspond to the state $|n, p\rangle$ with the energy $E_n = J + h_z \nu_n$ in the single domain approximation. The normalized wave function coefficients of such a single domain state calculated numerically having the biggest overlap for the quantum number $n = 12$ and the corresponding analytically predicted wave function coefficients $\psi_{n=12,l}(p = 0) = J_{(l-12)/2}(2J_a/h_z)$ in the two domain wall approximation are shown in Figure 3.19(a). We see good agreement between the numerically calculated coefficients for $N_{dw} \leq 6$ and the analytically predicted $\psi_{n,l}(p = 0)$ in Eq. (3.168) from the redefined Hamiltonian in the case of the WZL. We see that for the energy eigenstate with $n = 12$ the average domain length is $\langle l \rangle \approx 12$ while domains with the maximal $l_{max} = 18$ and the minimal length $l_{min} = 6$ give the biggest contributions.

In Figure 3.19(b) we can see the good agreement between the numerically calculated eigenvalues for $N_{dw} \leq 6$ for the finite chain and the eigenvalues of the redefined Hamiltonian (3.29) in $N_{dw} \leq 2$ approximation, and the analytically estimated energy levels in the low-energy region. The spectrum of these states becomes equidistant when the parameter n exceeds a certain value that agrees with the analytical estimate for when $\nu_n = n$ which is $n > 2J_a/h_z + 1 \approx 9$ for the magnetic field $h_z = 0.05J$ and the $\mathrm{CoCl_2 \cdot 2H_2O}$ material parameters in Eq. (3.31).

We will also be interested in the transition matrix element of the spin operator $\hat{S}^z_{q=0}$ between the numerically calculated single domain states $|\chi_n\rangle$ and the ground state $|\chi_0\rangle$, which can be seen to behave as $\alpha_n\sqrt{N}$ according to Figure 3.20(a). Therefore to a good approximation the coefficient α_n corresponds to the transition matrix element of the spin operator $\sum_i \hat{S}^z_i$ between the excited sate $|\chi_n\rangle$ and the $1/\sqrt{N}$ redefinition of the ground state $|\chi_0\rangle$

$$\alpha_n = \langle \chi_n | \hat{S}^z_{q=0} \frac{1}{\sqrt{N}} | \chi_0 \rangle. \tag{3.194}$$

We can therefore compare α_n to the transition matrix element of $\hat{S}^z_{q=0}$ between excited states and

---

[2] We can consider bound state of a domain wall and an anti-domain wall as a single domain or a particle. In this sense we can term the two domain wall approximation as a *single particle approximation*.

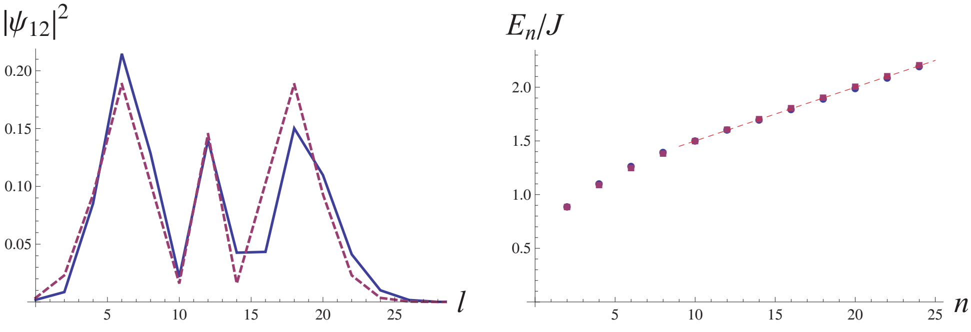

(a) (b)

Figure 3.19: (a) The normalized wave function coefficients squared of one domain states with fixed quantum number $n = 12$ (the solid blue line) as a function of domain length l in the $N_{dw} \leq 6$ approximation in the magnetic field $h_z = 0.05J$ for $N = 34$ sites using the parameters in Eq. (3.31). The dashed magenta line corresponds to the analytical solution of wave function coefficients in terms of the Bessel function $\psi_{n=12,l}(p = 0) = J_{(l-12)/2}(2J_a/h_z)$. (b) Excitation energy of one domain states as a function of quantum number n. The solid blue circles refer to the $N_{dw} \leq 6$ approximation, while the solid magenta squares describe results for the redefined Hamiltonian (3.29) for $N_{dw} \leq 2$. The dashed red line shows the analytical solution of the WZL equidistant spectrum $E_n = J + h_z n$ for $n > 2J_a/h_z + 1$ in the magnetic field $h_z = 0.05J$.

the ground state of the redefined Hamiltonian (3.29) which is given by Eq. (3.120). In particular, in Figure 3.20(a) the best fitted function $\alpha_2\sqrt{N}$ (corresponding to the red dashed line) of the numerically calculated matrix element $\langle\chi_2|\hat{S}^z_{q=0}|\chi_0\rangle$ connecting the first excited single domain state in the even sector and the ground state has the coefficient $\alpha_2 = 0.157$ which is relatively close to the $\mathbf{S}^z_{2,0} = 0.165$ obtained from the redefined Hamiltonian.

In Figure 3.19(b) we can see a good agreement between α_n for different level numbers n in the $N_{dw} \leq 6$ approximation for $N = 34$ spins (the solid blue circles) and the matrix elements $\mathbf{S}^z_{n,m=0}$, see Eq. (3.120), for single domain states for $N_{dw} \leq 2$ (the solid magenta squares) derived from the redefined Hamiltonian. Note that α_n drops very fast with increasing n. The finite size effects influence crucially only the states with the high number n.

3.8.2 Two domain states

The construction in Eq. (3.193) can also be used to estimate the energy of states having two domains. Approximate two domain states can be expressed as pairs with total momentum zero of two single domain states with quantum numbers n, m and relative momentum p separated by a distance d between domain centres. We take the creation operator of the two domain state to be

$$b^\dagger_{n,m}(d) = \sum_p e^{-ipd} a^\dagger_n(p)\, a^\dagger_m(-p), \tag{3.195}$$

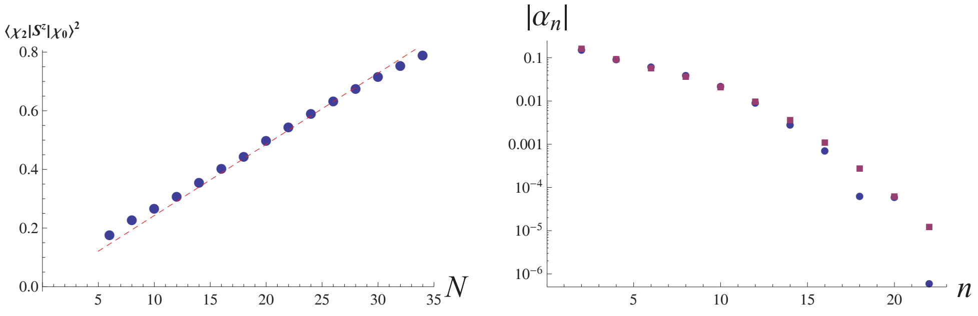

(a) (b)

Figure 3.20: (a) Square matrix element of the spin operator $\sum_i \hat{S}_i^z$ between the first excited single domain state and the ground state for $N_{dw} \leq 6$ approximation (the solid blue circles) as a function of the system size N. The used coupling parameters are given by Eq. (3.31). The red dashed line corresponds to the best fitted function $\left(\alpha_2\sqrt{N}\right)^2$, where the coefficient is $\alpha_2 = 0.157$. (b) Transition matrix element $|\alpha_n|$ between single domain states and the ferromagnetic state with the $1/\sqrt{N}$ redefinition of the coupling for $N = 34$ sites (the solid blue circles) as a function of level number n. The solid magenta symbols describe the matrix element $\mathbf{S}^z_{n,m=0}$ given by Eq. (3.120) for the redefined Hamiltonian. Here a logarithmic scale was used.

where the sum is performed over all momenta in the Brillouin zone. Using Eq. (3.193) the two particle creation operator can be written in terms spin operators as

$$
\begin{aligned}
b^\dagger_{n,m}(d) = \sum_p e^{-ipd} \sum_{l,l'} \left[\psi_{n,l}(p)\psi_{m,l'}(-p) + \psi_{n,l'}(p)\psi_{m,l}(-p)\right] \\
\times \left\{ \frac{1}{2} \sum_{D>\frac{l+l'}{2}} \cos(pD) \frac{1}{N} \sum_j \prod_{k=j}^{j+l-1} \hat{S}_k^- \left(\prod_{k'=j+D+\frac{l-l'}{2}}^{j+D-1+\frac{l+l'}{2}} \hat{S}_{k'}^- + \prod_{k'=j-D+\frac{l-l'}{2}}^{j-D-1+\frac{l+l'}{2}} \hat{S}_{k'}^- \right) \right. \\
\left. + \cos\left(p\frac{l+l'}{2}\right) \frac{1}{\sqrt{N}} \sum_j \prod_{k=j}^{j+l+l'-1} \hat{S}_k^- \right\}. \qquad (3.196)
\end{aligned}
$$

Its action on the ferromagnetic state gives the two domain (or two particle) state

$$
|n, m, d\rangle = b^\dagger_{n,m}(d)|0, 0\rangle, \qquad (3.197)
$$

which can be expressed in the explicit form

$$
\begin{aligned}
|n, m, d\rangle = \sum_p e^{-ipd} \sum_{l,l'} \left[\psi_{n,l}(p)\psi_{m,l'}(-p) + \psi_{n,l'}(p)\psi_{m,l}(-p)\right] \\
\times \left\{ \frac{1}{\sqrt{2}} \sum_{D>\frac{l+l'}{2}} \cos(pD)|l, l', D\rangle + \cos\left(p\frac{l+l'}{2}\right)|l + l'\rangle \right\}, \qquad (3.198)
\end{aligned}
$$

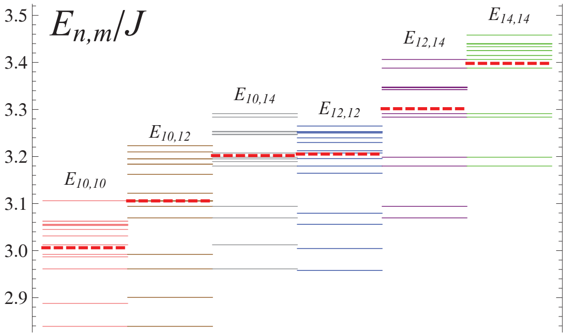

Figure 3.21: Excitation energy of two domain states $E_{n,m}$ labeled by quantum numbers n and m. Lines with same colors refers to fixed values of n and m, but different values of the distance d. The dashed thick red line shows the non-interacting energy of a two domain state as the sum of single domain state energies $E_n + E_m$.

where $|l + l'\rangle$ is a zero momentum state with domain length $l + l'$ in the $N_{dw} = 2$ sector and a $|l, l', D\rangle$ corresponds to a symmetrized two domain state with lengths l and l' separated by a distance D between their centres in the $N_{dw} = 4$ sector. For a finite system with periodic boundary conditions the D-value is limited by the minimal distance between the domain centres and takes values

$$\frac{l + l'}{2} < D < \frac{N}{2}. \tag{3.199}$$

The biggest overlap between numerically calculated energy eigenstates and the two domain states $|n, m, d\rangle$ gives a set of states and energies labeled by the numbers n, m, d each which gives the energy of a state having two domains, one of n, and other of m, separated by a distance d between their centres. Due to interactions between domains the energy levels for fixed quantum numbers n and m splits into several sub-levels corresponding to different separation d. The energy spectrum of these states for $N_{dw} \leq 6$ system is given in Figure 3.21 for a chain with $N = 34$ spins.

We can construct the energy shift

$$\Delta E_{n,m} = E_{n,m} - (E_n + E_m), \tag{3.200}$$

where $E_{n,m}$ is the energy of two domain states, and E_n and E_m are single domain state energies. The energy shift for the two domain states $|n, m, d\rangle$ as a function of the distance between domain centres d for different numbers n and m in the magnetic field $h_z = 0.05J$ is shown in Figure 3.22. We interpret this dependence as the interaction energy of two domains separated by d lattice spacings and speculate that the interaction energy for a finite chain length N can be characterized by the following functional form

$$\Delta E(d) = a - b\left(\frac{1}{d} + \frac{1}{N - d}\right), \tag{3.201}$$

which fits the results reasonably with the parameters: (a) $a = 0.21J$ and $b = 1.31J$ for $n =$

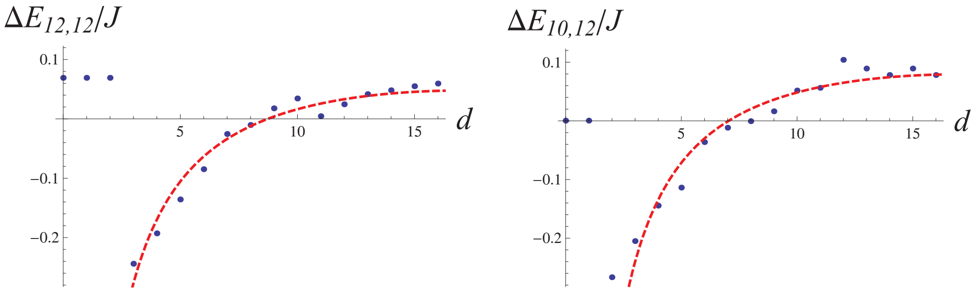

(a)

(b)

Figure 3.22: Two domain energy shift $E_{n,m} = E_{n,m} - (E_n + E_m)$ as a function of the separation distance d between domain centres in the magnetic field $h_z = 0.05J$ for quantum numbers (a) $n = m = 12$ and (b) $n = 10$ and $m = 12$. Other parameters as in Eq. (3.31). The red dashed line corresponds to the best fitting function $\Delta E(d) = a - b[1/d + 1/(N - d)]$ for the system size $N = 34$.

$m = 12$, (b) $a = 0.23J$ and $b = 1.29J$ for $n = 10$ and $m = 12$, see Figure 3.22. The positive value of a is caused by the restriction on the number of domain walls N_{dw} which tends to overestimate energies in higher domain wall sectors relative to those in lower sectors.

Due to finite size effects we are restricted from studying the interaction of two domain states with high quantum numbers m, n. In particular, in the case of $m = n$ when the average size of each domain is $\langle l \rangle \approx n$ and the maximal domain length in the state is $l_{max} \approx n + 2x'_0$, where $x'_0 = 2J_a/h_z$, the system size should be $N \geq 2n + 4x'_0$ in order to completely fit both states into the chain.

3.9 Laser Induced magnetic BOs

We have seen in Eq. (3.123) that the total magnetization of suitably prepared quantum states oscillates at the Bloch frequency. We will now outline a procedure for how to prepare such a state. Since the magnetic Bloch oscillations correspond to transitions between WZL levels, a direct method to generate the magnetic BOs at low temperature is to apply coherent far-infrared laser radiation. Using a short laser pulse with the proper frequency one can excite levels in the equidistant region of the energy spectrum and when turning off the laser pulse the magnetization of the material will continue to oscillate at the Bloch frequency.

Interaction of magnetic materials with electromagnetic radiation and electromagnetic response of various classes of correlated electron materials have been studied by many scientists, see the review [114]. In particular, at finite temperature the coupling of light with optical phonons and magnons can induce additional magnetic excitations [115, 116], that was also experimentally observed by using far infrared laser spectroscopy in $CoCl_2 \cdot 2H_2O$ as the coupled phonon-magnon mode at the energy $E_{ph} \approx 42.1\,\mathrm{K} = 1.15J$, see [117–119]. In order to induce the magnetic Bloch oscillations we need to avoid excitation of this phonon-magnon mode by applying the laser radiation with frequency corresponding to higher energies.

3.10 Magnetic dipole transition

The magnetic dipole transition (M1) corresponds to the leading part of the magnetic interaction of an electromagnetic wave with an atom[3]. Due to the small magnitude of the magnetic field in an electromagnetic wave the magnetic dipole interaction is much weaker than that of the electric dipole interaction (E1). The magnetic dipole transition couples states with the same parity in contrast to the electric dipole transition. The selection rules for the magnetic dipole transitions [120, 121] are

1. Changing of the total angular momentum quantum number J

$$\Delta J = 0, \pm 1, \qquad \text{except} \quad J = 0 \nleftrightarrow J = 0. \tag{3.202}$$

2. Changing of the projection of the total angular momentum M_J along a specified axis

$$\Delta M_J = 0, \pm 1. \tag{3.203}$$

3. No parity change

$$\pi_f = \pi_i. \tag{3.204}$$

   The parity of a state is defined as

$$\pi = (-1)^{\sum_i l_i}, \tag{3.205}$$

   where l_i is orbital momentum quantum number of the i-th electron in the atom. In fact, only electrons in odd orbitals (those with an odd orbital momentum l such as in the p, f, ...-shells) contribute to the total parity.

The first two selection rules can be easily understood since a photon is a boson and carries integer spin $S_{photon} = 1$.

In the case of magnetic materials with Co^{2+}-ions as magnetic centers (e.g. the cobalt salts $\mathrm{CsCoBr_3}$, $\mathrm{KCoF_3}$, $\mathrm{CsCoCl_3}$, $\mathrm{CoCl_2 \cdot 2H_2O}$ and $\mathrm{CoNb_2O_6}$) there are three unpaired electrons in the d-subshell (with angular momentum $l = 2$) in the ground state of the ion corresponding to the term ${}^4F(L = 3, S = \frac{3}{2})$, see Figure 3.3. Thus the parity of the ion ground state is even $\pi_i = (-1)^{\sum_i l_i} = (-1)^{3\times 2} = 1$ since filled orbitals and paired electrons do not change the parity. Excited levels of $3d$-electrons of the Co^{2+}-ion have the same even parity $\pi_f = (-1)^{3\times 2} = 1$ that complies with the 3rd rule of the magnetic dipole transition (M1). When taking into account crystal field effects in $\mathrm{CoCl_2 \cdot 2H_2O}$ due to neighboring Cl atoms and $\mathrm{H_2O}$ molecules, parity is still a good quantum number as these crystal field perturbations do not break inversion symmetry [92].

Therefore the electric dipole transitions (E1) are forbidden in $\mathrm{CoCl_2 \cdot 2H_2O}$ in contrast to the allowed magnetic dipole transitions (M1). Thus the far-infrared laser radiation interacts mainly through the magnetic component of the light wave. Therefore we can model the laser as an

---

[3] There is no radiation due to magnetic monopoles (M0), which do not seem to exist.

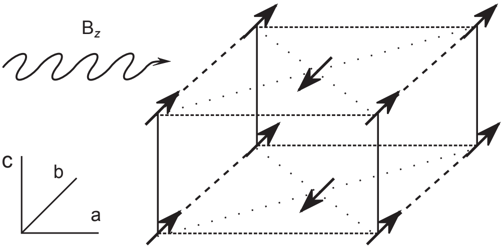

Figure 3.23: The spin z-axis corresponds to the crystallographic b axis in $\mathrm{CoCl_2} \cdot 2\mathrm{H_2O}$. The strong ferromagnetic J_z couples spins along the c axis. A laser beam is shown propagating at normal incidence to the $b-c$ plane with magnetic field polarization in the b direction.

extra time-dependent magnetic field which couples to the spins as

$$\hat{H}_{ext} = -\vec{B}(t) \sum_i \hat{\vec{S}}_i. \tag{3.206}$$

For a linearly polarized laser beam such that the magnetic field is along the z-axis which corresponds to the Ising direction, the effective coupling term becomes

$$\hat{H}_{ext} = -B_0^z \cos(\omega t) \sum_i \hat{S}_i^z, \tag{3.207}$$

where ω is the laser frequency and B_0^z is the laser magnetic field amplitude.

In a far-infrared laser experiment with frequency of the incoming radiation $\hbar\omega \approx J$ corresponds to a laser wavelength $\lambda \approx 0.3$ mm for $\mathrm{CoCl_2} \cdot 2\mathrm{H_2O}$ which is much larger than the lattice spacing $a \approx 3.5$ Å. The wave number of laser radiation $k = 2\pi/\lambda$ satisfies the relation $ka \ll 1$, so in a very good approximation the interaction with photon does not change momentum of spin states and we can neglect the k dependence in Eq. (3.207). Since we study a system at low temperature in the ground state, in the further consideration we will focus on the zero-momentum part of the energy spectrum.

3.11 Laser induced BOs

In order to generate the magnetic Bloch oscillations at very low temperatures we need to populate the excited levels in the equidistant part of the energy spectrum. We can use a laser with a wavelength in the far-infrared spectrum.

The interaction with a linearly polarized laser beam can be expressed as the coupling $\hat{H}_{ext}$ to an extra oscillating *magnetic* field with the frequency ω, see Eq. (3.207). We take the magnetic component of the polarized laser beam to be along the Ising axis which corresponds to the crystallographic b-direction in $\mathrm{CoCl_2} \cdot 2\mathrm{H_2O}$ [94, 95]. Such a setup can be made by cleaving the crystals in the $b-c$ plane (technical details of crystal growing and cleaving for this material are given in [119]) and directing the laser at normal incidence to this surface and polarizing the laser beam such that the magnetic field points along the b-direction, see Figure 3.23.

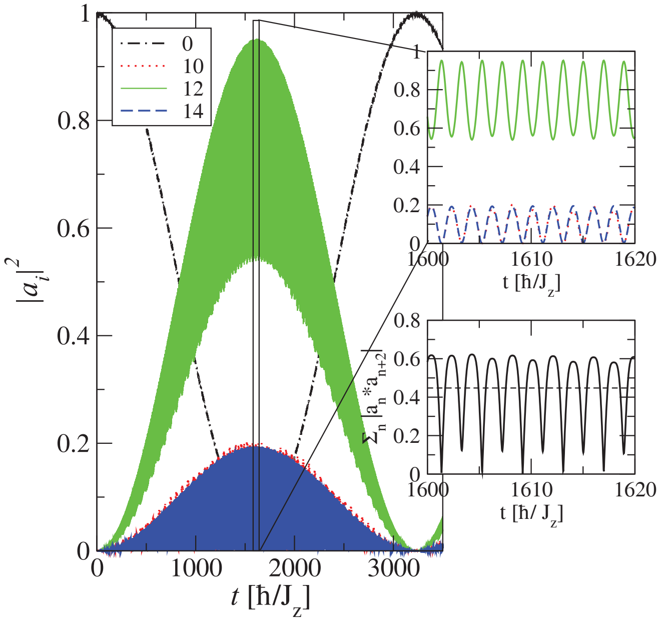

Figure 3.24: Population $|a_i|^2$ of selected energy levels i, indicated in the legend, as a function of time after turning on the laser, H_{ext}. The laser frequency is $\omega = (E_{n_0=12} - E_0)/\hbar$ and the magnetic field amplitude of the laser beam is $B_0^z = 0.2J$. The upper right panel shows a zoom in on the boxed time region. The lower right panel shows the time dependence of the sum of products of two nearby probability amplitudes, $\sum_n |a_n^* a_{n+2}|$. The time averaged value is shown as the horizontal dashed line. Time t is measured in units of $\hbar/J_z$ which is 0.2 ps for the $CoCl_2 \cdot 2H_2O$ material.

We assume that the laser beam is coherent along its front, and also through the crystal. The laser considered here have a wavelength of about $\lambda = 0.3$ mm thus for this approximation to be good the crystal should be thinner than this value. In the case of a thicker crystal there will be an additional phase-shift associated with the crystal thickness.

Starting in the ground state of the Hamiltonian (3.29), the time-dependent Schrödinger equation can be solved iteratively numerically with the laser field $\hat{H}_{ext}$ present. In the iterations we keep the 300 lowest energy states of the Hamiltonian with zero momentum and $N_{dw} \leq 2$. The laser frequency ω is tuned such that $\omega = (E_n - E_0)/\hbar$ where n corresponds to an energy level in the region where the spectrum is approximately equidistant. We choose the parameter $n = n_0 = 12$ corresponding to $E_{n_0} - E_0 \approx 1.6J$ for a static magnetic field $h_z = 0.05J$. In practice when using a laser with a fixed wavelength, resonance can instead be found by changing the static magnetic field thereby adjusting the energy levels. The iterative solution gives time-dependent amplitudes of the different energy levels. Figure 3.24 shows the probabilities of finding the system in selected levels as a function of time. Only even n states are excited because the $\hat{S}^z$-terms do not flip any spins.

The black dot-dashed curve in Figure 3.24 shows how the ground state is depleted. The minimum of the ground state population coincides with the maximum of the population of level

$n_0 = 12$, green solid curve, and occurs at a time

$$\tau = \pi\hbar/\omega_R, \tag{3.208}$$

where the oscillation frequency is

$$\omega_R = \sqrt{|B_0^z \alpha_{n_0}|^2 + (\omega - (E_{n_0} - E_0))^2}. \tag{3.209}$$

Here α_{n_0} is the matrix element of the $\hat{S}^z$ terms between the ground state and the $n = n_0 = 12$ excited state

$$\alpha_n = \langle n| \sum_i \hat{S}_i^z |0\rangle. \tag{3.210}$$

These oscillations are in essence Rabi oscillations [122].

Exciting the level $n = n_0$ alone does not give appreciable amplitude for Bloch oscillations as one also needs to populate the levels with $n + 2$ (or $n - 2$), see Eq. (3.123). This can be achieved by using a relatively large amplitude of the laser beam, we have used $B_0^z = 0.2J$, thereby causing off-resonant tunneling between the n and the $n \pm 2$ levels, see Fig. 3.24, the red dotted and blue dashed curves. These off-resonant tunneling processes are fast, thus the population of the nearby levels follows closely that of the central level.

In order to seek the maximum amplitude of the magnetic Bloch oscillations we turn off the laser (and the interaction H_{ext} term) at the maximum population of the central excited level. A close look at the time dependence of $a_n^* a_{n+2}$ near the cutoff time, reveals that the dominating terms have the same phase, thus the amplitude of BOs is proportional to $\sum_n |a_n^* a_{n+2}|$ which is shown in the lower inset of Figure 3.24. From this we see that it oscillates fast with a frequency corresponding to $E_{12} - E_0$. It may be difficult to turn off the laser exactly when this quantity is maximal. However, this is not a major concern as the time averaged value is about 75% of the maximum value.

Turning off the laser at a time τ when $\sum_n |a_n^* a_{n+2}|$ is maximal, and letting the system evolve further in time without $\hat{H}_{ext}$, produces the BOs shown in Figure 3.25. As our simulation only allows single domain excitations we have plotted the relative size of the domain, measured by the expectation value of the number of spins opposing the field $N_{1\downarrow}(t) = M_z(t) - N/2$ divided by its time average $\bar{N}_{1\downarrow} \approx n$ for excitation E_n. We see that the relative size of the domain oscillates between 0.6 and 1.4 corresponding to a size between 7.2 and 16.8 for $\bar{N}_{12} = 12$. Thus the amplitude is 4.8 which is close to the expected value $4J_a/h_z \times 0.6 = 5$ from Eq. (3.123). Allowing a finite density ρ of coherently oscillating domain states, the relative size of a single domain state shown in Figure 3.25 will be proportional to the experimentally relevant quantity, the time-dependent relative magnetization

$$\frac{M_z(t) - \bar{M}}{\bar{M}} = \frac{\rho \bar{N}_{1\downarrow}}{1/2 - \rho \bar{N}_{1\downarrow}} \left(\frac{N_{1\downarrow}(t)}{\bar{N}_{1\downarrow}} - 1 \right). \tag{3.211}$$

As is evident from Figure 3.25 the magnetic Bloch oscillations are not simple harmonic. A Fourier transformation of the beating pattern is shown in the lower panel of Figure 3.25, where two peaks are clearly visible. These peaks correspond to the frequencies $\omega_1 = (E_{14} - E_{12})/\hbar = 0.1J/\hbar$ and $\omega_2 = (E_{12} - E_{10})/\hbar = 0.11J/\hbar$. Thus the beating pattern appears due to the

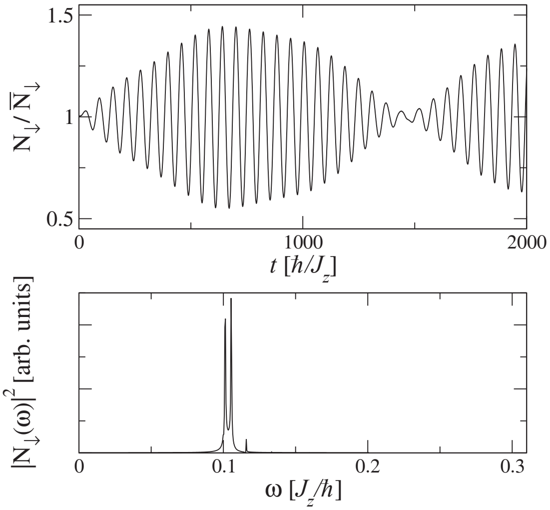

Figure 3.25: Size oscillations of a domain excitation, measured as the relative number of down spins $N_{1\downarrow}/\bar{N}_{1\downarrow}$ as a function of time after the laser is switched off (upper panel), and its Fourier spectrum (lower panel). The beating behaviour of the relative size oscillation is due to the deviation of the energy spectrum from equidistant and is described by the two frequencies which correspond to transitions to the off-resonance levels $\omega_1 = (E_{14} - E_{12})/\hbar = 0.1J/\hbar$ and $\omega_2 = (E_{12} - E_{10})/\hbar = 0.11J/\hbar$.

deviation of the energy levels from an equidistant ladder spectrum. This frequency difference can be made smaller by exciting higher energy bound states where the spectrum is closer to being equidistant, see Figure 3.9(a).

The laser polarization can also be arranged such as to have its magnetic field along the spin-x direction. This will induce transitions between states in the even and odd domain length sectors. In this case our simulations also show the magnetic Bloch oscillations, but now with more frequency components due to the deviation of the eigenenergies from equidistant spectrum, as in this case both the even and the odd sectors participate.

In order to observe the magnetic BOs we need to get a sizable population of the surrounding levels $n_0 \pm 2$ by off-resonant tunneling. This requires the use of a large laser amplitude, $B_0^z = 0.2J$, which, with a g-factor of 6.8 for $\mathrm{CoCl_2 \cdot 2H_2O}$ [88], corresponds to an amplitude of electric field in the beam of approximately $500\ \mathrm{MV/m}$. This is too large for real experiments since the dielectric breakdown field of most insulators is an order of magnitude less than this. We can decrease the laser amplitude. In this case, in order to get a reasonable population of the nearest off-resonant levels, it requires to have a longer exposition time τ, see Eq. (3.208) and Eq. (3.209). However it is essential that this time is shorter than the coherence time of the system, such that magnetic Bloch oscillations of different domains are coherent.

Instead we can change the laser polarization to get a magnetic component along the x-axis. This induces transitions between the even and odd n states which are closer to each other and so the laser amplitude can be reduced.

Another approach is to use two coherent small-amplitude laser beams each in resonance with nearby levels, that allows to excite resonantly two states. It will induce the magnetic Bloch oscillations corresponding to transitions between the excited energy levels. In that way we can avoid the large laser amplitude needed for the off-resonance tunneling process.

3.11.1 Two laser excitation of BOs

In order to get population of nearby levels with a smaller laser amplitude we can use two lasers, each in resonance with one of the two neighbouring levels $n_{01} = 12$ and $n_{02} = 14$. The simplest way to get coherent laser radiations at two frequencies is the use of nonlinear optical technique of second harmonic generation [123]. However, in our case we have to excite resonantly two nearby energy levels so the frequencies ω_1 and ω_2 of the laser beams should be relatively close. Therefore in order to obtain two coherent laser waves with tunable frequencies it is more prominent to use another nonlinear method of optical parametric light generation (OPG) used in *optical parametric oscillator* [124–126]. This parametric oscillator converts an input laser beam with frequency ω into two output beams of lower frequency ω_1 and ω_2 by means of second order nonlinear optical interaction so that the sum of the output frequencies is equal to the input wave frequency $\omega = \omega_1 + \omega_2$. When the power of the input laser beam is significantly above a particular threshold level, the two generated output beams are coherent to a very good approximation and behave as a laser-like wave with narrow linewidth [127].

In the case of two lasers with the frequencies ω_1 and ω_2 the time-dependent part of the Hamiltonian corresponding to the spin interaction with the linearly polarized laser beams becomes

$$\hat{H}_{ext} = -\big(B^z_{01}\cos(\omega_1 t) + B^z_{02}\cos(\omega_2 t + \phi)\big)\sum_i \hat{S}^z_i, \tag{3.212}$$

where ω_1 and ω_2 are the frequencies of two laser beams, B^z_{01} and B^z_{02} are magnetic field amplitudes, and ϕ is phase shift between the lasers. In particular, we use the following parameters

$$B^z_{01} = 0.01J, \qquad \omega_1 = (E_{n_{01}=12} - E_0)/\hbar, \tag{3.213}$$

$$B^z_{02} = 0.03J, \qquad \omega_2 = (E_{n_{02}=14} - E_0)/\hbar \tag{3.214}$$

and zero phase-shift $\phi = 0$ in our simulation. Since the spin operator $\hat{S}^z$ does not flip any spins only eigenstates with even numbers n in the energy spectrum can be excited.

The different level populations as a function of time after the lasers are turned on is shown in Figure 3.26. The ground state population corresponds to the black dot-dashed line and its minimum coincides with the maxima of the population of levels $n_{01} = 12$ and $n_{02} = 14$, and the first minimum occurs roughly at a time $2\times10^4\ \hbar/\mathrm{J_z}$ for the parameters used here. This time becomes larger for smaller laser amplitudes and it is inversely proportional to the magnitude of the laser field.

The population behaviour at the first maximum of the population curves, $\tau = 20\,440\ \hbar/\mathrm{J_z}$, is shown in the upper inset of Figure 3.26. Since the sum $\sum_n a^*_n a_{n+2}$ in the magnetization in Eq. (3.123) is dominated by the term with $n = 12$, the amplitude of the magnetic Bloch oscillations is proportional to the overlap $|a^*_{12}a_{14}|$ which is shown in the lower inset. The overlap has a beating pattern corresponding to the two laser frequencies ω_1 and ω_2, and its time-averaged value (the dashed line) is approximately $\langle|a^*_{12}a_{14}|\rangle \approx 0.48$. Since the overlap variation is rela-

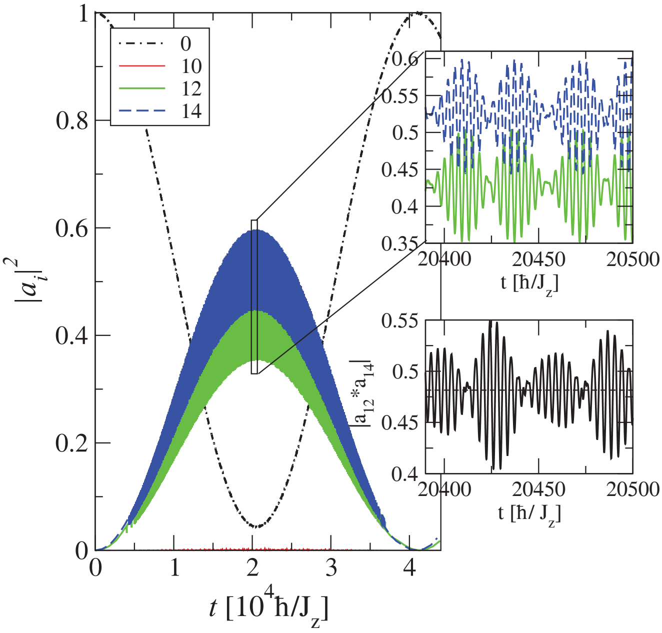

Figure 3.26: Population $|a_i|^2$ of selected energy levels i, indicated in the legend, as a function of time after turning on the two laser beams. The laser frequencies and amplitudes are $\omega_1 = (E_{n_{01}=12} - E_0)/\hbar$, $B^z_{01} = 0.01J$ and $\omega_2 = (E_{n_{02}=14} - E_0)/\hbar$, $B^z_{02} = 0.03J$. The upper right panel shows a zoom in on the boxed time region. The lower right panel shows the time dependence of $|a^*_{12}a_{14}|$. The time averaged value is shown as the horizontal dashed line. The time scale $\hbar/J_z$ is 0.2 ps for $CoCl_2 \cdot 2H_2O$.

tively small, it is not a major concern to turn off the lasers at non maximal overlap.

After turning off the laser at a time τ the spin system evolves further in time without $\hat{H}_{ext}$ and undergoes the magnetic Bloch oscillations which are shown in Figure 3.27. We see that the relative domain size of single domain excitations $N_{1\downarrow}/\bar{N}_{1\downarrow}$ oscillates between 0.7 and 1.3 corresponding to a size between 9.1 and 16.9 for $\bar{N}_{1\downarrow} \approx (12 + 14)/2 = 13$. Thus the amplitude is 3.9 which is close to the theoretically predicted value $4J_a/h_z \times 0.48 = 4.0$ in Eq. (3.123). At a finite density ρ of coherently oscillating domain states the relative size of a single domain state in the upper panel of Figure 3.27 is proportional to the time-dependent relative magnetization $(M_z(t) - \bar{M})/\bar{M}$ in Eq. (3.211). In the case of noninteracting domains we can estimate the density of domains per unit length as $\rho = c(1 - |a_0|^2)/\bar{N}_{1\downarrow}$, where $|a_0|^2$ corresponds to the population of the ground state and c is a constant of the order unity.

The Fourier spectrum of the oscillating size of a domain excitation corresponding to the magnetic BOs is shown in the lower panel of Figure 3.27, where a single peak is clearly visible very close to $\omega_B = 2h_z/\hbar$ at the frequency $\omega = (E_{14} - E_{12})/\hbar \approx 0.103J/\hbar$. This small deviation reflects the fact that the energy spectrum is not exactly equidistant and deviates from the WZL at low energies, see Figure 3.9(a).

We can change the phase shift ϕ in the interaction Hamiltonian $\hat{H}_{ext}$ in Eq. (3.212) between

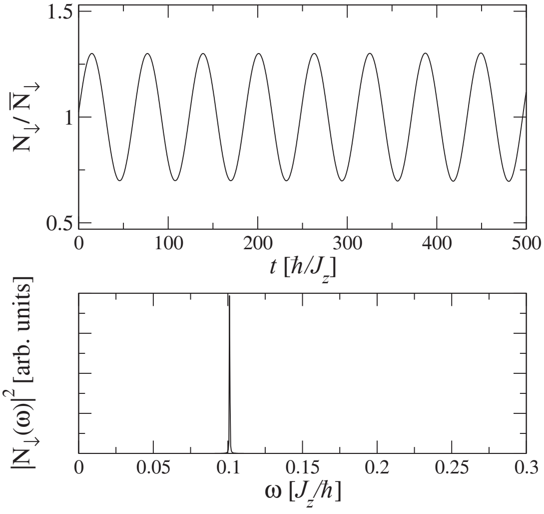

Figure 3.27: Size oscillations of a domain excitation, measured as the relative number of down spins $N_{1\downarrow}/\bar{N}_{1\downarrow}$ as a function of time after the lasers are turned off (upper panel), and its Fourier spectrum (lower panel). The oscillation frequency corresponds to transitions between the two resonance levels $\omega = (E_{n_{02}=14} - E_{n_{01}=12})/\hbar = 0.103\ J/\hbar$.

the laser beams but our simulations show that it does not change system behaviour at long time scale $t \gtrsim \tau$, since off-resonance transitions between the excited states n_{01} and n_{02} decrease any phase shift effects of the level populations at this time scale.

We can use another polarization of the laser beams, for example in order to get a magnetic field component along the x-direction, that will allow to excite also states in the odd sector and induce transitions between the even and odd n states. In this case our simulations also show the magnetic Bloch oscillations, but now at the Bloch frequency $\omega_B = h_z/\hbar$ which corresponds to the energy spacing between adjacent even and odd levels.

In addition to $\mathrm{CoCl_2 \cdot 2H_2O}$ we used the coupling parameters from Ref. [110] to study magnetic excitations in a quasi one-dimensional ferromagnet $\mathrm{CoNb_2O_6}$. Our calculations and numerical simulations also indicated that the magnetic BOs may be excited in this material by the similar way.

Here we considered the redefined Hamiltonian in Eq. (3.29) for $N_{dw} \leq 2$. Let us now discuss effects of interaction between domains in the ferromagnetic chain by including contributions from higher domain walls sectors.

Interaction effects

In order to address the effects of interactions between domains we perform a time-dependent numerical simulation of a $N = 32$ spin system with $N_{dw} \leq 6$ in the presence of the two lasers. The magnetization varies rapidly and has a large-scale weakly damped oscillating behavior due to dephasing coming from populating other levels, see Figure 3.28. The estimated damping time scale is roughly $t_{dmp} = 5 \times 10^4\ \hbar/J$. We expect that this time scale decreases when the

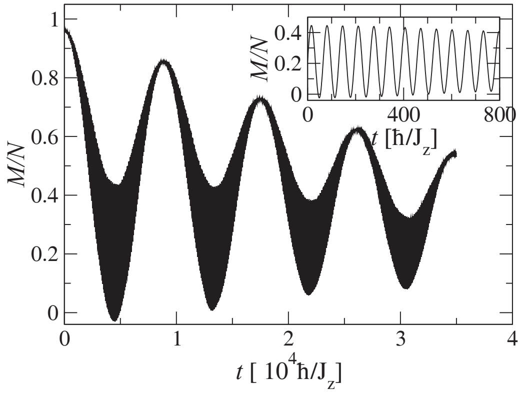

Figure 3.28: Magnetization per site as a function of time for a system with interaction in the presence of two laser beams with amplitudes and frequencies as in Figure 3.26 for chain length $N = 32$ and $N_{dw} \leq 6$ approximation. The inset shows the magnetization as a function of time after the two lasers have been turned off at $\tau = 4\,420\ \hbar/J$. The damping time t_{dmp} of the oscillations is roughly $5 \times 10^4\ \hbar/J$.

system size N increases.

The magnetization envelope reaches its first minimum at $t_m = 4\,420\ \hbar/J$ in Figure 3.28 which is shorter than the time of maximal population of excited levels $\tau = 20\,440\ \hbar/J$ for the redefined Hamiltonian in Figure 3.26 by a factor $k = t_m/\tau = 1/4.6$. This is a result coming from the $\sqrt{N}$-factor in the matrix element connecting the ferromagnetic state to the single domain states, see Figure 3.20(a), together with the near blocking by interactions and finite-size effects of states with $N_{dw} > 2$, see [128, 129]. For larger system sizes we expect that this ratio approaches

$$k = \frac{1}{\sqrt{R}}, \tag{3.215}$$

where R is the distance between domains in units of the lattice spacing a, such that beyond this distance the energy of domain-domain interaction is smaller than the perturbation magnitude $B^z_{01}\alpha_{12} \approx B^z_{02}\alpha_{14}$, where the redefined matrix element α_n coupling the ferromagnetic state to a single domain state is given in Eq. (3.194). This value corresponds to an energy scale of about $10^{-4}J$ for the $\mathrm{CoCl_2 \cdot 2H_2O}$ parameters in Eq. (3.31), since the magnetic field amplitude is $B^z_{01} = 0.01J$ and the matrix element is $\alpha_{n=12} \approx 0.01$ given in Figure 3.19(b). When domains are closer than the distance R the excitation of the second domain will be blocked by the presence of the first domain, therefore this multi-domain state will not be excited and will not participate in the resonance. This causes an increase of the Rabi frequency for this blocked system. We discuss this blocking effect further in a simplified toy model in Section 3.12.

After turning off of the lasers at the first magnetization envelope minimum at $t_m = 4\,420\ \hbar/J$ the magnetization continues to oscillate at the Bloch frequency $\omega_B = 2h_z = 0.1J$ with the Bloch period $T_B = 20\pi\ \hbar/J$ that is shown in the inset of Figure 3.28.

Thus it should be possible to excite the magnetic Bloch oscillation in the one-dimensional ferromagnet $\mathrm{CoCl_2 \cdot 2H_2O}$ using two resonant lasers at low temperatures in a static magnetic field. On turning off the lasers after an excitation time τ the total magnetization will oscillate at the Bloch frequency $\omega_B = 2h_z$ which is proportional to the applied static field. The estimated Bloch frequency is about 500 GHz for the parameters of $\mathrm{CoCl_2 \cdot 2H_2O}$ in a moderate 0.4 T magnetic field.

However collisions between excited domains can lead to dephasing behavior and associated decoherence that weakens the magnetic Bloch oscillations. Since the excited single domain states have flat dispersion and form the WZL, the domain excitations are heavy and localized. Therefore the interaction between domains plays an important role only at a high density of excitations when neighboring domains are close together. Static impurities and interactions between chains can also contribute to the dephasing in the real material, but the considered Bloch oscillations of domains are localized within a region $2A_B = 4x_0' = 8J_a/h_z$ that is roughly 17 sites for the used parameters in Eq. (3.31). So the effects of static impurities can be neglected if an impurity concentration is less than a few percent.

3.12 Rabi oscillation

In the previous section we considered the effects of an oscillating magnetic field from a laser beam on the spin system. We saw that when the frequency of the laser is in resonance with one of the excited levels the quantum system behavior is essentially that of a two-level system with transitions between the ground state and the excited level. This is the well-known physics of Rabi oscillations [130].

When allowing also states with more domain excitations $N_{dw} > 2$ we expect that as long as these domains can be treated as independent of each other the Rabi frequency Ω is unchanged, just as in the case for a dilute gas of atoms [131] where the Rabi frequency is set by the energies of a single atom. However we saw in the previous section that interactions between domains affected the Rabi frequency. Thus in order to get a general understanding of this it is helpful to illustrate and discuss these effects on the Rabi frequency in a simple toy model with interaction.

3.12.1 Rabi oscillations in a simple model with interaction

2-level systems

First consider a toy model where a single spin $S = \frac{1}{2}$ is placed in a permanent magnetic field with strength h along the z-axis. The Hamiltonian of the atom is

$$\hat{H}_0 = -h\left(\hat{S}^z - \frac{1}{2}\right). \tag{3.216}$$

There are two eigenstates, either parallel $|\uparrow\rangle$ or antiparallel $|\downarrow\rangle$ spin to the magnetic field, so we have a two-level system (see the Table 3.1). The ground state corresponds to the state with the spin along the field and has zero energy.

We can introduce a time-dependent perturbation $\hat{V}$ to the Hamiltonian in Eq. (3.216) and let it describe a harmonic oscillating magnetic field along the x-axis

$$\hat{V} = h_0 \cos{(\omega t)} \hat{S}^x, \tag{3.217}$$

Energy	State
0	$\vert\uparrow\rangle = \vert 0\rangle$
h	$\vert\downarrow\rangle = \vert 1\rangle$

Table 3.1: Eigenstates and eigenenergies of the Hamiltonian (3.216).

where h_0 is the amplitude of the oscillating field with frequency ω. The spin operator can be expressed in terms of the usual rising and lowering operators $\hat{S}^x = (\hat{S}^+ + \hat{S}^-)/2$ and it acts on the states as

$$\hat{S}^x|\uparrow\rangle = \frac{1}{2}|\downarrow\rangle, \qquad \hat{S}^x|\downarrow\rangle = \frac{1}{2}|\uparrow\rangle, \tag{3.218}$$

that gives the following matrix elements of the perturbation

$$V_{mn}(t) = \langle m|\hat{V}(t)|n\rangle = V_0 \cos(\omega t)(1-\delta_{mn}), \qquad V_0 = \frac{1}{2}h_0. \tag{3.219}$$

It is convenient to separate out the time-independent part of the matrix element

$$V_{mn}(t) = V_{mn}\cos(\omega t), \qquad V_{mn} = V_0(1-\delta_{mn}). \tag{3.220}$$

The Schrödinger equation of the perturbed system is

$$i\frac{\partial\psi}{\partial t} = \left(\hat{H}_0 + \hat{V}\right)\psi, \tag{3.221}$$

where the solution can be written in the form

$$\psi(t) = \sum_n a_n(t)e^{-iE_nt}|n\rangle, \tag{3.222}$$

where E_n are the energies of the unperturbed Hamiltonian and $a_n(t)$ are the probability amplitude of finding system in the state $|n\rangle$ at time t. We use system of units where the Plank constant is set equal to unity, $\hbar = 1$.

Substituting the last expression (3.222) into the Schrödinger equation (3.221) we obtain the following set of differential equations

$$\dot{a}_m(t) = -i\sum_n a_n(t)\,\langle m|\hat{V}(t)|n\rangle\, e^{i(E_m-E_n)t}, \tag{3.223}$$

which solutions correspond to *exact* solutions of the Schrödinger equation.

The most interesting case is the resonance behaviour of the system when the frequency ω of the external perturbation coincides with the difference between energy levels, $\omega = h$. In this case the equation set (3.223) consists of two differential equations and has the explicit form

$$\begin{cases} \dot{a}_0 = -ia_1V_0\left(1+e^{-i2ht}\right)/2, \\ \dot{a}_1 = -ia_0V_0\left(e^{i2ht}+1\right)/2. \end{cases} \tag{3.224}$$

Using the rotating wave approximation [121] we neglect the fast oscillating term $\langle e^{i2ht}\rangle_{\text{average}} \ll$

1 that gives the well-known equation for the harmonic oscillator

$$\ddot{a}_1 + \omega_0^2 a_1 = 0, \qquad \omega_0 = V_0/2. \tag{3.225}$$

It means that the population of the excited state, i.e. probability $|a_1|^2$, oscillates with the Rabi frequency

$$\Omega = 2\omega_0 = V_0. \tag{3.226}$$

If we assume that the two-level system is initially in the ground state

$$a_0(0) = 1, \qquad a_1(0) = 0, \tag{3.227}$$

the solutions of the equation set are the following

$$a_0(t) = \cos\omega_0 t, \qquad a_1(t) = \sin\omega_0 t. \tag{3.228}$$

The total magnetization of a quantum system in state $\psi(t)$ is

$$M(t) = \psi^\dagger(t)\sum_i \hat{S}_i^z\,\psi(t) = \sum_n |a_n(t)|^2\,\langle n|\sum_i \hat{S}_i^z|n\rangle. \tag{3.229}$$

In the case of a single spin the time-dependent magnetization becomes

$$M(t) = \sum_n |a_n(t)|^2\,\langle n|\hat{S}^z|n\rangle. \tag{3.230}$$

Both eigenstates contribute to the magnetization

$$M(t) = \frac{1}{2}\left(|a_0(t)|^2 - |a_1(t)|^2\right) = \frac{1}{2}\left(\cos^2\omega_0 t - \sin^2\omega_0 t\right) = \frac{1}{2}\cos 2\omega_0 t, \tag{3.231}$$

thus the magnetization oscillates also with frequency

$$\Omega = 2\omega_0 = V_0 = \frac{h_0}{2}, \tag{3.232}$$

which corresponds to the Rabi frequency in Eq. (3.226).

It should be noted that for harmonic perturbation which is off-resonance $\omega \neq h$, the total magnetization oscillates with the generalized Rabi frequency [121]

$$\Omega = \sqrt{|V_0|^2 + \delta^2}, \tag{3.233}$$

where $\delta = \omega - h$ is the detuning.

3-level systems

To explain how interaction might change the Rabi frequency we consider a simple extension of the two level system. We consider two spins $S = \frac{1}{2}$ in a magnetic field h along the z-axis. The unperturbed Hamiltonian of this system is

$$\hat{H}_0 = -h \sum_{i=1}^{2} \left(\hat{S}_i^z - \frac{1}{2} \right) . \tag{3.234}$$

Its ground state corresponds to the state where all spins point along the magnetic field and we have chosen the constant in the Hamiltonian (3.234) such that the ground state has zero energy. The quantum system has 4 available states (see Table 3.3).

Energy	**State**
0	$\vert \uparrow\uparrow\rangle$
h	$\vert \uparrow\downarrow\rangle$
h	$\vert \downarrow\uparrow\rangle$
$2h$	$\vert \downarrow\downarrow\rangle$

Table 3.2: Eigenstates and eigenenergies of the Hamiltonian (3.234).

Since the two states with one overturned spin have the same energy, it is convenient to rewrite their wave functions in the triplet and singlet combinations

$$\begin{aligned} |1\rangle &= \frac{1}{\sqrt{2}} \left(|\uparrow\downarrow\rangle + |\downarrow\uparrow\rangle \right) , \\ |1^*\rangle &= \frac{1}{\sqrt{2}} \left(|\uparrow\downarrow\rangle - |\downarrow\uparrow\rangle \right) . \end{aligned} \tag{3.235}$$

Using the Fourier transform

$$|p, l = 1\rangle = \frac{1}{\sqrt{N}} \sum e^{ipr_j} |r_j, l = 1\rangle \tag{3.236}$$

where the wave function $|r_j, l = 1\rangle$ corresponds to state with a single down spin at site r_j, the redefined wave functions $|1\rangle$ and $|1^*\rangle$ in Eq. (3.235) are states with definite momenta

$$\begin{aligned} |p = 0, l = 1\rangle &= \frac{1}{\sqrt{2}} \left(|\uparrow\downarrow\rangle + |\downarrow\uparrow\rangle \right) = |1\rangle, \\ |p = \pi, l = 1\rangle &= \frac{1}{\sqrt{2}} \left(|\uparrow\downarrow\rangle - |\downarrow\uparrow\rangle \right) = |1^*\rangle. \end{aligned} \tag{3.237}$$

We again consider the interaction with an oscillating external magnetic field with frequency ω along the x-axis

$$\hat{V} = h_0 \cos(\omega t) \sum_{i=1}^{N=2} \hat{S}_i^x , \tag{3.238}$$

where h_0 is the magnitude of the magnetic field and $N = 2$ is the total number of spins. The spin operator acts on the ground state as

$$\sum_i \hat{S}_i^x|0\rangle = \frac{1}{2}\sum_{i=1}^{N=2}\left(\hat{S}_i^+ + \hat{S}_i^-\right)|\uparrow\uparrow\rangle = \frac{1}{2}\sum_{i=1}^{N=2}\hat{S}_i^-|\uparrow\uparrow\rangle = \frac{1}{2}\left(|\uparrow\downarrow\rangle + |\downarrow\uparrow\rangle\right) = \frac{1}{\sqrt{2}}|1\rangle, \tag{3.239}$$

that gives the following non-zero matrix elements of the perturbation

$$\langle 1|\hat{V}|0\rangle = \langle 1|\hat{V}|2\rangle = V_{01}(t) = \sqrt{2}\frac{h_0}{2}\cos\omega t. \tag{3.240}$$

For further calculations it is convenient to extract the time-independent part of the matrix element

$$V_{01}(t) = V_{01}\cos\omega t, \qquad V_{01} = \sqrt{2}\frac{h_0}{2} = \sqrt{2}V_0, \tag{3.241}$$

where $V_0 = h_0/2$ is the matrix element of the time-independent part in Eq. (3.219), i.e. the same as in the simple one spin system. We can see that the matrix element is $\sqrt{N}$ times larger than for the single spin system considered in the previous section. It can be easy understood since there are now $N = 2$ places to insert a new overturned spin.

We can see from Eq. (3.240) that the state $|1^*\rangle$ is decoupled from the other states. This follows from the fact that the perturbation term $\hat{V}$ in Eq. (3.238) has zero momentum, thus couples only states with equal momenta. The state $|1^*\rangle$ is the only state with momentum $p = \pi$ and does therefore not couple to any of the other states with zero momenta $p = 0$. The perturbation couples the three states: $|0\rangle, |1\rangle, |2\rangle$. Therefore the quantum system of two spins in the magnetic field can be described effectively as a coupled 3-level system, see Table 3.3.

Energy	**State**
0	$\|0\rangle = \|\uparrow\uparrow\rangle$
h	$\|1\rangle = (\|\uparrow\downarrow\rangle + \|\downarrow\uparrow\rangle)/\sqrt{2}$
h	$\|1^*\rangle = (\|\uparrow\downarrow\rangle - \|\downarrow\uparrow\rangle)/\sqrt{2}$
$2h$	$\|2\rangle = \|\downarrow\downarrow\rangle$

Table 3.3: Energies and wave functions of the system of two spins in magnetic field. The state $|1^*\rangle$ is decoupled due to the zero-momentum perturbation.

The time dependence of the coupled states of the perturbed Hamiltonian $\hat{H} + \hat{V}$ can be expressed in the terms of the unperturbed states as in Eq. (3.222). It follows that the Schrödinger equation in the form of the equation set (3.223) becomes

$$\begin{cases} \dot{a}_0 = -ia_1V_{01}(t)\,e^{-iht}, \\ \dot{a}_1 = -iV_{01}(t)\left(a_0e^{iht} + a_2e^{-iht}\right), \\ \dot{a}_2 = -ia_1V_{01}(t)\,e^{iht}, \end{cases} \tag{3.242}$$

where a_n are probability amplitudes to find the system in the state $|n\rangle$ and the transition matrix element $V_{12}(t) = V_{01}(t)$, see Eq. (3.240). Considering the case of resonance $\omega = h$ and neglecting fast oscillating terms (i.e. applying the rotating wave approximation) we obtain

$$\begin{cases} \dot{a}_0 = -ia_1V_{01}/2, \\ \dot{a}_1 = -iV_{01}(a_0 + a_2)/2, \\ \dot{a}_2 = -ia_1V_{01}/2, \end{cases} \tag{3.243}$$

that gives the equation for a harmonic oscillator for expansion coefficient of the state $|1\rangle$ with a single overturned spin

$$\ddot{a}_1 + w^2 a_1 = 0, \qquad w = \frac{V_{01}}{\sqrt{2}} = V_0 = \Omega, \tag{3.244}$$

where $w = V_{01}/\sqrt{2} = \Omega$ that corresponds to the Rabi frequency (3.232) of a single spin.

If we assume that initially at moment $t = 0$ the system is in the ground state

$$a_0(0) = 1, \qquad a_1(0) = 0, \qquad a_2(0) = 0, \tag{3.245}$$

the differential equation set (3.243) has the following solutions

$$\begin{cases} a_0(t) = (1 + \cos wt)/2, \\ a_1(t) = -i \sin(wt)/\sqrt{2}, \\ a_2(t) = (\cos wt - 1)/2. \end{cases} \tag{3.246}$$

Since the state $|1\rangle$ with one overturned spin has zero magnetization, the total magnetization in Eq. (3.229) for the system behaves as

$$M(t) = |a_0(t)|^2 - |a_2(t)|^2 = (\cos\Omega t + 1)^2/4 - (\cos\Omega t - 1)^2/4 = \cos\Omega t. \tag{3.247}$$

We can conclude that the total magnetization of a 3-level system with two spins oscillates with the same Rabi frequency $\Omega_0 = \Omega$ as for the single spin despite the $\sqrt{N}$-times larger matrix element of the perturbation.

3-level systems with interaction

Now consider the interesting case of adding an interaction between the excited spins. That is when we add the following blocking term

$$\hat{V}_D = \Delta\left(\hat{S}_1^z - \frac{1}{2}\right)\left(\hat{S}_2^z - \frac{1}{2}\right) \tag{3.248}$$

to the Hamiltonian. This shifts the energy of the $|2\rangle = |\downarrow\downarrow\rangle$ state. Consider the limit where the state $|\downarrow\downarrow\rangle$ is blocked, $\Delta \to \infty$. Then the transition between the $|1\rangle$ and $|2\rangle$ states is not possible, as it is way off resonance and it means that the 3-level system of two spins reduces effectively to a two-level system. At the same time the matrix element between the available states $|0\rangle$ and $|1\rangle$ is $\sqrt{2}$-times larger than for a single spin two-level system, Eq. (3.241). Thus the Rabi frequency is increased to $\Omega_\infty = \sqrt{2}\Omega$ for this blocked system. In this case the total magnetization oscillates as

$$M_\infty(t) = \cos\sqrt{2}\Omega t = \cos\Omega_\infty t. \tag{3.249}$$

The similar phenomenon of blocking effect of collective oscillations was predicted and observed experimentally in optics with systems of cold Rydberg atoms [128, 129, 132, 133].

In the more general case of finite Δ the additional coupling of the two spins in Eq. (3.248) causes a positive energy shift of Δ for the level $|2\rangle = |\downarrow\downarrow\rangle$. This can be interpreted as an additional interaction energy between the two excited spins. The eigenstates are the same as for the 3-level system without interaction as discussed above (see Table 3.4). The matrix elements of the perturbation are the same as in Eq. (3.240) with

$$V_{01} = \sqrt{2}\frac{h_0}{2} = \sqrt{2}V_0, \tag{3.250}$$

where $V_0 = h_0/2$ is the transition matrix element given by Eq. (3.219) for the single spin system.

Energy	**State**
0	$\|0\rangle = \|\uparrow\uparrow\rangle$
h	$\|1\rangle = (\|\uparrow\downarrow\rangle + \|\downarrow\uparrow\rangle)/\sqrt{2}$
h	$\|1^*\rangle = (\|\uparrow\downarrow\rangle - \|\downarrow\uparrow\rangle)/\sqrt{2}$
$2h+\Delta$	$\|2\rangle = \|\downarrow\downarrow\rangle$

Table 3.4: Eigenstates and eigenenergies of the two spin system with an additional interaction which shifts the energy of the state $|2\rangle$. The state $|1^*\rangle$ is decoupled from the other three states.

Expressing the perturbed wave functions (3.222) in the terms of the unperturbed states the equation set (3.223) of the Schrödinger equation becomes

$$\begin{cases} \dot{a}_0 = -ia_1 V_{01}(t)\, e^{-iht}, \\ \dot{a}_1 = -iV_{01}(t)\left(a_0 e^{iht} + a_2 e^{-i(h+\Delta)t}\right), \\ \dot{a}_2 = -ia_1 V_{01}(t)\, e^{i(h+\Delta)t}, \end{cases} \qquad V_{01}(t) = V_{01}\cos\omega t. \tag{3.251}$$

At resonance, $\omega = h$, we have

$$\begin{cases} \dot{a}_0 = -ia_1 V_{01}\,(1 + e^{-i2ht})/2, \\ \dot{a}_1 = -iV_{01}\left\{a_0(e^{i2ht} + 1) + a_2(e^{-i\Delta t} + e^{-i(2h+\Delta)t})\right\}/2, \\ \dot{a}_2 = -ia_1 V_{01}\,(e^{i(2h+\Delta)t} + e^{i\Delta t})/2. \end{cases} \tag{3.252}$$

Since the shift $\Delta \geq 0$ and $\omega = h$, the rotating wave approximation simplifies Eq. (3.252) and gives

$$\begin{cases} \dot{a}_0 = -ia_1 V_{01}/2, \\ \dot{a}_1 = -iV_{01}\left(a_0 + a_2 e^{-i\Delta t}\right)/2, \\ \dot{a}_2 = -ia_1 V_{01}\, e^{i\Delta t}/2. \end{cases} \tag{3.253}$$

Taking the first derivative of the first equation, substituting into the second row and finding its derivative we finally obtain the following 3rd order differential equation

$$\dddot{a}_0 + i\Delta\,\ddot{a}_0 + w^2\dot{a}_0 + i\Delta\,\frac{w^2}{2}a_0 = 0, \qquad w = \frac{V_{01}}{\sqrt{2}} = V_0, \tag{3.254}$$

where the variable w corresponds to the Rabi frequency $\Omega = V_0$ of a single spin. We assume that the 3-level system is in the ground state $|0\rangle$ at the moment $t = 0$ which gives the following initial conditions for the coefficient a_0 and its derivatives

$$\begin{cases} a_0(0) = 1, \\ \dot{a}_0(0) = 0, \\ \ddot{a}_0(0) = -w^2/2. \end{cases} \tag{3.255}$$

The non-interacting limit $\Delta = 0$ and the blocking limit $\Delta \to \infty$ are found as:

1. In the limit of vanishing shift ($\Delta = 0$) the obtained Eq. (3.254) corresponds to the derivative of the equation for harmonic oscillator

   $$\frac{d}{dt}\left(\ddot{a}_0 + \omega^2 a_0\right) = 0, \qquad w = \Omega, \tag{3.256}$$

   that gives the oscillating total magnetization (3.247) with the Rabi frequency $\Omega_0 = \Omega$.
2. In the case of blocking due to the huge shift ($\Delta \to \infty$) the leading contribution comes from terms in Eq. (3.254) which are proportional to the shift Δ, and gives the harmonic equation

   $$\ddot{a}_0 + \frac{w^2}{2}a_0 = 0, \qquad w = \Omega, \tag{3.257}$$

   which implies that the total magnetization in Eq. (3.249) oscillates with the effective Rabi frequency $\Omega_\infty = 2\Omega/\sqrt{2} = \sqrt{2}\Omega$.

To find the transition region between these two limits we solve the homogeneous linear ordinary differential equation (3.254). The main idea of the method is to find a solution in the exponential form $a_0 = e^{xt}$ for possibly-complex values of x that results in the characteristic equation

$$x^3 + i\Delta\,x^2 + w^2x^2 + i\Delta\,\frac{w^2}{2} = 0, \qquad w = \Omega. \tag{3.258}$$

The obtained cubic equation can be solved explicitly by Cardano's method [134]. The analytic expression of the solution is quite complicated, but in the limit of weak interaction $\Delta \ll \Omega$ the first order solution in Δ/w is

$$\begin{aligned} a_0(t) &\approx \frac{1}{4}\left(2e^{-i\frac{\Delta}{2}t} + e^{i(w+\frac{\Delta}{4})t} + e^{-i(w-\frac{\Delta}{4})t}\right), \\ a_2(t) &\approx \frac{1}{4}\left(-2e^{-i\frac{\Delta}{2}t} + e^{i(w+\frac{5}{4}\Delta)t} + e^{-i(w-\frac{5}{4}\Delta)t}\right). \end{aligned} \tag{3.259}$$

In this case the total magnetization depends on the interaction energy as

$$M_{\Delta\ll\Omega} = \cos\Omega t\,\cos\frac{3}{4}\Delta t = \frac{1}{2}\left(\cos\left(\Omega + \frac{3}{4}\Delta\right)t + \cos\left(\Omega - \frac{3}{4}\Delta\right)t\right). \tag{3.260}$$

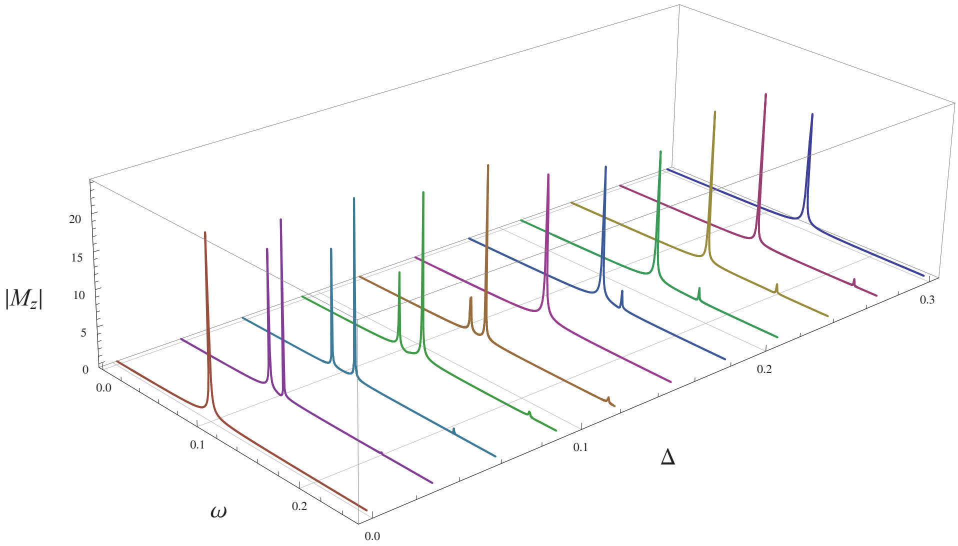

Figure 3.29: Total magnetization Fourier spectrum for the 3-level system for different values of the interaction Δ. The Fourier amplitude is given in arbitrary units along the vertical axis. For weak coupling $\Delta \ll \Omega$ the magnetization frequency is split into two components around the Rabi frequency $\Omega = 0.1$. For increasing values of Δ one of the frequency peaks weakens and moves to higher frequencies while the second peak persists and approach the frequency $\Omega_\infty = \sqrt{2}\Omega$. The crossover between the two-peak structure and the single peak at Ω_∞ happens at $\Delta \sim \Omega$.

We can see that for small interaction Δ the magnetization oscillation frequency is split into two components around the Rabi frequency Ω (this splitting is linear in Δ to the lowest order). The exact analytical solution of Eq. (3.254) with the initial conditions in Eq. (3.255) shows that intensity of one of the frequency components disappears with increasing interaction Δ, while the frequency of the other component shifts to the value $\Omega_\infty = \sqrt{2}\Omega$, see Figure 3.29 where the amplitude Fourier spectrum of the total magnetization as a function of the interaction Δ is shown for the 3-level system. This can also be seen from Figure 3.30 for fixed values of the interaction Δ.

Generalization to N spins

In the general case of a system of N spins one can expect that without interactions between the spins the total magnetization will oscillate with the same Rabi frequency $\Omega_0 = \Omega$ as for a single spin. In the case of an additional interactions between states, that shifts energy levels, magnetization behaves complicated and has components which oscillate with different frequencies and intensities. With increasing the interaction energy the biggest contribution comes from terms with higher frequency. In the limit of large interaction when the energy shift is much large than

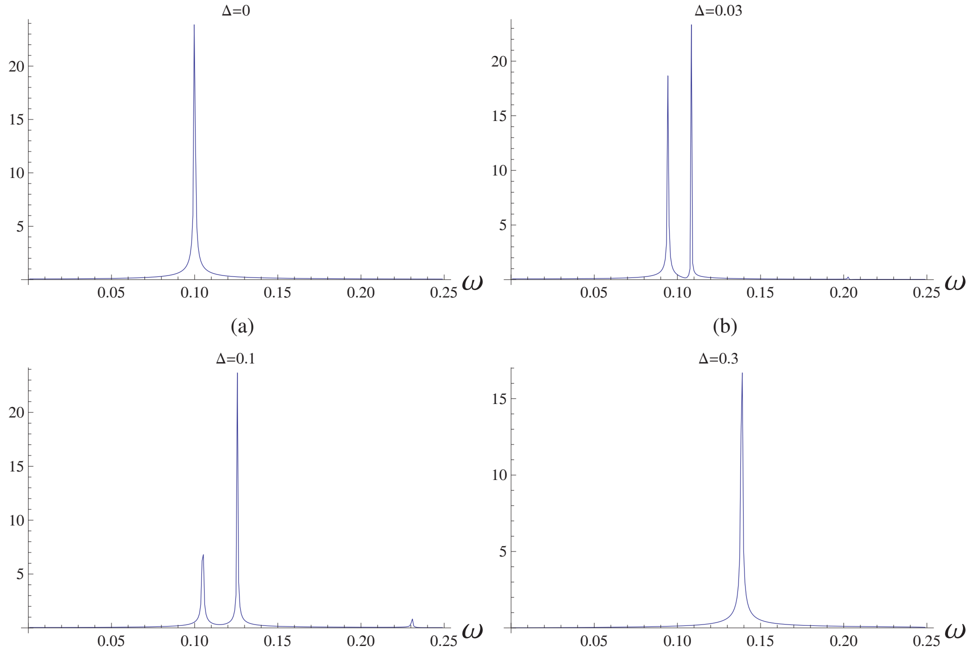

(a) (b) (c) (d)

Figure 3.30: Amplitude Fourier spectrum of the total magnetization given in Figure 3.29 for the 3-level system with interaction for fixed values of the energy shift $\Delta = 0, 0.03, 0.1, 0.3$. Horizontal axis describes the oscillation frequency. The amplitude is given in arbitrary units along the vertical axis. The transition matrix element corresponding to the Rabi frequency of single spin is $\Omega = V_0 = 0.1$. In absence of the interaction ($\Delta = 0$) frequency of the magnetization coincides with the Rabi frequency $\Omega_0 = \Omega$. In the case of blocking ($\Delta \gg \Omega$) the total magnetization oscillates with the effective Rabi frequency $\Omega_\infty = \sqrt{2}\Omega$.

the transition matrix element corresponding to the Rabi frequency ($\Delta \gg \Omega = V_0$), the blocking effect becomes crucial and the total magnetization oscillates with the high effective Rabi frequency $\Omega_\infty = \sqrt{N}\Omega$. It means that due to blocking the system of N spins behaves effectively as a two level system with the transition matrix element $V_{01} = \sqrt{N}V_0$ which causes so huge increase of the effective Rabi frequency.

It is necessary to note that in the case of perturbation due to oscillating magnetic field along the z-axis as discussed in Sections 3.10 and 3.11 the corresponding transition matrix of the operator $\hat{S}^z$ has also diagonal elements which correspond to magnetization of the eigenstates. This causes additional oscillations of the probability coefficients $a_n(t)$ at the resonance frequency ω. Therefore the level population $|a_n|^2$ will oscillate with the doubled resonance frequency 2ω. In the case of the oscillating laser field at the resonance frequency $\omega \approx 1.6J/\hbar$ this can be seen in the upper right panel of Figure 3.24, where the period of the level population is in a good agreement with the predicted value $T_n = 2\pi/(2\omega) \approx 1.96\,\hbar/J$.

3.13 Magnets in nonuniform field

An other possible model, where magnetic Bloch oscillations can be obtained, is a one-dimensional magnet with an easy-axis anisotropy in a nonuniform magnetic field [135–138].

3.13.1 Antiferromagnetic chain

In the case of antiferromagnetic (AF) spin system the magnetic BOs can be viewed, at least semiclassically, as a result of applying a constant force on *an antiferromagnetic domain wall*. This requires a nonuniform magnetic field. For an antiferromagnetic spin chain in an inhomogeneous longitudinal magnetic field with zero next-nearest-neighbor coupling $J_B = 0$ and absence of a transverse magnetic field $h_x = 0$ the Hamiltonian becomes

$$\hat{H_{AF}} = \hat{H}_z^{AF} + \hat{H}_a + \hat{H}_\perp, \tag{3.261}$$

where the $\hat{H}_z^{AF}$ term is

$$\hat{H}_z^{AF} = |J_z| \sum_i \hat{S}_i^z \hat{S}_{i+1}^z - \sum_i h_z(i) \hat{S}_i^z, \tag{3.262}$$

and the terms $\hat{H}_a$ and $\hat{H}_\perp$ are given in Eq. (3.3). The magnetic field along the z-axis increases linearly along the chain with constant magnetic field gradient b_z and can be written as $h_z(i) = ib_z$ (the lattice parameter is set equal to unity).

In the case of strong anisotropy with antiferromagnetic coupling $|J_z|$ the largest, the magnetic system behaves as an Ising-like antiferromagnet. This coupling causes antiferromagnetic order where z-components of neighboring spins are anti-aligned. In this case the first excited state corresponds to a single anti-domain wall excitation ($N_{ADW} = 1$) in the spin system and each such state can be described as

$$|j, Q\rangle_{AF} = |\ldots \uparrow\downarrow\uparrow \overset{j}{\downarrow}\downarrow \uparrow\downarrow\uparrow \ldots\rangle, \tag{3.263}$$

where the index $j = 1, 2, \ldots, N$ gives the position of the anti-domain wall, N is the total number of spins in the chain, and $\uparrow$ indicates a spin-up along the z-axis. The charge Q is defined by the first spin at the end of the antiferromagnetic chain as $Q = +1$ for spin-down and $Q = -1$ for spin-up, see [51, 139].

Acting on the state in Eq. (3.263) the Hamiltonian term $\hat{H}_a$ (corresponding to the sum of $\hat{S}_i^+ \hat{S}_{i+1}^+$ and $\hat{S}_i^- \hat{S}_{i+1}^-$) always creates an additional anti-domain wall, while the term $\hat{H}_\perp$ (which involves $\hat{S}_i^+ \hat{S}_{i+1}^-$) can also translate the AF domain wall by two lattice sites.

Considering the low energy excitations one can use the simplest single anti-domain wall approximation ($N_{ADW} \leq 1$) that gives the following effective Hamiltonian [51] describing the system

$$\hat{H}^{AF}_{N_{ADW} \leq 1} |j, Q\rangle = \left[\frac{|J_z|}{2} - (-1)^j \frac{b_z Q}{2} \left(j + \frac{1}{2} \right) \right] |j, Q\rangle + J_\perp (|j+2, Q\rangle + |j-2, Q\rangle), \quad (3.264)$$

where the boundary effects were neglected and the position of the anti-domain wall is $2 < j < N - 2$. This expression is similar to the ferromagnetic Hamiltonian in the single domain wall approximation ($N_{dw} \leq 1$) that can be used with suitable modifications for analysis of the oscillatory dynamics in an antiferromagnetic spin chain.

The energy spectrum of the Hamiltonian (3.264) is equidistant and consists of the WZL

$$E_n^{AF} = (-1)^n \frac{b_z}{2} \left(n + \frac{1}{2} \right). \quad (3.265)$$

Transition between the energy states n and $n+2$ describes the oscillatory motion of anti-domain wall in the AF system in a linear magnetic field. The Bloch frequency of the oscillations is

$$\omega_B^{AF} = b_z, \quad (3.266)$$

where b_z is the magnetic field gradient.

3.13.2 Ferromagnetic chain

While our focus has been on domain walls and their oscillatory motion, ferromagnetic magnons can also undergo the Bloch oscillations. This was predicted in an easy-axis one-dimensional ferromagnet in an inhomogeneous external field by using spin wave description by solving the phenomenological Landau-Lifshitz equation [136]. The quantum mechanical description in terms of the oscillatory dynamics of the magnons is given in the paper [138].

The Hamiltonian of a one-dimensional isotopic infinite ferromagnetic chain of spins $S = 1/2$ in a nonuniform magnetic field is

$$\hat{H} = c_0 - \sum_i J \left(\hat{S}_i^x \hat{S}_{i+1}^x + \hat{S}_i^y \hat{S}_{i+1}^y + \hat{S}_i^z \hat{S}_{i+1}^z \right) - \sum_i h_z(i) \hat{S}_i^z, \quad (3.267)$$

where J is the exchange interaction energy, $h_z(i)$ is the inhomogeneous field along the z-axis, and c_0 is a constant chosen so that the ground state energy of the ferromagnet equals zero. In the case of a linear magnetic field its magnitude is

$$h_z(i) = h_0 + b_z i, \tag{3.268}$$

where h_0 is the permanent field component, b_z is the magnetic field gradient, and the lattice parameter a is set equal to unity. Considering the low energy spectrum in the finite h_0-field an excited state corresponds to a single overturned spin (*magnon*) in the ferromagnetic chain and each state can be described in the following way

$$|j\rangle = |\ldots\uparrow\uparrow\uparrow\overset{j}{\downarrow}\uparrow\uparrow\uparrow\ldots\rangle = \hat{S}_j^-|0\rangle, \tag{3.269}$$

where $\hat{S}_i^-$ is the lowering spin operator and the index $j = 1, 2, \ldots, N$ gives the overturned spin position. The ferromagnetic state corresponds to the state $|0\rangle = |\downarrow\downarrow\downarrow\ldots\downarrow\downarrow\rangle$. In order to solve the eigenvalue problem the eigenstate $|\nu\rangle$ with energy E_ν can be expressed in the basis of the states in Eq. (3.269) as

$$|\nu\rangle = \sum_i \psi_{\nu,i}|i\rangle, \tag{3.270}$$

where $\psi_{\nu,i}$ are normalized wave function coefficients.

In this case the Schrödinger equation becomes

$$2\frac{j-\nu}{x_A}\psi_{\nu,j} = \psi_{\nu,j-1} + \psi_{\nu,j+1}, \qquad -\infty < j < \infty, \tag{3.271}$$

where the parameter x_A is

$$x_A = \frac{J}{b_z}. \tag{3.272}$$

The expression in Eq. (3.271) corresponds to the recurrent relation of the Bessel functions [107], so its solution is given in terms of the Bessel function $J_\nu(x)$ as

$$\psi_{\nu,j} = J_{\nu-j}(x_A), \tag{3.273}$$

where the argument x_A describes the localization length of the eigenstate with energy E_ν. The energy spectrum of the spin system consists of equidistant energy levels

$$E_\nu = (J + h_0) + b_z\nu \tag{3.274}$$

and forms a typical Wannier-Zeeman ladder.

In order to analyze dynamics of the spin system we can consider the time evolution of the total longitudinal magnetization

$$M_z(t) = \langle\chi(t)|\sum_i \hat{S}_i^z|\chi(t)\rangle, \tag{3.275}$$

where a general time-dependent state of the quantum system can be expressed in terms of the eigenstates in Eq. (3.270) as

$$|\chi(t)\rangle = \sum_{\nu} a_{\nu}(t)\, e^{-iE_{\nu}t}|\nu\rangle, \tag{3.276}$$

where the coefficient a_{ν} as a function of time describes the population of eigenstate $|\nu\rangle$ with energy E_{ν}. Since the spin operator $\hat{S}^z$ does not change a spin state the corresponding matrix element is

$$\langle\nu|\hat{S}^z_i|\mu\rangle = \frac{1}{2}\delta_{\mu,\nu} - \psi_{\nu,i}\,\psi_{\mu,i}(1-\delta_{\nu 0})(1-\delta_{\nu\mu}). \tag{3.277}$$

Using properties of the Bessel functions and the transition matrix element in Eq. (3.277) the total magnetization becomes

$$M_z(t) = \frac{N}{2} - \sum_n |a_n(t)|^2 n - 2x_A \sum_n \Re\left(a^*_n(t)a_{n+1}(t)e^{-i\omega_B t}\right), \qquad \omega_B = b_z, \tag{3.278}$$

where the parameter $x_A = J/b_z$ describes the magnitude of the oscillation. The real part of the oscillating term can be written in the form

$$\sum_n \Re\left(a^*_n a_{n+1} e^{-i\omega_B t}\right) = \sum_n \rho_n \cos(\omega_B t - \phi_n), \tag{3.279}$$

where ρ_n and ϕ_n are absolute value and argument of the overlap respectively

$$\rho_n = |a^*_n a_{n+1}|, \qquad \phi_n = \arg(a^*_n a_{n+1}). \tag{3.280}$$

The last term in Eq. (3.278) corresponds to the magnetic BOs and depends on the overlap between neighbouring states. Therefore the Bloch oscillations can be observed directly as time-dependent oscillations in the longitudinal magnetization at the Bloch frequency

$$\omega_B = b_z. \tag{3.281}$$

Consider now the dynamical structure factor for the spin system at non-zero temperature which is given by Eq. (3.141) and can be rewritten in real space as

$$S^{\alpha\beta}_{i,j}(\omega) = \sum_{m,n} \frac{1}{Z} e^{-\beta_T E_n} \langle n|\hat{S}^{\alpha}_i|m\rangle\langle m|\hat{S}^{\beta}_j|n\rangle\, \delta\big(\omega - (E_m - E_n)\big), \tag{3.282}$$

where $|n\rangle$ and $|m\rangle$ correspond to excited states with energy E_n and E_m respectively, Z is the partition function, β_T is the inverse temperature, and i and j are positions of spins in the chain. Using the transition matrix element in Eq. (3.277) and explicit form of the wave function coefficients in Eq. (3.273) the dynamical structure factor S^{zz} becomes

$$\begin{aligned} S^{zz}_{ij}(\omega) = {}& \frac{1}{4}\delta(\omega) + \sum_{n,m} \frac{e^{-\beta_T E_n}}{Z}\, \delta(E_m - E_n - \omega) \\ & \times (1-\delta_{n0})(1-\delta_{nm}) J_{n-i}(x_A)\, J_{n-j}(x_A)\, J_{m-i}(x_A)\, J_{m-j}(x_A), \end{aligned} \tag{3.283}$$

where the first term corresponds to the squared bulk magnetization.

Since the spin operators $\hat{S}^{\pm}$ overturn only a single spin their matrix elements are

$$\langle\nu|\hat{S}_i^{+}|\mu\rangle = \psi_{\mu,i}\,\delta_{\nu 0}(1-\delta_{\mu 0}), \qquad \langle\mu|\hat{S}_i^{-}|\nu\rangle = \psi^{*}_{\mu,j}\,\delta_{\nu 0}(1-\delta_{\mu 0}), \tag{3.284}$$

where the asterisk $*$ is notation of the complex conjugate. In this case the dynamical structure factor S^{+-} becomes

$$S_{ij}^{+-}(\omega) = \frac{1}{Z}\sum_{m\neq 0}\delta(J+h_0+b_z m-\omega)\,J_{m-i}(x_A)\,J_{m-j}(x_A), \tag{3.285}$$

where the argument of the Bessel function is $x_A = J/b_z$. In order to simplify this expression we can introduce new variables: distance $l = j - i$ and position of "center of mass" $R = (i+j)/2$. Using the Graf's theorem for the Bessel functions and performing the Fourier transform the structure factor can be written as

$$S_R^{+-}(q,\omega) = \frac{1}{Z\sqrt{N}}\sum_{m\neq 0}\delta(J+h_0+b_z m-\omega)\,J_{2R-2m}(2x_A|\cos q|). \tag{3.286}$$

Due to properties of the Bessel function the dynamical structure factor S_R^{+-} has maximal intensity of peaks at $|R-m| \approx |\cos q|J/b_z$ and it is localized around $\omega = J + h_0 + b_z R$. The structure factor behaviour for the fixed parameter R and the magnetic gradient field $b_z = 0.1J$ and $h_0 = 0$ is shown in Figure 3.31.

By the same way the structure factor S_R^{-+} can be expressed as

$$S_R^{-+}(q,\omega) = \frac{e^{-\beta_T(J+h_0)}}{Z\sqrt{N}}\sum_{m\neq 0}e^{-\beta_T b_z m}\delta(J+h_0+b_z m+\omega)\,J_{2R-2m}(2x_A|\cos q|), \tag{3.287}$$

where the argument is $x_A = J/b_z$.

3.13.3 Bloch frequency in gradient field

We can see that in both cases the Bloch frequency of the magnetic BOs in a one-dimensional magnet in a linear external field in Eqs. (3.266) and (3.281) is proportional to the field gradient b_z which value is naturally restricted in real experiments. The Bloch frequency in usual physical system of units is given by

$$\hbar\omega_B = g\mu_B B\frac{a}{L}, \tag{3.288}$$

where $\mu_B = 5.79\times 10^{-5}$ eV/T is Bohr magneton, g is the spin g-factor, a is lattice parameter, and L is sample length. For typical magnetic materials the lattice constant a is about a few Ångströms [58], while the typical size of a magnetic crystal is of the order of a centimeter. The field strength B of the strongest permanent magnets usually does not exceed a few Tesla [140]. It gives the following estimate of the Bloch frequency of a single soliton at $\omega_B \approx 10^3$ s^{-1} which expressed in units of Kelvins corresponds to extremely low energy scale $\hbar\omega_B \approx 10^{-8}$ K.

Therefore it is extremely hard to observe these magnetic Bloch oscillations in a gradient magnetic field in laboratory experiments since this phenomenon will be suppressed by thermal

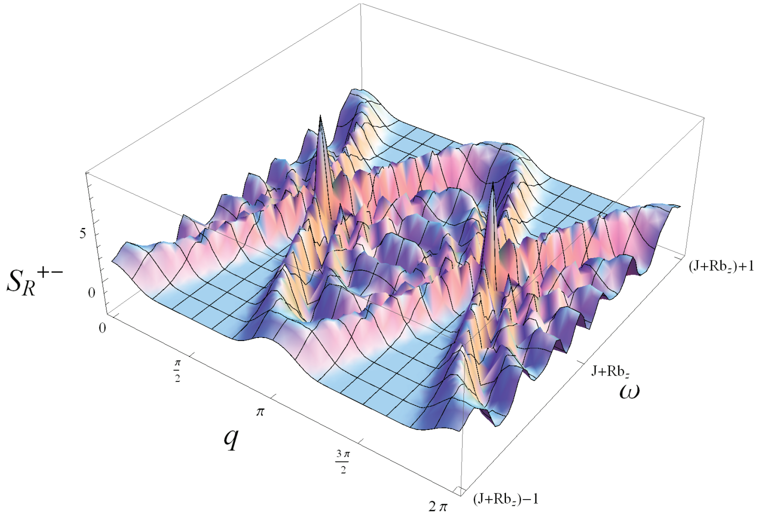

Figure 3.31: The dynamical structure factor $S_R^{+-}(q,\omega)$ in arbitrary units given by Eq. (3.286) for the fixed parameter R for ferromagnetic chain in linear magnetic field with gradient $b_z = 0.1J$ and $h_0 = 0$. In order to generate the plot Dirac delta-functions were approximated by a Gaussian distributions with variance 10^{-3}.

excitations in magnets.

3.14 Summary

We studied excitations in quantum magnets caused by motion of domain walls which can exhibit Bloch oscillations in an applied magnetic field. We investigated the possibility to observe signatures of the magnetic Bloch oscillations in a one-dimensional easy-axis ferromagnetic spin system subject to an external field at low temperature. Using the quantum mechanical approach we found the energy and the wave function of excited states corresponding to the bound states of domain and anti-domain walls. In a noninteracting gas approximation of such excitations the energy spectrum and the wave functions were calculated analytically by restricting the maximal number of the domain walls to be less or equal to two. We analyzed in details the obtained result for different spin system parameters and found regions in momentum space where the energy levels are equidistantly spaced (also in the presence of exchange couplings), that corresponds to the Wannier-Zeeman ladder.

We also calculated analytically the neutron scattering dynamic structure factor at zero and finite temperatures. Our results show that the neutron scattering signatures of the magnetic BOs are more pronounced at finite temperatures. We found that a relatively high temperature is favorable since it allows to excite a bigger number of domain walls performing oscillations, but the high temperature leads also to collisions between domain walls that destroy BO. In particular, we considered material parameters corresponding to the salt $\mathrm{CoCl_2 \cdot 2H_2O}$, as a prominent candidate of observing the magnetic BOs, and determined optimal parameters for the temperature and the magnetic field to find significant neutron scattering signatures of the magnetic Bloch oscillations.

In addition to the study of the thermal excitation of BOs we proposed to use far-infrared lasers in order to induce the magnetic Bloch oscillations in one-dimensional anisotropic ferromagnets at low temperature. We focused on the material parameters of $\mathrm{CoCl_2 \cdot 2H_2O}$ and considered electromagnetic interaction of the laser radiation with magnetic Co-ions in this material. We investigated numerically dynamics of the induced total magnetization and found that it is possible to excite the magnetic BOs in the $\mathrm{CoCl_2 \cdot 2H_2O}$ material by using the resonant laser beams with proper frequencies in a static magnetic field at low temperatures. After turning off the lasers at an exposition time the total magnetization continues to oscillate at the Bloch frequency which is proportional to the applied field. Our analytical calculations and numerical simulations show that due to the relatively small transition matrix elements the application of a single laser beam requires a higher laser intensity and a longer exposition time than for two laser beams with resonant frequencies of the nearest energy levels in the WZL.

Allowing also states with a bigger number of domain walls we performed simulations taking into account the interaction between domain walls for a spin system of size $N = 32$. Analysing dynamics of this quantum system we found that the interactions cause a blocking effect which accelerate the excitation process. Also for the used parameters the dephasing time scale due to domain-wall interactions is longer than the exposition time needed to excite significantly the BOs.

In addition, we also considered the possibility to obtain magnetic Bloch oscillations in one-dimensional magnets subject to a gradient magnetic field and obtained the analytic expressions for the dynamical structure factors. We found that the magnetic BOs in the nonuniform field are extremely hard observable in laboratory experiments.

While we focused mostly on the material parameters for $\mathrm{CoCl_2 \cdot 2H_2O}$, our main results are analytic and can also be applied with minor changes to theoretical and experimental research for the magnetic Bloch oscillations in other similar magnetic materials, for example in $\mathrm{CoNb_2O_6}$.

Chapter 4

Impurity in a Heisenberg antiferromagnet

Modern experimental techniques can probe materials at high spatial resolution, the atomic scale, that allows to investigate local magnetization around impurities in antiferromagnets, for example, by Knight shifts in nuclear magnetic resonance (NMR) experiments [141–143]. In addition, magnetic force microscopy (MFM) [144, 145] and spin-polarized scanning tunneling microscopy (SP-STM) offer also the unique possibility to study magnetic materials directly on the spatial scale of individual atoms [146–148].

The general interests in antiferromagnets are rooted in the discovery of high-temperature superconductivity (high-T_c) in 1986 [149]. Cuprate superconductors, such as $\mathrm{La_2CuO_4}$ and $\mathrm{Nd_2CuO_4}$, can be considered as quasi-two-dimensional materials which contain weakly coupled copper-oxide ($\mathrm{CuO_2}$) layers [150]. The superconducting properties of cuprates are determined by electrons moving within these layers [151]. At half-filling the electrons cannot move and the material behaves as an insulating antiferromagnet [152] which magnetic properties can be described by an square-lattice antiferromagnetic spin-$1/2$ Heisenberg Hamiltonian [153, 154].

Low-temperature properties of a quantum Heisenberg antiferromagnet can be studied by mapping the model onto a quantum-mechanical nonlinear σ-model [155, 156]. Furthermore when this model has long-range order at zero temperature, the long-wavelength behavior of a two-dimensional Heisenberg antiferromagnet at finite temperatures can be described by a purely classical σ-model, with parameters renormalized by the quantum fluctuations [157, 158]. In the same spirit, in the work [159] a single vacancy in an antiferromagnet subjected to an external field was studied by using a renormalized classical description.

Another way of studying Heisenberg antiferromagnets is to employ the spin-wave expansion. Developed in the 50's [160, 161] this approach allows a systematic treatment of quantum fluctuations in ordered magnets. In order to use spin-wave theory on the Heisenberg model we can apply the Holstein-Primakoff [162] or the Dyson-Maleev transformation [163, 164], that allows to simplify and treat this model in terms of bosonic magnon operators. The Holstein-Primakoff representation gives excellent results for a broken symmetry phase and can be used to investigate low-temperature properties of a two-dimensional Heisenberg model, see [165, 166].

In this chapter we will describe how the Holstein-Primakoff transformation is employed to treat analytically a general impurity in a Heisenberg antiferromagnet in an external magnetic field.

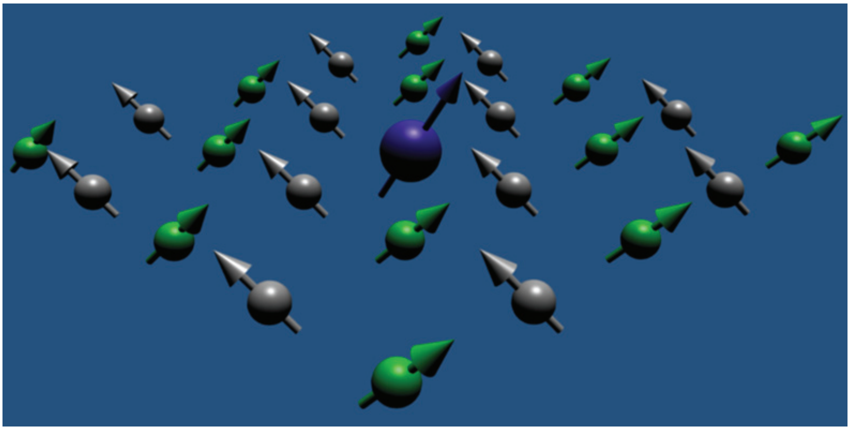

Figure 4.1: Schematic illustration of an impurity in an ordered 2D antiferromagnet in external field. The blue sphere corresponds to the impurity while the green and grey spheres describe antiferromagnetically ordered bulk spins of two sublattices. The magnetic field is perpendicular to the plane of the spins. Not shown is how the impurity affects its neighbouring spins via interactions which is the main objective of this chapter.

4.1 Hamiltonian

We consider the following Hamiltonian describing a Heisenberg magnet in a magnetic field

$$\hat{H} = \sum_{\langle i,j \rangle} J_{ij} \hat{\vec{S}}_i \cdot \hat{\vec{S}}_j - \sum B_i \hat{S}_i^z \tag{4.1}$$

on a hyper cubic lattice where each site has Z nearest neighbors. In the general case the couplings J_{ij} and magnetic field B_i are site-dependent that allows to investigate a single impurity in an otherwise uniform antiferromagnet in a homogeneous field, see Figure 4.1. We consider the case when all bulk bounds not connected to an impurity are equal and antiferromagnetic with a magnitude $J > 0$. The impurity with spin S_0 resides on site $i = 0$ and is connected to its neighbors by a general coupling constant J_0 which can be either ferromagnetic or antiferromagnetic, see Figure 4.2(a). The antiferromagnet is subjected to an uniform magnetic field directed along the z-axis with magnitude B. In the general case the impurity spin has its own gyromagnetic factor for its Zeeman coupling to the external field, thus the magnitude of the effective magnetic field on the impurity site is written B_0 which can be different from B. We assume that the applied field is small, $B < J$, and that the spin system is at zero temperature.

For further calculation it is convenient to rewrite the Hamiltonian (4.1) as

$$\hat{H} = \hat{H}_{bulk} + \hat{H}_{imp}, \tag{4.2}$$

where the Hamiltonian is divided into two terms corresponding to contributions from the bulk

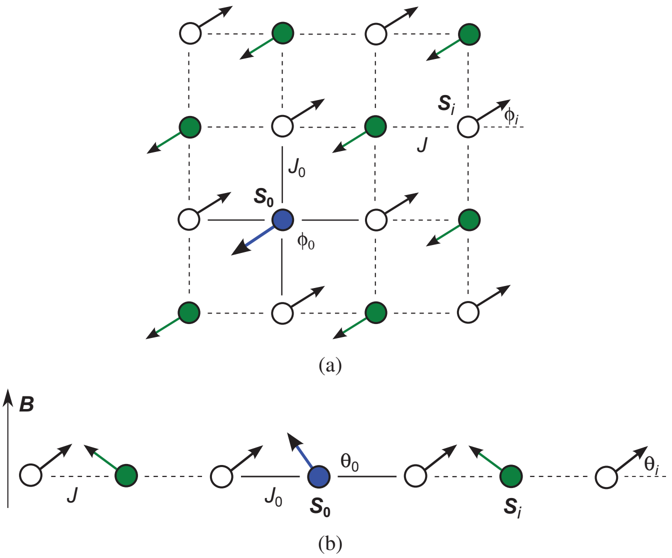

Figure 4.2: The rotation symmetry is broken by an applied field and the spins exhibit an ordered canted state (a) Top view of this state. The solid blue circle describes the impurity spin S_0 which is coupled to neighbor S_i-spins by constant J_0. The spin directions are parameterized by the angles θ_i and ϕ_i. (b) Front view of the canted state. The green and white circles show antiferromagnetically ordered bulk spins of the two sublattices. The applied field $\vec{B}$ is directed along the z-axis.

spins and the impurity

$$\hat{H}_{bulk} = J \sum_{\langle i,j \rangle} \hat{\vec{S}}_i \cdot \hat{\vec{S}}_j - B \sum_i \hat{S}_i^z, \tag{4.3}$$

$$\hat{H}_{imp} = J_0 \sum_{\langle 0,j \rangle} \hat{\vec{S}}_0 \cdot \hat{\vec{S}}_j - B_0 \hat{S}_0^z - J \sum_{\langle 0,j \rangle} \hat{\vec{S}}_{i=0} \cdot \hat{\vec{S}}_j + B \hat{S}_{i=0}^z. \tag{4.4}$$

In the expression for $\hat{H}_{imp}$ the sum is performed over all Z nearest neighbours of the impurity site.

We can study the Hamiltonian in Eq. (4.2) with spin-wave theory which is an expansion in fluctuations about an ordered classical state. To find the appropriate classical state to expand about we note that an applied magnetic field breaks the rotation symmetry and causes the spins to cant along the z-axis in an ordered antiferromagnet [167, 168], thus the classical state of the antiferromagnet in the external field corresponds to the canted state of spins which is shown in Figure 4.2(b).

In order to parameterize this canted state so that the classical spin configuration is directed along the z-axis, we introduce rotated spins $\vec{S}_i'$ so that its z-component points along a direction described by the latitude θ_i and azimuthal ϕ_i angles, see Figure 4.2. In this case the rotated spin components are related to the spins $\vec{S}_i$ in the global coordinate frame as [113]

$$\begin{aligned} S_i^x &= (S_i'^x \sin\theta_i - S_i'^z \cos\theta_i)\cos\phi_i - S_i'^y \sin\phi_i, \\ S_i^y &= (S_i'^x \sin\theta_i - S_i'^z \cos\theta_i)\sin\phi_i - S_i'^y \cos\phi_i, \\ S_i^z &= S_i'^x \cos\theta_i + S_i'^z \sin\theta_i. \end{aligned} \tag{4.5}$$

Inserting these relations into the Hamiltonian in Eq. (4.2) we obtain the Hamiltonian expressed in terms of rotated spins for arbitrary angles, which will be determined later. In order to use spin-wave theory and employ quantum fluctuations about the ordered classical state we apply the Holstein-Primakoff transformation [162] which maps from the angular momentum operators to boson creation and annihilation operators and can be written as

$$\hat{S}^+ = \sqrt{2S - a^\dagger a}\, a, \tag{4.6}$$

$$\hat{S}^- = a^\dagger \sqrt{2S - a^\dagger a}, \tag{4.7}$$

$$\hat{S}^z = S - a^\dagger a, \tag{4.8}$$

where $\hat{S}_i^\pm = \hat{S}_i^x \pm i\hat{S}_i^y$ are the usual spin raising and lowering operators, and creation and annihilation operators obey the commutation relation

$$[a, a^\dagger] = 1. \tag{4.9}$$

Expanding the square roots in Taylor series and keeping terms up to the first order of $1/S$ we can rewrite the spin operators as

$$\hat{S}^x \approx \sqrt{\frac{S}{2}}\left[a^\dagger + a - \frac{1}{4S}(a^\dagger a^\dagger a + a^\dagger a a)\right], \tag{4.10}$$

$$\hat{S}^y \approx i\sqrt{\frac{S}{2}}\left[a^\dagger - a - \frac{1}{4S}(a^\dagger a^\dagger a - a^\dagger a a)\right]. \tag{4.11}$$

By inserting these expressions for the spin operator $\hat{\vec{S}}'$ into the Hamiltonian in Eq. (4.2) we get terms with different powers of bosonic operators.

4.1.1 Minimization Condition

The zeroth order term in the bosonic operators corresponds to the energy of the classical state of spins oriented along the S'^z direction. For simpler notation let us to return to the general expression of the Hamiltonian in Eq. (4.1). In this case the zeroth order (constant) terms give

$$\hat{H}_0 = \sum_{\langle i,j \rangle} J_{ij} S_i S_j \left(\cos\theta_i \cos\theta_j \cos\phi_{ij} + \sin\theta_i \sin\theta_j\right) - \sum_i B_i S_i \sin\theta_i, \tag{4.12}$$

where the relative angles are $\phi_{ij} = \phi_i - \phi_j$ and S_i are spin quantum numbers. Minimizing with respect to the variable ϕ_{ij} gives the following condition

$$-J_{ij} S_i S_j \cos\theta_i \cos\theta_j \sin\phi_{ij} = 0 \tag{4.13}$$

meaning that the relative angles ϕ_{ij} should be equal to 0 or π. In order to be a *minimum* of the energy it needs to obey

$$-J_{ij}\cos\phi_{ij} > 0, \tag{4.14}$$

which means that $\phi_{ij} = \pi$ for an antiferromagnetic coupling ($J_{ij} > 0$) and $\phi_{ij} = 0$ for a ferromagnetic ($J_{ij} < 0$). This can be written in the equivalent form

$$-\cos(\phi_{ij}) = \nu_{ij}, \qquad \nu_{ij} = \operatorname{sgn} J_{ij} = \frac{J_{ij}}{|J_{ij}|}. \tag{4.15}$$

In the case of a homogeneous magnet with uniform coupling $J = J_{ij}$ we can use the parameter $\nu = \nu_{ij} = \operatorname{sgn} J$.

For further simplification we select the rotation angle ϕ_0 on the impurity site, so that it is either 0 or π. In this case using the minimization conditions in Eq. (4.15) the general Hamiltonian can be written as

$$\begin{aligned}\hat{H} =& \sum_{\langle i,j\rangle} J_{ij}\Big[\cos(\theta_i + \nu_{ij}\theta_j)\left(\hat{S}_i^{\prime x}\hat{S}_j^{\prime x} - \nu_{ij}\hat{S}_i^{\prime z}\hat{S}_j^{\prime z}\right) - \nu_{ij}\hat{S}_i^{\prime y}\hat{S}_j^{\prime y} \\ &+ \sin(\theta_i + \nu_{ij}\theta_j)\left(\nu_{ij}\hat{S}_i^{\prime x}\hat{S}_j^{\prime z} + \hat{S}_i^{\prime z}\hat{S}_j^{\prime x}\right)\Big] - \sum_i B_i\left(\hat{S}_i^{\prime x}\cos\theta_i + \hat{S}_i^{\prime z}\sin\theta_i\right).\end{aligned} \tag{4.16}$$

Now we can return to the special case of a single impurity embedded in a homogeneous spin-S antiferromagnet described by the Hamiltonian (4.2). In order to simplify the model and treat it analytically we assume that the variation in the latitude angles θ_i is relatively small for all bulk sites i which are away from the impurity. Therefore the latitude angles can be approximated with one site independent value of $\theta_i = \theta$.[1] The impurity site $i = 0$ keeps a separate angle θ_0. In addition, the ordered antiferromagnetic state can be described by two sublattices which are parameterized by staggered azimuthal angles $\phi_i = \phi_{even}$ and $\phi_j = \phi_{odd}$ for the corresponding sublattices.

Applying this assumption the zeroth order term of the Hamiltonian (4.2) in the bosonic operators becomes

$$\begin{aligned}\hat{H}_0 =& -NS\left(\frac{JSZ}{2}\cos 2\theta + B\sin\theta\right) + ZS\big(JS\cos 2\theta - |J_0|S_0\cos(\theta + \nu_0\theta_0)\big) \\ &+ BS\sin\theta - B_0S_0\sin\theta_0,\end{aligned} \tag{4.17}$$

where S_0 and S are spins of the impurity and the bulk sites respectively, N is the total number of sites, and the variable ν_0 denotes the sign of the impurity coupling

$$\nu_0 = \operatorname{sgn} J_0 = \frac{J_0}{|J_0|}, \tag{4.18}$$

which can be antiferromagnetic ($J_0 > 0$) or ferromagnetic ($J_0 < 0$). Minimizing Eq. (4.17)

---

[1] In Sections 4.7.1 and 4.7.2 we will consider a site-dependent shift of the latitude angles θ_i in order to calculate the non-trivial local variation of the magnetization.

with respect to the latitude angle θ_0 on the impurity site we obtain

$$J_0 SZ \sin(\theta + \nu_0 \theta_0) - B_0 \cos\theta_0 = 0, \tag{4.19}$$

which can be solved to yield

$$\tan \nu_0 \theta_0 = \frac{B_0}{J_0 SZ \cos\theta} - \tan\theta. \tag{4.20}$$

Minimizing the zeroth order Hamiltonian in Eq. (4.17) also with respect to the latitude angle θ and taking into account the leading terms for the bulk contribution in the thermodynamic limit, $N \to \infty$, we finally obtain the following energy minimization conditions

$$\sin\theta = \frac{B}{2SZJ}, \qquad \phi_{even} - \phi_{odd} = \pi, \tag{4.21}$$

$$\tan\theta_0 = \frac{B_0}{|J_0| SZ \cos\theta} - \nu_0 \tan\theta, \qquad \cos\phi_0 = \nu_0. \tag{4.22}$$

We see that the minimization conditions on the bulk angles θ and ϕ do not depend on the impurity and are identical to the expressions for a uniform antiferromagnet in a magnetic field. This fact is a natural result of taking the thermodynamic limit.

Limiting cases

Consider some limiting cases.

- The same impurity coupling $J_0 = J$ and $B_0 = B$ implies that $\theta_0 = \theta$ regardless of the impurity spin magnitude S_0.
- Extreme impurity coupling $|J_0| \gg J$ implies that the lattitude angle of the impurity is $\theta_0 = -\nu_0 \theta$. The impurity spin is directed parallel to the bulk spin polarization in the case of strong ferromagnetic coupling ($J_0 < 0$), while it is antiparallel in the case of antiferromagnetic interaction ($J_0 > 0$).
- Isolated impurity with $J_0 = 0$, a vacancy, gives $\theta_0 = \pi/2$ for $B_0 > 0$ and $\theta_0 = -\pi/2$ for $B_0 < 0$. The spin of the impurity is directed along the applied local field.
- Classical limit of large bulk spins implies $\theta = 0$ and $\theta_0 = 0$, so that all spins tend to be ordered in the same plane.

4.1.2 Linear Terms

The non-collinearity of the spins in the canted state results in the appearance of terms which are of linear order in the bosonic operators. The linear terms of the Hamiltonian corresponding to the bulk part contribution in Eq. (4.3) is

$$\hat{H}^1_{bulk} = JSZ\sqrt{\frac{S}{2}} \left(\sin 2\theta - \frac{B}{JSZ} \cos\theta \right) \sum_i \left(a_i + a_i^\dagger \right), \tag{4.23}$$

which actually vanish by applying the minimization condition for the latitude angle θ, Eq. (4.21). The linear terms of the impurity Hamiltonian in Eq. (4.4) however do not vanish. They can be written as

$$\hat{H}^1_{imp} = C_0 \left(a_0 + a_0^\dagger \right) + \frac{C}{Z} \sum_{\langle 0,j \rangle} \left(a_j + a_j^\dagger \right), \tag{4.24}$$

where sum is performed over the nearest neighbors of the impurity spin, and $a_0^\dagger$, a_0 are the bosonic operators corresponding to the impurity spin. The constants C_0 and C are given by the relations

$$C_0 = J_0 S Z \sqrt{\frac{S_0}{2}} \sin(\nu_0 \theta_0 + \theta) - B_0 \sqrt{\frac{S_0}{2}} \cos\theta_0, \tag{4.25}$$

$$C = J_0 S_0 Z \sqrt{\frac{S}{2}} \nu_0 \sin(\nu_0 \theta_0 + \theta) - JSZ \sqrt{\frac{S}{2}} \sin 2\theta. \tag{4.26}$$

Using the minimization conditions in Eqs. (4.21) and (4.22) the constant C_0 vanishes while the second constant can be written equivalently as

$$C = \sqrt{\frac{S}{2}} \left(\frac{S_0}{S} \nu_0 B_0 \cos\theta_0 - B \cos\theta \right). \tag{4.27}$$

Thus the impurity part gives the only contribution to the first order terms of the Hamiltonian in the bosonic operators

$$\hat{H}_1 = \hat{H}^1_{imp} = \frac{C}{Z} \sum_{\langle 0,j \rangle} \left(a_j + a_j^\dagger \right). \tag{4.28}$$

It is convenient to work in the momentum space by applying Fourier transforms

$$a_i = \frac{1}{\sqrt{N}} \sum_{\vec{k}} a_{\vec{k}} e^{i\vec{k}\cdot\vec{r}_i} \tag{4.29}$$

and introduce the usual γ_k characteristic of a crystal lattice

$$\gamma_{\vec{k}} = \frac{1}{Z} \sum_{\vec{r}} e^{i\vec{k}\cdot\vec{r}} = \frac{2}{Z} \big(\cos k_x + \cos k_y + \dots \big), \qquad -1 \leq \gamma_{\vec{k}} \leq 1, \tag{4.30}$$

where the momentum $\vec{k}$ is given in units of the inverse lattice spacing a as $k_i \in [-\frac{\pi}{a}, \frac{\pi}{a}]$. In this case the linear terms of the Hamiltonian in Eq. (4.28) can be expressed as

$$\hat{H}_1 = \frac{C}{\sqrt{N}} \sum_{\vec{k}} \gamma_{\vec{k}} \left(a_{\vec{k}} + a_{\vec{k}}^\dagger \right). \tag{4.31}$$

4.1.3 Quadratic Terms

For the quadratic terms of the Hamiltonian we keep, as a first approximation, the leading order N terms coming from to the bulk part. Using this approximation we omit quadratic terms from the impurity part which can change the overall magnitude in the local order around the impurity. However, it was shown from numerical studies in [169] that this effect is relatively small, and we can neglect the impurity quadratic terms in order to calculate the bulk magnetization. This approximation implies that the quadratic terms of the Hamiltonian do not depend on the impurity and are given by

$$\hat{H}_2 \approx \hat{H}^2_{bulk} = \frac{1}{2}\sum_{\vec{k}} \left\{ A_{\vec{k}} a^\dagger_{\vec{k}} a_{\vec{k}} + B_{\vec{k}} a_{\vec{k}} a_{-\vec{k}} + h.c. \right\}, \tag{4.32}$$

where the momentum-dependent coefficients are

$$A_{\vec{k}} = JSZ(\cos 2\theta - \gamma_{\vec{k}} \sin^2\theta) + B\sin\theta, \tag{4.33}$$
$$B_{\vec{k}} = JSZ\,\gamma_{\vec{k}} \cos^2\theta, \tag{4.34}$$

which are also known from the standard spin-wave theory [170]. Using the minimization conditions in Eq. (4.21) the coefficient $A_{\vec{k}}$ and the sum of the coefficients $A_{\vec{k}}$ and $B_{\vec{k}}$ can be written as

$$A_{\vec{k}} = JSZ(1 - \gamma_{\vec{k}} \sin^2\theta), \tag{4.35}$$
$$A_{\vec{k}} + B_{\vec{k}} = JSZ(1 + \gamma_{\vec{k}} \cos 2\theta). \tag{4.36}$$

We can parameterize the last sum as

$$A_{\vec{k}} + B_{\vec{k}} = f \times (1 + g\gamma_{\vec{k}}) \tag{4.37}$$

in terms of constants f and g which are

$$f = JSZ, \qquad\qquad g = \cos 2\theta \tag{4.38}$$

to leading order in $1/S$.

The quadratic bulk terms in the Hamiltonian in Eq. (4.32) can be diagonalized by using the canonical Bogoliubov transformation [171]

$$\begin{aligned} a_{\vec{k}} &= u_{\vec{k}} b_{\vec{k}} + v_{\vec{k}} b^\dagger_{-\vec{k}}, & [b_{\vec{k}}, b^\dagger_{\vec{k}}] &= 1, \\ a^\dagger_{\vec{k}} &= u_{\vec{k}} b^\dagger_{\vec{k}} + v_{\vec{k}} b_{-\vec{k}}, & |u_{\vec{k}}|^2 - |v_{\vec{k}}|^2 &= 1, \end{aligned} \tag{4.39}$$

to yield the following quadratic Hamiltonian

$$\hat{H}_2 = \sum_{\vec{k}} \omega_{\vec{k}} b^\dagger_{\vec{k}} b_{\vec{k}} + \frac{1}{2}\sum_{\vec{k}} \left(\omega_{\vec{k}} - A_{\vec{k}}\right), \tag{4.40}$$

where the coefficient $\omega_{\vec{k}}$ is

$$\omega_{\vec{k}} = \sqrt{A^2_{\vec{k}} - B^2_{\vec{k}}}. \tag{4.41}$$

The second summand in the quadratic Hamiltonian in Eq. (4.40) is a constant part which can be lumped together with the zeroth order Hamiltonian $\hat{H}_0$ given in Eq. (4.17). Using the expressions in Eqs. (4.34) and (4.35) the coefficient $\omega_{\vec{k}}$ becomes

$$\omega_{\vec{k}} = JSZ\sqrt{\left(1-\gamma_{\vec{k}}\right)\left(1+\cos 2\theta\gamma_{\vec{k}}\right)}. \tag{4.42}$$

The canonical transformation coefficients have real values and obey the relations

$$u_{\vec{k}}^2 + v_{\vec{k}}^2 = \frac{A_{\vec{k}}}{\omega_{\vec{k}}}, \qquad 2u_{\vec{k}}v_{\vec{k}} = -\frac{B_{\vec{k}}}{\omega_{\vec{k}}}. \tag{4.43}$$

In addition, the quadratic bulk Hamiltonian gives the following expectation values for the nearest-neighbor sites [170, 172]

$$\begin{aligned}
\delta = \langle a_i a_i \rangle &= \frac{1}{N}\sum_{\vec{k}} u_{\vec{k}}v_{\vec{k}} = -\frac{1}{N}\sum_{\vec{k}} \frac{B_{\vec{k}}}{2\omega_{\vec{k}}}, \\
\Delta = \langle a_i a_j \rangle &= \frac{1}{N}\sum_{\vec{k}} \gamma_{\vec{k}} u_{\vec{k}}v_{\vec{k}} = -\frac{1}{N}\sum_{\vec{k}} \gamma_{\vec{k}}\frac{B_{\vec{k}}}{2\omega_{\vec{k}}}, \\
m = \langle a_i^\dagger a_j \rangle &= \frac{1}{N}\sum_{\vec{k}} \gamma_{\vec{k}} v_{\vec{k}}^2 = \frac{1}{N}\sum_{\vec{k}} \gamma_{\vec{k}}\frac{A_{\vec{k}}}{2\omega_{\vec{k}}}, \\
n = \langle a_i^\dagger a_i \rangle &= \frac{1}{N}\sum_{\vec{k}} v_{\vec{k}}^2 = \frac{1}{N}\sum_{\vec{k}} \frac{A_{\vec{k}}}{2\omega_{\vec{k}}} - \frac{1}{2}.
\end{aligned} \tag{4.44}$$

Due to the bulk nature of the quadratic term in this approximation the expectation values in Eq. (4.44) do not depend on the site positions i and j. In Table 4.1 we show the typical bulk values calculated numerically in a uniform spin-$1/2$ antiferromagnet for the two different values of the applied field strength.

	$\mathbf{B = 0.4J}$	$\mathbf{B = 0}$
δ	-0.280	0
Δ	-0.247	-0.276
m	0.0258	0
n	0.1684	0.1966

Table 4.1: Expectation values given by Eq. (4.44) for the nearest-neighbor sites in a two-dimensional uniform spin-$1/2$ antiferromagnet. Different values of the external magnetic field B are indicated in the table header row.

4.2 High-order corrections

Changes to the constant terms

Evaluating the expected value of the quadratic part in Eq. (4.32) in its ground state gives an angle-dependent part which contributes to the constant terms of the Hamiltonian. This is achieved by using the canonical Bogoliubov transformation and writing the bosonic operators $a_{\vec{k}}^\dagger$, $a_{\vec{k}}$ in terms of the $b_{\vec{k}}^\dagger$, $b_{\vec{k}}$ operators. Since the non-zero contribution comes only from terms in the form of $\langle b^\dagger_{\vec{k}} b_{\vec{k}} \rangle$, we get the following additional contribution proportional to N from the quadratic terms to the constant bulk Hamiltonian $\hat{H}_0$ in Eq. (4.17)

$$\hat{H}^0_{bulk,1/S} = NJSZ \left(\Delta \cos^2\theta - m \sin^2\theta + n \cos 2\theta + \frac{B}{JSZ} n \sin\theta \right). \tag{4.45}$$

This term will modify the energy minimization conditions in Eq. (4.21). In order to find new renormalized angles minimizing the energy we need to take the derivative with respect to θ. Since the bulk parameters Δ, m and n depend implicitly on the latitude angle θ through the coefficients $A_{\vec{k}}$ and $B_{\vec{k}}$ we must also differentiate them. However, it turns out that the contributions from the differentiation of the bulk parameters cancel exactly, so the final result of these calculation is the same as for angle-independent bulk parameters. Therefore including contribution of the quadratic terms in Eq. (4.45) gives the following renormalized conditions for the energy minimized state

$$\begin{aligned} \sin\theta|^{ren}_{min} &= \frac{B}{2JSZ}\left(1 + \frac{\Delta + m + n}{S}\right) = \sin\bar{\theta}\left(1 + \frac{\Delta + m + n}{S}\right), \\ \cos\theta|^{ren}_{min} &= \cos\bar{\theta}\left(1 - \tan^2\bar{\theta}\,\frac{\Delta + m + n}{S}\right) \end{aligned} \tag{4.46}$$

where we used the notations for the minimizing latitude angle given by Eq. (4.21)

$$\sin\bar{\theta} = \frac{B}{2JSZ}. \tag{4.47}$$

For further calculations it is convenient to write down also the following expressions

$$\begin{aligned} \sin 2\theta|^{ren}_{min} &\approx \sin 2\bar{\theta}\left[1 + \left(1 - \tan^2\bar{\theta}\right)\frac{\Delta + m + n}{S}\right], \\ \cos 2\theta|^{ren}_{min} &\approx \cos 2\bar{\theta} - 4\sin^2\bar{\theta}\,\frac{\Delta + m + n}{S}. \end{aligned} \tag{4.48}$$

Changes to linear terms

We can improve the used approximation by including the third order terms in the spin wave expansion. Taking into account the cubic terms of the Hamiltonian in the terms of the bosonic operators and taking their expectation values we get an additional bulk contribution which can modify the linear terms of the Hamiltonian in Eq. (4.31).

The cubic terms of the Hamiltonian corresponding to the bulk part have the form

$$\begin{aligned} \hat{H}^3_{bulk} = &- J\sqrt{\frac{S}{2}} \sum_{\langle i,j\rangle} \left[\frac{1}{4}\left(a^\dagger_i \hat{n}_i + \hat{n}_i a_i\right) + \left(a^\dagger_i + a_i\right)\hat{n}_j + \frac{1}{4}\left(a^\dagger_j \hat{n}_j + \hat{n}_j a_j\right) \right. \\ &\left. + \left(a^\dagger_j + a_j\right)\hat{n}_i \right] \sin 2\theta + \frac{B}{4\sqrt{2S}} \sum_i \left(a^\dagger_i \hat{n}_i + \hat{n}_i a_i\right)\cos\theta, \end{aligned} \tag{4.49}$$

where the bosonic operator is $\hat{n}_i = a^\dagger_i a_i$. Expressing the bosonic operators $a^\dagger_k$, a_k in terms of the $b_k^\dagger$, b_k operators and taking the expectation values we get the following correction

$$\begin{aligned}\hat{H}^1_{bulk,3} =& - JSZ\sqrt{\frac{S}{2}}\Bigg[\left(\frac{n+m+\Delta}{S}+\frac{2n+\delta}{4S}\right)\sin 2\theta \\ &- \frac{2n+\delta}{4S}\frac{B}{JSZ}\cos\theta\Bigg]\sum_i\left(a_i^\dagger + a_i\right),\end{aligned} \tag{4.50}$$

which contribute to the linear bulk terms of the Hamiltonian $\hat{H}^1_{bulk}$ given in Eq. (4.23). The total expression for the linear terms corresponding to the bulk part of the Hamiltonian becomes

$$\begin{aligned}H^1_{bulk|_{total}} =& H^1_{bulk} + H^1_{bulk,3} = JSZ\sqrt{\frac{S}{2}}\Bigg[\left(1-\frac{n+m+\Delta}{S}-\frac{2n+\delta}{4S}\right)\sin 2\theta \\ &- \left(1-\frac{2n+\delta}{4S}\right)\frac{B}{JSZ}\cos\theta\Bigg]\sum_i\left(a_i^\dagger + a_i\right).\end{aligned} \tag{4.51}$$

Inserting the minimizing value θ and expanding the obtained expression to order $1/S$ we find that the linear bulk term vanishes also to this order.

Changes of quadratic terms

Taking into account the expectation values of the quartic Hamiltonian terms for the bulk part gives the following contribution to the quadratic Hamiltonian

$$\begin{aligned}\hat{H}^2_{bulk,4} =& -\frac{J}{4}\sum_{\langle i,j\rangle}\Bigg[\Big\{(2n+\delta+4\Delta)\cos 2\theta + 2n - \delta\Big\}\left(a_i^\dagger a_j^\dagger + a_i a_j\right) \\ &+ \Big\{(2n+\delta+4m)\cos 2\theta - 2n + \delta\Big\}\left(a_i^\dagger a_j + a_i a_j^\dagger\right) \\ &+ \Big\{(m+\Delta)\cos 2\theta + m - \Delta\Big\}\left(a_i^\dagger a_i^\dagger + a_i a_i\right) \\ &+ 4\Big\{(m+\Delta+2n)\cos 2\theta + \Delta - m\Big\}a_i^\dagger a_i.\end{aligned} \tag{4.52}$$

Applying the Fourier transform this expression can be written as

$$\begin{aligned}\hat{H}^2_{bulk,4} =& -\frac{JZ}{8}\sum_{\langle i,j\rangle}\Bigg[\Big\{\big((2n+\delta+4\Delta)\cos 2\theta + 2n - \delta\big)\gamma_{\vec{k}} + (m+\Delta)\cos 2\theta + m - \Delta\Big\} \\ &\times\left(a_{\vec{k}}^\dagger a_{-\vec{k}}^\dagger + a_{\vec{k}} a_{-\vec{k}}\right) + 2\Big\{\big((2n+\delta+4m)\cos 2\theta - 2n + \delta\big)\gamma_{\vec{k}} \\ &+ 2\big((m+\Delta+2n)\cos 2\theta + \Delta - m\big)\Big\}a_{\vec{k}}^\dagger a_{\vec{k}}.\end{aligned} \tag{4.53}$$

Therefore, additional contributions to the coefficients $A_{\vec{k}}$ and $B_{\vec{k}}$ from the expectation values of the quartic order terms in the Hamiltonian for the bulk part are

$$\begin{aligned} A_{\vec{k},1/S} = -\frac{JZ}{4}\Bigg[& 2\big\{(m+\Delta+2n)\cos 2\theta + \Delta - m\big\} \\ & + \gamma_{\vec{k}}\left\{\big((2n+\delta)+4m\big)\cos 2\theta - 2n + \delta\right\}\Bigg], \end{aligned} \tag{4.54}$$

$$\begin{aligned} B_{\vec{k},1/S} = -\frac{JZ}{4}\Bigg[& \big\{(m+\Delta)\cos 2\theta + m - \Delta\big\} \\ & + \gamma_{\vec{k}}\left\{\big((2n+\delta)+4\Delta\big)\cos 2\theta + 2n - \delta\right\}\Bigg]. \end{aligned} \tag{4.55}$$

Using the renormalized latitude angle θ for the minimization conditions in Eq. (4.46) and adding these corrections $A_{\vec{k},1/S}$ and $B_{\vec{k},1/S}$ the coefficients can be written in the form

$$\begin{aligned} A_{\vec{k}} = & JSZ\Bigg[\left(1-\frac{n}{S}\right)\cos 2\theta - \frac{\Delta}{S}\cos^2\theta + 2\left(1-\frac{n+\Delta+m/2}{S}\right)\sin^2\theta \\ & - \gamma_{\vec{k}}\left\{\left(1+2\frac{\Delta+m+n/2}{S}\right)\sin^2\theta + \frac{m}{S}\cos 2\theta + \frac{\delta}{2S}\cos^2\theta\right\}\Bigg], \end{aligned} \tag{4.56}$$

$$\begin{aligned} B_{\vec{k}} = & - JSZ\Bigg[\frac{1}{2S}\big(m\cos^2\theta - \Delta\sin^2\theta\big) \\ & - \gamma_{\vec{k}}\left\{\left(1-\frac{n}{S}\right)\cos^2\theta - \frac{\Delta}{S}\cos 2\theta - 2\left(\frac{\Delta+m+n}{S} - \frac{\delta}{4S}\right)\sin^2\theta\right\}\Bigg]. \end{aligned} \tag{4.57}$$

Therefore taking into account the $1/S$ corrections the sum $A_{\vec{k}} + B_{\vec{k}}$ becomes

$$\begin{aligned} A_{\vec{k}} + B_{\vec{k}} = & JSZ\Bigg[1 - \frac{2n+2\Delta+m}{2S} - \frac{m+\Delta}{2S}\sin^2\theta \\ & + \gamma_{\vec{k}}\left(\cos 2\theta - \frac{2n+2m+2\Delta+\delta}{2s} - \sin^2\theta\frac{2n+2m+2\Delta-\delta}{s}\right)\Bigg], \end{aligned} \tag{4.58}$$

that can be also inferred from [170].

4.3 Magnetization around impurity

The magnetization in the z-direction, along the applied field, corresponds to the expectation value of the $\hat{S}^z$ spin operator given by

$$M_i^z = \langle \hat{S}_i^z \rangle = \langle \hat{S}_i'^x \rangle \cos\theta_i + \langle \hat{S}_i'^z \rangle \sin\theta_i. \tag{4.59}$$

Using the spin wave expansion in Eqs. (4.8) and (4.10) the longitudinal magnetization can be expressed in terms of bosonic variables up to quadratic order of $1/S$ as

$$M_i^z \approx \sin\theta_i \left(S_i - \langle a_i^\dagger a_i \rangle \right) + \cos\theta_i \sqrt{\frac{S_i}{2}} \left(\langle a_i^\dagger \rangle + \langle a_i \rangle \right), \tag{4.60}$$

where S_i is the spin moment on site i.

The transversal magnetization is defined similarly by the expectation value $\langle \hat{S}_i^x \rangle$ of the spin operator

$$M_i^x = \left(\langle \hat{S}_i'^x \rangle \sin\theta_i - \langle \hat{S}_i'^z \rangle \cos\theta_i \right) \cos\phi_i - \langle \hat{S}_i'^y \rangle \sin\phi_i. \tag{4.61}$$

Applying the minimization conditions for the azimuthal angles ϕ_i in Eqs. (4.15) and (4.18) the transversal magnetization can written as

$$M_i^x = \left(\delta_{i,0}\nu_0 + (1-\delta_{i,0})(-\nu)^{R_i} \right) \left(\langle \hat{S}_i'^x \rangle \sin\theta_i - \langle \hat{S}_i'^z \rangle \cos\theta_i \right), \tag{4.62}$$

where we introduced the parameter $R_i = (x_i + y_i + \ldots)$ which describes the alternating pattern of the local magnetization in the case of a uniform antiferromagnet, $J > 0$ and $\nu = \operatorname{sgn} J = 1$.

4.3.1 Linear shift

In order to calculate the expectation value of the bosonic terms in Eq. (4.60) we perform a shift of the bosonic operators

$$a_i \to a_i' + \alpha_i \tag{4.63}$$

to get rid of the remaining linear terms in the Hamiltonian in Eq. (4.31). This operator shift corresponds to a variation of the latitude angle θ_i and depends on bulk site. Since this shift does not change the Hamiltonian coefficients (the contribution from cubic terms is neglected), α_k is real and symmetric in momentum space. Applying the operator shift the linear Hamiltonian in Eq. (4.31) becomes

$$\hat{H}_1' = \frac{C}{\sqrt{N}} \sum_{\vec{k}} \gamma_{\vec{k}} \left(a_{\vec{k}}' + a_{\vec{k}}'^\dagger \right) + 2\frac{C}{\sqrt{N}} \sum_{\vec{k}} \gamma_{\vec{k}} \alpha_{\vec{k}}, \tag{4.64}$$

while the quadratic Hamiltonian in Eq. (4.40) becomes

$$\begin{aligned}\hat{H}_2' =& \sum_{\vec{k}} \omega_{\vec{k}} b_{\vec{k}}'^{\dagger} b_{\vec{k}}' + \sum_{\vec{k}} \left(A_{\vec{k}} + B_{\vec{k}}\right) \alpha_{\vec{k}} \left(a_{\vec{k}}' + a_{\vec{k}}'^{\dagger}\right) \\ &+ \frac{1}{2} \sum_{\vec{k}} \left(\omega_{\vec{k}} - A_{\vec{k}}\right) + \sum_{\vec{k}} \left(A_{\vec{k}} + B_{\vec{k}}\right) \alpha_{\vec{k}}^2. \end{aligned} \tag{4.65}$$

The second term in the last expression of the transformed quadratic Hamiltonian is linear in terms of the bosonic operators and gives additional contribution to the linear Hamiltonian. Therefore the shift of the bosonic operators results in the following linear terms of the Hamiltonian

$$\hat{H}_1 = \sum_{\vec{k}} \left[\left(A_{\vec{k}} + B_{\vec{k}}\right) \alpha_{\vec{k}} + \frac{C}{\sqrt{N}} \gamma_{\vec{k}}\right] \left(a_{\vec{k}}' + a_{\vec{k}}'^{\dagger}\right). \tag{4.66}$$

In order for the linear terms to vanish we should choose the operator shift as

$$\alpha_{\vec{k}} = -\frac{C}{\sqrt{N}} \frac{\gamma_{\vec{k}}}{A_{\vec{k}} + B_{\vec{k}}}, \tag{4.67}$$

where the momentum-independent coefficient C is given by Eq. (4.27). Using inverse Fourier transform the shift can be written as

$$\alpha_i = -\frac{C}{N} \sum_{\vec{k}} \frac{\gamma_{\vec{k}}}{A_{\vec{k}} + B_{\vec{k}}} e^{i\vec{k}\cdot\vec{r}_i}. \tag{4.68}$$

We can see that the shift of the bosonic bulk operators in Eq. (4.67) is symmetric and has a real value

$$\alpha_{-k} = \alpha_k, \qquad\qquad \alpha_k^{\dagger} = \alpha_k. \tag{4.69}$$

This shift gives also additional contributions, the last terms in Eqs. (4.64) and (4.65), to the constant terms of the Hamiltonian.

4.3.2 Alternating magnetization

Since the shift α_i is just a constant, shifting the bosonic operator gives the following expression for the longitudinal magnetization

$$M_i^z \approx \sin\theta_i \left(S - |\alpha_i|^2 - \langle a_i'^{\dagger} a_i' \rangle\right) + \sqrt{\frac{S}{2}} \cos\theta_i \left(\alpha_i^* + \alpha_i\right), \tag{4.70}$$

where we have used the fact that $\langle a_i' \rangle = 0$ because the Hamiltonian in terms of the shifted bosonic operators are quadratic. We can therefore also apply the usual bulk theory to calculate the corresponding site-independent expectation value $n = \langle a_i^{\dagger} a_i \rangle$ in Eq. (4.44) away from the impurity site $i = 0$. Therefore the magnetization becomes

$$M_i^z \approx \sin\theta \left(S - \alpha_i^2 - n\right) + \sqrt{2S}\, \alpha_i \cos\theta, \qquad i \neq 0, \tag{4.71}$$

where we used the fact that the shift is a real number $\alpha_i^\dagger = \alpha_i$.

Keeping the next order terms in the spin-wave expansion in Eq. (4.10) we obtain finally the following expressions for the transversal and longitudinal magnetization away from the impurity site

$$M^z_{i\neq 0} = \sqrt{2S}\alpha_i\left(1 - \frac{\alpha_i^2}{4S} - \frac{n+\delta/2}{2S}\right)\cos\theta + \left(S - \alpha_i^2 - n\right)\sin\theta, \tag{4.72}$$

$$M^x_{i\neq 0} = (-\nu)^{R_i}\left[\sqrt{2S}\alpha_i\left(1 - \frac{\alpha_i^2}{4S} - \frac{n+\delta/2}{2S}\right)\sin\theta - \left(S - \alpha_i^2 - n\right)\cos\theta\right], \tag{4.73}$$

where the parameter $R_i = (x_i + y_i + \ldots)$ describes the alternating behaviour of the local magnetization in the case of antiferromagnetic bulk coupling.

The leading order term of the magnetization along the applied field in Eq. (4.71) is

$$M^z_{i\neq 0} \sim \sqrt{2S}\,\alpha_i\cos\theta + (S-n)\sin\theta, \tag{4.74}$$

where the first term expresses spatial dependence around the impurity while the second one describes the uniform bulk magnetization. As is shown in our Article III [173] the sign of the operator shift α_i depends on which sublattice the i-site belongs to as a global factor $e^{i\vec{Q}\cdot\vec{r}} = (-1)^{R_i} = (-1)^{x_i+y_i+\ldots}$ where $\vec{Q} = (\pi,\pi,\ldots)$ is the antiferromagnetic wave vector. Therefore, it is convenient to write the shift of the bosonic operators as

$$\alpha_i = (-1)^{R_i}\tilde{\alpha}_i, \qquad R_i = x_i + y_i + \ldots, \tag{4.75}$$

where $\tilde{\alpha}_i$ is the shift magnitude.

Due to the alternating-sign magnetization around the impurity it is convenient to introduce the two sublattices (for *odd* and *even* sites, see Figure 4.2) and to express the bulk magnetization in terms of an alternating (staggered) and a non-alternating (uniform) part

$$M^z_{alt}(\vec{r}) = \frac{M^z(\vec{r}_{odd}) - M^z(\vec{r}_{even})}{2}, \tag{4.76}$$

$$M^z_{unif}(\vec{r}) = \frac{M^z(\vec{r}_{odd}) + M^z(\vec{r}_{even})}{2}, \tag{4.77}$$

where $\vec{r}$ corresponds to a position on the even sublattice. Therefore, the uniform magnetization takes the form

$$M^z_{unif,i} = \sin\theta\left(S - \tilde{\alpha}_i^2 - n\right), \tag{4.78}$$

which decays fast to its uniform bulk value

$$M^z_{bulk} = (S-n)\sin\theta \tag{4.79}$$

given by Eq. (4.74), see [174].

The most interesting part of this study of the antiferromagnet is the alternating magnetization

$$M^z_{alt,i} = -\sqrt{2S}\cos\theta\,\tilde{\alpha}_i, \tag{4.80}$$

which does not decay so rapidly with increasing distance from the impurity. The variable $\tilde{\alpha}_i$ defines and characterises its principal behaviour.

In order to find an analytical expression for $\tilde{\alpha}_i$ the sum over the momentum k in the reciprocal space in Eq. (4.68) can be calculated by expanding the integrand about the minimum of the denominator which is at the antiferromagnetic point $\vec{Q} = (\pi, \pi, \ldots)$. Doing this we obtain in the square lattice ($D = 2$ and $Z = 4$) and the cubic lattice ($D = 3$ and $Z = 6$) cases for bulk sites

$$\tilde{\alpha}_{i \neq 0} \approx \frac{CZ}{2\pi f g^2} \begin{cases} \mathrm{K}_0(r_i/d), & D = 2, \\ e^{-r_i/d}/(2r_i), & D = 3, \end{cases} \tag{4.81}$$

where C is the site independent parameter given by Eq. (4.27) and $r_i = \sqrt{x_i^2 + y_i^2 + z_i^2}$ is the distance from the impurity in units of the lattice spacing a, for details see Appendix A.4. The function $\mathrm{K}_0(x)$ is the zeroth order modified Bessel function of the second kind [175] which decays as $\mathrm{K}_0(x) \approx \sqrt{\frac{\pi}{2x}} e^{-x}$ for large arguments [65]. It means that in the square lattice the alternating magnetization also decays exponentially as $M^z_{alt,i} \sim e^{-r_i/d}/\sqrt{r_i}$ for the large distance r_i from the impurity. The characteristic decay scale is

$$d = \sqrt{\frac{g}{Z(1-g)}} \tag{4.82}$$

in both cases. Using relations for the f and g parameters in Eq. (4.38) these results allows to rewrite the alternating magnetization in the explicit form

$$M^z_{alt,i \neq 0} \approx \sqrt{\frac{2}{S}} \frac{C \cos\theta}{2\pi J \cos^2 2\theta} \begin{cases} \mathrm{K}_0(r_i/d), & D = 2, \\ e^{-r_i/d}/(2r_i), & D = 3, \end{cases} \tag{4.83}$$

where the decay scale is a universal characteristic

$$d = \sqrt{\frac{\cos 2\theta}{2Z \sin^2\theta}}, \tag{4.84}$$

which depends only on properties of the host magnet in the bulk. Only the constant coefficient C given by Eq. (4.27) depends on the impurity properties S_0, J_0, and B_0.

The alternating magnetization behaviour around the impurity in the 2D antiferromagnet using the analytic expression in Eq. (4.83) in comparison with results from a quantum Monte-Carlo simulation[2] is shown in Figure 4.3(a). We can see that the leading order analytical result decays faster than the independent QMC data. It happens due to the crucial dependence of the characteristic decay scale d on the value of $A_{\vec{k}} + B_{\vec{k}}$ which was approximated in Eq. (4.36) with its leading order value. However we can improve this analytic result by including the next order $1/S$-corrections given by Eq. (4.58) for the renormalized minimization angles in Eq. (4.46). These corrections modify expressions for the constants f and g in Eq. (4.37) that results in a slower decay of the alternating magnetization and leads to a better agreement with the quantum Monte-Carlo data in Figure 4.3(a).

In the case of a vacancy $J_0 = 0$ we compare the obtained analytic result for the alternating

---

[2] The QMC data are given in our Article III [173], where the simulations were performed at a low temperature $T = 0.05J$ on a 128×128 square lattice.

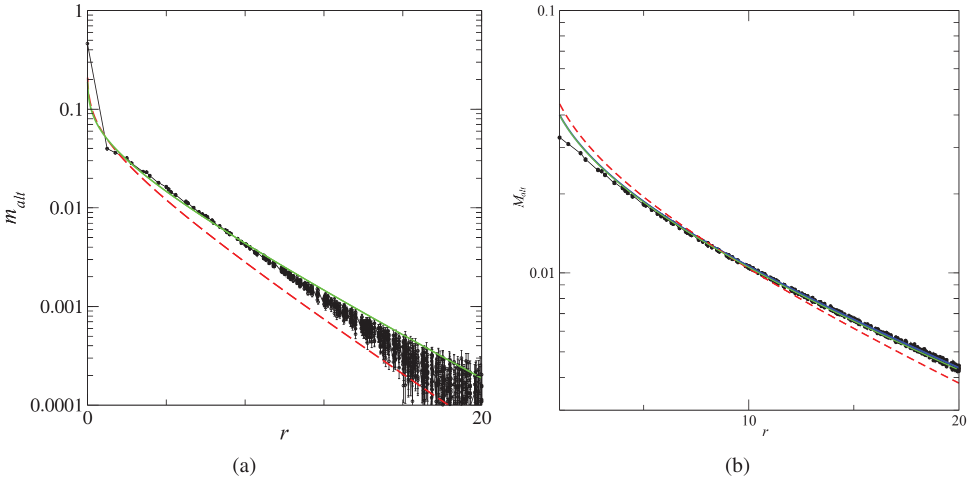

Figure 4.3: The alternating magnetization M^z_{alt} as a function of the distance r from the spin-$1/2$ impurity on the square lattice, $Z = 4$, in a spin-$1/2$ antiferromagnet for different values of the impurity coupling J_0. The dashed red line corresponds to the analytic result in Eq. (4.83) while the solid green line corresponds to the result with $1/S$-corrections for $A_{\vec{k}} + B_{\vec{k}}$ taken into account in Eq. (4.58) and the renormalized minimization angles in Eq. (4.46). (a) For the coupling $J_0 = 0.1J$ and $B = B_0 = 0.4J$ the black dots are the QMC data from our Article III. (b) In the case of a vacancy $J_0 = 0$ in the magnetic field $B = 0.1J$ the black dots describe independent QMC simulations while the blue solid curve corresponds to the results in the article [159]. Here a semi-logarithmic scale was used.

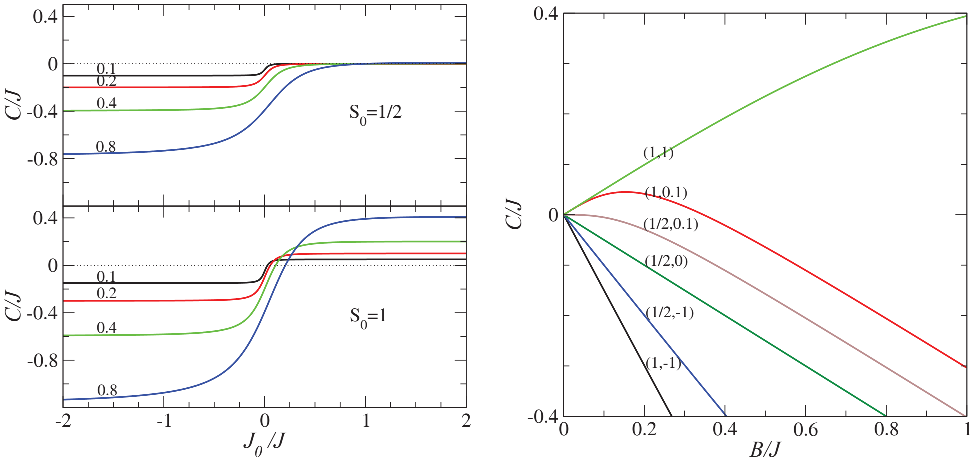

(a) (b)

Figure 4.4: (a) The coefficient C as a function of the impurity coupling J_0 for different impurity spins: $S_0 = 1/2$ (upper panel) and $S_0 = 1$ (lower panel) in different applied magnetic fields B which field strength (in units of J) is indicated by the numbers above each curve on the left side. (b) The coefficient C as a function of the magnetic field B for different values of the impurity spin S_0 and the coupling constant J_0 marked by numbers of (S_0, J_0) in the plot. Here the following parameters were used: $S = 1/2$, $Z = 4$, and $B_0 = B$.

magnetization with results of other studies in [159] and the quantum Monte Carlo simulations, see Figure 4.3(b). We can see again that the analytical result in Eq. (4.83) decays faster while taking into account the next order $1/S$-corrections gives a better agreement with the QMC data and almost coincides with the results from the article [159] where the authors used the renormalized parameters from other studies.

Magnitude of alternating magnetization

While the bulk decay scale of the induced alternating magnetization pattern is determined by the properties of the uniform host magnet, the *magnitude* of the alternating magnetization is given in terms of the coefficient C in Eq. (4.27), which depends on the type and the coupling strength of the impurity as shown in Figure 4.4.

We see from Figure 4.4(a) upper panel that for an impurity spin $S_0 = 1/2$ in a spin-$1/2$ host antiferromagnet the coefficient C is negative and rather small for small positive J_0. If the impurity coupling coincides with the coupling between bulk spins $J = J_0$ that corresponds to the uniform case the coefficient vanishes completely. As is shown in the upper panel in Figure 4.4(a) for large antiferromagnetic coupling the coefficient remains a quite small. For ferromagnetic coupling of the impurity, $J_0 < 0$, the coefficient C is negative and its magnitude becomes larger with increasing magnetic field B, see in Figure 4.4(b). From this we expect the biggest induced alternating magnetization pattern around a *ferromagnetically* coupled impurity. The sign change of the coefficient C indicates a sublattice change in the magnetization pattern when the spin orientation of the two sublattices reverses direction.

A similar behaviour is seen for a spin $S_0 = 1$ impurity embedded in a spin-$1/2$ antiferromagnet, as is shown in Figure 4.4(a) bottom panel, except for antiferromagnetic couplings the coefficient C is no longer necessarily small and it changes sign at a small positive value of J_0. In the case of strong magnetic field B the magnitude $|C|$ changes linearly with field strength except large antiferromagnetic couplings, see Figure 4.4(b).

Limiting cases

We consider some limiting cases of the parameters describing the coefficient C and the alternating magnetization behaviour.

- The same impurity coupling $J_0 = J$ and $B_0 = B$ implies that $C = \frac{1}{\sqrt{2S}}(S_0 - S)B\cos\theta$.
- Extremely large impurity coupling $|J_0| \gg J$ implies that $C = \frac{1}{\sqrt{2S}}(\nu_0 B_0 S_0 - BS)\cos\theta$.
- Isolated impurity with $J_0 = 0$ gives $C = -\sqrt{\frac{S}{2}}BS\cos\theta$.

Limit of large bulk S-spins

In addition we can consider the classical limit of large S-spin of the bulk sites in the antiferromagnet. In this case the energy minimization condition for the latitude angle in Eq. (4.21) gives $\theta \approx 0$ which reflects the obvious fact that the large bulk spins tend to be antiferromagnetically ordered in the same plane. Using Taylor series expansion of the analytic expressions in Eqs. (4.26) and (4.82) we obtain the following asymptotic behaviour for the constant coefficient

$$C \approx \sqrt{\frac{S}{2}}\left(B_0\nu_0\frac{S_0}{S} - B\right) + \frac{B^3}{8\sqrt{2S}SJ^2Z^2} \tag{4.85}$$

and the characteristic decay scale

$$d = \frac{1}{\sqrt{Z}}\sqrt{2\left(\frac{JSZ}{B}\right)^2 - 1} \approx \sqrt{2Z}S\frac{J}{B} - \frac{B}{\sqrt{8Z^3}JS}, \tag{4.86}$$

describing the alternating magnetization pattern. Using Eqs. (4.80) and (4.81) and keeping the leading order terms the alternating magnetization can be written in the explicit form

$$M^z_{alt,i\neq 0} \approx \frac{1}{2\pi J}\left(B - B_0\nu_0\frac{S_0}{S}\right)\begin{cases} \mathrm{K}_0\left(\dfrac{r_i}{\sqrt{2Z}SJ/B}\right), & D = 2, \\ \dfrac{e^{-\frac{r_i}{\sqrt{2Z}SJ/B}}}{2r_i}, & D = 3. \end{cases} \tag{4.87}$$

In this limit the uniform bulk magnetization given in Eq. (4.79) is described by the classical relation which gives

$$M^z_{bulk} \approx S\sin\theta = \frac{B}{2JZ}. \tag{4.88}$$

We can see that the characteristic decay scale in Eq. (4.87) has linear dependence on the magnitude of the coupling J and the bulk S-spin as

$$d \sim \sqrt{2Z} S \frac{J}{B}. \tag{4.89}$$

It means that increasing the magnetic coupling between bulk sites (through the coupling J or the spin S) results in a slower decay of the alternating magnetization, while the magnitude of the alternating part of the magnetization will decrease in accordance with Eq. (4.87). In contrast the magnetization pattern decays faster when the applied magnetic field B gets larger.

4.4 Spin wave velocity and decay scale

Taking the logarithm of the alternating magnetization in Eq. (4.83) we find at large distances r_i from the impurity

$$\ln\left(M^z_{alt,i}\right) \sim -\frac{r_i}{d}, \tag{4.90}$$

where we neglected the $\ln(r_i)$ term since for large distances the relation $\ln(x) \ll x$ is valid. Thus the magnetization slope in the semi-logarithmic plot in Figure 4.3 corresponds to the reciprocal value of the characteristic decay scale d. This decay scale is connected to the spin wave velocity c of the host antiferromagnet as

$$c = d\,B. \tag{4.91}$$

In order to show this we consider the magnon dispersion in momentum space given by the diagonalized quadratic bulk Hamiltonian in Eq. (4.40) where the coefficient $\omega_{\vec{k}}$ describes the magnon energy.

The coefficient $\omega_{\vec{k}}$ in Eq. (4.42) as a function of the wave vector $\vec{k}$ along a path in the first Brillouin zone is shown in Figure 4.5. In the case of an applied magnetic field B a gap opens at $\vec{k} = (\frac{\pi}{a}, \frac{\pi}{a})$ which value is equal to the field strength.

In order to analyse the gap behaviour we can expand the function $\gamma_{\vec{k}}$ around the antiferromagnetic point $\vec{Q}$ which gives

$$\gamma_{\vec{k}+\vec{Q}} \approx -1 + \frac{a^2}{Z}\vec{k}^2 + \dots, \qquad \vec{Q} = \left(\frac{\pi}{a}, \frac{\pi}{a}, \dots\right), \tag{4.92}$$

where a is the lattice spacing. This allows to rewrite the coefficient $\omega_{\vec{k}}$ in the explicit form

$$\omega_{\vec{k}} = JSZ\sqrt{\left(1-\gamma_{\vec{k}}\right)\left(1+\cos 2\theta\gamma_{\vec{k}}\right)} \approx B\sqrt{1 + \frac{a^2}{2Z}\frac{\cos 2\theta}{\sin^2\theta}\vec{k}^2}. \tag{4.93}$$

Expanding the square root in the case of finite but not too large magnetic field we get

$$\omega_{\vec{k}} = \begin{cases} B + \dfrac{a^2 B}{2Z}\dfrac{\vec{k}^2}{\sec 2\theta - 1}, & \dfrac{a^2}{2Z}\dfrac{\cos 2\theta}{\sin^2\theta} \ll 1, \\ JSa\sqrt{2Z\cos 2\theta}|\vec{k}|, & \text{otherwise}, \end{cases} \tag{4.94}$$

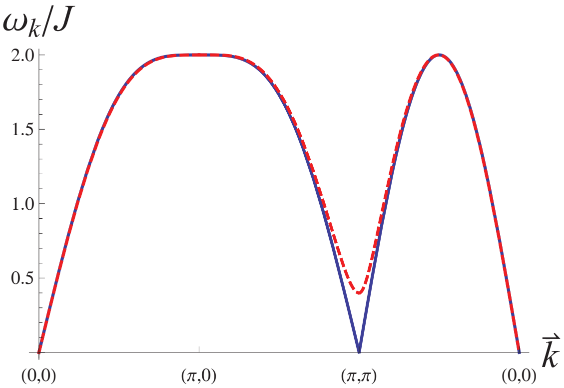

Figure 4.5: The magnon dispersion $\omega_{\vec{k}}$ in units of J as a function of the wave vector $\vec{k}$ along a path in the first Brillouin zone. The solid blue curve correspond to the case of the vanishing magnetic field $B = 0$, while the dashed red curve describes the dispersion at the field strength $B = 0.4J$. Here a lattice constant $a = 1$ was used.

which can expressed in the following form

$$\omega_{\vec{k}} = \begin{cases} B + \dfrac{1}{2m}\vec{k}^2, & \dfrac{a^2}{2Z}\dfrac{\cos 2\theta}{\sin^2\theta} \ll 1, \\ c|\vec{k}|, & \text{otherwise}, \end{cases} \tag{4.95}$$

where the coefficient c corresponds to the *spin wave velocity* given by

$$c = JSa\sqrt{2Z\cos 2\theta}. \tag{4.96}$$

In the limit of vanishing magnetic field this is the well-known leading-order spin wave theory result for the spin wave velocity of a uniform antiferromagnet [58]. Using the minimizing conditions in Eq. (4.21) for the gap the coefficient m is

$$m = \frac{2Z}{a^2 B}\frac{\sin^2\theta}{\cos 2\theta} = \frac{B}{c^2}, \tag{4.97}$$

which corresponds to the *effective mass* of the dispersion minimum. With the expressions in Eqs. (4.96) and (4.97) for c and m we see that the leading-order characteristic decay constant d given by Eq. (4.84) can be also written as

$$d = a\sqrt{\frac{\cos 2\theta}{2Z\sin^2\theta}} = \frac{1}{\sqrt{Bm}} = \frac{1}{mc} = \frac{c}{B}, \tag{4.98}$$

that gives the relation in Eq. (4.91). These results are in agreement with analytic results using a renormalized classical description for the induced magnetization around a vacancy at $J_0 = 0$ obtained in [159].

4.4.1 Magnetization pattern

Taking into account the next order $1/S$-corrections for the renormalized minimizing angles in Eq. (4.46) we get the following expression for the magnetization along magnetic field

$$\begin{aligned} M^z_{i\neq 0,\,1/S} =& -\sqrt{2S}(-1)^{R_i}\tilde{\alpha}_i\left(1-\frac{\tilde{\alpha}_i^2}{4S}-\frac{n+\delta/2}{2S}-\tan^2\theta\frac{\Delta+m+n}{S}\right)\cos\theta \\ &+\left(S-\tilde{\alpha}_i^2-n\right)\left(1+\frac{\Delta+m+n}{S}\right)\sin\theta, \end{aligned} \tag{4.99}$$

where $R_i = x_i + y_i + \dots$ and $\tilde{\alpha}_i$ describes the bosonic shift given in Eq. (4.83).

The local magnetization at different positions $(x_i, y_i = 0)$ close to the impurity in a two-dimensional spin-$1/2$ antiferromagnet is shown in Figure 4.6, where the longitudinal magnetization demonstrates an alternating pattern and its magnitude decreases exponentially with distance from the impurity to the uniform bulk value given in Eq. (4.79). We can see that the analytical results (square symbols) are in a good agreement and lie reasonably close to the independent QMC data (solid circles) with the exception of the nearest neighbor site around the impurity. For the impurity spin $S_0 = 1/2$ at the coupling $J_0 = J$ the oscillating magnetization pattern vanishes completely as it is the case of the uniform antiferromagnet, see Figure 4.6(a).

In the case of an $S_0 = 1$ impurity the oscillations of the magnetization are also large for the ferromagnetic coupling J_0 in Figure 4.6(b). We can see that the sublattice pattern changes for J_0 being antiferromagnetic. This reflect the fact that the coefficient C changes its sign in Figure 4.4 and the spin orientation of the sublattices reverses direction.

4.5 Magnetization on impurity site

At the impurity site the leading order term of the longitudinal magnetization is given by the classical expression

$$M^z_0 = S_0 \sin\theta_0, \tag{4.100}$$

where the latitude angle θ_0 is defined by the minimization conditions in Eq. (4.22). In Figure 4.7 we show this magnetization for different values of the impurity spin S_0 in comparison with quantum Monte-Carlo calculations. In the case of antiferromagnetic impurity coupling ($J_0 > 0$) and for $S_0 = S = 1/2$ this classical expression gives a reasonable agreement with the independent QMC simulations. However for other spin values S_0 and ferromagnetic impurity ($J_0 < 0$) the classical result in Eq. (4.100) is rather far of the QMC data. The maximum of the magnetization in Figure 4.7 corresponds to the value of $J_0 = 0$ which reflects the fact that an uncoupled (isolated) impurity is directed along the magnetic field.

In order to improve the classical result we need to take into account the quantum corrections to Eq. (4.100). The most important of these is the mixing bilinear terms in the quadratic Hamiltonian connecting the impurity to its bulk neighbors. This is the topic of the next section.

The classical result for the longitudinal magnetization in Eq. (4.100) can be also improved analytically by taking into account classical latitude angles θ_1 and θ_2 for the nearest and next-nearest neighbour spins around the impurity site. This will be discussed in Section 4.7.

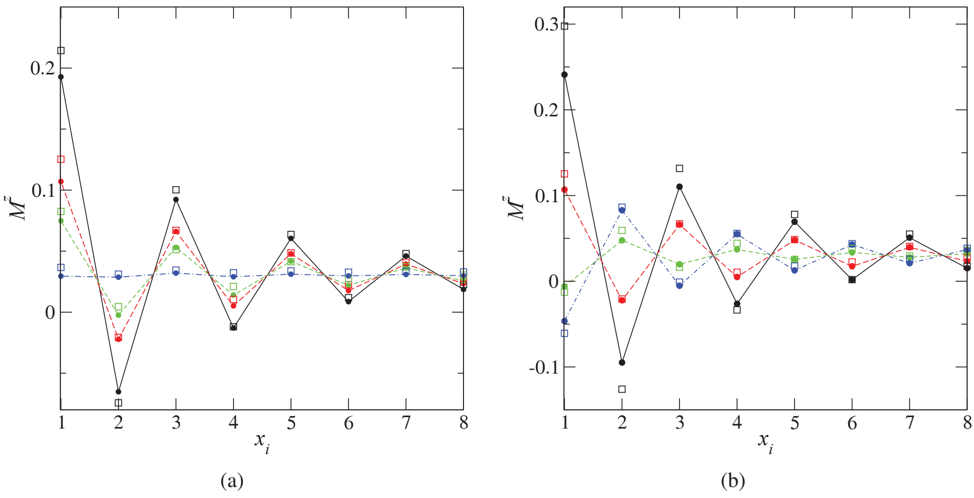

(a)

(b)

Figure 4.6: Longitudinal magnetization as a function of horizontal distance x_i from the impurity site as calculated by QMC simulations (solid circles) and the analytic spin wave theory (squares) for different impurity properties in a bulk spin-$1/2$ antiferromagnet subject to an external field $B = B_0 = 0.4J$. (a) Spin of the impurity is $S_0 = 1/2$ and the color lines correspond to different values of $J_0/J = -2$ (black solid), 0 (red long dashed), 0.1 (green dot-dashed) and 0.5 (blue dot-dashed). (b) The impurity spin is $S_0 = 1$ and the color lines describe different values of the impurity coupling $J_0/J = -1$ (black solid), 0 (red long dashed), 0.2 (green dashed) and 1 (blue dot-dashed). QMC error bars are smaller than the size of the solid circles.

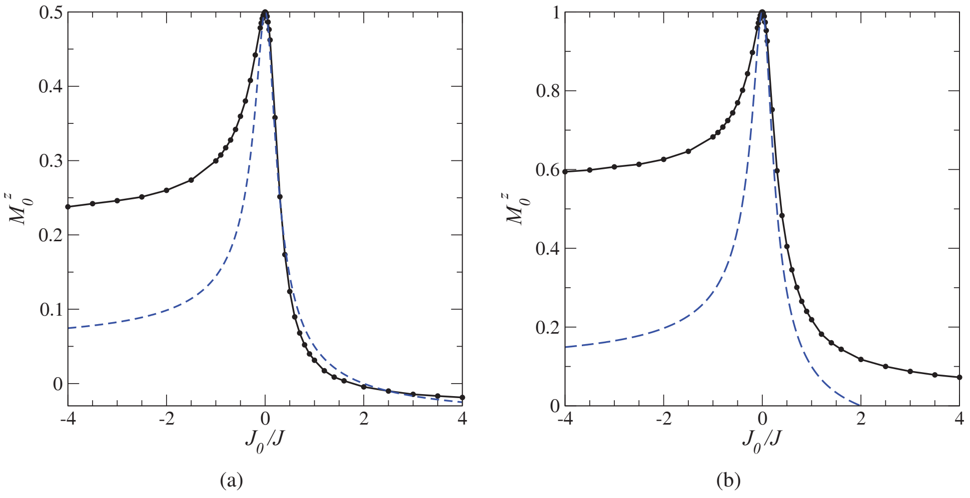

(a)

(b)

Figure 4.7: Magnetization on the impurity site as a function of a coupling J_0 to a bulk spin-$1/2$ antiferromagnet for different values of the impurity spin: (a) $S_0 = 1/2$ and (b) $S_0 = 1$. The dashed blue curve corresponds to the classical result given in Eq. (4.100), while the black dots are data from the quantum Monte-Carlo simulations.

4.6 Shift of bosonic operators on impurity site

In the previous calculations we used an approximation where we neglected contributions from the impurity part of the Hamiltonian beyond linear order. These, however, play a crucial role for the magnetization on the impurity site. Taking into account the most important of these gives additional terms in the Hamiltonian which after applying the spin wave expansion depend on both the bulk spin bosonic operators ($a_i^\dagger$ and a_i) and bosonic operators of the impurity spin ($a_0^\dagger$ and a_0). Keeping terms up to the second order of the bosonic operators we obtain a bilinear Hamiltonian, which can be diagonalized by using a transformation (shift) of the impurity bosonic operators in order to get rid of the linear terms corresponding to the bosonic operators of the impurity spin.

4.6.1 The quadratic terms of Hamiltonian

Keeping terms up to the second order of the bosonic operators the impurity part of the Hamiltonian in Eq. (4.16) is given by

$$\begin{aligned}\hat{H}_{imp} =& \frac{J_0}{2}\sqrt{SS_0}\sum_{\langle 0,j\rangle}\left[\left(a_0^\dagger a_j^\dagger + a_0 a_j\right)(\cos\beta+\nu_0) + \left(a_0^\dagger a_j + a_0 a_j^\dagger\right)(\cos\beta-\nu_0)\right]\\ &+ (J_0 SZ\nu_0\cos\beta + B_0\sin\theta_0)a_0^\dagger a_0,\end{aligned} \tag{4.101}$$

where $a_i^\dagger$ and a_i are the bulk spin bosonic operators, $a_0^\dagger$ and a_0 are bosonic operators of the impurity spin. Here we introduced the new angle variable

$$\beta = \theta + \nu_0\theta_0, \tag{4.102}$$

which has the following value

$$\sin\beta|_{min} = \frac{B_0\cos\theta_0}{J_0 SZ} \tag{4.103}$$

by applying the conditions in Eqs. (4.21) and (4.22) minimizing the ground state energy.

We can rewrite the impurity Hamiltonian in Eq. (4.101) in the following form

$$\hat{H}_{imp} = A\sum_{\langle 0,j\rangle}\left(a_0^\dagger a_j^\dagger + a_0 a_j\right) + B\sum_{\langle 0,j\rangle}\left(a_0^\dagger a_j + a_0 a_j^\dagger\right) + Da_0^\dagger a_0, \tag{4.104}$$

where the constant coefficients A, B and D are given by

$$\begin{aligned}A &= \frac{J_0}{2}\sqrt{SS_0}(\cos\beta+\nu_0),\\ B &= \frac{J_0}{2}\sqrt{SS_0}(\cos\beta-\nu_0),\\ D &= J_0 SZ\nu_0\cos\beta + B_0\sin\theta_0 = J_0 SZ\cos\beta\,(\nu_0+\tan\beta\tan\theta_0).\end{aligned} \tag{4.105}$$

The first two coefficients A and B describe the bilinear mixing terms in the quadratic impurity Hamiltonian in Eq. (4.104) connecting the impurity to its neighbor spins, while the coefficient D corresponds to the quadratic terms in the bosonic impurity operators only.

Performing the sift of the bosonic bulk operators in Eq. (4.63) the impurity Hamiltonian becomes

$$\begin{aligned}\hat{H}_{imp} =& A\sum_{\langle 0,j\rangle}\left(a_0^\dagger a_j^\dagger + a_0 a_j\right) + B\sum_{\langle 0,j\rangle}\left(a_0^\dagger a_j + a_0 a_j^\dagger\right) + D a_0^\dagger a_0 \\ &+ a_0^\dagger \sum_{\langle 0,j\rangle}\left(A\alpha_j^* + B\alpha_j\right) + a_0 \sum_{\langle 0,j\rangle}\left(A\alpha_j + B\alpha_j^*\right),\end{aligned} \tag{4.106}$$

where the bulk shift α_i is given by Eq. (4.68) and for simplification we omitted primes for the shifted bulk operators.

4.6.2 Shift of Impurity Operators

Consider now the transformation of variables for the impurity bosonic operator

$$a_0 \to a_0' = c a_0 + f\sum_{\langle 0,i\rangle} a_i + g\sum_{\langle 0,i\rangle} a_i^\dagger + \alpha. \tag{4.107}$$

It is convenient for further calculations to use the implicit sum over all impurity neighbors, so we can rewrite Eq. (4.107) as

$$a_0 \to a_0' = c a_0 + f a_i + g a_i^\dagger + \alpha. \tag{4.108}$$

The transformation coefficients c, f, g and α are complex numbers in the general case. The operator shift in Eq. (4.108) should satisfy the commutation relation of the bosonic operators $[a_0', a_0'^\dagger] = 1$ which gives the following relation between the transformation coefficients

$$|c|^2 + Z(|f|^2 - |g|^2) = 1. \tag{4.109}$$

4.6.3 Transformed Hamiltonian

Since the bosonic variables for the impurity and the bulk spins are independent and correspond to the different sites, the commutation relations between them are equal to zero. Applying the transformation of the bosonic operators in Eq. (4.108) the quadratic Hamiltonian given by Eq. (4.106) can be expressed as a sum of two terms

$$\hat{H}_{imp} = F_1(a_0, a_0^\dagger, a_i, a_i^\dagger) + F_2(a_i, a_i^\dagger, a_j, a_j^\dagger), \tag{4.110}$$

where F_1 and F_2 are functions of their arguments. The second term is a just contribution to the bulk part of the Hamiltonian and is not interesting for us now. The first term of the Hamiltonian contains linear terms of the impurity bosonic operators and can be written in the explicit form

$$\begin{aligned}F_1(a_0, a_0^\dagger, a_i, a_i^\dagger) =& c^*(A + Dg)a_0^\dagger a_i^\dagger + c(A + Dg^*)a_0 a_i + c^*(B + Df)a_0^\dagger a_i \\ &+ c(B + Df^*)a_0 a_i^\dagger + c^*(D\alpha + A\alpha_i^* + B\alpha_i)a_0^\dagger \\ &+ c(D\alpha^* + A\alpha_i + B\alpha_i^*)a_0 + D|c|^2 a_0^\dagger a_0,\end{aligned} \tag{4.111}$$

where c, f, g and α are the impurity transformation coefficients, and α_i is the linear shift of the bulk bosonic operators given by Eq. (4.68). The last term in Eq. (4.111) is quadratic in terms of the impurity bosonic operators and does not contribute to the linear impurity Hamiltonian.

In order to get rid of the linear terms of the impurity contribution we consider the first term of the Hamiltonian in Eq. (4.110) and equate it to zero. This gives the following relations between the transformation coefficients

$$\begin{aligned} &A + Dg = 0, && A + Dg^* = 0, \\ &B + Df = 0, && B + Df^* = 0, \\ &D\alpha + A\alpha_i^* + B\alpha_i = 0, && D\alpha^* + A\alpha_i + B\alpha_i^* = 0. \end{aligned} \tag{4.112}$$

Since the constants A, B and D in Eq. (4.105) are real, the transformation coefficients f and g are also real numbers. Taking into account the fact that the bulk shift α_i is a real value, we get a real bosonic coefficient α and the following relations

$$g = -\frac{A}{D}, \qquad f = -\frac{B}{D}, \qquad \alpha = -\frac{A+B}{D}\alpha_j = (f+g)\,\alpha_j, \tag{4.113}$$

where the constants A, B and D are given by Eq. (4.105). Using the commutation relation of the bosonic operators resulting in Eq. (4.109) we have the additional condition

$$c = \sqrt{1 - Z(f^2 - g^2)}. \tag{4.114}$$

The explicit form of the coefficients for the transformation of the impurity bosonic operators in Eq. (4.108) is

$$\begin{aligned} &g = -\sqrt{\frac{S_0}{S}}\frac{\cos\beta + \nu_0}{2Z\cos\beta(\nu_0 + \tan\beta\tan\theta_0)}, && f = -\sqrt{\frac{S_0}{S}}\frac{\cos\beta - \nu_0}{2Z\cos\beta(\nu_0 + \tan\beta\tan\theta_0)}, \\ &\alpha = -\sqrt{\frac{S_0}{S}}\frac{1}{Z(\nu_0 + \tan\beta\tan\theta_0)}\alpha_j, && c = \sqrt{1 + \frac{S_0}{S}\frac{\nu_0}{Z\cos\beta(\nu_0 + \tan\beta\tan\theta_0)^2}}. \end{aligned} \tag{4.115}$$

Some limiting cases

Consider some limiting cases of the parameters.

- The same impurity parameters $J_0 = J$ and $B_0 = B$ gives that there is no impurity in case of $S_0 = S$. Using the expressions in Eqs. (4.21) and (4.22) of the latitude angles minimizing the ground state energy we obtain

  $$\theta_0|_{min} = \theta, \qquad \beta|_{min} = 2\theta. \tag{4.116}$$

  That gives the following formulas for the coefficients

  $$\begin{aligned} &g = -\sqrt{\frac{S_0}{S}}\frac{\cos^2\theta}{Z}, && f = \sqrt{\frac{S_0}{S}}\frac{\sin^2\theta}{Z}, \\ &\alpha = -\sqrt{\frac{S_0}{S}}\frac{\cos 2\theta}{Z}\alpha_j, && c = \sqrt{1 + \frac{S_0}{S}\frac{\cos 2\theta}{Z}}. \end{aligned} \tag{4.117}$$

- Extremely large impurity coupling $|J_0| \gg J$. In this case the angles minimizing the energy become

$$\theta_0|_{min} = -\nu_0 \theta, \qquad\qquad \beta|_{min} = 0. \tag{4.118}$$

  That gives the following expressions for the transformation coefficients of the impurity bosonic operators

$$\begin{aligned} g &= -\sqrt{\frac{S_0}{S}\frac{\nu_0+1}{2Z}}, & f &= -\sqrt{\frac{S_0}{S}\frac{\nu_0-1}{2Z}}, \\ \alpha &= -\sqrt{\frac{S_0}{S}\frac{\nu_0}{Z}}\alpha_j, & c &= \sqrt{1+\frac{S_0}{S}\frac{\nu_0}{Z}}. \end{aligned} \tag{4.119}$$

  From the last equation we see that the transformation coefficient c is a real value except in the case of an extreme ferromagnetic impurity which gives the following condition

$$S_0 \leqslant SZ \tag{4.120}$$

  for all the transformation coefficients being real numbers.

- Isolated impurity with $J_0 = 0$ implies that the ground state angles are

$$\begin{aligned} \theta_0|_{min} &= \frac{\pi}{2}\operatorname{sgn} B_0, \\ \beta|_{min} &= \theta + \nu_0\frac{\pi}{2}\operatorname{sgn} B_0, \end{aligned} \tag{4.121}$$

  which results in the following expressions for the transformation coefficients

$$g = f = \alpha = 0, \quad c = 1. \tag{4.122}$$

  It means that the impurity bosonic variables do not change in this case.

4.6.4 Magnetization on Impurity Site

The magnetization on the impurity site in the z-direction is given by the expression

$$M_0^z = \sin\theta_0 \langle \hat{S'}_0^z \rangle + \cos\theta_0 \langle \hat{S'}_0^x \rangle, \tag{4.123}$$

where $\langle \hat{S'}_0^z \rangle$ and $\langle \hat{S'}_0^z \rangle$ are expectation values of the rotated spin operators.

Using spin wave expansion in Eqs. (4.10) and (4.11) and keeping terms up to the first order of $1/S$ the impurity spin operators can be expressed in terms of bosonic variables as

$$\begin{aligned} \hat{S}_0^z &= S_0 - a_0^\dagger a_0, \\ \hat{S}_0^x &\approx \sqrt{\frac{S_0}{2}}\left[a_0^\dagger + a_0 - \frac{1}{4S_0}\left(a_0^\dagger a_0^\dagger a_0 + a_0^\dagger a_0 a_0\right)\right], \\ \hat{S}_0^y &\approx i\sqrt{\frac{S_0}{2}}\left[a_0^\dagger - a_0 - \frac{1}{4S_0}(a_0^\dagger a_0^\dagger a_0 - a_0^\dagger a_0 a_0)\right]. \end{aligned} \tag{4.124}$$

Inserting these expressions for the rotated impurity spin operator $\hat{S}_0'$ into the longitudinal magnetization on the impurity site we obtain terms with different power of the impurity bosonic operators $a_0^\dagger$ and a_0.

The leading order magnetization

In the first approximation we consider the leading terms to order $1/S_0$ of the operator expansion by neglecting the cubic terms

$$\hat{S}^x_{0\,\langle 1\rangle} \approx \sqrt{\frac{S_0}{2}}\left(a_0^\dagger + a_0\right), \tag{4.125}$$

that gives the magnetization on the impurity site along the applied magnetic field

$$M^z_{0\,\langle 1\rangle} = \sin\theta_0\left(S_0 - \langle a_0^\dagger a_0\rangle\right) + \cos\theta_0\sqrt{\frac{S_0}{2}}\left(\langle a_0^\dagger\rangle + \langle a_0\rangle\right). \tag{4.126}$$

Applying the shift of bulk bosonic operator in Eq. (4.63) and the transformation of the impurity bosonic variables in Eq. (4.108) we obtain the following expectation values

$$\begin{aligned}\langle a_0^\dagger\rangle = \langle a_0\rangle &= \alpha = (f+g)\alpha_i, \\ \langle a_0^\dagger a_0\rangle &= g^2 Z + (f^2+g^2)\langle a_i^\dagger a_j\rangle + 2fg\langle a_i a_j\rangle + (f+g)^2\alpha_i\alpha_j,\end{aligned} \tag{4.127}$$

where we used the implicit sum by indices i, j over all impurity neighbors. By analogy to the bulk parameters in Eq. (4.44) we can introduce new variables which depend only on bulk sites of the nearest impurity neighbors

$$\begin{aligned}\tilde{m} &= \frac{1}{Z^2}\sum_{\substack{\langle 0,i\rangle\\ \langle 0,j\rangle}}\langle a_i^\dagger a_j\rangle = \frac{1}{N}\sum_k v_k^2\gamma_k^2 = \frac{1}{2N}\sum_k\left(\frac{A_k}{\omega_k} - 1\right)\gamma_k^2, \\ \tilde{\Delta} &= \frac{1}{Z^2}\sum_{\substack{\langle 0,i\rangle\\ \langle 0,j\rangle}}\langle a_i a_j\rangle = \frac{1}{N}\sum_k u_k v_k\gamma_k^2 = -\frac{1}{2N}\sum_k\frac{B_k}{\omega_k}\gamma_k^2\end{aligned} \tag{4.128}$$

and an additional variable concerning the shift of the bosonic operators of the impurity

$$\tilde{\alpha}_0 = \frac{1}{Z}\sum_{\langle 0,i\rangle}\alpha_i = \frac{1}{\sqrt{N}}\sum_k\alpha_k\gamma_k. \tag{4.129}$$

In Table 4.2 we show the typical modified bulk values calculated numerically in a uniform spin-$1/2$ antiferromagnet for the two different values of the applied field strength.

Taking into account the expectation values in Eq. (4.127) the longitudinal magnetization on the impurity site in Eq. (4.126) becomes

$$\begin{aligned}M^z_{0\,\langle 1\rangle} =& \sin\theta_0\left\{S_0 - \left[g^2 Z + (f^2+g^2)Z^2\tilde{m} + 2fgZ^2\tilde{\Delta} + (f+g)^2 Z^2\tilde{\alpha}_0^2\right]\right\} \\ &+ \sqrt{2S_0}\cos\theta_0(f+g)Z\tilde{\alpha}_0.\end{aligned} \tag{4.130}$$

For further simplification it is convenient to redefine the variable α given by Eq. (4.113) as a

	$\mathbf{B = 0.4J}$	$\mathbf{B = 0}$
$\tilde{m}$	0.1245	0.1506
$\tilde{\Delta}$	−0.0259	0

Table 4.2: Expectation values corresponding to the modified bulk variables given by Eq. (4.128) for the nearest-neighbor sites in a two-dimensional uniform spin-$1/2$ antiferromagnet. Different values of the external magnetic field B are indicated in the table header row.

shift of the impurity bosonic operators

$$\alpha_0 \equiv \alpha = (f+g)Z\tilde{\alpha}_0, \tag{4.131}$$

that allows to rewrite the magnetization in Eq. (4.130) in the form

$$M^z_{0\,\langle 1\rangle} = \sin\theta_0 \left\{ S_0 - \left[\alpha_0^2 + g^2 Z + (f^2+g^2)Z^2\tilde{m} + 2fgZ^2\tilde{\Delta} \right] \right\} + \cos\theta_0 \sqrt{2S_0}\,\alpha_0. \tag{4.132}$$

Using the relations in Eqs. (4.27), (4.36) and (4.67) and applying the integration rule given by Eq. (A.65) in Appendix A.4 we can express the variable $\tilde{\alpha}_0$ in the explicit form

$$\begin{aligned}\tilde{\alpha}_0 &= -\frac{1}{N}\sum_{\vec{k}} \frac{C\gamma_{\vec{k}}^2}{A_{\vec{k}}+B_{\vec{k}}} = -\frac{C}{JSZ}\frac{1}{N}\sum_{\vec{k}} \frac{\gamma_{\vec{k}}^2}{1+\gamma_{\vec{k}}\cos 2\theta} \\ &= \sqrt{\frac{S}{2}}\left(\sin 2\theta - \frac{|J_0|}{J}\frac{S_0}{S}\sin\beta \right) \frac{1}{\cos^2 2\theta} \left[\frac{4}{\pi(1+\sin 2\theta)} \mathrm{K}\left(\frac{1-\sin 2\theta}{1+\sin 2\theta} \right) - 1 \right],\end{aligned} \tag{4.133}$$

where the special function $\mathrm{K}(x)$ is a complete elliptic integral of the first kind [107] and given by Eq. (A.61). Therefore for the shift in Eq. (4.131) we obtain

$$\alpha_0 = \sqrt{\frac{S_0}{2}} \frac{\frac{|J_0|}{J}\frac{S_0}{S}\sin\beta - \sin 2\theta}{\nu_0 + \tan\beta\tan\theta_0} \frac{1}{\cos^2 2\theta} \left[\frac{4}{\pi(1+\sin 2\theta)} \mathrm{K}\left(\frac{1-\sin 2\theta}{1+\sin 2\theta} \right) - 1 \right]. \tag{4.134}$$

Substituting these formulae to the expression of the impurity magnetization in Eq. (4.132) we get finally

$$\begin{aligned} M^z_{0\,\langle 1\rangle} =& S_0 \sin\theta_0 \Bigg(1 - \frac{\alpha_0^2}{S_0} - \frac{1}{S}\frac{1}{4Z\cos^2\beta\,(\nu_0+\tan\beta\tan\theta_0)^2} \Big\{ (\nu_0+\cos\beta)^2 \\ &+ 2Z\left[(1+\cos^2\beta)\tilde{m} - (1-\cos^2\beta)\tilde{\Delta} \right] \Big\} \Bigg) + \cos\theta_0\sqrt{2S_0}\alpha_0, \end{aligned} \tag{4.135}$$

where the factor α_0 is given in Eq. (4.134). For further analysis it is convenient to define the normalized magnetization on the impurity site

$$\tilde{M}^z_0 = \frac{M^z_0}{S_0}, \tag{4.136}$$

which allows to compare the magnetization behaviour for different values of the impurity spin.

In Figure 4.8 we plot the normalized impurity magnetization M^z_0/S_0 for different values of

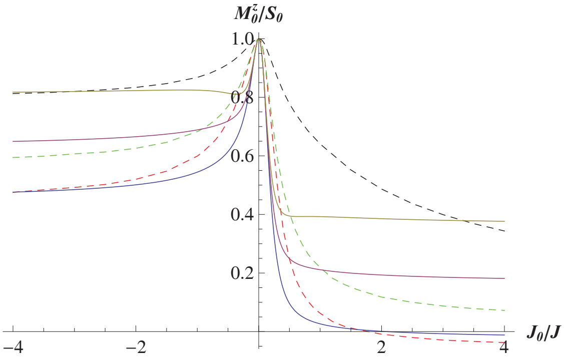

Figure 4.8: The normalized magnetization on the impurity site M_0^z/S_0 as a function of the coupling strength J_0 in a two-dimensional spin-$1/2$ antiferromagnet. The analytical results for different values of the impurity spin $S_0 = 1/2$, 1 and $3/2$ (the solid blue, purple and brown lines respectively) are compared with the independent quantum Monte-Carlo simulations for the same spin values (the dashed red, green and black lines respectively). The applied magnetic field is $B_0 = B = 0.4J$.

the impurity spin S_0 as a function of the coupling strength J_0 and compare the analytical result in Eq. (4.135) with the independent quantum Monte-Carlo calculations for different spins of the impurity. We can see a reasonably good agreement of the analytical results in the case of strong ferromagnetic coupling $J_0 < 0$ of the impurity.

In order to improve these results we need to take into account higher order terms of the impurity Hamiltonian which complicate considerably the analytic calculations.

4.7 Corrections due to site-dependent angles θ_i

Another approach to improve the calculations of the impurity magnetization is to improve the description of the classical state by parameterizing it by more bulk angles.

4.7.1 Magnetization with θ_1

If we include additional parameter θ_1 to the problem as latitude angle for the nearest impurity neighbors we get additional terms to the constant term of the Hamiltonian that results in the following equations for the energy minimization condition

$$\begin{cases} \tan\theta_0 = \dfrac{B_0 - J_0 SZ\sin\theta_1}{|J_0|SZ\cos\theta_1}, \\ \tan\theta_1 = \dfrac{B - J_0 S_0\sin\theta_0 - JS(Z-1)\sin\theta}{|J_0|S_0\cos\theta_0 + JS(Z-1)\cos\theta}, \\ \sin\theta = \dfrac{B}{2JSZ}. \end{cases} \tag{4.137}$$

In order to minimize the energy the azimuthal angles ϕ_0 and ϕ_1 have to obey

$$\begin{cases} -J_0 \cos(\phi_0)\cos(\phi_1) > 0, \\ \sin\phi_1 = 0. \end{cases} \tag{4.138}$$

We can chose the coordinate system where the azimuthal angle ϕ_1 of the nearest neighbour site is equal to π that gives the minimizing condition for the impurity angle similar to Eq. (4.22)

$$\cos\phi_0 = \nu_0, \qquad \phi_1 = \pi, \qquad -\cos\phi_{ij} = \nu, \qquad \text{for } i, j \neq 0, 1. \tag{4.139}$$

We can solve the equation set in Eq. (4.137) numerically, but it can be also solved analytically by using approximations $\cos\theta_1 \approx \cos\theta$ and keeping linear terms in a series expansion that gives the following expressions for the latitude angles minimizing the energy

$$\tan\theta_0|_{min} \approx \frac{B_0 - \frac{BJ_0}{2J}}{|J_0| SZ\cos\theta_0} + \frac{B_0\frac{S_0}{S} - \nu_0 B}{JSZ(Z-1)\cos\theta}, \tag{4.140}$$

$$\tan\theta_1|_{min} \approx \frac{B(Z+1) - 2\nu_0 B_0 \frac{S_0}{S\cos\theta}}{2JSZ(Z-1)\cos\theta}. \tag{4.141}$$

It is necessary to note that the approximation of $\tan\theta_0|_{min}$ given in Eq. (4.140) is a rather accurate. Comparing to numerical calculations it differs by $\lesssim 1\%$ for the typical conditions $Z = 4$, $S = S_0 = 1/2$, and $B = B_0 = 0.4J$ under consideration. While the approximated $\tan\theta_1|_{min}$ in Eq. (4.141) is independent of the impurity exchange constant J_0, however its exact value depends on the coupling J_0 through θ_0 in the equation set (4.137). Therefore, comparing to numerical calculations the approximated $\tan\theta_1|_{min}$ has a relative error $\sim 1\%$ which increases up to 40% in the limit of the vanishing impurity coupling J_0.

For further calculations it is convenient to introduce new angular variables

$$\beta_0 = \theta_1 + \nu_0\theta_0, \qquad \beta_1 = \theta + \theta_1, \tag{4.142}$$

where $\theta_0, \theta_1, \theta$ are the latitude angles on the impurity, nearest neighbors and other bulk sites respectively. This inclusion of the nearest neighbors angle θ_1 leads to a change of the shift in Eq. (4.68) of the bulk bosonic variables

$$\alpha_i = -\frac{1}{N}\sum_{\vec{k}} \sqrt{\frac{S}{2}} \Bigg[\Bigg\{ \Bigg(\frac{|J_0|}{J}\frac{S_0}{S}\sin\beta_0 - \sin 2\theta \Bigg) + \frac{B}{JS}(\cos\theta - \cos\theta_1) \Bigg\} \gamma_{\vec{k}} \\ + (\sin\beta_1 - \sin 2\theta)\Big((Z-1)\gamma_{\vec{k}} + Z\gamma_{\vec{k}}^2 - 1 \Big) \Bigg] \frac{e^{i\vec{k}\cdot\vec{r}_i}}{1 + \gamma_{\vec{k}}\cos 2\theta}. \tag{4.143}$$

It gives additional contribution to the shift of impurity bosonic operator $\tilde{\alpha}_0$ which is defined by

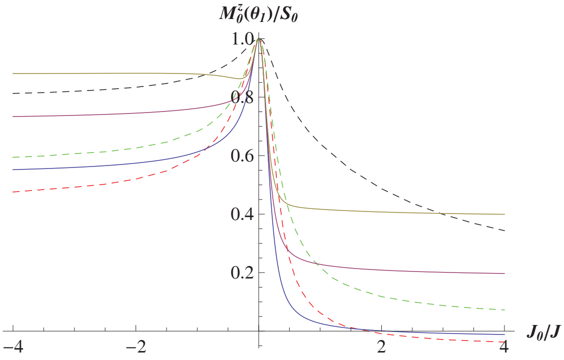

Figure 4.9: Comparison of the normalized impurity magnetization M_0^z/S_0 by introduction of additional angle θ_1 for different values of the impurity spins $S_0 = 1/2$, 1 and $3/2$ (the blue, purple and brown curves respectively) with results of the independent quantum Monte-Carlo simulations (the dashed red, green and black lines respectively).

Eq. (4.129) and can be expressed as

$$\begin{aligned}\tilde{\alpha}_0 = -\sqrt{\frac{S}{2}}\Bigg[&\left\{\left(\frac{|J_0|}{J}\frac{S_0}{S}\sin\beta_0 - \sin 2\theta\right) + \frac{B}{JS}(\cos\theta - \cos\theta_1)\right\} I_2 \\ &+ (\sin\beta_1 - \sin 2\theta)\Big((Z-1)I_2 + ZI_3 - I_1\Big)\Bigg],\end{aligned} \tag{4.144}$$

where we introduce the following notations

$$I_1 = \frac{1}{N}\sum_{\vec{k}}\frac{\gamma_{\vec{k}}}{1+g\gamma_{\vec{k}}}, \qquad I_2 = \frac{1}{N}\sum_{\vec{k}}\frac{\gamma_{\vec{k}}^2}{1+g\gamma_{\vec{k}}}, \tag{4.145}$$

$$I_3 = \frac{1}{N}\sum_{\vec{k}}\frac{\gamma_{\vec{k}}^3}{1+g\gamma_{\vec{k}}} \tag{4.146}$$

by using the sum relations given by Eqs. (A.64), (A.65) and (A.66) in the Appendix A.4, where the constant $g = \cos 2\theta$ in the leading order approximation is defined in Eq. (4.36). Therefore the impurity bosonic shift α_0 given by Eq. (4.131) can be expressed in the final form

$$\begin{aligned}\alpha_0 =& \sqrt{\frac{S_0}{2}}\,\frac{1}{\nu_0 + \tan\beta\tan\theta_0}\Bigg[\Bigg\{\left(\frac{|J_0|}{J}\frac{S_0}{S}\sin\beta_0 - \sin 2\theta\right) \\ &+ \frac{B}{JS}(\cos\theta - \cos\theta_1)\Bigg\} I_2 + (\sin\beta_1 - \sin 2\theta)\big\{(Z-1)I_2 + ZI_3 - I_1\big\}\Bigg].\end{aligned} \tag{4.147}$$

One should note that the change of the minimization angle θ_0 in Eqs. (4.140) and (4.141) gives a more dominating contribution to the impurity magnetization than the change of the impurity variable α_0 due to the shift of the impurity bosonic operators.

Taking into account the latitude angles of the impurity neighbours results also in renormalization of the bulk parameters $\tilde{m}$ and $\tilde{\Delta}$ given in Eq. (4.128). As a first approximation, we can assume that the modified bulk variables are unchanged. In this case the normalized impurity magnetization $\tilde{M}_0^z = M_0^z/S_0$ taking into account of additional neighbors angle θ_1 as a function of the impurity coupling J_0 is shown in Figure 4.9. The obtained analytical results are also compared with the results of the independent Monte-Carlo simulations.

4.7.2 Corrections due to θ_1 and θ_2

We can also consider the second line of impurity neighbors sites and introduce their latitude angle θ_2 that gives additional contribution to the constant terms of the Hamiltonian and leads to the following combined equations

$$\begin{cases} \tan\theta_0 = \dfrac{B_0 - J_0 SZ \sin\theta_1}{|J_0| SZ \cos\theta_1}, \\ \tan\theta_1 = \dfrac{B - J_0 S_0 \sin\theta_0 - JS(z-1)\sin\theta_2}{|J_0| S_0 \cos\theta_0 + JS(Z-1)\cos\theta_2}, \\ \tan\theta_2 = \dfrac{\frac{2B}{JS} - (Z-1)\sin\theta_1 - (2Z-3)\sin\theta}{(Z-1)\cos\theta_1 + (2Z-3)\cos\theta}, \\ \sin\theta = \dfrac{B}{2JSZ}. \end{cases} \tag{4.148}$$

This equation set can be solved accurately numerically that enables to change the minimization latitude angle θ_0 and improve results for the magnetization on the impurity site.

In Figure 4.10 we show the impurity magnetization calculated by the classical relation in Eq. (4.100) improved by taking into account the different angles for the impurity neighbors in order to find the latitude angle θ_0 on the impurity site. Including variation of the neighbor bulk angles results in better agreement with the quantum Monte-Carlo simulations or ferromagnetic couplings $J_0 > 0$ for a spin-$1/2$ impurity, while for positive J_0 these results coincide with the classical result in a spin-$1/2$ antiferromagnet as is shown in Figure 4.10(a). In the case of the impurity spin $S_0 = 1$ differing from the bulk spins we see in Figure 4.10(b) that taking into account the different angles if the impurity neighbors gives a proper agreement with the QMC data in contrast to the classical result.

Taking into account more latitude angles θ_i for the bulk sites is extremely hard in analytic form. However, these calculations can be performed numerically by solving the general minimization conditions which can be written in the form of the equation set

$$\tan\theta_i = \frac{B_i - \sum_{\langle i,j\rangle} J_{ij} S_j \sin\theta_j}{\sum_{\langle i,j\rangle} |J_{ij}| S_j \cos\theta_j}, \tag{4.149}$$

where the sum is performed over all the nearest neighbours of each i-site. In our Article III [173] we numerically diagonalized the quadratic bosonic Hamiltonian keeping track of all the bulk angles θ_i by the relaxation method where the boundary conditions were specified to fit the minimization conditions in Eq. (4.21) for a typical lattice size (28×28).

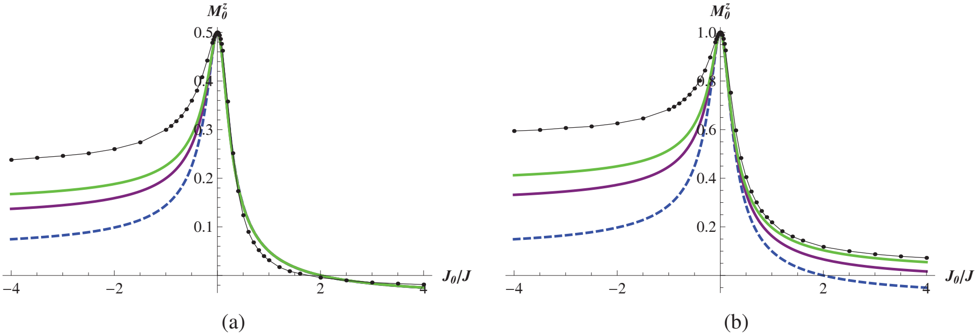

Figure 4.10: Magnetization on the impurity site given by classical relation in Eq. (4.100) taking into account different angles for impurity neighbors as a function of a coupling J_0 to a bulk spin-$1/2$ antiferromagnet for different values of the impurity spin: (a) $S_0 = 1/2$ and (b) $S_0 = 1$. The solid purple curve is the analytic results including the angle θ_1 for the nearest neighbors, the solid green curves describes also taking into account the latitude angles θ_2, while the dashed blue line corresponds to the classical result and the black dots are the QMC data in Figure 4.7. The applied magnetic field is $B = B_0 = 0.4J$.

4.8 Linear response theory

We can apply also another approach within the framework of spin wave theory in order to study analytically a general impurity in a Heisenberg antiferromagnet in an external magnetic field. Considering an impurity in an otherwise uniform magnet as a *static perturbation* allows to apply perturbation theory in order to find the local magnetization. Since we study *static* properties of the spin system, the time-independent variant of linear response theory (LRT) [176–178] is appropriate and answers how the equilibrium system changes in response to an external time-independent perturbation. Within this framework the Hamiltonian of the quantum system is

$$\hat{H} = \hat{H}_0 + \hat{V}, \tag{4.150}$$

where $\hat{H}_0$ is the unperturbed Hamiltonian and $\hat{V}$ is the time-independent perturbation. The corresponding Schrödinger equation is

$$\hat{H}|\psi\rangle = E|\psi\rangle. \tag{4.151}$$

Using stationary perturbation theory [86, 120] we are looking for the eigenenergy E and the wave function $|\psi\rangle$ in the general form

$$|\psi\rangle = \sum_n c_n|\psi_n^{(0)}\rangle, \qquad c_n = c_n^{(0)} + c_n^{(1)} + c_n^{(2)} + \ldots, \tag{4.152}$$

$$E = E^{(0)} + E^{(1)} + E^{(2)} + \ldots, \tag{4.153}$$

where $\psi_n^{(0)}$ and $E^{(0)}$ are the eigenfunctions and the eigenenergies of the unperturbed Hamiltonian $\hat{H}_0$, $c_m^{(k)}$ are expansion coefficients, and the number in parentheses (k) corresponds to the k-order correction. The perturbed wave functions are normalized $\langle\psi|\psi\rangle = 1$. In further calculations we will consider the case of a non-degenerate energy spectrum.

For the unperturbed system the coefficients of the eigen function $|\psi_n^{(0)}\rangle$ in Eq. (4.152) are given by the relation

$$c_m^{(0)} = \delta_{mn}. \tag{4.154}$$

Perturbation theory gives the well-known result for the first-order corrections

$$E_n^{(1)} = \langle\psi_m^{(0)}|\hat{V}|\psi_m^{(0)}\rangle = V_{nn}, \qquad\qquad V_{mn} = \langle\psi_m^{(0)}|\hat{V}|\psi_n^{(0)}\rangle, \tag{4.155}$$

where V_{mn} is a matrix element of the perturbation operator connecting the unperturbed m- and n-states. The corrections to the $|\psi_n^{(0)}\rangle$ wave function coefficients are

$$c_m^{(1)} = \frac{V_{mn}}{E_n^{(0)} - E_m^{(0)}}, \qquad\qquad \text{for } m \neq n, \tag{4.156}$$

while the coefficient $c_n^{(1)}$ is arbitrary and can be chosen equal to zero. Thus the wave functions can be written in the explicit form

$$|\psi_n^{(\mathrm{I})}\rangle = |\psi_n^{(0)}\rangle + |\psi_n^{(1)}\rangle, \qquad\qquad |\psi_n^{(1)}\rangle = \sum_{m\neq n} \frac{V_{mn}}{E_n^{(0)} - E_m^{(0)}} |\psi_m^{(0)}\rangle. \tag{4.157}$$

The perturbed wave functions are orthogonal and normalized, $|\psi_n^{(\mathrm{I})}| \approx 1$, is valid up to the second order terms. This linear approximation is applicable only if the perturbation is relatively small as compared with the difference of the energy levels

$$|V_{mn}| \ll |E_n^{(0)} - E_m^{(0)}|. \tag{4.158}$$

The weak perturbation causes change of an observable parameter corresponding to the expectation values of operator $\hat{O}$ in the quantum system. This variation of the observable can be written in the first-order approximation as

$$\langle\Delta\hat{O}\rangle = \langle\hat{O}\rangle^{(\mathrm{I})} - \langle\hat{O}\rangle^{(0)}, \tag{4.159}$$

where the expectation values for different correction orders are given by

$$\langle\hat{O}\rangle^{(0)} = \langle\psi^{(0)}|\hat{O}|\psi^{(0)}\rangle, \qquad\qquad \langle\hat{O}\rangle^{(\mathrm{I})} = \langle\psi^{(\mathrm{I})}|\hat{O}|\psi^{(\mathrm{I})}\rangle. \tag{4.160}$$

Therefore the change of the observable becomes

$$\begin{aligned}\langle\Delta\hat{O}\rangle &= \Big(\langle\psi^{(1)}|\hat{O}|\psi^{(0)}\rangle + \langle\psi^{(0)}|\hat{O}|\psi^{(1)}\rangle\Big) + \langle\psi^{(1)}|\hat{O}|\psi^{(1)}\rangle = \\ &= 2\Re\langle\psi^{(1)}|\hat{O}|\psi^{(0)}\rangle + \langle\psi^{(1)}|\hat{O}|\psi^{(1)}\rangle, \end{aligned}\tag{4.161}$$

where $\Re$ denotes the real part. Taking into account the wave function corrections in Eq. (4.157) the first term in Eq. (4.161) can be written in the form

$$\langle\psi^{(1)}|\hat{O}|\psi^{(0)}\rangle = \sum_n \sum_{m\neq n} c^*_{nm} \langle\psi^{(0)}_m|\hat{O}|\psi^{(0)}_n\rangle = \sum_n \sum_{m\neq n} \frac{V_{nm}\langle\psi^{(0)}_m|\hat{O}|\psi^{(0)}_n\rangle}{E^{(0)}_m - E^{(0)}_n}. \tag{4.162}$$

Considering the case where the system is initially in the ground state $|0\rangle = |\psi^{(0)}_0\rangle$ with zero ground state energy we get

$$\langle\psi^{(1)}|\hat{O}|\psi^{(0)}\rangle = -\sum_{m\neq 0} \frac{V_{0m}}{E^{(0)}_m}\langle\psi^{(0)}_m|\hat{O}|0\rangle. \tag{4.163}$$

Neglecting the second term in Eq. (4.161) corresponding to the second order corrections gives the linear response to the time-independent perturbation in the explicit form

$$\langle\Delta\hat{O}\rangle = -2\Re\sum_{m\neq 0}\langle 0|\hat{V}|\psi^{(0)}_m\rangle\,\langle\psi^{(0)}_m|\hat{O}|0\rangle\frac{1}{E^{(0)}_m}. \tag{4.164}$$

Taking into account also the second order corrections the response becomes

$$\langle\Delta\hat{O}\rangle^{(\mathrm{II})} = 2\Re\langle\psi^{(1)}|\hat{O}|\psi^{(0)}\rangle + 2\Re\langle\psi^{(2)}|\hat{O}|\psi^{(0)}\rangle + \langle\psi^{(1)}|\hat{O}|\psi^{(1)}\rangle, \tag{4.165}$$

where the correction to the unperturbed eigenfunctions is given by [86]

$$\begin{aligned}|\psi^{(2)}_n\rangle = &\sum_{m\neq k}\sum_{k\neq n}\frac{V_{mk}V_{kn}}{(E^{(0)}_n - E^{(0)}_k)(E^{(0)}_n - E^{(0)}_m)}|\psi^{(0)}_m\rangle \\ &-\sum_{m\neq n}\frac{V_{nn}V_{mn}}{\left(E^{(0)}_n - E^{(0)}_m\right)^2}|\psi^{(0)}_m\rangle - \frac{|\psi^{(0)}_n\rangle}{2}\sum_{m\neq n}\frac{|V_{mn}|^2}{\left(E^{(0)}_n - E^{(0)}_m\right)^2},\end{aligned} \tag{4.166}$$

while the perturbed wave functions $|\psi^{(\mathrm{II})}_n\rangle = |\psi^{(0)}_n\rangle + |\psi^{(1)}_n\rangle + |\psi^{(2)}_n\rangle$ should be normalized to unity.

In order to see how our previous results can be obtained using linear response theory we focus on the local longitudinal magnetization which is described by the z-component of the spin operator. In this case the operator of the experimental observable is site-dependent and corresponds to

$$\hat{O} = \hat{S}^z_i. \tag{4.167}$$

For further calculations we will use the following notations for the eigenfunctions and eigenenergies of the unperturbed Hamiltonian

$$|m\rangle = |\psi^{(0)}_m\rangle, \qquad E_m = E^{(0)}_m. \tag{4.168}$$

4.8.1 The case of a vacancy

First of all we will consider a single vacancy in a Heisenberg antiferromagnet described by the Hamiltonian

$$\hat{H} = \hat{H}_{bulk} + \hat{H}_{vac}, \tag{4.169}$$

where the bulk Hamiltonian is given by Eq. (4.3) and is to be considered as the unperturbed Hamiltonian, while the vacancy Hamiltonian is treated as a static perturbation

$$\hat{H}_{vac} = \hat{V}_{vac,J} + \hat{V}_{vac,B}, \tag{4.170}$$

where we divided the perturbation into two parts corresponding to the absence of the interaction between the vacancy and bulk sites

$$\hat{V}_{vac,J} = -J \sum_{\langle 0,j \rangle} \hat{\vec{S}}_{i=0} \cdot \hat{\vec{S}}_j \tag{4.171}$$

and the absence of the interaction with the applied magnetic field

$$\hat{V}_{vac,B} = +B\hat{S}^z_{i=0}. \tag{4.172}$$

This separation of the perturbation is convenient due to different operator forms of the interactions.

Performing the Holstein-Primakoff expansion in Eqs. (4.8)–(4.11) in the rotated coordinate frame in Eq. (4.5) and keeping the leading and linear terms we get the expression for the operator of the observable

$$\hat{O} = \hat{S}^z_i \approx \sin\theta_i \left(S_i - a^\dagger_i a_i \right) + \cos\theta_i \sqrt{\frac{S_i}{2}} \left(a^\dagger_i + a_i \right). \tag{4.173}$$

The non-zero transition matrix element of the vacancy perturbation due to the magnetic field becomes

$$\langle m | \hat{V}_{vac,B} | 0 \rangle = B\sqrt{\frac{S}{2}} \cos\theta \langle m | (a^\dagger_{i=0} + a_{i=0}) | 0 \rangle, \tag{4.174}$$

while the perturbation part of the interaction with the surrounding bulk sites gives

$$\langle m | \hat{V}_{vac,J} | 0 \rangle = -JS\sqrt{\frac{S}{2}} \sin 2\theta \Big[Z \langle m | (a^\dagger_{i=0} + a_{i=0}) | 0 \rangle + \langle m | \sum_{\langle 0,j \rangle} (a^\dagger_j + a_j) | 0 \rangle \Big]. \tag{4.175}$$

Applying the Fourier transform the matrix elements can be written in momentum space as

$$\langle \vec{k} | \hat{V}_{vac,B} | 0 \rangle = \sqrt{\frac{S}{2}} \cos\theta \frac{1}{\sqrt{N}} \sum_{\vec{k}} \langle \vec{k} | (a^\dagger_{\vec{k}} + a_{\vec{k}}) | 0 \rangle, \tag{4.176}$$

$$\langle \vec{k} | \hat{V}_{vac,J} | 0 \rangle = -JS\sqrt{\frac{S}{2}} \sin 2\theta \frac{Z}{\sqrt{N}} \sum_{\vec{k}} \langle \vec{k} | (a^\dagger_{\vec{k}} + a_{\vec{k}})(1 + \gamma_{\vec{k}}) | 0 \rangle. \tag{4.177}$$

The spin operator of the observable in Eq. (4.173) has the following non-zero transition elements

$$\langle 0|\hat{O}|m\rangle = \langle 0|\hat{S}_i^z|m\rangle = \sqrt{\frac{S}{2}}\cos\theta\langle 0|(a_i^\dagger + a_i)|m\rangle, \tag{4.178}$$

which can be written in momentum space as

$$\langle 0|\hat{O}(\vec{r}_i)|\vec{k}\rangle = \sqrt{\frac{S}{2}}\cos\theta\frac{1}{\sqrt{N}}\sum_{\vec{k}}\langle 0|(a_{\vec{k}}^\dagger\, e^{i\vec{k}\cdot\vec{r}_i} + a_{\vec{k}}\, e^{-i\vec{k}\cdot\vec{r}_i})|\vec{k}\rangle. \tag{4.179}$$

Using the canonical Bogoliubov transformation in Eq. (4.39) we can express the bosonic operators $a_{\vec{k}}^\dagger$, $a_{\vec{k}}$ in terms of the magnon creation and annihilation operators $b_{\vec{k}}^\dagger$, $b_{\vec{k}}$ which act on the system eigenstates as

$$b_{\vec{k}}^\dagger|0\rangle = |\vec{k}\rangle, \qquad\qquad b_{\vec{k}}|\vec{k}\rangle = |0\rangle. \tag{4.180}$$

This allows to calculate the non-zero transition matrix elements of the bosonic operator

$$\langle\vec{k}|a_{\vec{k}}^\dagger|0\rangle = u_{\vec{k}} + v_{\vec{k}}, \tag{4.181}$$

where the transformation coefficients $u_{\vec{k}}$ and $v_{\vec{k}}$ obey the relations in Eq. (4.43). Employing Eq. (4.164) for the linear response and taking into account the fact that the $E_{\vec{k}}$ eigenenergies[3] of the unperturbed bulk Hamiltonian can be determined from the diagonalized quadratic Hamiltonian in Eq. (4.40) and correspond to the coefficient $\omega_{\vec{k}}$ given by Eq. (4.41), we get the following corrections to the magnetization on site-i

$$\Delta M^z_{vac,B} = -BS\cos^2\theta\,\frac{1}{N}\sum_{\vec{k}}\frac{1}{A_{\vec{k}} + B_{\vec{k}}}\,\cos\left(\vec{k}\cdot\vec{r}_i\right), \tag{4.182}$$

$$\Delta M^z_{vac,J} = 2JS^2Z\cos^2\theta\,\sin\theta\,\frac{1}{N}\sum_{\vec{k}}\frac{(1+\gamma_{\vec{k}})}{A_{\vec{k}} + B_{\vec{k}}}\,\cos\left(\vec{k}\cdot\vec{r}_i\right), \tag{4.183}$$

where the coefficients $A_{\vec{k}}$ and $B_{\vec{k}}$ are given in Eqs. (4.35) and (4.34). Using the minimization conditions in Eq. (4.21) the total linear response to the vacancy becomes

$$\Delta M^z_{vac} = \Delta M^z_{vac,B} + \Delta M^z_{vac,J} = 2JS^2Z\cos^2\theta\,\sin\theta\,\frac{1}{N}\sum_{\vec{k}}\frac{\gamma_{\vec{k}}}{A_{\vec{k}} + B_{\vec{k}}}\,\cos\left(\vec{k}\cdot\vec{r}_i\right), \tag{4.184}$$

which can be written in the explicit form [179]

$$\Delta M^z_{vac}(\vec{r}_i) = S\cos\theta\,\sin 2\theta\,\frac{1}{N}\sum_{\vec{k}}\frac{\gamma_{\vec{k}}}{1 + \gamma_{\vec{k}}\cos 2\theta}\,\cos\left(\vec{k}\cdot\vec{r}_i\right). \tag{4.185}$$

Performing the sum over all momenta in Eq. (4.185) as is shown in Appendix A.4 the magnetization correction due to the vacancy in a uniform two-dimensional spin-S antiferromagnet

---

[3] The ground state energy is chosen equal to zero.

becomes

$$\Delta M^z_{vac} = S \sin\theta \, \tan 2\theta \begin{cases} 1 - \dfrac{4}{\pi(1+\sin 2\theta)} \mathrm{K}\left(\dfrac{1-\sin 2\theta}{1+\sin 2\theta}\right), & i = 0, \\ (-1)^{R_i} \dfrac{-2}{\pi \cos 2\theta} \mathrm{K}_0\left(\dfrac{r}{d}\right), & \text{otherwise,} \end{cases} \tag{4.186}$$

where $R_i = x_i + y_i$ describes the alternating behaviour, d is the decay scale given by Eq. (4.84), $\mathrm{K}(x)$ is the complete elliptic integral of the first kind, and $K_0(x)$ is the zeroth-order modified Bessel function of the second kind.

Since the uniform magnetization M^z_{bulk} of the unperturbed antiferromagnet is given by the classical relation in Eq. (4.79), in the case of a vacancy the local spacial magnetization pattern around the vacancy is determined by the correction in Eq. (4.185) within LRT

$$M^z_{vac}(\vec{r}_i) = (S - n)\sin\theta + \Delta M^z_{vac}(\vec{r}_i), \tag{4.187}$$

where the bulk parameter n is given by Eq. (4.44) and corresponds to the quantum corrections from the quadratic bulk Hamiltonian.

4.8.2 The case of a general impurity

In the case of an embedded general impurity the Hamiltonian contains additional terms which can be considered as extra static perturbations. The impurity Hamiltonian can be also divided into two parts

$$\hat{H}_{imp} = \hat{V}_{imp,J_0} + \hat{V}_{imp,B_0}, \tag{4.188}$$

which correspond to the interaction between the impurity and bulk sites through the coupling constant J_0 as

$$\hat{V}_{imp,J_0} = J_0 \sum_{\langle 0,j \rangle} \hat{\vec{S}}_0 \cdot \hat{\vec{S}}_j \tag{4.189}$$

and the Zeeman coupling of the impurity to the external magnetic field

$$\hat{V}_{imp,B_0} = -B_0 \hat{S}^z_0. \tag{4.190}$$

This perturbation $\hat{V}_{imp,B_0}$ is described by the impurity spin operator $\hat{S}^z_0$ which can be written in terms of the *impurity* bosonic operators $a^\dagger_0$ and a_0 in Eq. (4.124) by applying the Holstein-Primakoff transformation. These impurity operators do not change the eigenstates of the unperturbed bulk Hamiltonian, thus only the diagonal matrix element has non-zero value

$$\langle m | \hat{V}_{imp,B_0} | 0 \rangle \sim \delta_{m,0}. \tag{4.191}$$

This gives in accordance with Eq. (4.164) that within linear response theory the correction to the magnetization due to the interaction of the impurity with the magnetic field vanishes

$$\Delta M^z_{imp,B_0} = 0. \tag{4.192}$$

Applying the Holstein-Primakoff transformation in the rotated coordinate frame and using the minimization conditions in Eq. (4.21) we get the following off-diagonal matrix elements for the part of the impurity perturbation corresponding to the coupling to the surrounding bulk sites

$$\langle m|\hat{V}_{imp,J_0}|0\rangle = J_0 S_0 \sqrt{\frac{S}{2}} \big(\sin\theta_0 \cos\theta + \nu_0 \cos\theta_0 \sin\theta \big) \langle m| \sum_{\langle 0,j \rangle} (a_j^\dagger + a_j)|0\rangle, \tag{4.193}$$

which can be written in the Fourier space in the form

$$\langle \vec{k}|\hat{V}_{imp,J_0}|0\rangle = J_0 S_0 Z \sqrt{\frac{S}{2}} \nu_0 \sin\beta \, \frac{1}{\sqrt{N}} \sum_{\vec{k}} \langle \vec{k}|(a_{\vec{k}}^\dagger + a_{\vec{k}})|0\rangle, \tag{4.194}$$

where $\nu_0 = \mathrm{sgn}\, J_0$ and the angle $\beta = \theta + \nu_0 \theta_0$. Employing the Bogoliubov transformation and taking into account the transition matrix elements of the observable operator in Eq. (4.179) and the bosonic bulk operators in Eq. (4.181) we get the correction to the bulk magnetization due to the impurity coupling

$$\Delta M^z_{imp,J_0} = -\nu_0 J_0 S_0 S Z \sin\beta \, \cos\theta \, \frac{1}{N} \sum_{\vec{k}} \frac{\gamma_{\vec{k}}}{A_{\vec{k}} + B_{\vec{k}}} \, \cos\big(\vec{k}\cdot\vec{r}_i\big), \tag{4.195}$$

which can be written in the explicit form

$$\Delta M^z_{imp,J_0}(\vec{r}_i) = -\frac{|J_0|}{J} S_0 \sin\beta \, \cos\theta \, \frac{1}{N} \sum_{\vec{k}} \frac{\gamma_{\vec{k}}}{1 + \gamma_{\vec{k}} \cos 2\theta} \, \cos\big(\vec{k}\cdot\vec{r}_i\big). \tag{4.196}$$

The total linear response due to the embedded impurity contains also the contribution from the vacancy calculated in Eq. (4.185) that gives the magnetization pattern around the impurity

$$\begin{aligned} \Delta M^z(\vec{r}_i) =& \Delta M^z_{vac} + \Delta M^z_{imp,J_0} + \Delta M^z_{imp,B_0} = \\ &= \left(S \sin 2\theta - \frac{|J_0|}{J} S_0 \sin\beta \right) \sum_{\vec{k}} \frac{\gamma_{\vec{k}}}{1 + \gamma_{\vec{k}} \cos 2\theta} \, \cos\big(\vec{k}\cdot\vec{r}_i\big). \end{aligned} \tag{4.197}$$

Applying the minimization conditions in Eqs. (4.21), (4.22) and (4.103) we can rewrite the correction to the magnetization in Eq. (4.197) in the compact form

$$\Delta M^z(\vec{r}_i) = -\frac{C}{JZ} \sqrt{\frac{2}{S}} \frac{1}{N} \sum_{\vec{k}} \frac{\gamma_{\vec{k}}}{1 + \gamma_{\vec{k}} \cos 2\theta} \, \cos\big(\vec{k}\cdot\vec{r}_i\big), \qquad i \neq 0, \tag{4.198}$$

where the coefficient C is given by Eq. (4.27).

Taking into account the uniform magnetization of the unperturbed bulk antiferromagnet given by the classical relation containing the quantum corrections in Eq. (4.79) the local longitudinal magnetization around the impurity becomes

$$M^z(\vec{r}_i) = M^z_{bulk} + \Delta M^z = (S - n) \sin\theta - \frac{C}{JZ} \sqrt{\frac{2}{S}} \frac{1}{N} \sum_{\vec{k}} \frac{\gamma_{\vec{k}}}{1 + \gamma_{\vec{k}} \cos 2\theta} \, \cos\big(\vec{k}\cdot\vec{r}_i\big), \tag{4.199}$$

which can be written in the general form

$$M^z(\vec{r}_i) = (S-n)\sin\theta - \sqrt{2S}\,\frac{C}{N}\sum_{\vec{k}} \frac{\gamma_{\vec{k}}}{A_{\vec{k}}+B_{\vec{k}}}\,\cos\left(\vec{k}\cdot\vec{r}_i\right), \qquad i \neq 0. \tag{4.200}$$

Comparing the obtained result in Eq. (4.200) with the leading order terms in Eq. (4.74) with the bosonic shift α_i given by Eq. (4.68) we see that linear response theory gives the same result for the local bulk magnetization as the direct calculations of the expectation value of the spin operator $\hat{S}^z$ performed in Section 4.3.

4.9 Summary

We studied statical local properties of spin-S antiferromagnets with an embedded impurity by using analytical spin wave approach. We calculated analytically the spatial magnetization pattern induced by a general magnetic impurity in a Heisenberg spin-S antiferromagnet in the presence of a magnetic field. The obtained analytical results are in a good agreement with the independent quantum Monte-Carlo simulations which were performed in our Article III. The complete analytical expressions for the local magnetization were obtained and examined for different values of the impurity spin S_0, coupling J_0 and strengths of the applied magnetic fields B and B_0. We found that the induced magnetization around the impurity has a alternating magnetization pattern along the field direction. We analyzed in details the form and characteristic scale of the magnetization decay to its uniform bulk value for the square and cubic lattices. Our analytic calculations show that the parameters and type of the impurity affect only the overall coefficient C describing the magnetization magnitude while the scale and shape of the magnetization decay are universal and depend only on the properties of the host magnet and the applied field.

In addition, we also verified our analytical calculations by employing linear response theory treatment considering an embedded impurity as a static perturbation to a uniform bulk antiferromagnet. In the case of a vacancy the expression for the local spatial magnetization is also derived analytically.

The obtained results can be applied to predict the detailed local magnetization pattern around general magnetic and non-magnetic impurities in isotropic antiferromagnets (e.g. from doping Zn, Co and Ni atoms in a quasi two-dimension $\mathrm{CuO_2}$-antiferromagnets) in experiments on the atomic scale by using, for example, MFM and SP-STM techniques.

Appendix A

Additional calculations

A.1 Schrieffer-Wolff transformation

In order to improve the procedure of numerically finding eigenvalues and eigenvectors of the Hamiltonian by including higher domain sectors without increasing the number of states one can use a technique of degenerate perturbation theory which is known as Schrieffer-Wolff transformation [180]. In general this method can be implemented for study a quantum many-body system when description of the system at the low-energy must be extracted from a full Hamiltonian describing the full-energy spectrum. In our case of studying the low-energy excitations in a finite system we can obtain a low-energy effective Hamiltonian by unitary transformation (so-called *direct rotation*) that decouples high-energy and low-energy domain walls subspaces. The detailed description of the technique for general quantum many-body systems is given in Ref. [181].

Consider $\hat{H}$ as some unperturbed diagonal Hamiltonian and a perturbation $\hat{V}$ which couples different subspaces. Using perturbation theory for the states in the low-energy subspace and retaining terms up to second order the matrix element of the effective Hamiltonian in the low-energy subspace can be written

$$\langle i|\hat{H}_{eff}|j\rangle_{\text{low}} = E_i\delta_{ij} + \langle i|\hat{V}|j\rangle + \sum_{k\in\text{high}} \frac{\langle i|\hat{V}|k\rangle\langle k|\hat{V}|j\rangle}{2}\left(\frac{1}{E_i - E_k} - \frac{1}{E_k - E_j}\right), \tag{A.1}$$

where indexes i, j describe states in the low-energy subspace and E_i are the eigenenergies of the unperturbed Hamiltonian. The effective Hamiltonian in Eq. (A.1) contains corrections from the high-energy subspace that allows to include the *leading contribution* of the higher sectors.

The advantage with this method is that effects of the high energy states can be included without having to diagonalize larger matrices. However, in our case when including perturbations from sectors with higher number of domain walls $N_{dw} > 6$, that requires to calculate all available states in the $N_{dw} = 8$ sector, the number of states rises dramatically with the system size N. In addition, for a larger perturbation we have to keep higher order terms of the Taylor series expansion which include contributions from higher sectors, see [181], that finally also increases the number of states and complicates the calculations.

We found that the effective Hamiltonian method for $N_{dw} \leq 4$ with leaving at least the second order terms in Eq. (A.1) gives underestimated energy levels in contrast to the eigenvalues

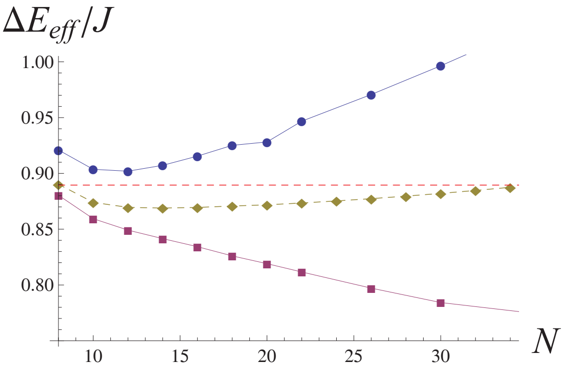

Figure A.1: Energy gap of the effective Hamiltonian between the ground state and the first excited state in even sector for different N_{dw} as a function of the system size N. The solid lines describe the maximum N_{dw} of low-energy subspace of the Schrieffer-Wolff transformation: blue solid line with circles is $N_{dw} = 2$ and magenta squares is $N_{dw} = 4$. The dashed brown line with diamonds shows the full contribution of the $N_{dw} \leq 6$ sectors of the full Hamiltonian in Eq. (3.18). The dashed red line describes the energy gap for the $N_{dw} \leq 2$ redefined Hamiltonian in Eq. (3.29).

of the full Hamiltonian for $N_{dw} \leq 6$, see Figure A.1. Including higher order terms in the Taylor expansion of the effective Hamiltonian requires contributions from higher N_{dw} sectors. In particular, keeping up to the third order terms of the effective low-energy Hamiltonian with the maximal number of domain walls $N_{dw} = 4$ needs contribution from states in the higher $N_{dw} \leq 8$ sectors which are restricted due to performance for the finite system size $N_{dw} = 34$.

Therefore in the case of the Hamiltonian in Eq. (3.1) with the parameters given by Eq. (3.31) the Schrieffer-Wolff transformation does not essentially improve the numerical description of the quantum spin system, so we do not use it.

A.2 Dynamical structure factors

A.2.1 $S^{-+}(q, \omega)$

When we consider transitions between the ground state and excited states we get non-zero contribution to the S^{-+} dynamical structure factor

$$S^{-+}(q, \omega) = \sum_{n}^{\infty} \delta(\omega - E_n(q))\, I_n^{-+}(q), \tag{A.2}$$

where I_n^{-+} is corresponding normalized relative intensity of the n-th mode

$$I_n^{-+}(q) = \left| C_1 C_0^n(0)\delta_{q,0} + 2e^{-iq/2} \sum_{l>1} C_l C_{l-1}^n(q) \cos(ql/2) \right|^2 . \tag{A.3}$$

The leading terms of the intensity give

$$I_n^{-+}(q) \approx \Big(C_1 C_0^n(0)\delta_{q,0} + 2C_2 C_1^n(q)\cos q\Big)^2. \tag{A.4}$$

In the case of $h_\perp = 0$ there is only non-zero wave functions corresponding states with even domain length l in the ground state that gives zero intensity at $q = 0$.

A.2.2 $S^{++}(q,\omega)$ and $S^{--}(q,\omega)$

When we consider transitions between the ground state and excited states we get non-zero contribution to the S^{++} and S^{--} dynamical structure factors

$$S^{++}(q,\omega) = \Big(S^{--}(q,\omega)\Big)^\dagger = \sum_n^\infty \delta(\omega - E_n(q))\, I_n^{++}(q), \tag{A.5}$$

where I_n^{++} is corresponding normalized relative intensity of the n-th mode which is given for leading contribution by

$$\begin{aligned} I_n^{++}(q) \quad &= \quad \left(C_0 C_1^n(q) + 2\sum_{l>0} C_l C_{l+1}^n(q)\cos(ql/2)\right) \\ &\quad \times \left(C_1 C_0^n(0)\delta_{q,0} + 2\sum_{l>1} C_l C_{l-1}^n(q)\cos(ql/2)\right). \end{aligned} \tag{A.6}$$

The leading terms of the intensity give

$$I_n^{++}(q) \approx C_1 C_0^n(0)\Big(C_0 C_1^n(0) + 2C_1 C_2^n(0)\Big)\delta_{q,0} + 2C_0 C_2 C_1^{n2}(q)\ \cos q. \tag{A.7}$$

In the case of $h_\perp = 0$ only states with even domain length l are in the ground state that gives zero intensity $I_n^{++} = 0$ at zero momentum $q = 0$.

A.3 Relation to system of units SI

In our calculation we use a system of units where the energy and the magnetic fields are expressed in terms of the coupling constant J_z. For the material parameters of $\mathrm{CoCl_2 \cdot 2H_2O}$ given in Eq. (3.31) this gives the following relation to units in the International System of Units (SI):

1. **Energy:**

$$J_z = 36.5\ \mathrm{K} = 3.15\ \mathrm{meV} = 5.03 \times 10^{-12}\ \mathrm{J}, \tag{A.8}$$

so for energy in terms of the coupling constant we have

$$E_{SI} = E \times 5.03 \times 10^{-12}\ [\mathrm{J}]. \tag{A.9}$$

2. **Magnetic field:**

$$B_{SI} = \frac{BJ_z}{g\mu_B}, \tag{A.10}$$

where $\mu_B = 5.79 \times 10^{-5}$ eV/T $= 9.27 \times 10^{-24}$ J/T is the Bohr magneton, g is the spin g-factor and the magnetic field B is expressed in units of J_z. In case of $\mathrm{CoCl_2 \cdot 2H_2O}$ the g-factor is

$$g_{\mathrm{CoCl_2 \cdot 2H_2O}} = 6.81 \pm 0.10, \tag{A.11}$$

see Ref. [88]. So we get the relation

$$B_{SI} = B \times 7.98\ [\mathrm{T}], \tag{A.12}$$

that gives the following values

$$h_z = 0.4\ \mathrm{T}, \qquad B_0^z = 1.6\ \mathrm{T} \tag{A.13}$$

for the static magnetic field, $h_z = 0.05J_z$, and magnitude of the magnetic field, $B_0^z = 0.2J_z$, in the laser beam. In the case of two lasers with the largest magnitude of the magnetic component, $B_{02}^z = 0.03J_z$, we get the value $B_{02}^z = 0.24$ T.

The magnitude of the electric field in an electromagnetic wave is related to the magnitude of the magnetic field by $E = cB$, where c is the speed of light. This gives the following relation of the electric field to magnetic field amplitude expressed in units of J_z

$$E_{SI} = B \times 2.39 \times 10^9\ [\mathrm{V/m}]. \tag{A.14}$$

The laser beam electric field is thus $E = 4.8 \times 10^8$ V/m when the laser beam magnetic field is $B_0^z = 0.2J_z$. In the case of two lasers the largest electric component of the radiation is $E_{02} = 7.2 \times 10^7$ V/m for the magnetic field amplitude $B_{02}^z = 0.03J_z$.

It is interesting to estimate the intensity of the laser beam. The optical intensity of an electromagnetic wave is given by

$$I = \frac{cB_0^2}{2\mu_0}, \tag{A.15}$$

where $\mu_0 = 4\pi \times 10^{-7}$ H/m is the vacuum permeability and $c = 3 \times 10^8$ m/s is the speed of light, that gives the intensity of the laser beam $I = 3.1 \times 10^{14}$ W/m^2. If the cross section of the laser beam is $A = 1$ mm^2 then the laser with magnetic field amplitude $B_0^z = 0.2J_z$ will produce radiation power of about $P = 3 \times 10^8$ W. In the case of two lasers the corresponding optical intensity of the "brightest" laser beam is $I_{02} = 6.9 \times 10^{12}$ W/m^2.

3. **Time scale:**

$$t_{SI} = t\frac{\hbar}{J_z}, \tag{A.16}$$

where $\hbar = 6.58 \times 10^{-16}$ eV · s $= 1.055 \times 10^{-34}$ J · s is the reduced Planck constant. Therefore

$$t_{SI} = t \times 2.09 \times 10^{-13}\ [\mathrm{s}]. \tag{A.17}$$

So a time unit of $\hbar/J_z$ corresponds to 0.2 ps for the $\mathrm{CoCl_2 \cdot 2H_2O}$ material.

A.3.1 Natural line width

Let us estimate an upper limit of the life time of the laser excited levels. The spontaneous emission rate [121] for a transition connecting an excited state with energy E_n to a state with E_m is given by

$$A_{n,m} = \frac{\mu_0 \omega_{n,m}^3 |\vec{p_\mu}|^2}{3\pi\hbar^3 c^3}, \qquad \omega_{n,m} = \frac{E_n - E_m}{\hbar}, \tag{A.18}$$

where the vacuum permeability is $\mu_0 = 4\pi \times 10^{-7}$ H/m, c is the speed of light and $\vec{p_\mu}$ is the transition matrix element of the magnetic dipole operator between levels n and m

$$\vec{p_\mu} = g\mu_B \vec{V}_s, \tag{A.19}$$

where g is the spin g-factor and $\vec{V}$ is the matrix element of the spin operator $\sum_i \vec{S}_i$. So the emission rate becomes

$$A_{n,m} = \frac{\mu_0 (g\mu_B)^2 (E_n - E_m)^3}{3\pi\hbar^4 c^3} |\vec{V}_{m,n}|^2, \tag{A.20}$$

since the transition matrix element is complex in general case the last factor is

$$|\vec{V}|^2 = |V^x|^2 + |V^y|^2 + |V^z|^2. \tag{A.21}$$

The total spontaneous emission rate of an excited state and its life time are given by

$$A_n = \sum_{m=0}^{n} A_{n,m}, \qquad \tau_n = \frac{1}{A_n}. \tag{A.22}$$

Using the material parameters in Eq. (3.31) for a single particle excitation at the energy level $E_{n=12} = 1.6J$ in $\mathrm{CoCl_2 \cdot 2H_2O}$ we get the life time $\tau_{n=12} \approx 20$ days.

This is certainly an upper limit as there are other mechanisms of level broadening. For example due to lattice distortion and impurities in the material that causes decreasing of the life time τ.

A.4 Integral Expressions

A.4.1 Sum I

We can consider the following sum

$$I = \frac{1}{N} \sum_{\vec{k}} \frac{e^{i\vec{k}\cdot\vec{r}}}{1 + b\gamma_{\vec{k}}}, \tag{A.23}$$

where $\gamma_{\vec{k}}$ can be represented for a quadratic lattice ($Z = 4$) in the two dimensional case as

$$\gamma_k = \frac{1}{2}(\cos k_x a + \cos k_y a), \qquad\qquad k_i \in \left[-\frac{\pi}{a}, \frac{\pi}{a}\right], \tag{A.24}$$

where a is a lattice constant. We assume that $a = 1$ for simplification of further calculation.

We apply the usual transformation rule of a sum to an integral

$$\frac{1}{N}\sum_{\vec{k}} = \frac{1}{(2\pi)^n}\int d\vec{k}, \tag{A.25}$$

where n is the dimension of a lattice ($n = 2$ in the case of a two-dimensional system). Therefore the sum in Eq. (A.23) can be written in the following way

$$I = \frac{1}{4\pi^2}\int \frac{e^{i\vec{k}\cdot\vec{r}}}{1 + b\gamma_{\vec{k}}} d\vec{k} \tag{A.26}$$

The leading contribution to the integral is defined by maximal value of its integrand. In the case of $0 \leq b \leq 1$, that is valid for $b = \cos 2\theta$ in our model, denominator in the integrand in Eq. (A.23) is minimized for the $\vec{k}$ coinciding with the antiferromagnetic wave vector $\vec{Q} = (\pi, \pi)$ where the parameter $\gamma_{\vec{k}}$ can be approximated as

$$\gamma_{\vec{k}} \approx -1 + \frac{\vec{k}^2}{4} + \ldots \tag{A.27}$$

at $\vec{k} \to \vec{Q} + \vec{k}$. Therefore the leading contribution in the integral is given by

$$I \approx e^{i\vec{Q}\cdot\vec{r}}\frac{1}{4\pi^2}\int \frac{e^{i\vec{k}\cdot\vec{r}}}{1 - b + b\vec{k}^2/4} d\vec{k} = (-1)^R I', \tag{A.28}$$

where the distance $R = x + y$ in units of the lattice spacing describes the spatial alternating pattern while the rest term I' gives the magnitude

$$I' = \frac{1}{4\pi^2}\int \frac{e^{i\vec{k}\cdot\vec{r}}}{1 - b + \frac{b}{4}\vec{k}^2} d\vec{k} = \frac{1}{4\pi^2}\int_{-\pi}^{\pi} dk_x \int_{-\pi}^{\pi} dk_y \frac{e^{i(xk_x + yk_y)}}{1 - b + \frac{b}{4}(k_x^2 + k_y^2)}. \tag{A.29}$$

We can see that the domain of integration is a square: $k_x \in [-\pi, \pi]$ and $k_y \in [-\pi, \pi]$. Since the major contribution in Eq. (A.29) is given by the integrand at the vanishing $\vec{k}$, we can extend the integration domain to a circle with large radius that allows to simplify the integral in the polar coordinate system parameterized by azimuth angle ϕ and radial coordinate k. Applying the transformations

$$\vec{k}^2 = k^2, \qquad\qquad \vec{k}\cdot\vec{r} = \cos\phi, \tag{A.30}$$

$$d\vec{k} = k\; dk\; d\phi, \tag{A.31}$$

the integral in Eq. (A.29) becomes

$$I' = \frac{1}{4\pi^2} \int_0^\infty dk \int_0^{2\pi} d\phi \frac{k}{A + Bk^2} \cos(kr\cos\phi), \tag{A.32}$$

where we expanded the integration domain to all real plane, and the coefficients A and B are

$$A = 1 - b, \qquad B = b/4. \tag{A.33}$$

Using the integral representation of the Bessel function of integer order [65]

$$J_0(x) = \frac{1}{\pi} \int_0^\pi \cos(x\cos t)\, dt, \tag{A.34}$$

we can perform integration over the azimuthal angle ϕ in Eq. (A.32) that gives

$$I' = \frac{1}{2\pi} \int_0^\infty \frac{k\, J_0(kr)}{A + Bk^2}\, dk, \tag{A.35}$$

where $J_0(x)$ is the Bessel function of the zeroth order. Introducing new integration variable

$$t = k^2, \qquad dt = 2k\, dk \tag{A.36}$$

and using table integral of cylinder functions [107] #6.532.4 we get

$$I' = \frac{1}{4\pi} \int_0^\infty \frac{J_0\left(r\sqrt{t}\right)}{A + Bk^2}\, dt = \frac{1}{2\pi B} \mathrm{K}_0\left(r\sqrt{A/B}\right), \tag{A.37}$$

where $K_0(x)$ is the zeroth-order modified (hyperbolic) Bessel function of the second kind [175], which main properties are given in Appendix B. Putting the explicit form of the coefficients A and B in Eq. (A.33) the integral I' can be written down as

$$I' = \frac{2}{\pi b} \mathrm{K}_0\left(2r\sqrt{1/b - 1}\right), \tag{A.38}$$

Therefore the sum in Eq. (A.23) becomes finally

$$I = \frac{1}{N} \sum_{\vec{k}} \frac{e^{i\vec{k}\cdot\vec{r}}}{1 + b\gamma_{\vec{k}}} \approx (-1)^R \frac{2}{\pi b} \mathrm{K}_0\left(2r\sqrt{\frac{1-b}{b}}\right), \tag{A.39}$$

where the distance $R = x + y$ describes the alternating pattern, and K_0 is the zeroth-order modified Bessel function of the second kind. We can introduce the characteristic decay scale d and rewrite the argument of the modified Bessel function as $K_0(r/d)$, that gives

$$d = \frac{1}{2}\sqrt{\frac{b}{1-b}} = \sqrt{\frac{\cos 2\theta}{8\sin^2\theta}} \tag{A.40}$$

for the used parameter $b = \cos 2\theta$.

A.4.2 Sum I_0

We can consider now the sum

$$I_0 = \frac{1}{N}\sum_{\vec{k}} \frac{1}{1+b\gamma_{\vec{k}}}, \tag{A.41}$$

which corresponds to the particular case of the sum I given by Eq. (A.23) at $r = 0$. Transforming the sum into the integral we get

$$I_0 = \frac{1}{4\pi^2}\int \frac{d\vec{k}}{1+b\gamma_{\vec{k}}} = \frac{1}{4\pi^2}\int_{-\pi}^{\pi} dk_x \int_{-\pi}^{\pi} \frac{dk_y}{\left(1+\frac{b}{2}\cos k_y\right)+\frac{b}{2}\cos k_x}. \tag{A.42}$$

The last integral corresponds to a tabulated integral [107, 182] which can be found as

$$\int \frac{dx}{\tilde{a}+\tilde{b}\cos x} = \frac{2}{\sqrt{\tilde{a}^2-\tilde{b}^2}} \arctan\left(\frac{(\tilde{a}-\tilde{b})\tan\frac{x}{2}}{\sqrt{\tilde{a}^2-\tilde{b}^2}}\right), \qquad \text{for } \tilde{a}^2 > \tilde{b}^2, \tag{A.43}$$

where the variables in our case are

$$\tilde{a} = 1+\frac{b}{2}\cos k_y, \qquad \tilde{b} = \frac{b}{2}, \tag{A.44}$$

which give that the inequality $\tilde{a}^2 > \tilde{b}^2$ is identically true. The definite integral in Eq. (A.43) over its interval $[-\pi, \pi]$ has the value

$$\int_{-\pi}^{\pi} \frac{dk_x}{\tilde{a}+\tilde{b}\cos k_x} = \frac{2\pi}{\sqrt{\tilde{a}^2-\tilde{b}^2}}. \tag{A.45}$$

That enables to reduce the double integral in Eq. (A.42) to the single integral

$$\begin{aligned} I_0 =& \frac{1}{2\pi}\int_{-\pi}^{\pi} \frac{dk_y}{\sqrt{\left(1+\frac{b}{2}\cos k_y\right)^2-\left(\frac{b}{2}\right)^2}} \\ =& \frac{1}{2\pi}\frac{1}{\sqrt{1-\frac{b^2}{4}}}\int_{-\pi}^{\pi} \frac{dk_y}{\sqrt{1+\tilde{a}\cos k_y}\sqrt{1+\tilde{b}\cos k_y}}, \end{aligned} \tag{A.46}$$

where the variables $\tilde{a}$ and $\tilde{b}$ were redefined

$$\tilde{a} = \frac{b}{2-b}, \qquad \tilde{b} = \frac{b}{2+b}. \tag{A.47}$$

The integral in Eq. (A.46) can be written in the following form

$$I_0 = \frac{1}{\pi}\frac{1}{\sqrt{1-\frac{b^2}{4}}}\int_{-1}^{1} \frac{dy}{\sqrt{1-y^2}\sqrt{1+\tilde{a}y}\sqrt{1+\tilde{b}y}} \tag{A.48}$$

by using integration variable

$$y = \cos k_y, \qquad dy = -\sin k_y\, dk_y. \tag{A.49}$$

We can introduce new variables for further simplification of the integral

$$k = \sqrt{\frac{1+\tilde{a}}{1-\tilde{a}}}\sqrt{\frac{1-\tilde{b}}{1+\tilde{b}}} = \frac{1}{\sqrt{1-b^2}}, \tag{A.50}$$

$$z = \sqrt{\frac{\tilde{a}-1}{\tilde{a}+1}}\sqrt{\frac{1-y}{1+y}} = i\sqrt{1-b}\sqrt{\frac{1-y}{1+y}}, \tag{A.51}$$

where z appears as a complex variable: $z \in \mathbb{C}$ and $z \in (-i\infty, 0]$. It enables to transform the integral in Eq. (A.48) to the form

$$\int_{-1}^{+1} \frac{dy}{\sqrt{1-y^2}\sqrt{1+\tilde{a}y}\sqrt{1+\tilde{b}y}} = -2i\sqrt{\frac{1-b^2/4}{1-b^2}} \int_0^{i\infty} \frac{dz}{\sqrt{1-z^2}\sqrt{1-k^2z^2}}. \tag{A.52}$$

On the other hand an incomplete elliptic integral of the first kind $\mathrm{F}(x;k)$ in Jacobi's form [65, 182] is defined as

$$\mathrm{F}(x;k) = \int_0^x \frac{dt}{\sqrt{(1-t^2)(1-k^2t^2)}}, \tag{A.53}$$

where x is amplitude and k is elliptic modulus or eccentricity [65]. Therefore the integral in Eq. (A.48) can be written

$$I_0 = -\frac{2i}{\pi\sqrt{1-b^2}} \lim_{z\to\infty} \mathrm{F}\left(iz; \frac{1}{\sqrt{1-b^2}}\right). \tag{A.54}$$

Using properties of this special function $\mathrm{F}(x;k)$ [65] we can express its limit value for the imaginary amplitude as

$$\lim_{z\to\infty} \mathrm{F}(iz;k) = i\,\mathrm{K}\left(\sqrt{1-k^2}\right), \tag{A.55}$$

where special function $\mathrm{K}(x)$ is complete elliptic integral of the first kind which is defined as

$$\mathrm{K}(x) = \int_0^1 \frac{dt}{\sqrt{(1-t^2)(1-x^2t^2)}}. \tag{A.56}$$

That gives following expression of the integral in Eq. (A.54) as a special function of complex argument

$$I_0 = \frac{2}{\pi\sqrt{1-b^2}}\,\mathrm{K}\left(i\frac{b}{\sqrt{1-b^2}}\right). \tag{A.57}$$

Using transformation properties of the complete elliptic integral of the first kind [183]

$$\mathrm{K}(x) = \frac{2}{1+\sqrt{1-x^2}}\,\mathrm{K}\left(\frac{1-\sqrt{1-x^2}}{1+\sqrt{1-x^2}}\right), \tag{A.58}$$

we get the final analytical expression of the integral

$$I_0 = \frac{1}{N}\sum_{\vec{k}} \frac{1}{1+b\gamma_{\vec{k}}} = \frac{4}{\pi\left(1+\sqrt{1-b^2}\right)}\,\mathrm{K}\left(\frac{1-\sqrt{1-b^2}}{1+\sqrt{1-b^2}}\right). \tag{A.59}$$

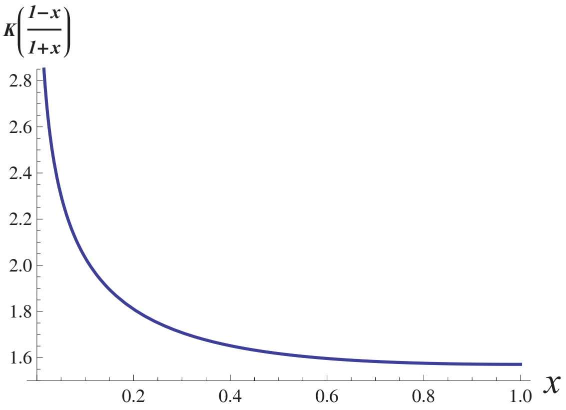

Figure A.2: Complete elliptic integral of the first kind $\mathrm{K}\left(\frac{1-x}{1+x}\right)$ as a function of its argument for $x = \sqrt{1-b^2}$ and $x \in [0,1]$.

The special function $\mathrm{K}(x)$ is the complete elliptic integral of the first kind which is defined in [107] as

$$\mathrm{K}(x) = \int_0^{\pi/2} \frac{d\theta}{\sqrt{1 - x^2 \sin^2\theta}} = \int_0^1 \frac{dt}{\sqrt{(1-t^2)(1-x^2t^2)}} \tag{A.60}$$

and can be expressed as the infinite power series, see [65]

$$\mathrm{K}(x) = \frac{\pi}{2}\left(1 + \sum_{n=1}^{\infty}\left[\prod_{j=1}^{n}\frac{2j-1}{2j}\right]^2 x^n\right) = \frac{\pi}{2}\left(1 + \sum_{n=1}^{\infty}\left[\frac{(2n)!}{2^{2n}n!^2}\right]^2 x^{2n}\right). \tag{A.61}$$

The series representation gives the special value $\mathrm{K}(0) = \pi/2$.

In Figure A.2 we plot the complete elliptic integral of the first kind $\mathrm{K}\left(\frac{1-x}{1+x}\right)$ as a function of its argument $x = \sqrt{1-b^2}$ which varies in the domain $x \in [0,1]$ and corresponds to the bulk parameter $x = \sin 2\theta$ in our model.

A.4.3 Additional Sums

Using the integral representation in Eq. (A.25) we can calculate other similar sums. Consider sum which can be represented as integral

$$I_1 = \frac{1}{N}\sum_{\vec{k}} \frac{\gamma_{\vec{k}}}{1 + b\gamma_{\vec{k}}} = \frac{1}{4\pi^2}\int \frac{\gamma_{\vec{k}}}{1 + b\gamma_{\vec{k}}} d\vec{k} \tag{A.62}$$

and can be simplified in the following way

$$\int \frac{\gamma_{\vec{k}}}{1 + b\gamma_{\vec{k}}} d\vec{k} = \frac{1}{b}\int \frac{(1 + b\gamma_{\vec{k}}) - 1}{1 + b\gamma_{\vec{k}}} d\vec{k} = \frac{1}{b}\left(\int d\vec{k} - \int \frac{d\vec{k}}{1 + b\gamma_{\vec{k}}}\right). \tag{A.63}$$

The first integral is equal to volume of integration domain that in our case gives 4π. The second term corresponds to the integral I_0 given in Eq. (A.59). Therefore we get the final expression

$$\begin{aligned} I_1 =& \frac{1}{N}\sum_{\vec{k}} \frac{\gamma_{\vec{k}}}{1+b\gamma_{\vec{k}}} = \frac{1}{b}(1-I_0) \\ =& \frac{1}{b}\left[1-\frac{4}{\pi\left(1+\sqrt{1-b^2}\right)}\,\mathrm{K}\left(\frac{1-\sqrt{1-b^2}}{1+\sqrt{1-b^2}}\right)\right]. \end{aligned} \tag{A.64}$$

The other sums can be calculated by the same way

$$\begin{aligned} I_2 =& \frac{1}{N}\sum_{\vec{k}} \frac{\gamma_{\vec{k}}^2}{1+b\gamma_{\vec{k}}} = \frac{1}{b^2}(I_0-1) \\ =& \frac{1}{b^2}\left[\frac{4}{\pi\left(1+\sqrt{1-b^2}\right)}\,\mathrm{K}\left(\frac{1-\sqrt{1-b^2}}{1+\sqrt{1-b^2}}\right)-1\right]. \end{aligned} \tag{A.65}$$

$$\begin{aligned} I_3 =& \frac{1}{N}\sum_{\vec{k}} \frac{\gamma_{\vec{k}}^3}{1+b\gamma_{\vec{k}}} = \frac{1}{b^3}\left(I_0-1-\frac{b^2}{4}\right) \\ =& \frac{1}{b^3}\left[\frac{4}{\pi\left(1+\sqrt{1-b^2}\right)}\,\mathrm{K}\left(\frac{1-\sqrt{1-b^2}}{1+\sqrt{1-b^2}}\right)-1-\frac{b^2}{4}\right]. \end{aligned} \tag{A.66}$$

In our case the parameter b is

$$b = \cos 2\theta, \qquad \sqrt{1-b^2} = \sin 2\theta, \tag{A.67}$$

that gives the following value of the I_2 integral

$$I_2(\cos\theta) = \frac{1}{\cos^2 2\theta}\left[\frac{4}{\pi(1+\sin 2\theta)}\,\mathrm{K}\left(\frac{1-\sin 2\theta}{1+\sin 2\theta}\right)-1\right]. \tag{A.68}$$

A.4.4 Integrals in the 3D case

We will consider system with a cubic lattice $Z=6$ with the lattice spacing $a=1$. In this case the γ-factor becomes

$$\gamma_{\vec{k}} = \frac{1}{Z}\sum_j e^{i\vec{k}\cdot\vec{r}_j} = \frac{2}{Z}\sum_{i=x,y,z}\cos k_i r_i = \frac{\cos k_x r_x + \cos k_z r_z + \cos k_z r_z}{3}. \tag{A.69}$$

Applying the integral transformation to the sum in Eq. (A.23) we get

$$I(r) = \frac{1}{N}\sum_{\vec{k}} \frac{e^{i\vec{k}\cdot\vec{r}}}{1+b\gamma_{\vec{k}}} = \frac{1}{4\pi^2}\int \frac{e^{i\vec{k}\cdot\vec{r}}}{1+b\gamma_{\vec{k}}}\,d\vec{k}, \tag{A.70}$$

where $\vec{k}$ is a 3-vector defined in the cube $k_{i=x,y,z}\in[-\pi,\pi]$ and the parameter $b=\cos 2\theta$ in our model. The leading contribution to the integral is defined by maximal value of the integrand, where the denominator is minimal for the $\vec{k}$ coinciding with the antiferromagnetic wave vector $\vec{Q} = (\pi, \pi, \pi)$. The parameter $\gamma_{\vec{k}}$ can be approximated at $\vec{k} \to \vec{Q} + \vec{k}$ as

$$\gamma_{\vec{k}} \approx -1 + \frac{\vec{k}^2}{6} + \dots \tag{A.71}$$

Therefore the leading contribution in the integral in Eq. (A.70) is given by

$$I \approx e^{i\vec{Q}\vec{r}} \frac{1}{(2\pi)^3} \int \frac{e^{i\vec{k}\vec{r}}}{1 - b + b\vec{k}^2/6} \, d\vec{k} = (-1)^R I', \tag{A.72}$$

where the distance $R = x + y + z$ describes the spatial alternating pattern and the integral I' corresponds to the magnitude

$$I' = \frac{1}{(2\pi)^3} \int \frac{e^{i\vec{k}\cdot\vec{r}}}{1 - b + \frac{b}{6}\vec{k}^2} \, d\vec{k}. \tag{A.73}$$

The leading contribution in this integral comes from the integrand at the vanishing $\vec{k}$, thus we can extend the cubic domain of integration to a sphere with large radius. This procedure allows to simplify the integral in the spherical coordinate system parameterized by angles θ and ϕ, and radial coordinate k, which can be chosen so that the $\vec{r}$-vector is parallel to the z-axis. In this case we get the following transformation relations

$$\vec{k}^2 = k^2, \qquad\qquad \vec{k} \cdot \vec{r} = \cos\theta, \tag{A.74}$$

$$d\vec{k} = k^2 \sin\theta \; dk \; d\theta \; d\phi. \tag{A.75}$$

Extending the integration domain to all space the integral in Eq. (A.73) becomes

$$I' = \frac{1}{(2\pi)^3} \int_0^\infty dk \int_0^\pi d\theta \int_0^{2\pi} d\phi \frac{k^2}{A + Bk^2} \cos(kr\cos\theta)\sin\theta, \tag{A.76}$$

where the coefficients A and B are

$$A = 1 - b, \qquad\qquad B = \frac{b}{6}. \tag{A.77}$$

Since the integrand in Eq. (A.76) does not depend on ϕ, the integration over this azimuthal angle results in the factor 2π only. Using the standard substitution for the trigonometric integrals

$$t = \cos\theta, \qquad\qquad dt = -\sin\theta \; d\theta, \tag{A.78}$$

we can perform the integration over the polar angle

$$\int_0^\pi \cos(kr\cos\theta)\sin\theta \, d\theta = -\int_{-1}^1 \cos(krt)\, dt = 2\frac{\sin(kr)}{kr}, \tag{A.79}$$

that gives

$$I' = \frac{1}{2\pi^2} \int_0^\infty \frac{k\, \sin(kr)}{A + Bk^2}\, dk. \tag{A.80}$$

Using the table integral [107]

$$\int_0^\infty \frac{x\, \sin(ax)}{1 + bx^2}\, dx = \frac{\pi}{2b} e^{-a/\sqrt{b}}, \tag{A.81}$$

the integral I' becomes

$$I' = \frac{1}{4\pi} \frac{e^{-r\sqrt{A/B}}}{Br} = \frac{3}{2\pi} \frac{e^{-r\sqrt{6(1/b-1)}}}{br} \tag{A.82}$$

by substituting the explicit form of the coefficients A and B given in Eq. (A.77). Therefore in the case of the cubic lattice the sum in Eq. (A.70) is

$$I = \frac{1}{N} \sum_{\vec{k}} \frac{e^{i\vec{k}\cdot\vec{r}}}{1 + b\gamma_{\vec{k}}} \approx (-1)^R \frac{3}{2\pi b} \frac{e^{-r\sqrt{6\frac{1-b}{b}}}}{r}, \tag{A.83}$$

where the distance $R = x + y + z$ describes the alternating pattern. The argument of the exponential function can be expressed in terms of the characteristic decay scale d which is given as

$$d = \sqrt{\frac{b}{6(b-1)}} = \sqrt{\frac{\cos 2\theta}{12 \sin^2 \theta}} \tag{A.84}$$

for the used parameter $b = \cos 2\theta$.

Furthermore we can also consider the following sum

$$I_1(r) = \frac{1}{N} \sum_{\vec{k}} \frac{\gamma_{\vec{k}}}{1 + b\gamma_{\vec{k}}} e^{i\vec{k}\cdot\vec{r}} = \frac{1}{b} \left(\frac{1}{N} \sum_{\vec{k}} e^{i\vec{k}\cdot\vec{r}} - \frac{1}{N} \sum_{\vec{k}} \frac{e^{i\vec{k}\cdot\vec{r}}}{1 + b\gamma_{\vec{k}}} \right), \tag{A.85}$$

where the last term corresponds to the calculated integral $I(r)$ in Eq. (A.83), while the first term becomes

$$\frac{1}{N} \sum_{\vec{k}} e^{i\vec{k}\cdot\vec{r}} = \delta_{r,0}. \tag{A.86}$$

Therefore the integral in Eq. (A.85) can be expressed as

$$I_1(r) = \frac{1}{N} \sum_{\vec{k}} \frac{\gamma_{\vec{k}}}{1 + b\gamma_{\vec{k}}} e^{i\vec{k}\cdot\vec{r}} = \frac{1}{b} \big(\delta_{r,0} - I(r) \big). \tag{A.87}$$

It is necessary to note that the analytical result in Eq. (A.83) gives a very good agreement with results of numerical integration only for large distances r. However, for small distance this is a bit rough analytical approximation because of weak convergence of the integrand in the case of 3D system. In comparison with the numerical calculations of the integral for the typical bulk parameters, $S = 1/2$ and $B = 0.4J$, the approximated analytical expression in Eq. (A.83) gives a ratio error ε about 10% for the two nearby sites around the impurity and about 1.5–2% for larger distances r.

If we compare the expressions in Eqs. (A.40) and (A.84) for the characteristic decay scale obtained in the case of the square and cubic lattices, we can see that in general case the decay scale d can be written down as

$$d = \sqrt{\frac{b}{Z(b-1)}}. \tag{A.88}$$

Thus this is very sensitive to the exact value of the coefficient b which is prefactor of $\gamma_{\vec{k}}$ in the summand denominator in Eq. (A.23).

Appendix B

Properties of Bessel function

B.1 Asymptotic and recurrent relations

For non-negative order $\alpha > 0$ Bessel function has the following asymptotic forms

$$J_\alpha(x) \sim \frac{1}{\Gamma(\alpha+1)}\left(\frac{x}{2}\right)^\alpha \qquad \text{for} \quad 0 < x \ll \sqrt{\alpha+1}, \tag{B.1}$$

$$J_\alpha(x) \sim \sqrt{\frac{2}{\pi x}}\cos\left(x - \frac{\alpha\pi}{2} - \frac{\pi}{4}\right) \qquad \text{for} \quad x \gg |\alpha^2 - 1/4|, \tag{B.2}$$

where $\Gamma(x)$ is the gamma function corresponding to factorial $\Gamma(n) = (n-1)!$ for positive integer arguments [107] which grows faster than an exponential function and is given by Stirling's formula $\Gamma(n+1) \sim \sqrt{2\pi n}\,(n/e)^n$ for $n \to \infty$.

The asymptotic expression for the Bessel function of large argument is

$$J_{-\nu}(-\nu\xi) \approx \frac{\xi^{-\nu}e^{-\nu\sqrt{1-\xi^2}}}{\sqrt{-2\pi\nu}\,\sqrt[4]{1-\xi^2}\left(1+\sqrt{1-\xi^2}\right)^{-\nu}}, \tag{B.3}$$

which is valid for $\nu \to \infty$ and $0 < \xi < 1$, see [65].

For integer order of the Bessel function the relation is valid

$$J_{-n}(x) = (-1)^n J_n(x). \tag{B.4}$$

The recurrent relations are given by

$$J_{\alpha-1}(x) + J_{\alpha+1}(x) = \frac{2\alpha}{x}J_\alpha(x), \tag{B.5}$$

$$J_{\alpha-1}(x) - J_{\alpha+1}(x) = 2\frac{dJ_\alpha}{dx}. \tag{B.6}$$

The integral representation of the Bessel function of integer order [65] is

$$J_n(x) = \frac{1}{2\pi}\int_{-\pi}^{\pi} e^{-i(nt - x\sin t)}\,dt. \tag{B.7}$$

The modified (hyperbolic) Bessel function of the second kind (or the Macdonald function) [175] is defined by

$$\mathrm{K}_\alpha(x) = \frac{\pi}{2}\frac{i^\alpha J_{-\alpha}(ix) - i^{-\alpha}J_\alpha(ix)}{\sin(\alpha\pi)} \tag{B.8}$$

or using the integral representation we get

$$\mathrm{K}_\alpha(x) = \int_0^\infty e^{-x\cosh t}\cosh(\alpha t)\,dt. \tag{B.9}$$

The asymptotic behavior of the modified Bessel function of the second kind for large argument is given [65] by

$$\begin{aligned}\mathrm{K}_\alpha(x) \approx& \sqrt{\frac{\pi}{2x}}e^{-x}\Bigg(1 + \frac{\mu-1}{8x} + \frac{(\mu-1)(\mu-9)}{2!(8x)^2} \\ &+ \frac{(\mu-1)(\mu-9)(\mu-25)}{3!(8x)^3} + \dots + \frac{\prod_{j=1}^n(\mu-(2j-1)^2)}{n!(8x)^n} + \dots\Bigg),\end{aligned} \tag{B.10}$$

where $\mu = 4\alpha^2$. This gives for the zeroth order of the modified Bessel function

$$\mathrm{K}_0(x) \approx \sqrt{\frac{\pi}{2x}}e^{-x}\left(1 - \frac{1}{8x} + \frac{9}{2!(8x)^2} + \dots + (-1)^n\frac{\prod_{j=1}^n(2j-1)^2}{n!(8x)^n} + \dots\right), \tag{B.11}$$

which leading term is

$$\mathrm{K}_0(x) \sim \sqrt{\frac{\pi}{2x}}e^{-x}, \qquad \text{for } x \to \infty. \tag{B.12}$$

B.2 Sums

Identities of the sums for the Bessel function products [108] are

$$\sum_{l=l_0}^\infty J_{l-\nu}^2(x) = -\frac{x}{2}J_{l_0-\nu}^2(x)\frac{\partial}{\partial\nu}\left[\frac{J_{l_0-\nu-1}(x)}{J_{l_0-\nu}(x)}\right] \tag{B.13}$$

and

$$\sum_{k=1}^\infty J_{k+\nu}(x)J_{k+\mu}(x) = \frac{x}{2}\frac{J_{1+\nu}(x)J_{1+\mu}(x)}{\nu-\mu}\left(\frac{J_\nu(x)}{J_{1+\nu}(x)} - \frac{J_\mu(x)}{J_{1+\mu}(x)}\right). \tag{B.14}$$

Neumann's addition theorem for Bessel functions [65] gives

$$J_\nu(x \pm y) = \sum_{k=-\infty}^\infty J_{\nu\mp k}(x)\;J_k(y). \tag{B.15}$$

In the special case of the parameters we get

$$\sum_{k=-\infty}^\infty J_k^2(x) = 1. \tag{B.16}$$

Graf's addition theorem [65] states that

$$\sum_{k=-\infty}^{\infty} J_{k+\nu}(u)\, J_k(v)\; \sin(k\phi) = J_\nu(w)\; \sin(\nu\chi), \tag{B.17}$$

$$\sum_{k=-\infty}^{\infty} J_{k+\nu}(u)\, J_k(v)\; \cos(k\phi) = J_\nu(w)\; \cos(\nu\chi), \tag{B.18}$$

where ν is an integer or zero, and the following relations are used

$$\begin{aligned} w &= \sqrt{u^2 + v^2 - 2uv\cos\phi}, \\ w\cos\chi &= u - v\cos\phi, \\ \sin\chi &= v\sin\phi. \end{aligned} \tag{B.19}$$

Bibliography

[1] S. Shinkevich, O. F. Syljuåsen, and S. Eggert, “Spin wave calculation of the magnetization around an impurity in Heisenberg antiferromagnets in a magnetic field,” in *Moscow International Symposium on Magnetism (MISM)*, (Moscow), p. 310, M. V. Lomonosov MSU, MAX Press, Aug 2011.

[2] S. Shinkevich and O. F. Syljuåsen, “Spectral signatures of magnetic Bloch oscillations in 1D ferromagnets,” in *The 19-th International Conference on Magnetism (ICM2012)*, (Busan, Korea), p. 207, Korean Physical Society and Korean Magnetics Society, Jul 2012.

[3] L. Kelvin, “I. Nineteenth century clouds over the dynamical theory of heat and light,” *Philosophical Magazine, Series 6*, vol. 2, no. 7, pp. 1–40, 1901.

[4] A. A. Michelson and E. W. Morley, “On the relative motion of the Earth and the luminiferous ether,” *American Journal of Science, Series 3*, vol. 34, pp. 333–345, Nov 1887.

[5] G. Kirchhoff, “Ueber das verhältniss zwischen dem emissionsvermögen und dem absorptionsvermögen der körper für wärme und licht,” *Annalen der Physik und Chemie*, vol. 185, no. 2, pp. 275–301, 1860.

[6] P. A. Brockhaus and I. A. Efron, *Brockhaus and Efron Encyclopedic Dictionary*, vol. VIII. St. Petersburg: Semenovsk’s Typolithography, 1892.

[7] M. Planck, “Entropie und temperatur strahlender wärme,” *Annalen der Physik*, vol. 306, pp. 719–737, Apr 1900.

[8] M. Planck, “Üeber das gesetz der energieverteilung im normalspectrum,” *Annalen der Physik*, vol. 309, pp. 553–563, Jan 1901.

[9] M. Born and P. Jordan, “Zur quantenmechanik,” *Zeitschrift für Physik*, vol. 34, pp. 858–888, Sep 1925.

[10] E. Schrödinger, “Quantisierung als eigenwertproblem,” *Annalen der Physik*, vol. 384, pp. 361–376, Jan 1926.

[11] P. Drude, “Zur elektronentheorie der metalle,” *Annalen der Physik*, vol. 306, no. 3, pp. 566–613, 1900.

[12] P. Drude, “Zur elektronentheorie der metalle; ii. Teil. Galvanomagnetische und thermomagnetische effecte,” *Annalen der Physik*, vol. 308, no. 11, pp. 369–402, 1900.

[13] A. Sommerfeld, “Zur elektronentheorie der metalle auf grund der Fermischen statistik,” *Zeitschrift für Physik*, vol. 47, pp. 1–32, Jan 1928.

[14] E. Fermi, “Sulla quantizzazione del gas perfetto monoatomico,” *Rendiconti Lincei*, vol. 3, pp. 145–149, 1926.

[15] P. A. M. Dirac, “On the theory of quantum mechanics,” *Proceedings of the Royal Society of London. Series A*, vol. 112, pp. 661–677, Oct 1926.

[16] W. Lenz, “Beitrag zum verständnis der magnetischen eigenschaften in festen körpern,” *Physikalische Zeitschrift*, vol. 21, pp. 613–615, 1920.

[17] E. Ising, “Beitrag zur theorie des ferromagnetismus,” *Zeitschrift für Physik*, vol. 31, pp. 253–258, Feb 1925.

[18] M. Niss, “History of the Lenz-Ising model 1920-1950: From ferromagnetic to cooperative phenomena,” *Archive for History of Exact Sciences*, vol. 59, pp. 267–318, Mar 2005.

[19] W. Heisenberg, “Zur theorie des ferromagnetismus,” *Zeitschrift für Physik*, vol. 49, pp. 619–636, May 1928.

[20] W. Pauli, “Über den zusammenhang des abschlusses der elektronengruppen im atom mit der komplexstruktur der spektren,” *Zeitschrift für Physik*, vol. 31, pp. 765–783, Feb 1925.

[21] H. Bethe, “Zur theorie der metalle. I. Eigenwerte und eigenfunktionen der linearen atomkette,” *Zeitschrift für Physik*, vol. 71, pp. 205–226, Jun 1931.

[22] W. Nolting and A. Ramakanth, *Quantum Theory of Magnetism*. Singapore: Springer Berlin Heidelberg, 2009.

[23] M. R. Freeman and B. C. Choi, “Advances in magnetic microscopy,” *Science*, vol. 294, pp. 1484–1488, Nov 2001.

[24] F. J. Giessibl, “Advances in atomic force microscopy,” *Rev. Mod. Phys.*, vol. 75, pp. 949–983, Jul 2003.

[25] R. Erni, M. D. Rossell, C. Kisielowski, and U. Dahmen, “Atomic-resolution imaging with a sub-50-pm electron probe,” *Phys. Rev. Lett.*, vol. 102, p. 096101, Mar 2009.

[26] N. D. Browning, M. A. Bonds, G. H. Campbell, J. E. Evans, T. LaGrange, K. L. Jungjohann, D. J. Masiel, J. McKeown, S. Mehraeen, B. Reed, and M. Santala, “Recent developments in dynamic transmission electron microscopy,” *Current Opinion in Solid State and Materials Science*, vol. 16, pp. 23–30, Feb 2012.

[27] R. G. Wheeler, F. M. Reames, and E. J. Wachtel, “Status of experiments on far-infrared absorption spectroscopy in magnetic material,” *Journal of Applied Physics*, vol. 39, pp. 915–922, Feb 1968.

[28] D. Bloor and G. M. Copland, “Far infrared spectra of magnetic ions in crystals,” *Reports on Progress in Physics*, vol. 35, p. 1173, Sep 1972.

[29] A. V. Kimel, A. Kirilyuk, P. A. Usachev, R. V. Pisarev, A. M. Balbashov, and T. Rasing, “Ultrafast non-thermal control of magnetization by instantaneous photomagnetic pulses,” *Nature*, vol. 435, pp. 655–657, Jun 2005.

[30] A. Kirilyuk, A. V. Kimel, and T. Rasing, “Ultrafast optical manipulation of magnetic order,” *Rev. Mod. Phys.*, vol. 82, pp. 2731–2784, Sep 2010.

[31] Y. Au, M. Dvornik, T. Davison, E. Ahmad, P. S. Keatley, A. Vansteenkiste, B. Van Waeyenberge, and V. V. Kruglyak, “Direct excitation of propagating spin waves by focused ultrashort optical pulses,” *Phys. Rev. Lett.*, vol. 110, p. 097201, Feb 2013.

[32] S. Shinkevich and O. F. Syljuåsen, “Numerical simulations of laser-excited magnetic Bloch oscillations,” *Phys. Rev. B*, vol. 87, p. 060401, Feb 2013.

[33] I. A. Zaliznyak and S.-H. Lee, *Modern Techniques for Characterizing Magnetic Materials*, ch. Magnetic Neutron Scattering, pp. 3–64. Springer, Apr 2005.

[34] L. Abelmann, “Magnetic force microscopy,” in *Encyclopedia of Spectroscopy and Spectrometry* (J. Lindon, ed.), pp. 1415–1425, Oxford: Academic Press, 2nd ed., Feb 2010.

[35] R. Wiesendanger, “Spin mapping at the nanoscale and atomic scale,” *Rev. Mod. Phys.*, vol. 81, pp. 1495–1550, Nov 2009.

[36] F. Bloch, “Über die quantenmechanik der elektronen in kristallgittern,” *Zeitschrift fur Physik*, vol. 52, pp. 555–600, Jul 1929.

[37] C. Zener, “A theory of the electrical breakdown of solid dielectrics,” *Proceedings of the Royal Society of London. Series A*, vol. 145, pp. 523–529, Jul 1934.

[38] E. E. Mendez, F. Agulló-Rueda, and J. M. Hong, “Stark localization in GaAs-GaAlAs superlattices under an electric field,” *Phys. Rev. Lett.*, vol. 60, pp. 2426–2429, Jun 1988.

[39] L. Esaki and R. Tsu, “Superlattice and negative differential conductivity in semiconductors,” *IBM Journal of Research and Development*, vol. 14, pp. 61–65, Jan 1970.

[40] M. Ben Dahan, E. Peik, J. Reichel, Y. Castin, and C. Salomon, “Bloch oscillations of atoms in an optical potential,” *Phys. Rev. Lett.*, vol. 76, pp. 4508–4511, Jun 1996.

[41] S. R. Wilkinson, C. F. Bharucha, K. W. Madison, Q. Niu, and M. G. Raizen, “Observation of atomic Wannier-Stark ladders in an accelerating optical potential,” *Phys. Rev. Lett.*, vol. 76, pp. 4512–4515, Jun 1996.

[42] B. P. Anderson and M. A. Kasevich, “Macroscopic quantum interference from atomic tunnel arrays,” *Science*, vol. 282, pp. 1686–1689, Nov 1998.

[43] O. Morsch, J. H. Müller, M. Cristiani, D. Ciampini, and E. Arimondo, “Bloch oscillations and mean-field effects of Bose-Einstein condensates in 1D optical lattices,” *Phys. Rev. Lett.*, vol. 87, p. 140402, Sep 2001.

[44] G. Monsivais, M. del Castillo-Mussot, and F. Claro, “Stark-ladder resonances in the propagation of electromagnetic waves,” *Phys. Rev. Lett.*, vol. 64, pp. 1433–1436, Mar 1990.

[45] A. Kavokin, G. Malpuech, A. Di Carlo, P. Lugli, and F. Rossi, “Photonic Bloch oscillations in laterally confined Bragg mirrors,” *Phys. Rev. B*, vol. 61, pp. 4413–4416, Feb 2000.

[46] G. Malpuech, A. Kavokin, G. Panzarini, and A. Di Carlo, “Theory of photon Bloch oscillations in photonic crystals,” *Phys. Rev. B*, vol. 63, p. 035108, Jan 2001.

[47] R. Sapienza, P. Costantino, D. Wiersma, M. Ghulinyan, C. J. Oton, and L. Pavesi, “Optical analogue of electronic Bloch oscillations,” *Phys. Rev. Lett.*, vol. 91, p. 263902, Dec 2003.

[48] H. Sanchis-Alepuz, Y. A. Kosevich, and J. Sánchez-Dehesa, “Acoustic analogue of electronic Bloch oscillations and resonant Zener tunneling in ultrasonic superlattices,” *Phys. Rev. Lett.*, vol. 98, p. 134301, Mar 2007.

[49] Z. He, S. Peng, F. Cai, M. Ke, and Z. Liu, “Acoustic Bloch oscillations in a two-dimensional phononic crystal,” *Phys. Rev. E*, vol. 76, p. 056605, Nov 2007.

[50] M. M. de Lima, Y. A. Kosevich, P. V. Santos, and A. Cantarero, “Surface acoustic Bloch oscillations, the Wannier-Stark ladder, and Landau-Zener tunneling in a solid,” *Phys. Rev. Lett.*, vol. 104, p. 165502, Apr 2010.

[51] J. Kyriakidis and D. Loss, “Bloch oscillations of magnetic solitons in anisotropic spin-$\frac{1}{2}$ chains,” *Phys. Rev. B*, vol. 58, pp. 5568–5583, Sep 1998.

[52] A. M. Kosevich, “Bloch oscillations of magnetic solitons as an example of dynamical localization of quasiparticles in a uniform external field (Review),” *Low Temperature Physics*, vol. 27, pp. 513–541, Jul 2001.

[53] L. D. Landau and E. M. Lifshits, *Short Course of Theoretical Physics: Mechanics. Electrodynamics*, vol. 1. Moscow: Nauka, 1969.

[54] J. Callaway, *Quantum Theory of the Solid State*. Academic Press, 2nd ed., Mar 1991.

[55] V. Grecchi and A. Sacchetti, “Acceleration theorem for Bloch oscillators,” *Phys. Rev. B*, vol. 63, p. 212303, May 2001.

[56] J. C. Slater and G. F. Koster, “Simplified LCAO method for the periodic potential problem,” *Phys. Rev.*, vol. 94, pp. 1498–1524, Jun 1954.

[57] I. M. Lifshits, M. Y. Azbel, and M. I. Kaganov, *Electron theory of metals*. Special research report, New York: Consultants Bureau, 1973.

[58] C. Kittel, *Introduction to Solid State Physics*. New York: Wiley, 8th ed., Nov 2004.

[59] H. Jones and C. Zener, “A general proof of certain fundamental equations in the theory of metallic conduction,” *Proceedings of the Royal Society of London. Series A*, vol. 144, no. 851, pp. 101–117, 1934.

[60] M. Holthaus, "Bloch oscillations and Zener breakdown in an optical lattice," *J. Opt. B: Quantum Semiclass. Opt.*, vol. 2, pp. 589–604, Oct 2000.

[61] T. Hartmann, F. Keck, H. J. Korsch, and S. Mossmann, "Dynamics of Bloch oscillations," *New Journal of Physics*, vol. 6, no. 1, p. 2, 2004.

[62] G. H. Wannier, "Wave functions and effective hamiltonian for Bloch electrons in an electric field," *Phys. Rev.*, vol. 117, pp. 432–439, Jan 1960.

[63] V. Grecchi and A. Sacchetti, "Wannier–Bloch oscillators," *Communications in Mathematical Physics*, vol. 197, pp. 553–569, Oct 1998.

[64] S. Flügge, *Practical Quantum Mechanics: I*, vol. 1 of *Grundlehren Der Mathematischen Wissenschaften*. Berlin - New York: Springer-Verlag GmbH, 1st ed., Sep 1971.

[65] M. Abramowitz and I. A. Stegun, *Handbook of Mathematical Functions with Formulas, Graphs, and Mathematical Tables*. New York: Dover, 9th Dover printing, 10th GPO printing ed., 1964.

[66] F. W. J. Olver, *Asymptotics and Special Functions*. No. 11 in Computer science and applied mathematics: A.P.I.C. Studies in Data Processing, New York: Academic Press, 1974.

[67] N. W. Ashcroft and N. D. Mermin, *Solid State Physics*. Philadelphia: Saunders College, 1st ed., Jan 1976.

[68] E. Sondheimer, "The mean free path of electrons in metals," *Advances in Physics*, vol. 1, pp. 1–42, Jan 1952.

[69] E. E. Mendez and G. Bastard, "Wannier-Stark ladders and Bloch oscillations in superlattices," *Physics Today*, vol. 46, pp. 34–42, Jun 1993.

[70] D. R. Lide, ed., *CRC Handbook of Chemistry and Physics : a ready-reference book of chemical and physical data*. Boca Raton, Fla: CRC Press, 84th ed., Jun 2003.

[71] E. F. Schubert, *Quantum Mechanics Applied to Semiconductor Devices*. Rensselaer Polytechnic Institute, New York, 1st ed., 2004.

[72] H. T. Grahn, ed., *Semiconductor Superlattices: Growth and Electronic Properties*. Singapore: World Scientific Publishing Co. Inc., Aug 1995.

[73] J. Feldmann, K. Leo, J. Shah, D. A. B. Miller, J. E. Cunningham, T. Meier, G. von Plessen, A. Schulze, P. Thomas, and S. Schmitt-Rink, "Optical investigation of Bloch oscillations in a semiconductor superlattice," *Phys. Rev. B*, vol. 46, pp. 7252–7255, Sep 1992.

[74] C. Waschke, H. G. Roskos, R. Schwedler, K. Leo, H. Kurz, and K. Köhler, "Coherent submillimeter-wave emission from Bloch oscillations in a semiconductor superlattice," *Phys. Rev. Lett.*, vol. 70, pp. 3319–3322, May 1993.

[75] K. Leo, "Interband optical investigation of Bloch oscillations in semiconductor superlattices," *Semiconductor Science and Technology*, vol. 13, p. 249, Mar 1998.

[76] M. Kenzelmann, C. D. Batista, Y. Chen, C. Broholm, D. H. Reich, S. Park, and Y. Qiu, "$S = \frac{1}{2}$ chain in a staggered field: High-energy bound-spinon state and the effects of a discrete lattice," *Phys. Rev. B*, vol. 71, p. 094411, Mar 2005.

[77] I. E. Dzialoshinskii, "Thermodynamic theory of weak ferromagnetism in antiferromagnetic substances," *Sov. Phys. JETP*, vol. 5, no. 6, pp. 1259–1272, 1957.

[78] T. Moriya, "Anisotropic superexchange interaction and weak ferromagnetism," *Phys. Rev.*, vol. 120, pp. 91–98, Oct 1960.

[79] J. Villain, "Propagative spin relaxation in the Ising-like antiferromagnetic linear chain," *Physica B+C*, vol. 79, pp. 1–12, Jan 1975.

[80] H. Yoshizawa, K. Hirakawa, S. K. Satija, and G. Shirane, "Dynamical correlation functions in a one-dimensional Ising-like antiferromagnetic $\mathrm{CsCoCl_3}$: A neutron scattering study," *Phys. Rev. B*, vol. 23, pp. 2298–2307, Mar 1981.

[81] S. E. Nagler, W. J. L. Buyers, R. L. Armstrong, and B. Briat, "Propagating domain walls in $\mathrm{CsCoBr_3}$," *Phys. Rev. Lett.*, vol. 49, pp. 590–592, Aug 1982.

[82] S. E. Nagler, W. J. L. Buyers, R. L. Armstrong, and B. Briat, "Observation of the villain mode in $\mathrm{CsCoBr_3}$," *Journal of Magnetism and Magnetic Materials*, vol. 31, pp. 1213–1214, Feb 1983.

[83] C. Heid, H. Weitzel, W. Gonschorek, J. Norwig, H. Fuess, P. Burlet, M. Bonnet, and T. Vogt, "Magnetic phase diagram of $\mathrm{CoNb_2O_6}$: A neutron diffraction study," *Journal of Magnetism and Magnetic Materials*, vol. 151, pp. 123–131, Nov 1995.

[84] S. Kobayashi, S. Mitsuda, and K. Prokes, "Low-temperature magnetic phase transitions of the geometrically frustrated isosceles triangular Ising antiferromagnet $\mathrm{CoNb_2O_6}$," *Phys. Rev. B*, vol. 63, p. 024415, Dec 2000.

[85] G. Herzberg, *Atomic Spectra and Atomic Structure*. New York: Dover publication, 2nd ed., 1944.

[86] L. D. Landau and E. M. Lifshits, *Quantum Mechanics: Non-Relativistic Theory*, vol. 3 of *Course of Theoretical Physics*. Butterworth-Heinemann, 3rd ed., Jan 1981.

[87] S. Blundell, *Magnetism in Condensed Matter*. Oxford Master Series in Condensed Matter Physics, New York: Oxford University Press, 1st ed., Dec 2001.

[88] J. B. Torrance and M. Tinkham, "Excitation of multiple-magnon bound states in $\mathrm{CoCl_2{\cdot}2H_2O}$," *Phys. Rev.*, vol. 187, pp. 595–606, Nov 1969.

[89] G. M. Copland and P. M. Levy, "Direct exchange between d electrons," *Phys. Rev. B*, vol. 1, pp. 3043–3050, Apr 1970.

[90] W. J. L. Buyers, T. M. Holden, E. C. Svensson, R. A. Cowley, and M. T. Hutchings, "Excitations in KCoF_3. II. Theoretical," *J. Phys. C: Solid St. Phys.*, vol. 4, no. 14, pp. 2139–2159, 1971.

[91] S. E. Nagler, W. J. L. Buyers, R. L. Armstrong, and B. Briat, "Ising-like spin-½ quasi-one-dimensional antiferromagnets: Spin-wave response in $\mathrm{CsCo}X_3$ salts," *Phys. Rev. B*, vol. 27, pp. 1784–1799, Feb 1983.

[92] B. K. Vainshtein, "Elektronograficheskoe opredelenie struktury $\mathrm{CoCl}_2 \cdot 2\mathrm{H}_2\mathrm{O}$," *Dokl. Akad. Nauk. SSSR*, vol. 68, no. 2, pp. 301–304, 1949.

[93] B. Morosin and E. J. Graber, "A reinvestigation of the crystal structure of $\mathrm{CoCl}_2 \cdot 2\mathrm{H}_2\mathrm{O}$," *Acta Crystallographica*, vol. 16, pp. 1176–1178, Nov 1963.

[94] A. Narath, "Antiferromagnetism in $\mathrm{CoCl}_2 \cdot 2\mathrm{H}_2\mathrm{O}$. I. Magnetic structure," *Phys. Rev.*, vol. 136, pp. A766–A771, Nov 1964.

[95] B. Morosin, "Lattice parameters between 5° and 298°K and crystal structure at 5°K of cobalt chloride dihydrate," *The Journal of Chemical Physics*, vol. 44, pp. 252–257, Jan 1966.

[96] M. Date and M. Motokawa, "Spin-cluster resonance in the Ising spin system," *Journal of the Physical Society of Japan*, vol. 24, pp. 41–50, Jan 1968.

[97] T. Shinoda, H. Chihara, and S. Seki, "Heat capacity of $\mathrm{CoCl}_2 \cdot 2\mathrm{H}_2\mathrm{O}$ between 7 and 120° k and its anomaly associated with magnetic transition," *J. Phys. Soc. Japan*, vol. 19, pp. 1637–1648, Sep 1964.

[98] J. B. Torrance and M. Tinkham, "Far-infrared absorption in $\mathrm{CoCl}_2{\cdot}2\mathrm{H}_2\mathrm{O}$," *Journal of Applied Physics*, vol. 39, pp. 822–823, Feb 1968.

[99] J. B. Torrance and M. Tinkham, "Magnon bound states in anisotropic linear chains," *Phys. Rev.*, vol. 187, pp. 587–594, Nov 1969.

[100] H. C. Fogedby and H. H. Jensen, "Energy spectrum of the anisotropic magnetic chain," *Phys. Rev. B*, vol. 6, pp. 3444–3446, Nov 1972.

[101] H. C. Fogedby, "Magnetic excitation spectrum of $\mathrm{CoCl}_2 \cdot 2\mathrm{H}_2\mathrm{O}$," *Phys. Rev. B*, vol. 10, pp. 4000–4013, Nov 1974.

[102] H. J. Mikeska, S. Miyashita, and G. H. Ristow, "S=1/2 magnetic chains as domain wall systems," *Journal of Physics: Condensed Matter*, vol. 3, p. 2985, Apr 1991.

[103] R. Coldea, D. A. Tennant, E. M. Wheeler, E. Wawrzynska, D. Prabhakaran, M. Telling, K. Habicht, P. Smeibidl, and K. Kiefer, "Quantum criticality in an Ising chain: Experimental evidence for emergent E8 symmetry," *Science*, vol. 327, pp. 177–180, Jan 2010.

[104] J. K. Kjems, J. Als-Nielsen, and H. Fogedby, "Spin-wave dispersion in $\mathrm{CoCl}_2{\cdot}2\mathrm{D}_2\mathrm{O}$: A system of weakly coupled Ising chains," *Phys. Rev. B*, vol. 12, pp. 5190–5197, Dec 1975.

[105] N. B. Christensen, K. Lefmann, I. Johannsen, and O. Jørgensen, “Magnetic Bloch oscillations in the near-Ising antiferromagnet $CoCl_2{\cdot}2D_2O$,” *Physica B: Condensed Matter*, vol. 276–278, pp. 784–785, Mar 2000.

[106] W. Montfrooij, G. E. Granroth, D. G. Mandrus, and S. E. Nagler, “Spin dynamics of the quasi-one-dimensional ferromagnet $CoCl_2{\cdot}2D_2O$,” *Phys. Rev. B*, vol. 64, p. 134426, Sep 2001.

[107] I. Gradstein and I. Ryzhik, *Table of integrals, series, and products*. Academic Press, 4th ed., 1980.

[108] A. P. Prudnikov, Y. A. Brychkov, and O. I. Marichev, *Integrals and Series: Special Functions*, vol. 2 of *Integrals and Series*. New York: Gordon and Breach, 1990.

[109] S. Shinkevich and O. F. Syljuåsen, “Spectral signatures of magnetic Bloch oscillations in one-dimensional easy-axis ferromagnets,” *Phys. Rev. B*, vol. 85, p. 104408, Mar 2012.

[110] S. B. Rutkevich, “On the weak confinement of kinks in the one-dimensional quantum ferromagnet $CoNb_2O_6$,” *Journal of Statistical Mechanics: Theory and Experiment*, vol. 2010, no. 07, p. P07015, 2010.

[111] P. Anderson, *Concepts in Solids: Lectures on the Theory of Solids*. Advanced book classics series, World Scientific Publishing Company Inc., 1997.

[112] G. L. Squires, *Introduction to the Theory of Thermal Neutron Scattering*. Dover books on physics, Dover Publications Inc., reprint ed., Jun 1997.

[113] V. T. Vodnev, A. F. Naumovich, and N. F. Naumovich, *Basic mathematical formulas. Handbook.* Minsk: Vyshehjshaya Shkola, 2nd ed., 1988.

[114] D. N. Basov, R. D. Averitt, D. van der Marel, M. Dressel, and K. Haule, “Electrodynamics of correlated electron materials,” *Rev. Mod. Phys.*, vol. 83, pp. 471–541, Jun 2011.

[115] Y. R. Shen and N. Bloembergen, “Interaction between light waves and spin waves,” *Phys. Rev.*, vol. 143, pp. 372–384, Mar 1966.

[116] P. A. Fleury and R. Loudon, “Scattering of light by one- and two-magnon excitations,” *Phys. Rev.*, vol. 166, pp. 514–530, Feb 1968.

[117] K. A. Hay and J. B. Torrance, “Magnon-phonon interaction observed in far infrared studies of $FeCl_2{\cdot}2H_2O$ and $CoCl_2{\cdot}2H_2O$,” *Journal of Applied Physics*, vol. 40, pp. 999–1000, Mar 1969.

[118] D. F. Nicoli and M. Tinkham, “Far-infrared laser spectroscopy of the linear Ising system $\mathrm{CoCl_2 \cdot 2H_2O}$,” *Phys. Rev. B*, vol. 9, pp. 3126–3140, Apr 1974.

[119] C. A. Helms, J. F. Scott, and D. J. Toms, “Light scattering from phonons and magnons in $\mathrm{CoCl_2 \cdot 2H_2O}$,” *Journal of Raman Spectroscopy*, vol. 8, pp. 335–339, Dec 1979.

[120] E. Fermi, *Notes on Quantum Mechanics*. Chicago: University Of Chicago Press, 2nd ed., Jul 1995.

[121] D. J. Griffiths, *Introduction to Quantum Mechanics*. Addison-Wesley, 2nd ed., Apr 2004.

[122] D. Budker, D. F. Kimball, and D. P. DeMille, *Atomic physics: An exploration through problems and solutions*. New York: Oxford University Press, 2nd ed., Nov 2008.

[123] P. A. Franken, A. E. Hill, C. W. Peters, and G. Weinreich, "Generation of optical harmonics," *Phys. Rev. Lett.*, vol. 7, pp. 118–119, Aug 1961.

[124] S. E. Harris, M. K. Oshman, and R. L. Byer, "Observation of tunable optical parametric fluorescence," *Phys. Rev. Lett.*, vol. 18, pp. 732–734, May 1967.

[125] D. Klyshko, "Coherent photon decay in a nonlinear medium," *JETP Letters*, vol. 6, pp. 23–25, Jul 1967.

[126] D. A. Kleinman, "Theory of optical parametric noise," *Phys. Rev.*, vol. 174, pp. 1027–1041, Oct 1968.

[127] F. Duarte, ed., *Tunable Laser Applications*. Optical Science and Engineering, New York: CRC Press, 2nd ed., Aug 2008.

[128] M. D. Lukin, M. Fleischhauer, R. Cote, L. M. Duan, D. Jaksch, J. I. Cirac, and P. Zoller, "Dipole blockade and quantum information processing in mesoscopic atomic ensembles," *Phys. Rev. Lett.*, vol. 87, p. 037901, Jun 2001.

[129] E. Urban, T. A. Johnson, T. Henage, L. Isenhower, D. D. Yavuz, T. G. Walker, and M. Saffman, "Observation of Rydberg blockade between two atoms," *Nat. Phys.*, vol. 5, pp. 110–114, Feb 2009. 1745-2473.

[130] I. I. Rabi, S. Millman, P. Kusch, and J. R. Zacharias, "The molecular beam resonance method for measuring nuclear magnetic moments. the magnetic moments of ${}_3\mathrm{Li}^6$, ${}_3\mathrm{Li}^7$ and ${}_9\mathrm{F}^{19}$," *Phys. Rev.*, vol. 55, pp. 526–535, Mar 1939.

[131] J. E. Williams and M. J. Holland, "Preparing topological states of a Bose-Einstein condensate," *Nature*, vol. 401, pp. 568–572, Oct 1999.

[132] R. H. Dicke, "Coherence in spontaneous radiation processes," *Phys. Rev.*, vol. 93, pp. 99–110, Jan 1954.

[133] Y. O. Dudin, L. Li, F. Bariani, and A. Kuzmich, "Observation of coherent many-body Rabi oscillations," *Nat. Phys.*, vol. 1745-2481, Sep 2012.

[134] N. Jacobson, *Basic Algebra I*. Dover Books on Mathematics Series, New York: Dover Publications, 2nd ed., Jun 2009.

[135] E. Smith, "Isotropic X-Y chain in an inhomogeneous magnetic field," *Physica*, vol. 53, pp. 289–303, May 1971.

[136] A. M. Kosevich, V. V. Gann, A. I. Zhukov, and V. P. Voronov, “Magnetic soliton motion in a nonuniform magnetic field,” *JETP*, vol. 87, pp. 401–407, Aug 1998.

[137] I. M. Babich and A. M. Kosevich, “Relaxation of Bloch oscillations of a magnetic soliton in a nonuniform magnetic field,” *Low Temperature Physics*, vol. 27, pp. 35–39, Jan 2001.

[138] V. V. Gann and Y. A. Kosevich, “Bloch oscillations of spin waves in a nonuniform magnetic field,” *Low Temperature Physics*, vol. 36, pp. 722–727, Aug 2010.

[139] H.-B. Braun and D. Loss, “Chirality correlation of spin solitons: Bloch walls, spin-$1/2$ solitons and holes in a 2D antiferromagnetic background,” *Int. J. Mod. Phys. B*, vol. 10, pp. 219–234, Jan 1996.

[140] M. Kumada, E. I. Antokhin, Y. Iwashita, M. Aoki, and E. Sugiyama, “Super strong permanent dipole magnet,” *IEEE Transactions on Applied Superconductivity*, vol. 14, pp. 1287–1289, Jun 2004.

[141] M. Butler, V. Jaccarino, N. Kaplan, and H. J. Guggenheim, “Nuclear-magnetic-resonance study of impurity effects in a Heisenberg antiferromagnet,” *Phys. Rev. B*, vol. 1, pp. 3058–3083, Apr 1970.

[142] J. A. van Luijk, A. F. M. Arts, and H. W. de Wijn, “Local magnetizations in impure two-dimensional antiferromagnets,” *Phys. Rev. B*, vol. 21, pp. 1963–1993, Mar 1980.

[143] M. Takigawa, N. Motoyama, H. Eisaki, and S. Uchida, “Field-induced staggered magnetization near impurities in the $S = 1/2$ one-dimensional Heisenberg antiferromagnet $\mathrm{Sr_2CuO_3}$,” *Phys. Rev. B*, vol. 55, pp. 14129–14132, Jun 1997.

[144] Y. Martin and H. K. Wickramasinghe, “Magnetic imaging by "force microscopy" with 1000 Å resolution,” *Appl. Phys. Lett.*, vol. 50, pp. 1455–1457, Mar 1987.

[145] U. Hartmann, “Magnetic force microscopy,” *Annual Review of Materials Science*, vol. 29, pp. 53–87, Aug 1999.

[146] S. Heinze, M. Bode, A. Kubetzka, O. Pietzsch, X. Nie, S. Blügel, and R. Wiesendanger, “Real-space imaging of two-dimensional antiferromagnetism on the atomic scale,” *Science*, vol. 288, pp. 1805–1808, Jun 2000.

[147] W. A. Hofer and A. J. Fisher, “Determining surface magnetization and local magnetic moments with atomic scale resolution,” *Surface Science*, vol. 515, pp. L487–L492, Sep 2002.

[148] A. R. Smith, “Atomic-scale spin-polarized scanning tunneling microscopy and atomic force microscopy: A review,” *Journal of Scanning Probe Microscopy*, vol. 1, pp. 3–20, Jun 2006.

[149] J. Bednorz and K. Müller, “Possible high T_c superconductivity in the $\mathrm{BaLaCuO}$ system,” *Zeitschrift für Physik B Condensed Matter*, vol. 64, no. 2, pp. 189–193, 1986.

[150] Z. Kazei and I. Krynetskii, *Magnetic Properties of Non-Metallic Inorganic Compounds Based on Transition Elements: Perovskite-type layered cuprates (high-T(c) superconductors and related compounds)*, vol. 27 F2s of *Numerical Data and Functional Relationships in Science and Technology. Group III: Condensed Matter*. Berlin: Springer-Verlag, 2002 ed., Sep 2002.

[151] M. P. Marder, *Condensed Matter Physics*. New Jersey: John Wiley & Sons, 2nd ed., Nov 2010.

[152] J. Sólyom, *Fundamentals of the Physics of Solids: Normal, Broken-Symmetry, and Correlated Systems*, vol. 3 of *Theoretical Solid State Physics: Interaction Among Electrons*. Berlin: Springer, Dec 2010.

[153] E. Manousakis, "The spin-½ Heisenberg antiferromagnet on a square lattice and its application to the cuprous oxides," *Rev. Mod. Phys.*, vol. 63, pp. 1–62, Jan 1991.

[154] M. A. Kastner, R. J. Birgeneau, G. Shirane, and Y. Endoh, "Magnetic, transport, and optical properties of monolayer copper oxides," *Rev. Mod. Phys.*, vol. 70, pp. 897–928, Jul 1998.

[155] F. D. M. Haldane, "Continuum dynamics of the 1-D Heisenberg antiferromagnet: Identification with the O(3) nonlinear sigma model," *Phys. Lett. A*, vol. 93, pp. 464–468, Feb 1983.

[156] F. D. M. Haldane, "Nonlinear field theory of large-spin Heisenberg antiferromagnets: Semiclassically quantized solitons of the one-dimensional easy-axis Néel state," *Phys. Rev. Lett.*, vol. 50, pp. 1153–1156, Apr 1983.

[157] S. Chakravarty, B. I. Halperin, and D. R. Nelson, "Two-dimensional quantum Heisenberg antiferromagnet at low temperatures," *Phys. Rev. B*, vol. 39, pp. 2344–2371, Feb 1989.

[158] J. Dai and W.-M. Zhang, "Quantum nonlinear σ model for arbitrary spin Heisenberg antiferromagnets," *Phys. Rev. Lett.*, vol. 95, p. 167205, Oct 2005.

[159] S. Eggert, O. F. Syljuåsen, F. Anfuso, and M. Andres, "Universal alternating order around impurities in antiferromagnets," *Phys. Rev. Lett.*, vol. 99, p. 097204, Aug 2007.

[160] P. W. Anderson, "An approximate quantum theory of the antiferromagnetic ground state," *Phys. Rev.*, vol. 86, pp. 694–701, Jun 1952.

[161] R. Kubo, "The spin-wave theory of antiferromagnetics," *Phys. Rev.*, vol. 87, pp. 568–580, Aug 1952.

[162] T. Holstein and H. Primakoff, "Field dependence of the intrinsic domain magnetization of a ferromagnet," *Phys. Rev.*, vol. 58, pp. 1098–1113, Dec 1940.

[163] F. J. Dyson, "General theory of spin-wave interactions," *Phys. Rev.*, vol. 102, pp. 1217–1230, Jun 1956.

[164] S. V. Maleev, "Scattering of slow neutrons in ferromagnets," *Sov. Phys. JETP*, vol. 6, no. 4, pp. 776–784, 1958.

[165] A. Auerbach, *Interacting Electrons and Quantum Magnetism*. Graduate Texts in Contemporary Physics Series, New York: Springer, Sep 1994.

[166] G. D. Mahan, *Condensed Matter in a Nutshell*. In a Nutshell, New Jersey: Princeton University Press, Oct 2010.

[167] M. Andres, *Korrelationen in niedrigdimensionalen Spinsystemen: Induzierte magnetische Ordnung und exakte Grundzustände*. Dissertation, University of Kaiserslautern, Feb 2008.

[168] M. Mourigal, M. E. Zhitomirsky, and A. L. Chernyshev, "Field-induced decay dynamics in square-lattice antiferromagnets," *Phys. Rev. B*, vol. 82, p. 144402, Oct 2010.

[169] N. Bulut, D. Hone, D. J. Scalapino, and E. Y. Loh, "Static vacancies on a 2D Heisenberg spin-1/2 antiferromagnet," *Phys. Rev. Lett.*, vol. 62, pp. 2192–2195, May 1989.

[170] M. E. Zhitomirsky and A. L. Chernyshev, "Instability of antiferromagnetic magnons in strong fields," *Phys. Rev. Lett.*, vol. 82, pp. 4536–4539, May 1999.

[171] N. N. Bogoliubov, "On the theory of superfluidity," *J. Phys. (USSR)*, vol. 11, pp. 23–32, 1947.

[172] M. E. Zhitomirsky and T. Nikuni, "Magnetization curve of a square-lattice Heisenberg antiferromagnet," *Phys. Rev. B*, vol. 57, pp. 5013–5016, Mar 1998.

[173] S. Shinkevich, O. F. Syljuåsen, and S. Eggert, "Spin-wave calculation of the field-dependent magnetization pattern around an impurity in Heisenberg antiferromagnets," *Phys. Rev. B*, vol. 83, p. 054423, Feb 2011.

[174] G. E. Castilla and S. Chakravarty, "Spin-wave expansion of the staggered magnetization of a square-lattice Heisenberg antiferromagnet at $T = 0$," *Phys. Rev. B*, vol. 43, pp. 13687–13690, Jun 1991.

[175] G. N. Watson, *A Treatise on the Theory of Bessel Functions*. Cambridge Mathematical Library, Cambridge: Cambridge University Press, 2nd ed., Aug 1995.

[176] R. Kubo, "Statistical-mechanical theory of irreversible processes. I. General theory and simple applications to magnetic and conduction problems," *J. Phys. Soc. Jpn.*, vol. 12, pp. 570–586, Jun 1957.

[177] D. N. Zubarev, *Nonequilibrium Statistical Thermodynamics*. Studies in Soviet science: Physical sciences, Consultants Bureau, Oct 1974.

[178] A. Fetter and J. Walecka, *Quantum Theory of Many-particle Systems*. Dover Books on Physics, Dover Publications, dover ed., May 2003.

[179] O. F. Syljuåsen, "Linear spin wave treatment of an impurity in Heisenberg antiferromagnet in a magnetic field." Nov 2006.

[180] J. R. Schrieffer and P. A. Wolff, "Relation between the Anderson and Kondo Hamiltonians," *Phys. Rev.*, vol. 149, pp. 491–492, Sep 1966.

[181] S. Bravyi, D. P. DiVincenzo, and D. Loss, "Schrieffer-Wolff transformation for quantum many-body systems," *Annals of Physics*, vol. 326, no. 10, pp. 2793–2826, 2011.

[182] H. B. Dwight, *Tables of Integrals and Other Mathematical Data*. New York: The Macmillan Company, 4th ed., Dec 1966.

[183] Wolfram Research Inc., "The Wolfram functions site," *http://functions.wolfram.com/*, 2013.

Part II

Papers

Contribution

My contributions to the papers are the following.

- In the first article I performed all the analytical and numerical calculations. I considered and analysed different parameter regimes in order to observe signatures of magnetic BOs. I prepared all the graphs and collaborated in writing and improving the article.
- I did all the analytical calculations and numerical computations in the Article II. I investigated different parameter regimes in order to excite the magnetic BOs and found optimal parameters to use in potential experiments. I participated in the writing of the article and approved the final version of the article.
- I did all the analytical calculations in the Article III and analysed the results by comparing them to numerical data obtained through numerical spin-wave calculations and quantum Monte-Carlo simulations by Prof. Olav F. Syljuåsen. I made all inputs to the graphs in the article involving the analytical results. I participated in the writing of the article by making comments on the structure, checking equations and pointed out ways to improve the writing.

PHYSICAL REVIEW B **85**, 104408 (2012)

Spectral signatures of magnetic Bloch oscillations in one-dimensional easy-axis ferromagnets

Sergey Shinkevich and Olav F. Syljuåsen
Department of Physics, University of Oslo, P. O. Box 1048 Blindern, N-0316 Oslo, Norway

(Received 28 December 2011; revised manuscript received 17 February 2012; published 13 March 2012)

Domain walls in a one-dimensional gapped easy-axis ferromagnet can exhibit Bloch oscillations in an applied magnetic field. We investigate how exchange couplings modify this behavior within an approximation based on noninteracting domain-wall bound states. In particular, we obtain analytical results for the spectrum and the dynamic structure factor, and show where in momentum space to expect equidistant energy levels, the Wannier-Zeeman ladder, which is the spectral signature of magnetic Bloch oscillations. We compare our results to previous calculations employing a single domain-wall approximation, and make predictions relevant for the material $CoCl_2 \cdot 2H_2O$.

DOI: 10.1103/PhysRevB.85.104408 PACS number(s): 75.40.Gb, 75.60.Ch, 75.10.Jm

I. INTRODUCTION

Quantum mechanics predicts that a particle in a periodic potential will undergo oscillatory motion in response to a *constant* force. This rather counterintuitive phenomenon, known as Bloch oscillations (BO), was controversial for a long time, but has now been experimentally demonstrated in very clean semiconductor superlattices[1] and Bose-Einstein condensates.[2]

Can Bloch oscillations also exist in magnetic systems? Kyriakidis and Loss[3] discussed this possibility. They considered a system where the particle is a propagating domain-wall excitation in an easy-axis one-dimensional ferromagnet, and concluded that magnetic BO should indeed exist. In particular, the blue crystalline material $CoCl_2 \cdot 2H_2O$ was identified as a promising candidate for observing magnetic BO. Searches using neutron scattering were performed,[4,5] but did not find evidence of BO.

Another very similar system where one can expect BO of magnetic domain walls is the Ising model in a magnetic field having both longitudinal and transversal components.[6] Such a model is believed to be realized in $CoNb_2O_6$ where indeed an intriguing frequency spectrum has recently been observed.[7] However, in the region of momentum space where one expects to find the quantum-mechanical spectral signature of BO—a spectrum with equidistant energy levels, the so-called Wannier-Zeeman ladder (WZL)—the spectral weight in the experiment in Ref. 7 is dominated by a strong feature attributed to additional couplings in the Hamiltonian, a "kinetic bound state," stabilized by next-nearest-neighbor interactions.[7,8] Thus it appears that additional terms in the Hamiltonian prevent BO in $CoNb_2O_6$.

This might also be the case in $CoCl_2 \cdot 2H_2O$ where the kinetic bound state will be generated by a nearest-neighbor spin flip exchange coupling that, indeed, is present in $CoCl_2 \cdot 2H_2O$,[4] but neglected in Ref. 3. It is the main goal of this article to investigate its influence on the WZL in $CoCl_2 \cdot 2H_2O$.

Our results show that the WZL is present in certain regions of momentum space also in the presence of the exchange couplings. However, the neutron scattering spectral weight of the WZL in $CoCl_2 \cdot 2H_2O$ is less than 1% of the total spectral weight at these momenta, thus making it difficult to observe the WZL at zero temperature in inelastic neutron scattering experiments.

At finite temperatures, the neutron scattering signatures of the WZL are more pronounced. We find that a relatively high temperature is favorable as the number of domain walls performing BO are exponentially suppressed with temperature below the largest ferromagnetic coupling. Unfortunately, a high temperature leads also to collisions of domain walls that destroy BO. For $CoCl_2 \cdot 2H_2O$, we find that this collision rate is determined by the velocity of the kinetic bound state and the distance between domain-walls bound states that gets smaller as the temperature increases. A way to alleviate this is to increase the applied magnetic field that leads to a reduced collision rate. However, a large magnetic field makes the intrinsic signature of BO weaker as it reduces the BO amplitude. In searching for a compromise, we find significant neutron scattering signatures of BO at finite frequencies in $CoCl_2 \cdot 2H_2O$ at the temperature $T = J_z/2$, magnetic field $h_z = 0.2J_z$, and momentum transfer $q = \pi/2$ where the first Bloch mode at $\omega_B = 2h_z$ carries about 12% of the total spectral weight.

While we focus on the material parameters for $CoCl_2 \cdot 2H_2O$, our results are analytic and can, with minor efforts, also be used for aiding searches for magnetic BO in other similar materials.

II. HAMILTONIAN

We start with the spin-$1/2$ XYZ ferromagnetic Hamiltonian for a chain with nearest-neighbor coupling in a magnetic field,

$$H = -\sum_i \left(J_x S_i^x S_{i+1}^x + J_y S_i^y S_{i+1}^y + J_z S_i^z S_{i+1}^z + h_z S_i^z \right), \quad (1)$$

which can be written as

$$H = H_z + H_a + H_\perp, \quad (2)$$

where

$$H_z = -J_z \sum_i S_i^z S_{i+1}^z - h_z \sum_i S_i^z,$$

$$H_a = -J_a \sum_i (S_i^+ S_{i+1}^+ + S_i^- S_{i+1}^-),$$

$$H_\perp = -J_\perp \sum_i (S_i^+ S_{i+1}^- + S_i^- S_{i+1}^+)$$

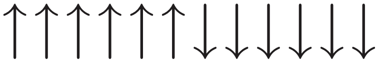

FIG. 1. A spin state with a single domain wall.

with $J_a = (J_x - J_y)/4$ and $J_\perp = (J_x + J_y)/4$ and $S_i^\pm = S_i^x \pm iS_i^y$ are the usual raising and lowering operators. We will assume that J_z is by far the largest coupling thus the system has an easy axis and its behavior is Ising like. The ferromagnetic coupling causes neighboring spins to align their z components, and with a large J_z, the excitation energy of a state is mainly dependent on the number of antialigned spin neighbors, or domain walls. Each domain wall costs an energy of $J_z/2$ (our J_z is twice that of Ref. 9). Thus the ground state is approximately the ferromagnetic state where all spins are aligned along the z axis. In the absence of a magnetic field and other couplings, the first excited state has a single domain wall, see Fig. 1. This domain wall can be placed between any of the spins, implying a macroscopic degeneracy. The H_a term lifts this degeneracy resulting in a band dispersion describing the dynamics of a single domain wall. This mode was first predicted by Villain[10] and was subsequently observed in neutron scattering experiments.[11,12]

Kyriakidis and Loss treated a single domain wall in the presence of a finite magnetic field and predicted BO.[3] The BO are caused by H_a together with the magnetic field that causes the domain wall to oscillate. While the single domain wall approximation is presumably good on short time scales where collisions between domain walls can be ignored, it will break down at longer time scales. In a finite magnetic field, this time scale is likely to be very short as a domain wall and an antidomain wall are closely bound together. The energy cost of a domain of spins antialigned with the field is proportional to the magnetic field times the number of spins in the domain. Thus the magnetic field induces a linear potential between a domain wall and an antidomain wall, which confines them in a bound state. Therefore the low-energy excitations will not be isolated single domain walls, but rather bound states of domain-wall/antidomain-wall pairs that define the boundaries of a spin cluster of overturned spins, see Fig. 2. The far-infrared light absorption experiments on the quasi-one-dimensional material $CoCl_2 \cdot 2H_2O$ in a magnetic field have been explained in terms of such spin cluster excitations.[9,13] In the bound state picture, H_a and the magnetic field cause the bound state to shrink and expand. This is what gives rise to the BO and the WZL.

Going beyond the single domain-wall approximation also allows the inclusion of the spin-flip exchange Hamiltonian $H_\perp$. The action of $H_\perp$ on the single domain-wall state shown in Fig. 1 produces a high-energy state having three domain walls. In contrast when $H_\perp$ acts on the minimal bound state—a single overturned spin, see Fig. 2 right—it can move the whole bound state without introducing extra domain walls, thus $H_\perp$ acts directly in the low-energy Hilbert space of a single bound state. This minimal bound state is the analog to the kinetic bound state in $CoNb_2O_6$.

FIG. 2. Two bound states.

In zero magnetic field, the predictions for the neutron scattering dynamic structure factor were shown to be independent[14] of whether one considered noninteracting domain walls[10] or bound states.[15] However, as argued above, this does not hold in a finite magnetic field, at least not on longer time scales. In this paper, we will treat the single bound state exactly in the low-energy subspace to two domain walls and assume that thermally the system can be well approximated by a noninteracting gas of such bound states.

III. QUANTUM MECHANICS OF A SINGLE BOUND STATE

Let us represent a bound state of a domain wall and an antidomain wall as the state

$$|j,l\rangle = \left|\dots\uparrow\uparrow\underbrace{\overset{j}{\downarrow}\downarrow\dots\downarrow}_{l}\uparrow\uparrow\dots\right\rangle, \tag{3}$$

where the index $j = 1,2,\dots,N$ gives the starting position of the down-spin cluster and $l = 1,\dots,N$ describes its length. N is the total number of spins in the chain, which we will take to be a macroscopic number. We will extend this representation of states to $l = 0$ in order to also include the ferromagnetic state $|j,0\rangle$, which is independent of j. The action of the Hamiltonian on such a state can be written as

$$\begin{aligned} H|j,l\rangle = {} & (1-\delta_{l,0})\{J_z|j,l\rangle + h_z l|j,l\rangle - J_a[|j,l+2\rangle \\ & + |j-2,l+2\rangle + (|j,l-2\rangle + |j+2,l-2\rangle) \\ & \times (1-\delta_{l,2})(1-\delta_{l,1})]\} - J_a(|j,2\rangle\delta_{l,0} + |j,0\rangle\delta_{l,2}) \\ & - J_\perp(|j+1,1\rangle + |j-1,1\rangle)\delta_{l,1}, \end{aligned} \tag{4}$$

where we have neglected terms that result in more than two domain walls.

We consider a system with periodic boundary conditions. This ensures translational invariance and the total momentum of the bound state will be a good quantum number. It is thus convenient to express the Hamiltonian in the momentum basis $|p,l\rangle = e^{-ipl/2}\sum_j e^{-ipj}|j,l\rangle$, where p denotes the total momentum of the bound state (we use units where the lattice spacing is one). Note that the ferromagnetic state necessarily has zero momentum $|p = 0,0\rangle$. In the momentum basis, the Hamiltonian is diagonal in p and acts as follows:

$$\begin{aligned} H|p,l\rangle = {} & (1-\delta_{l,0})\{[J_z + h_z l - 2J_\perp \cos p\,\delta_{l,1}]|p,l\rangle \\ & - 2J_a \cos p\,[|p,l+2\rangle + (1-\delta_{l,1})(1-\delta_{l,2}) \\ & \times |p,l-2\rangle]\} - J_a(|p,2\rangle\delta_{l,0} + |p,0\rangle\delta_{l,2})\delta_{p,0}. \end{aligned} \tag{5}$$

Because H_a flips two spins, the state sectors with even and odd values of l are decoupled. Note that $H_\perp$ only affects the odd l sector. This follows from the fact that $H_\perp$ is only nonzero

$$
\begin{array}{rcll|rcll}
 & H_a & & & & H_\perp & & \\
\uparrow\uparrow\uparrow\uparrow\uparrow\uparrow & \rightarrow & \uparrow\uparrow\downarrow\downarrow\uparrow\uparrow & ,+2 & \uparrow\uparrow\uparrow\uparrow\uparrow\uparrow & \rightarrow & 0 & \\
\uparrow\downarrow\downarrow\uparrow\uparrow\uparrow & \rightarrow & \uparrow\downarrow\downarrow\downarrow\downarrow\uparrow & ,0 & \uparrow\downarrow\downarrow\uparrow\uparrow\uparrow & \rightarrow & \uparrow\downarrow\uparrow\downarrow\uparrow\uparrow & ,+2 \\
\uparrow\uparrow\downarrow\uparrow\uparrow\uparrow & \rightarrow & \uparrow\uparrow\downarrow\downarrow\downarrow\uparrow & ,0 & \uparrow\uparrow\downarrow\uparrow\uparrow\uparrow & \rightarrow & \uparrow\uparrow\uparrow\downarrow\uparrow\uparrow & ,0
\end{array}
$$

FIG. 3. Examples of the actions of H_a on particular states from the 0 and 2 domain-wall sectors. Only cases that yield the minimal amount of increase in domain walls are shown. Operating with H_a are shown on the left, while the right-hand side shows the effects of operating with $H_\perp$. The increase in the number of domain walls is indicated to the right of each process. Note that H_a has the ability to move domain walls without increasing their number when acting on a state with one or more domain walls (left side, the two lowest processes), while $H_\perp$ lacks this ability with the exception that it can move a single overturned spin without creating new domain walls (right side, the lowest process).

when it acts on the state with a single down spin, the action on all other states produces more domain walls, see Fig. 3.

In order to solve the eigenvalue problem, we first parametrize the energy eigenvalues as

$$E_n(p) = J_z + h_z \mu_n, \tag{6}$$

where p is the total momentum, n is a positive integer, which labels the internal excitation mode of the bound state, and μ_n depends on p and coupling constants of the Hamiltonian. Because the excitation spectrum separates into distinct sectors, we will reserve the odd(even) n values for labeling the energy levels in the l odd(even) sector. The energy of the nth mode is found by determining the dimensionless quantity μ_n from the following equations:

$$\frac{J_{-(\mu_n+1)/2}(x)}{J_{1-(\mu_n+1)/2}(x)} = z, \quad n \in \text{odd}, \tag{7}$$

$$\frac{J_{-\mu_n/2}(x)}{J_{1-\mu_n/2}(x)} = 0, \quad n \in \text{even}, \tag{8}$$

with $J_\nu(x)$ being the Bessel function of the first kind of order ν. The upper(lower) equation is obtained by considering the odd(even) l sector. Here, we have introduced the new variables

$$x = \frac{2J_a \cos p}{h_z}, \quad z = \frac{J_\perp}{J_a}. \tag{9}$$

The even sector equation (8) is only valid for $p \neq 0$. The $p = 0$ case will be considered separately below.

Both equations are of the form

$$\frac{J_{-\nu}(x)}{J_{1-\nu}(x)} = \gamma, \tag{10}$$

where γ is a constant. Analytical solutions of this equation has been found in some limits.[16] To get an intuitive picture of the solutions of Eq. (10), we have plotted the left-hand side of the equation for a particular value of x in Fig. 4 as the black solid curve. For $\gamma \to 0$, relevant for the even sector and the small z limit of the odd sector, the solutions are gotten by the zero crossings of the curve. We see that they occur almost exactly at positive integer values of ν, except for the lowest value which is somewhat below 1. In Fig. 5, we show these values of ν as a function of x for $\gamma = 0$. To a very good approximation, ν is a positive integer as long as $\nu \geqslant 1 + |x|$. For the even l sector where $\mu = 2\nu$, this implies that the solutions μ_n, $n \in \{2,4,6,\ldots\}$ are to a good approximation *even* integers $\mu_n = n$ when $n \geqslant 2|x| + 2$. For lower values of n, μ_n is generally lower and depends on x. For small γ, relevant for the odd l sector where $\mu = 2\nu - 1$ when z is small, the solutions are very similar to the case $\gamma = 0$. This means that the solutions μ_n, $n \in \{1,3,5,\ldots\}$ are odd integers $\mu_n = n$ for $n \geqslant 2|x| + 1$. The qualitative effects on the solutions ν of changing γ for a fixed value of x can be inferred from Fig. 4. While the higher-energy levels do not change substantially for this value of x, the lowest-energy level decreases with increasing γ. In Fig. 6, we have plotted the solutions of Eq. (10) as functions of x for a fixed value of $\gamma = 2$. For positive x, the lowest energy state decreases with increasing x. This decrease becomes linear at large x and its slope can be found by writing the Bessel function

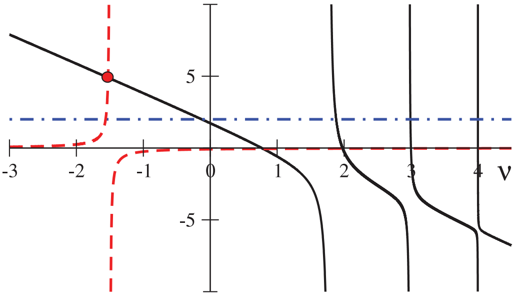

FIG. 4. (Color online) The behavior of the ratio of Bessel functions $J_{-\nu}(x = 1)/J_{1-\nu}(x = 1)$ as a function of ν is shown as the black solid curve. The blue dot-dashed line marks the value $\gamma = 2$, while the red dashed curve shows the right-hand side of Eq. (14) for $y = 3$. The red circle indicates the crossing point that gives the lowest energy solution $\nu_0 = \mu_0/2$ of the $p = 0$ even sector.

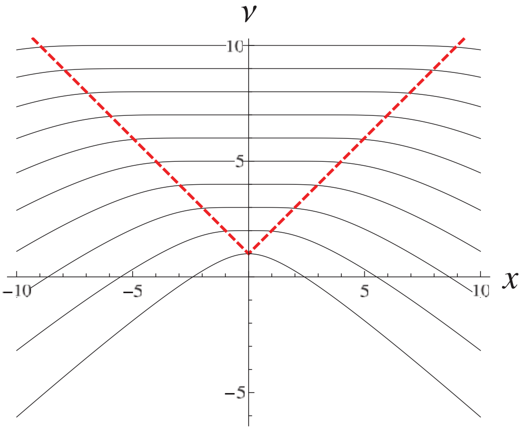

FIG. 5. (Color online) Solutions ν of Eq. (10) as a function of x for $\gamma = 0$. The red dashed line is the line $\nu = 1 + |x|$.

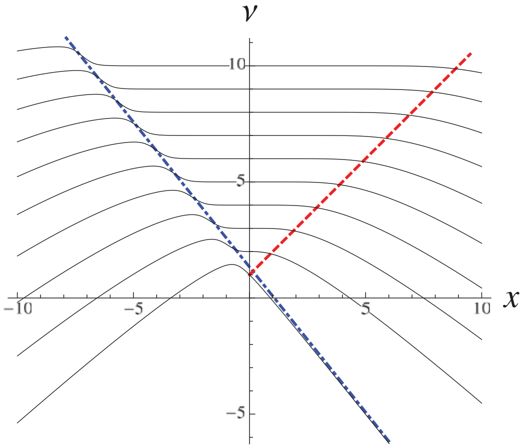

FIG. 6. (Color online) Solutions ν of Eq. (10) as a function of x for $\gamma = 2$. The dot-dashed blue line has slope $(\gamma + \gamma^{-1})/2$ and the red dashed line is the line $\nu = 1 + x$ for positive x.

ratio $J_{-\nu}(x)/J_{1-\nu}(x) = -\{\nu/x + \frac{d}{dx}\ln[J_{-\nu}(x)]\}^{-1}$ and using the asymptotic expression[17]

$$J_{-\nu}(-\nu\theta) \sim \frac{\theta^{-\nu}e^{-\nu\sqrt{1-\theta^2}}}{\sqrt{-2\pi\nu}(1-\theta^2)^{1/4}(1+\sqrt{1-\theta^2})^{-\nu}} \tag{11}$$

valid for $\nu \to \infty$ and $0 < \theta < 1$. We find that the lowest-energy state solution decreases as $\nu \sim -(\gamma + \gamma^{-1})x/2$ for $x \to \infty$ and $\gamma > 1$. A line with this slope is overlaid on the plot in Fig. 6 for $\gamma = 2$. The large x limit corresponds to the limit of vanishing magnetic field. Using the asymptotic result and the definitions of γ and x, we get for the lowest excited state in the limit of vanishing h_z, $E = J_z + h_z(2\nu - 1) \sim J_z - 2J_\perp[1 + (J_a/J_\perp)^2]\cos p$ corresponding to a spin wave excitation. This result can also be obtained by second-order perturbation theory in the limit of vanishing magnetic field when $J_z \gg J_\perp \gg J_a$.

Extrapolating the spin-wave line to negative x, we see that it coincides smooth steplike behaviors of the energy levels. These steps become sharper and higher as γ is increased and become a step discontinuity of unit one for $\gamma \to \infty$. This feature restricts the existence of the WZL for odd n to $n > (\gamma + \gamma^{-1})|x| + 1$ for $x < 0$ and $\gamma > 1$.

From these considerations, it follows that a momentum-independent WZL

$$E_n = J_z + h_z n, \tag{12}$$

with integer n, is restricted to high energies where

$$n > 1 + \frac{2J_a}{h_z} \times \begin{cases} 2, & J_\perp \leqslant J_a, \\ J_\perp/J_a + J_a/J_\perp, & J_\perp > J_a. \end{cases} \tag{13}$$

For $p = 0$, the sector with domain walls of even l will also couple to the ferromagnetic state. Thus, at $p = 0$, the equation for the energy levels in the even sector is different from the one at $p \neq 0$, Eq. (8). For $p = 0$, we get

$$\frac{J_{-\mu_n/2}(x_0)}{J_{1-\mu_n/2}(x_0)} = -\frac{x_0}{4(y + \mu_n)}, \tag{14}$$

where $y = J_z/h_z$ and $x_0 = 2J_a/h_z$. A similar equation including also the effects of an optical phonon at $p = 0$ was obtained in Ref. 13. The equation for $p = 0$ has an additional negative solution $\mu_0 < 0$ well separated from the other positive solutions. This solution arises from the singular behavior of the left-hand side in the vicinity of $\mu = -y$. Figure 4 shows a graphical solution of Eq. (14) with $\mu = 2\nu$ for fixed values $x_0 = 1$ and $y = 3$. Because of the rapid variations of the ratio of Bessel functions on the left-hand side around positive even integer values of μ, we see that a relatively small finite value of the right-hand side changes only slightly the even integer solutions found for $p \neq 0$ in the even sector. However, at low energies, there is a crucial difference. The right-hand side has a singularity at $\mu = 2\nu = -y$. The left-hand side is positive for negative μ and increases as $\mu \to -\infty$ while the right-hand side is negative for $\mu > y$ before it changes sign as μ passes y. Thus somewhere below this singularity a negative solution μ_0 will occur. This means that the ground-state energy will be negative as $J + h_z\mu = 0$ for $\mu = -y$. For $J_a \ll J_z$, we find for the lowest-energy solution approximately

$$\begin{aligned} E_0 = J_z + h_z\mu_0 &\approx -\frac{J_z + 2h_z}{6}\left[1 - \sqrt{1 - \frac{12J_a^2}{(J_z + 2h_z)^2}}\right] \\ &\approx -\frac{J_a^2}{J_z + 2h_z} \end{aligned} \tag{15}$$

consistent with what is expected from second-order perturbation theory.

The energy eigenfunctions are given by $|n,p\rangle = \sum_{l=0}^{\infty}\psi_{n,l}(p)|p,l\rangle$ with coefficients

$$\psi_{n,l}(p) \propto \left[\frac{1 - (-1)^l}{2}\right] J_{(l-\mu_n)/2}(x) \tag{16}$$

valid for n odd and

$$\begin{aligned} \psi_{n,l}(p) \propto \left[\frac{1 + (-1)^l}{2}\right]\Bigg[& J_{(l-\mu_n)/2}(x)(1 - \delta_{l,0}) \\ & - \frac{J_a}{E_n(p=0)} J_{(2-\mu_n)/2}(x)\delta_{p,0}\delta_{l,0}\Bigg] \end{aligned} \tag{17}$$

for n even. Note that only the odd(even) l coefficients are nonzero for odd(even) n. For small x, the Bessel function is maximal when $l = \mu_n \approx n$. Qualitatively, this implies that for large magnetic fields, the nth mode of the bound state is dominated by the state having n overturned spins. This domination is total at $p = \pi/2$, $3\pi/2$ where $x = 0$.

These energy wave functions are orthogonal when the variable μ_n obeys one of the Eqs. (7), (8), or (14) due to the Bessel function property[18]

$$\begin{aligned} &\sum_{k=1}^{\infty} J_{k+\nu}(x)J_{k+\mu}(x) \\ &\quad = \frac{x}{2}\frac{J_{1+\nu}(x)J_{1+\mu}(x)}{\nu - \mu}\left[\frac{J_\nu(x)}{J_{1+\nu}(x)} - \frac{J_\mu(x)}{J_{1+\mu}(x)}\right]. \end{aligned} \tag{18}$$

IV. DYNAMIC STRUCTURE FACTOR

Having the eigenfunctions $|n,p\rangle$ and energies $E_n(p)$, we can calculate the dynamic structure factor, which at zero temperature, is

$$S^{\alpha\alpha'}(q,\omega) = \sum_n \langle 0,0|S^{\alpha}_{-q}|n,q\rangle\langle n,q|S^{\alpha'}_{q}|0,0\rangle \times \delta\{\omega - [E_n(q) - E_0(0)]\}, \tag{19}$$

where $|0,0\rangle$ is the ground state and we have restricted the intermediate states to the states $|n,q\rangle$ in the zero and two domain-wall sectors that restricts the energy transfer $\omega < 2J_z$. In the following, we will consider S^{xx}, S^{yy}, and S^{zz} separately.

For S^{xx} and S^{yy}, it is convenient to consider the raising and lowering operators $S^{\pm} = S^x \pm iS^y$. Expressed in terms of these the transverse dynamic structure factors, S^{xx} and S^{yy} are

$$\begin{aligned} S^{xx} &= \tfrac{1}{4}[(S^{+-} + S^{-+}) + (S^{--} + S^{++})],\\ S^{yy} &= \tfrac{1}{4}[(S^{+-} + S^{-+}) - (S^{--} + S^{++})]. \end{aligned}$$

The ground state has zero momentum and can for $J_a \ll J_z$ be approximated by the ferromagnetic state $|FM\rangle$ where all spins point along the magnetic field. The calculation is simplified greatly by this approximation as then the structure factors S^{--}, S^{++}, and S^{+-} are zero, which follows from $S^{+}|FM\rangle = 0$ implying that $S^{xx} = S^{yy} = \frac{1}{4}S^{+-}$. The action of S^{-} on the ferromagnetic state creates a state with one down spin, thus it belongs to the odd sector, and will have rather high energy, of the order $J_z + h_z$. Using the eigenfunctions, we find

$$S^{+-}(q,\omega) = \sum_{n=1}^{\infty} \delta[\omega - E_n(q)]\, I_n(q),$$

where I_n is normalized relative intensity of the nth mode,

$$I_n(q) = \frac{|\psi_{n,l=1}(q)|^2}{\sum_l |\psi_{n,l}(q)|^2}. \tag{20}$$

Using the expression for the wave functions and the following Bessel function identity

$$\sum_{l=l_0}^{\infty} J^2_{l-\nu}(x) = -\frac{x}{2} J^2_{l_0-\nu}(x) \frac{\partial}{\partial \nu}\left[\frac{J_{l_0-\nu-1}(x)}{J_{l_0-\nu}(x)}\right] \tag{21}$$

with l_0 an integer, the intensity can be expressed in the form

$$I_n(q) = \left\{ x \frac{\partial}{\partial \mu}\left[\frac{J_{\mu/2}(x)}{J_{\mu/2+1}(x)}\right]\right\}^{-1}\Bigg|_{\mu=-\mu_n}, \tag{22}$$

where μ_n is the solution of Eq. (7) for the odd domain length l.

For larger values of J_a/J_z, it is no longer adequate to approximate the ground state with the ferromagnetic state. Taking into account the exact nature of the ground state gives additional contributions to S^{+-} and the corresponding intensity becomes

$$I_n^{+-}(q) = \left[C_0^0 C_1^n(q) + 2\sum_{l>0} C_l^0 C_{l+1}^n(q)\cos(ql/2)\right]^2, \tag{23}$$

where we have used the following notation for the normalized wave functions:

$$C_l^n(q) = \frac{\psi_{n,l}(q)}{\sqrt{\sum_l |\psi_{n,l}(q)|^2}}. \tag{24}$$

We will omit the momentum label for the ground state C_l^0 as it has zero momentum. The leading terms of the intensity give the contribution

$$I_n^{+-}(q) \approx \left(C_0^0\right)^2 I_n(q) + 4C_0^0 C_2^0 C_1^n(q) C_3^n(q)\cos(q). \tag{25}$$

In this case, we also get nonzero contributions to S^{-+} and to S^{--}, S^{++} which cause S^{xx} to be different from S^{yy}. In the same notation as above, their contributions are

$$\begin{aligned} I_n^{-+}(q) &= \left| C_1^0 C_0^n(0)\delta_{q,0} + 2e^{-iq/2}\sum_{l>1} C_l^0 C_{l-1}^n(q)\cos(ql/2)\right|^2,\\ I_n^{++}(q) &= \left[C_0^0 C_1^n(q) + 2\sum_{l>0} C_l^0 C_{l+1}^n(q)\cos(ql/2)\right]\\ &\quad\times \left[C_1^0 C_0^n(0)\delta_{q,0} + 2\sum_{l>1} C_l^0 C_{l-1}^n(q)\cos(ql/2)\right],\\ I_n^{--}(q) &= [I_n^{++}(q)]^*, \end{aligned}$$

where the $*$ means complex conjugation. Approximating these with their leading terms, we get

$$I_n^{-+}(q) \approx \left[C_1^0 C_0^n(0)\delta_{q,0} + 2C_2^0 C_1^n(q)\cos q\right]^2, \tag{26}$$

$$\begin{aligned} I_n^{++}(q) &\approx C_1^0 C_0^n(0)\left[C_0^0 C_1^n(0) + 2C_1^0 C_2^n(0)\right]\delta_{q,0}\\ &\quad + 2C_0^0 C_2^0 \left[C_1^n(q)\right]^2 \cos q. \end{aligned} \tag{27}$$

Applying the operator S^z to the ground state does not change the parity of l, thus all contributing intermediate states have even n. It is convenient to split off the ground-state contribution as it has zero momentum and frequency, it represents the squared magnetization, and write

$$\begin{aligned} S^{zz}(q,\omega) &= \frac{1}{4}\left[N - 2\sum_l l\left(C_l^0\right)^2\right]^2 \delta_{q,0}\delta(\omega)\\ &\quad + \sum_n \delta[\omega - E_n(q)]\, I_n^{zz}(q), \end{aligned} \tag{28}$$

where

$$I_n^{zz}(q) = \frac{\left[\sum_{l=2}^{N} C_l^0 C_l^n(q)\sin(ql/2)\right]^2}{\sin^2(q/2)}. \tag{29}$$

The leading contribution of the sum is

$$\begin{aligned} I_n^{zz}(q) &= \frac{4E_0{}^2}{J_a^2}\frac{|\psi_{n,l=2}(q)|^2}{\sum_l |\psi_{n,l}(q)|^2}\cos^2(q/2)\\ &\approx \frac{4J_a^2}{(J_z + 2h_z)^2}\cos^2(q/2)\, I_n^{\mathrm{ev}}(q), \end{aligned} \tag{30}$$

where the introduced intensity I_n^{ev} corresponds to contribution from the states with even n and can be written as

$$I_n^{\mathrm{ev}}(q) = \left\{ x \frac{\partial}{\partial \mu}\left[\frac{J_{\mu/2}(x)}{J_{\mu/2+1}(x)}\right]\right\}^{-1}\Bigg|_{\mu=-\mu_n}, \tag{31}$$

where μ_n is the solution of the Eq. (8) for the even domain length l.

V. FINITE TEMPERATURE

At finite temperatures, the dynamic structure factor will in addition to transitions out of the ground state also get contributions that depend solely on the excited states. In particular, there will be contributions at low frequencies corresponding to the spacing between energy levels. It was these temperature-induced contributions that were the focus of the neutron scattering experiments in Refs. 4 and 5. We will consider such temperature-induced contributions at relatively low frequencies $\omega < J_z$.

At finite temperature, entropic factors make it favorable to break up a spin domain, thus inducing domain walls. The magnetic field confines pairs of domain walls leading to a picture of the finite-temperature state as consisting of several bound states; short spin-down domains, interspaced by longer spin-up domains. To handle these thermal states, we will use the exact quantum-mechanical treatment of an isolated bound state and neglect the interaction between different bound states. We expect the quality of this noninteracting bound state approximation to be good on time scales shorter than the typical collision time between bound states. This collision time can be estimated by the mean distance between the bound states, which is the typical size of a spin-up domain, divided by the velocity of a bound state. The typical length of a spin-up domain $\xi_\uparrow$ in units of the lattice spacing can be estimated from the emptiness formation probability for the Ising model in a magnetic field[19] and gives

$$\xi_\uparrow = \frac{1}{1-\alpha_\uparrow}, \tag{32}$$

where

$$\alpha_\uparrow = \frac{e^{\beta h_z/2}}{\cosh(\beta h_z/2) + \sqrt{\sinh^2(\beta h_z/2) + e^{-\beta J_z}}}, \tag{33}$$

where β is the inverse temperature. Using this and the maximum velocity of a spin-down bound state $v_{\max}$, we expect the independent bound state approximation to be good for frequencies

$$\omega > \frac{2\pi v_{\max}}{\xi_\uparrow}. \tag{34}$$

The bound-state velocity $v_n(p) = \frac{\partial E_n(p)}{\partial p}$ is largest for low-lying energy modes. For higher-energy modes, the dispersion becomes flatter and their velocity approaches zero. For the $n = 1$ mode, the energy varies as $E_1(p) \approx -2J_\perp[1 + (J_a/J_\perp)^2]\cos p$ for $J_\perp > J_a$ at low momenta p, which implies a maximum velocity $v_1 = 2J_\perp[1 + (J_a/J_\perp)^2]$. For $J_\perp < J_a$, the $n = 1$ mode behaves almost as the $n = 2$ mode, which for $2J_a/h_z < 1$, has a maximum velocity $v_2 \approx 2J_a^2/h_z$ that increases for smaller fields and approaches $v_2 \sim 4J_a$. Thus the maximum velocity of a bound state is $v_{\max} = \max(v_1, v_2)$.

The above validity criterion (34) takes into account the center of mass motion of the bound states. In addition, the quantum-mechanical uncertainty in the size of a bound state can also ruin the noninteracting bound state approximation. From the wave functions, we estimate the size uncertainty to be $\pm 2J_a/h_z$, which implies that adjacent bound states have nonoverlapping boundaries when

$$4J_a/h_z < \xi_\uparrow. \tag{35}$$

Keeping in mind these restrictions, we can write down the dynamic structure factor at low frequencies $\omega < J_z$ in the independent bound-state approximation as

$$S^{\alpha\alpha'}(q,\omega) = \sum_{p,m,m'} n_{m,p} \mathbf{S}^{\alpha\alpha'}_{m'm}(p,q) \times \delta\{\omega - [E_{m'}(p+q) - E_m(p)]\}, \tag{36}$$

where

$$\mathbf{S}^{\alpha\alpha'}_{m'm}(p,q) = \langle m,p|S^\alpha_{-q}|m',p+q\rangle\langle m',p+q|S^{\alpha'}_q|m,p\rangle$$

and $n_{m,p}$ is the occupation number of a bound state with internal energy index m and momentum p. Its functional form depends generally on the statistics of these excitations, but is expected to behave at low temperatures as $n_{m,p} \approx e^{-\beta[E_m(p)-E_0(0)]}\kappa(\beta)$, where κ is close to unity for $T < J_z$.

The action of the operator S^z on a state with a spin-down cluster of l spins and momentum p is

$$S^z_q|p,l\rangle = \frac{N}{2}|p,l\rangle\delta_{q,0} - \frac{1-e^{iql}}{1-e^{iq}}|p+q,l\rangle, \tag{37}$$

which implies that the matrix elements $\mathbf{S}^{zz}_{mn}$ is given by the expression

$$\mathbf{S}^{zz}_{mn} = \delta_{q,0}\left[\frac{N}{2}\sum_l C^n_l(p)C^m_l(p) - \sum_l l C^n_l(p)C^m_l(p)\right]^2 + (1-\delta_{q,0})\frac{1}{\sin^2 q/2}\left[\sum_l C^n_l(p)C^m_l(p+q)\sin\frac{ql}{2}\right]^2. \tag{38}$$

This expression is rather difficult to deal with analytically for general values of the parameters. However, in the region of parameters where we expect the spectrum to be the WZL, we can evaluate it analytically. Focusing on this region where $2J_a/h_z \ll 1$ and $J_\perp < J_a$, we get, see Appendix,

$$S^{zz}(q,\omega) = \frac{\kappa(\beta)e^{-\beta(J_z+h_z)}}{1-e^{-\beta h_z}}\sum_{k=-N}^{N} G_k(q)\,\delta(\omega - 2h_z k), \tag{39}$$

where the contribution from each mode for $q \neq 0$ is

$$G_0(q) = \frac{J_0^2(\zeta)}{\cosh(\beta h_z) - \cos q}\,\frac{e^{\beta h_z}+1}{2},$$

$$G_k(q) = \frac{J_k^2(\zeta)}{2\sin^2(q/2)}\begin{cases}1, & k > 0,\\ e^{\beta 2h_z k}, & k < 0,\end{cases}$$

and the argument of the Bessel function is $\zeta = \frac{2J_a}{h_z}|\sin q|$. For $q = 0$, we get also a contribution from the ground-state magnetization squared:

$$G_0(0) = \left(\frac{N}{2}\right)^2 - \frac{N}{1-e^{-\beta h_z}} + \frac{1}{2}\,\frac{e^{\beta h_z}+1}{\cosh(\beta h_z) - 1},$$

$$G_k(0) = \frac{1}{2}\left(\frac{2J_a}{h_z}\right)^2\begin{cases}1, & k = 1,\\ e^{-\beta 2h_z}, & k = -1,\\ 0, & |k| > 1.\end{cases}$$

Thus there are contributions for $\omega = 2h_z k$, where k is an integer. The $2h_z$ reflects the fact that S^z does not change the parity of l. If we introduce the Bloch frequency $\omega_B = 2h_z$, this gives a result similar to the expression found in Ref. 3. However, the temperature-dependent factors are different. In particular, we get a prefactor $e^{-\beta J_z}$, which is a consequence of the occupation number of bound states. This is in contrast to the factor $e^{-\beta J_z/2}$ expected in the single domain-wall approximation. A noteworthy feature of Eq. (39) is that increasing the magnetic field moves the spectral weight to lower Bloch frequencies. This follows from the fact that the maximum of the Bessel function squared $J_k(\zeta)$ for fixed ζ occurs when $k \approx \zeta - 1$.

For the transverse dynamic structure factor, we find

$$\mathbf{S}^{+-}_{mn}(p,q) = \left[C^n_0(0)C^m_1(q)\delta_{p,0} + 2\sum_{l>0} C^n_l(p)C^m_{l+1}(p+q) \times \cos\left(\frac{ql-p}{2}\right)\right]^2. \tag{40}$$

This expression can also be evaluated analytically in the region where the spectrum is the WZL, see Appendix,

$$S^{+-}(q,\omega) = \frac{\kappa(\beta)e^{-\beta J_z}}{e^{\beta h_z}-1}\sum_k \delta[\omega - h_z(2k+1)] \times 2J_k^2(\zeta)\begin{cases}1, & k > 1/2,\\ e^{\beta h_z(2k+1)}, & k < 1/2,\end{cases} \tag{41}$$

where $\zeta = \frac{2J_a}{h_z}|\sin q|$ and k is an integer variable. For the transverse structure factor, the excitations occur at frequencies that are an odd multiple of h_z, a consequence of the fact that S^- changes the parity of l, the number of overturned spins.

VI. COBALT CHLORIDE

$CoCl_2 \cdot 2H_2O$ is a quasi-one-dimensional anisotropic spin-1/2 magnet, proposed in Ref. 3 as a candidate exhibiting BO in a magnetic field. $CoCl_2 \cdot 2H_2O$ has a dominant ferromagnetic coupling J_z along the chains, which was determined from far-infrared absorption spectroscopy[9] to be $J_z = 36.5$ K. Other intrachain couplings J_x and J_y are smaller but nonzero. The values of these couplings as well as other interchain couplings have been inferred both from far-infrared spectroscopy[9] and from spin wave analysis of neutron scattering experiments.[4,5,20] In this paper, we use the following values to describe $CoCl_2 \cdot 2H_2O$:

$$J_z = 36.5\text{ K},\quad J_a = 3.8\text{ K},\quad J_\perp = 5.43\text{ K}. \tag{42}$$

An important consequence of interchain couplings in $CoCl_2 \cdot 2H_2O$ is that they cause the spins to order antiferromagnetically below $T_N = 17.3$ K. This implies that in the antiferromagnetic phase below T_N, the magnetic field h_z used here should be interpreted as a sum of the external applied magnetic field and an internal field, which arises due to the magnetic moments of neighboring chains.[9]

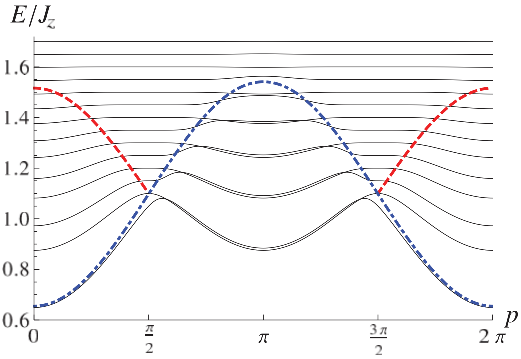

FIG. 7. (Color online) Energy levels vs momentum computed with the parameters in Eq. (42) for a magnetic field $h_z/J_z = 0.05$. The dot-dashed blue curve corresponds to the asymptotic dot-dashed line drawn in Fig. 6 but with $\gamma = 1.43$, and the red dashed curve corresponds to the red dashed line in Fig. 6.

We have plotted the energy levels $E_n(p)$ for the above couplings in Fig. 7. The WZL is present at low energies in the momentum region around $p = \pi/2$ $(3\pi/2)$ and is bounded by the red dashed and blue dot-dashed curves, which correspond to the asymptotic lines drawn in Fig. 6. For energies $E > J_z + 2h_z + 4J_a$, the spectrum is the WZL for $p = 0$ and for $E > J_z + h_z + 2J_\perp[1 + (J_a/J_\perp)^2]$, it extends also to the region above π so that the spectrum is the WZL for all momenta. For regions of energies where the spectrum is not WZL for all momenta, it is possible to see from Fig. 7 that the even levels are symmetric around $\pi/2$ while the odd levels lack this symmetry property. This is a consequence of the skewness of levels seen in Fig. 6.

In order to see the effects of $J_\perp$, we have in Fig. 8 also plotted the energy levels when $J_\perp = 0$ for comparison.[21] We see that the main effect of $J_\perp$ is to lower the energy of the lowest odd level and to shift the low-energy odd levels in the region $\pi/2 < p < 3\pi/2$ so that they almost coincide with the even levels. The even levels are unaffected by $J_\perp$.

The zero temperature transverse dynamic structure factor S^{+-} at $h_z/J_z = 0.05$ is shown in Fig. 9. Only transitions to odd n levels have nonzero intensity and it is seen that most of

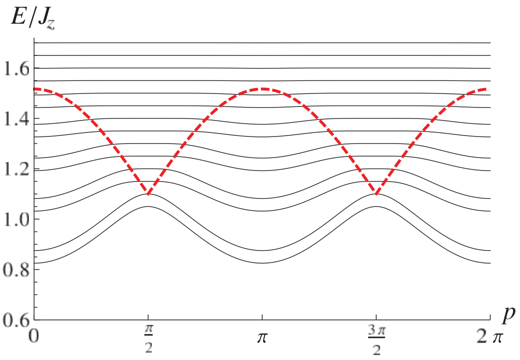

FIG. 8. (Color online) Energy levels vs momentum computed with $J_\perp = 0$, $J_a/J_z = 0.104$, and $h_z/J_z = 0.05$. The red dashed curve corresponds to the red dashed lines in Fig. 5 and marks the lower boundary of the WZL.

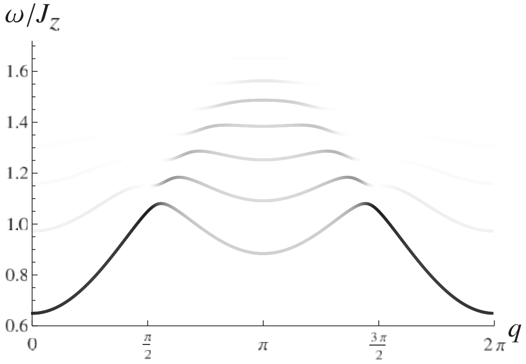

FIG. 9. Gray-scale plot of $S^{+-}(q,\omega)$ vs q and ω at $T=0$ for $J_\perp/J_z=0.149$, $J_a/J_z=0.104$, and $h_z/J_z=0.05$.

the spectral weight occurs for transitions to the spin-wave-like state $n=1$. The intensities of higher excited levels are weak in the momentum region around $p=\pi/2$ where we expect to see the WZL. Exactly at $p=\pi/2$, the size of the bound state is a good quantum number, thus higher excited bound states with $n>1$ have no amplitude to have the size $l=1$, which is the dominant intermediate state generated by neutron scattering on a ferromagnetic state. Any intensity of $n>1$ levels at $p=\pi/2$ reflects how the ground state deviates from being fully ferromagnetic. For the coupling constants relevant for $\mathrm{CoCl_2\cdot 2H_2O}$, the probability for finding all spins up in the ground state is roughly 99%, so fluctuation corrections to the ground state are small and the integrated spectral intensity above the $n=1$ mode is less than 1%. In Fig. 10, we show how the intensities Eq. (23) of the different levels vary for two momenta $q=0$ and $q=\pi$. For $q=0$, the intensities drop exponentially with frequency, but for $q=\pi$, the intensity decreases only slightly before it increases up to the energy where the WZL sets in and then drops rapidly. This also reflects the fact that the main contribution comes from transitions to the $l=1$ state.

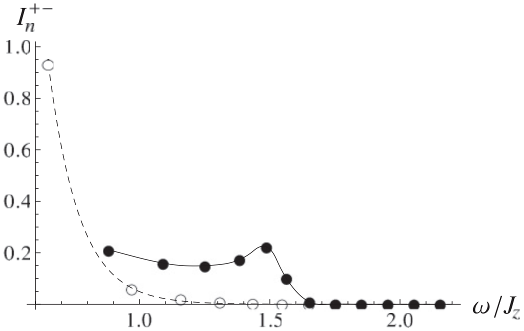

FIG. 10. Intensities $I^{+-}(q)$ vs ω at $T=0$ for $J_\perp/J_z=0.149$, $J_a/J_z=0.104$, and $h_z/J_z=0.05$. The results for two momenta are shown, $q=0$ (open circles, dashed line) and $q=\pi$ (solid circles, solid line). The lines are guides to the eye.

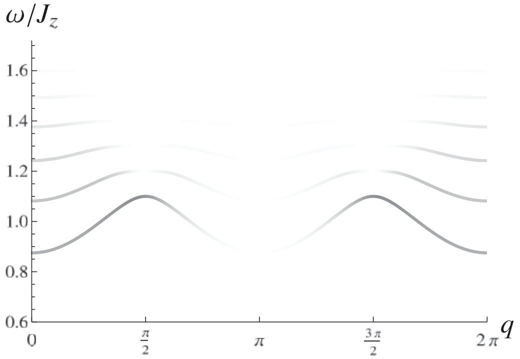

FIG. 11. Gray-scale plot of $S^{zz}(q,\omega)$ vs q and ω at $T=0$ for $J_\perp/J_z=0.149$, $J_a/J_z=0.104$, and $h_z/J_z=0.05$. The intensity of the plot has been increased by a factor 28 in order to make it visible on the same gray scale as used in Fig. 9.

The behavior of the longitudinal dynamic structure factor S^{zz} for parameters relevant for $\mathrm{CoCl_2\cdot 2H_2O}$ is shown in Fig. 11. Here, only excitations to even n levels are nonzero which implies that S^{zz} is independent of $J_\perp$. The total spectral weight of $S^{zz}(q\neq 0)$ is however much smaller than for S^{+-} because it is proportional to the probability for finding two overturned spins in the ground state. This is reflected by the small factor $J_a^2/(J_z+2h_z)^2$ in Eq. (30).

For finite T, the validity of the noninteracting bound-state approximation for $\mathrm{CoCl_2\cdot 2H_2O}$ used here is constrained mostly by $J_\perp$. Its relatively large value causes the $n=1$ bound state to have the largest velocity which according to the inequality (34) gives a lower bound on the frequency for which our approach is valid. If we require that this lowest frequency equals the Bloch frequency $\omega_B=2h_z$, the noninteracting bound-state approximation will be valid in the temperature/magnetic field region shaded dark gray in Fig. 12 for the parameters relevant for $\mathrm{CoCl_2\cdot 2H_2O}$. We do not expect

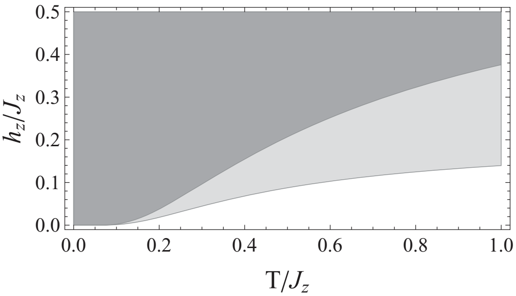

FIG. 12. Region of validity of the noninteracting bound state approximation using the parameters in Eq. (42). The region where the inequality (35) holds is shaded in light gray (which also overlaps entirely the dark gray region). The region where the noninteracting approximation can be used for frequencies down to the Bloch frequency $\omega_B=2h_z$, inequality (34), is shown in dark gray.

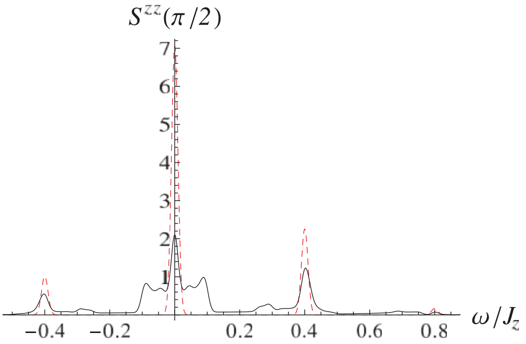

FIG. 13. (Color online) $S^{zz}(q=\pi/2,\omega)$ vs ω/J_z for $T=J_z/2$, $h_z/J_z=0.2$, and parameters from Eq. (42). The red dashed curve is the corresponding WZL result Eq. (39) using the same parameters. In order to generate the plot, δ functions were approximated by a Gaussian distributions with variance 10^{-4}. The vertical axis values are in multiples of $\kappa(\beta=2/J_z)$, a number of order unity.

our results to apply outside this region as a treatment of bound-state collisions is needed there.

In order to see finite temperature signatures of BO, a high temperature is needed to thermally occupy the bound state levels. However, at high temperatures, the validity of our approach is restricted to large magnetic fields, as seen from Fig. 12. Increasing the magnetic field has the disadvantage that the weights of the finite frequency Bloch peaks become small Eq. (39), thus weakening the signatures of BO. Therefore a judicial choice of temperature and magnetic field must be made to make observations possible.

The optimal magnetic field for the first resonance at ω_B is $h_z\sim J_a$. We will use a larger magnetic field, $h_z=0.2J_z$, as that allows our approach to be used up to a temperature $T\approx J_z/2$. We find that for S^{zz} the maximum intensity of the finite frequency WZL transitions occur at $q=\pi/2$. In Fig. 13, we have plotted our analytical result Eq. (38) numerically. We compare this with the expression obtained in the WZL limit Eq. (39) using the same parameters. We see a clear peak at the Bloch frequency $\omega_B=2h_z$ also when the conditions for the WZL are suboptimal as is the case with the parameters in Eq. (42). The WZL calculation (red dashed line) overestimates the weight of the peaks, but do reasonably capture their relative intensities. For higher temperatures, the WZL expression matches Eq. (38) better as then more emphasis is put on the higher-energy part of the spectrum which is more WZL-like for all momenta. We wish to emphasize that the thermally induced transitions here come with an overall factor $e^{-\beta J_z}$ which makes them difficult to observe at low temperatures.

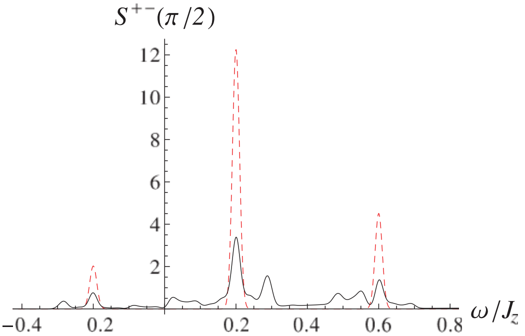

FIG. 14. (Color online) $S^{+-}(q=\pi/2,\omega)$ vs ω/J_z using the same parameters as in Fig. 13. The red dashed curve is the corresponding WZL result Eq. (41) using the same parameters. Delta-functions were approximated by a Gaussian distributions with variance 10^{-4}. The vertical axis values are in multiples of $\kappa(\beta=2/J_z)$, a number of order unity.

In Fig. 14, we have plotted S^{+-} using the same parameters as in Fig. 13. Peaks at frequencies corresponding to odd multiples of the magnetic field are clearly seen among other peaks caused by the dispersion of the lowest-energy modes.

VII. CONCLUSION

In this work, we have investigated the possibility of observing spectral signatures of magnetic BO in a one-dimensional anisotropic ferromagnetic spin system placed in a magnetic field. This system was considered previously[3] but within an approximation where only a single domain wall was included. We argue that the single domain-wall approximation is insufficient at a finite magnetic field. Instead, we consider a bound state of a domain wall and an antidomain wall; a spin cluster of adjacent spins antialigned with the magnetic field,[9] and treat the thermal state as a noninteracting gas of such excitations. This allows us to also include the effects of the additional coupling $J_\perp$, which probably is present in most anisotropic materials that have a nonzero value of J_a. For instance, in $CoCl_2\cdot 2H_2O$ for which neutron scattering searches for BO have been made, $J_\perp$ is bigger than J_a.

We have treated the quantum mechanics of the bound state and obtained its energy levels and wave functions. The spectrum in a magnetic field will be split by the magnetic field essentially into modes corresponding to the size (number of overturned spins) of the bound state. In the momentum region around $p=\pi/2$ ($p=3\pi/2$), the energy levels are equidistantly spaced down to the lowest energies. This corresponds to the WZL. For other momenta the exchange couplings, J_a and $J_\perp$, cause dispersion of the low-lying energy levels. This effect diminishes for higher energies and the spectrum becomes the WZL above a threshold energy for all momenta.

We have also calculated the neutron scattering dynamic structure factor at zero and low temperatures. At zero temperature, the expected response occurs at high frequencies and there should be considerable chances of seeing the magnetic field splitting of the spectrum. However, it will be difficult to see the WZL because of the low spectral weight in this region. This is because neutron scattering flips a single spin and couples most strongly to the bound states that have a significant amplitude of having a single down-spin cluster, which has a dispersion that is heavily influenced by $J_\perp$. The longitudinal channel is not influenced by $J_\perp$, but is much weaker at nonzero momentum.

Detecting BO at finite temperatures with neutron scattering seems more promising. However, the thermal occupation number of bound states implies that these signatures will be suppressed at low temperatures as $e^{-\beta J_z}$. This might be the reason for the nonobservation of BO in the neutron scattering experiments.[4,5] Nevertheless, it might still be possible that neutron scattering on $\mathrm{CoCl_2 \cdot 2H_2O}$ can be used to observe signatures of BO provided a careful selection of temperature and magnetic field is being made. In that respect, care must be taken so as to secure a big enough thermal population of bound states, a large intensity of the finite frequency resonance(s), and a regime where collisions of bound states do not destroy the BO.

APPENDIX: WZL STRUCTURE FACTORS

Let us calculate the dynamic structure factors at finite temperature in the limit where the spectrum is the WZL, that is $h_z \gg 2J_a$ and $J_\perp \ll J_a$. In this limit, $E_n(p) = J_z + h_z n$ and the wave functions are Bessel functions of integer order

$$C_l^n(p) = \frac{1+(-1)^{l-n}}{2} J_{\frac{l-n}{2}}(x_0 \cos p), \tag{A1}$$

where $x_0 = 2J_a/h_z \ll 1$. In the limit $x_0 \to 0$, these wave functions are normalized to unity. This also holds approximately at small finite x_0, which follows from the property of Bessel functions: $\sum_{k=-\infty}^{\infty} J_k^2(x) = 1$ and the fact that contributions from higher $J_k(x_0)$ decrease rapidly with k for small x_0. Thus only small errors are introduced by extending the sum to $-\infty$ at small finite x_0.

For $S^{zz}(q \neq 0,\omega)$, the matrix elements (38) become

$$\mathbf{S}^{zz}_{mn}\Big|_{q\neq 0} = \frac{1}{\sin^2 q/2}\Bigg\{\sum_{l>0} J_{\frac{l-n}{2}}(x_0\cos p) \times J_{\frac{l-m}{2}}[x_0\cos(p+q)] \sin\frac{ql}{2}\Bigg\}^2, \tag{A2}$$

where the sum over l goes over even(odd) integers when n and m both are even(odd), otherwise every term in the sum is zero. It is convenient to introduce a new integer-valued variable $t = (l-n)/2$ and rewrite the sum in the form

$$\sum_{t>-\frac{n}{2}} J_t(x_0\cos p)\, J_{t+\frac{n-m}{2}}[x_0\cos(p+q)] \sin\left[q\left(t+\frac{n}{2}\right)\right] = J_{\frac{n-m}{2}}(\zeta)\sin\left[\left(p-\frac{\pi}{2}\right)\frac{n-m}{2}+q\frac{n}{2}\right], \tag{A3}$$

where we introduced a new variable $\zeta = x_0|\sin q|$. The sum over the product of Bessel functions was performed by extending the sum to negative $-\infty$, which only induces small errors when $x_0 \ll 1$, and then using Graf's addition theorem[17]

$$\sum_{k=-\infty}^{\infty} J_{k+\nu}(u)\, J_k(v) \begin{matrix}\sin\\ \cos\end{matrix}(k\phi) = J_\nu(w) \begin{matrix}\sin\\ \cos\end{matrix}(\nu\chi) \tag{A4}$$

with the relations $w = \sqrt{u^2+v^2-2uv\cos\phi}$, $w\cos\chi = u - v\cos\phi$, and $w\sin\chi = v\sin\phi$.

The dynamic structure factor S^{zz} for $q \neq 0$ in the independent bound-state approximation can then be written in the form

$$S^{zz}(q,\omega)|_{q\neq 0} = \frac{\kappa(\beta)}{\sin^2 q/2}\sum_{m,n} e^{-\beta(J_z+h_z n)}\,\delta[\omega-(m-n)] \times J^2_{\frac{n-m}{2}}(\zeta)\begin{cases}1/2, & n\neq m,\\ \sin^2\left(q\frac{n}{2}\right), & n=m,\end{cases} \tag{A5}$$

where integration over momentum p was performed for integer values of n and m variables

$$\int_0^{2\pi}\frac{dp}{2\pi}\sin^2\left[\left(p-\frac{\pi}{2}\right)\frac{n-m}{2}+q\frac{n}{2}\right] = \begin{cases}1/2, & n\neq m,\\ \sin^2\left(q\frac{n}{2}\right), & n=m.\end{cases}$$

No transitions between the even and odd sectors are allowed, thus it is convenient to introduce a new integer-valued variable $k = (m-n)/2$ that describes the energy difference between the states involved in the transition.

We can reorder the double sum as

$$\sum_{m,n} = \left(\sum_{m\geqslant n}+\sum_{m<n}\right)\sum_n = \sum_{m\geqslant n}\sum_n + \sum_m\sum_{n>m} = \sum_n\sum_{k\geqslant 0}+\sum_m\sum_{k<0}, \tag{A6}$$

that allows us to rewrite the dynamic structure factor in the case of nonzero energy transitions, $k \neq 0$, in the following form:

$$S^{zz}|_{q\neq 0,\omega\neq 0} = \frac{\kappa(\beta)}{2\sin^2(q/2)}\frac{e^{-\beta J_z}}{e^{\beta h_z}-1}\sum_{k\neq 0}\delta(\omega-2h_z k)J_k^2(\zeta) \times \begin{cases}1, & k>0,\\ e^{\beta 2h_z k}, & k<0,\end{cases} \tag{A7}$$

where we used the expression for the sum of the first N terms of a geometric series

$$\sum_{n=1}^{N} e^{-\beta h_z n} = e^{-\beta h_z}\frac{1-e^{-\beta h_z N}}{1-e^{-\beta h_z}} \approx \frac{1}{e^{\beta h_z}-1}. \tag{A8}$$

For the zero mode, $k = 0$, in order to find the sum in Eq. (A5), we can use the following identity

$$\sum_{n=1}^{\infty}\sin^2(an)e^{-bn} = \frac{1}{1-e^{-b}}\frac{\sin^2 a}{2}\frac{1+e^{-b}}{\cosh b-\cos 2a}, \tag{A9}$$

which can be proved using Euler's formula and sum of terms of geometric series. This gives the contribution to the zero mode

$$S^{zz}\Big|_{\substack{q\neq 0\\ \omega=0}} = \kappa(\beta)e^{-\beta J_z}\frac{1+e^{-\beta h_z}}{1-e^{-\beta h_z}}\frac{\delta(\omega)}{2}\frac{J_0^2(\zeta)}{\cosh(\beta h_z)-\cos q}. \tag{A10}$$

Finally, combining together Eqs. (A7) and (A10), we obtain the dynamic structure factor:

$$S^{zz}(q,\omega)|_{q\neq 0} = \frac{\kappa(\beta)e^{-\beta(J_z+h_z)}}{1-e^{-\beta h_z}}\sum_{k=-N}^{N} G_k(q)\,\delta(\omega-2h_z k), \tag{A11}$$

where the contribution from each mode is

$$G_0 = \frac{J_0^2(\zeta)}{\cosh(\beta h_z) - \cos q}\,\frac{e^{\beta h_z}+1}{2}, \tag{A12}$$

$$G_k = \frac{J_k^2(\zeta)}{2\sin^2(q/2)}\begin{cases}1, & k>0,\\ e^{\beta 2 h_z k}, & k<0,\end{cases} \tag{A13}$$

and the argument of the Bessel function is $\zeta = \frac{2J_a}{h_z}|\sin q|$.

The leading contribution to the dynamic structure factor S^{+-} comes from transition between states with nonzero momentum p. Then the matrix element in Eq. (40) becomes

$$\mathbf{S}^{+-}_{mn}(p,q) = 4\left\{\sum_{l>0} J_{\frac{l-n}{2}}(x_0\cos p)\,J_{\frac{l+1-m}{2}}[x_0\cos(p+q)] \times \cos\left(\frac{ql-p}{2}\right)\right\}^2, \tag{A14}$$

where the sum over l is over even(odd) integers when n is even(odd) and m is odd(even). Introducing the new integer variable $t=(l-n)/2$ and summing over the product of Bessel functions using Graf's addition theorem gives

$$\sum_{t>-\frac{n}{2}} J_t(x_0\cos p)\,J_{t+\frac{n-m+1}{2}}[x_0\cos(p+q)] \times \cos\left[q\left(t+\frac{n}{2}\right)-\frac{p}{2}\right] = J_{\frac{n-m+1}{2}}(\zeta)\cos\left[\left(p-\frac{\pi}{2}\right)\frac{n-m+1}{2}+\frac{p}{2}+q\frac{n}{2}\right]. \tag{A15}$$

Since the only allowed transitions are between different parity sectors it is convenient to introduce the integer-valued quantity $k=(m-n-1)/2$. The integral over momentum is

$$\int_0^{2\pi}\frac{dp}{2\pi}\cos^2\left[\left(\frac{\pi}{2}-p\right)k+\frac{p}{2}+q\frac{n}{2}\right]=\frac{1}{2}.$$

After reordering of the double sum, we finally obtain

$$S^{+-}(q,\omega) = \frac{\kappa(\beta)e^{-\beta J_z}}{e^{\beta h_z}-1}\sum_k \delta[\omega - h_z(2k+1)] \times 2J_k^2(\zeta)\begin{cases}1, & k>1/2,\\ e^{\beta h_z(2k+1)}, & k<1/2,\end{cases} \tag{A16}$$

where $\zeta = \frac{2J_a}{h_z}|\sin q|$ and k is an integer.

---

[1] E. E. Mendez, F. Agullo-Rueda, and J. M. Hong, Phys. Rev. Lett. **60**, 2426 (1988).

[2] M. Ben Dahan, E. Peik, J. Reichel, Y. Castin, and C. Salomon, Phys. Rev. Lett. **76**, 4508 (1996).

[3] Jordan Kyriakidis and Daniel Loss, Phys. Rev. B **58**, 5568 (1998).

[4] W. Montfrooij, G. E. Granroth, D. G. Mandrus, and S. E. Nagler, Phys. Rev. B **64**, 134426 (2001).

[5] N. B. Christensen, K. Lefmann, I. Johannsen, and O. Jørgensen, Physica B **276**, 784 (2000).

[6] Z. Cai, L. Wang, X. C. Xie, U. Schollwöck, X. R. Wang, M. Di Ventra, and Y. Wang, Phys. Rev. B **83**, 155119 (2011).

[7] R. Coldea, D. A. Tennant, E. M. Wheeler, E. Wawrzynska, D. Prabhakaran, M. Telling, K. Habicht, P. Smeibidl, and K. Kiefer, Science **327**, 177 (2010).

[8] Jonas A. Kjäll, Frank Pollmann, and Joel E. Moore, Phys. Rev. B **83**, 020407(R) (2011).

[9] J. B. Torrance Jr. and M. Tinkham, Phys. Rev. **187**, 587 (1969); **187**, 595 (1969).

[10] J. Villain, Physica B+C **79**, 1 (1975).

[11] H. Yoshizawa, K. Hirakawa, S. K. Satija, and G. Shirane, Phys. Rev. B **23**, 2298 (1981).

[12] S. E. Nagler, W. J. L. Buyers, R. L. Armstrong, and B. Briat, Phys. Rev. Lett. **49**, 590 (1982); J. Magn. Magn. Mater. **31**, 1213 (1983).

[13] H. C. Fogedby, Phys. Rev. B **10**, 4000 (1974).

[14] S. E. Nagler, W. J. L. Buyers, R. L. Armstrong, and B. Briat, Phys. Rev. B **28**, 3873 (1983).

[15] N. Ishimura and H. Shiba, Prog. Theor. Phys. **63**, 743 (1980).

[16] S. B. Rutkevich, J. Stat. Mech. (2010) P07015.

[17] M. Abramowitz and I. A. Stegun, *Handbook of Mathematical Functions* (Dover, New York, 1972).

[18] A. P. Prudnikov, Yu. A. Brychkov, and O. I. Marichev, *Integrals and Series, 2: Special Functions* (Gordon and Breach, New York, 1990).

[19] M. Suzuki, Phys. Lett. A **301**, 398 (2002).

[20] J. K. Kjems, J. Als-Nielsen, and Hans Fogedby, Phys. Rev. B **12**, 5190 (1975).

[21] H. Shiba, Prog. Theor. Phys. **64**, 466 (1980).

II

PHYSICAL REVIEW B **87**, 060401(R) (2013)

Numerical simulations of laser-excited magnetic Bloch oscillations

Sergey Shinkevich and Olav F. Syljuåsen
Department of Physics, University of Oslo, P. O. Box 1048 Blindern, N-0316 Oslo, Norway

(Received 23 October 2012; revised manuscript received 22 January 2013; published 4 February 2013)

We propose to use lasers to excite magnetic Bloch oscillations in one-dimensional easy-axis ferromagnets at low temperatures. This proposal is investigated numerically in detail for material parameters relevant for $CoCl_2 \cdot 2H_2O$.

DOI: 10.1103/PhysRevB.87.060401 PACS number(s): 75.78.−n, 75.40.Mg, 75.10.Pq, 78.47.D−

According to quantum mechanics a particle in a periodic potential will oscillate in response to a constant force. Such Bloch oscillations (BOs) were predicted in the early days of quantum mechanics,[1,2] but have only recently been experimentally demonstrated in very clean semiconductor superlattices,[3] in Bose-Einstein condensates,[4] and in optical[5] and ultrasonic[6] superlattices.

In condensed-matter systems the particles need not be of the ordinary kind resembling electrons. In particular, an elementary particle in a one-dimensional anisotropic ferromagnet is a domain wall separating regions of up and down spins. Such domain walls can have a dispersion relation like that derived from a periodic potential, and in the presence of a uniform magnetic field these magnetic systems have been predicted to show BOs.[7] In particular the blue crystalline material $CoCl_2 \cdot 2H_2O$ and $CoNb_2O_6$ have been proposed as candidate materials. However, no BOs have been experimentally observed in these to date.[8,9]

In a recent paper[10] we have revisited the material $CoCl_2 \cdot 2H_2O$ and refined the predictions of Ref. 7 for detecting spectral signatures of BOs in neutron-scattering experiments, taking also into account extra interactions present in the material. While our result indicates that the spectral signatures of BOs can indeed be observed in neutron scattering, the signatures are relatively weak, at the 10% level of the total spectral weight at finite temperatures. This is a consequence of neutrons being a relatively weak probe as they cause only single spin-flip excitations.

We propose here a more direct way to excite BOs by keeping the material at low temperature and induce excitations using a short laser pulse. Upon turning off the laser pulse the magnetization of the material will continue oscillating at the Bloch frequency. It has been known since long ago[11,12] that light in the far-infrared frequency range can induce magnetic excitations in $CoCl_2 \cdot 2H_2O$, but no time dependence of the magnetization was studied there.

In this Rapid Communication we model the laser pulse as a time-dependent perturbation to the Hamiltonian and investigate its effects by solving the time-dependent Schrödinger equation numerically. We show that BOs can be generated this way, and give appropriate laser frequencies and pulse-duration times.

The magnetic properties of $CoCl_2 \cdot 2H_2O$ are described by the spin-1/2 Hamiltonian[11,13]

$$H = -\sum_i \left(J_z S_i^z S_{i+1}^z + h_z S_i^z \right) + H_d, \tag{1}$$

where H_d denotes subdominant terms to be discussed below. The ferromagnetic coupling $J_z = 36.5$ K[11] is the dominant term in the Hamiltonian. Alone it causes neighboring spins to align their spin z components, thus the energy of an excited state depends on the number of antialigned spin neighbors: domain walls, where each domain wall costs an energy of $J_z/2$. In the presence of an external magnetic field along the z axis, h_z, the energy will also depend on the number of spins opposing the field, implying pairwise confinement of domain walls. Such a bound state of two domain walls separating l overturned spins, known as a spin cluster excitation,[11] or simply a domain, has an energy $J_z + h_z l$ above the ground-state energy.

The term H_d describes additional couplings that partly give dynamics to the domain walls and partly induce more domain walls,

$$H_d = -\sum_i [J_a(S_i^+ S_{i+1}^+ + S_i^- S_{i+1}^-) + J_\perp(S_i^+ S_{i+1}^- + S_i^- S_{i+1}^+)], \tag{2}$$

where $J_a = 3.8$ K[9] and $J_\perp = 5.43$ K.[9] $S_i^\pm = S_i^x \pm i S_i^y$ are the usual raising and lowering operators. The J_a term can move a domain wall two lattice spacings, thus mixing states with even (or odd) l. Similarly $J_\perp$ gives kinetic energy to the $l = 1$ domain state. Both of these terms can also induce new domain-wall pairs. However, with J_z being the dominant coupling, extra domain walls will be energetically costly, thus we will restrict our calculations to states having a small number of domain walls N_{dw}.

When restricting to $N_{dw} \leqslant 2$, H can be diagonalized. The energy spectrum is $E_n = J_z + \mu_n h_z$, where μ_n is found by solving an equation involving a ratio of Bessel functions.[10,14,15] For high energies $\mu_n \approx n$, an integer, thus the energy spectrum becomes equidistant, the so-called Wannier-Zeeman ladder (WZL).[16] The corresponding energy eigenfunctions $|\psi_n\rangle$ are Bessel functions.[10] From these one can construct a time-dependent state $|\chi(t)\rangle = \sum_n a_n e^{-iE_n t}|\psi_n\rangle$. When this state is dominated by energy eigenstates with energies from the equidistant region, the time dependence of the magnetization $M_z(t) = \langle \chi(t)| \sum_i S_i^z |\chi(t)\rangle$ becomes

$$M_z(t) = c - 2x_0 \sum_n \mathrm{Re}(a_n^* a_{n+2} e^{-i\omega_B t}), \tag{3}$$

where c is a constant, $\omega_B = 2h_z/\hbar$ is the Bloch frequency, and $x_0 = 2J_a/h_z$. Thus the BO amplitude is proportional to $4J_a/h_z$ times a factor which depends on the probability amplitudes a_n of the excited states. Our BO amplitude is a factor 2 larger

1098-0121/2013/87(6)/060401(5)

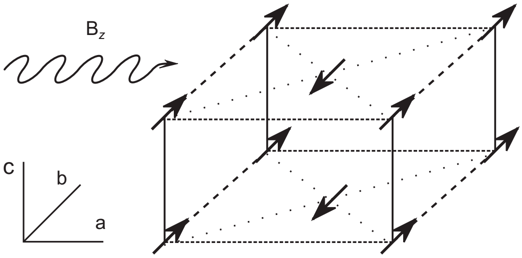

FIG. 1. In $CoCl_2 \cdot 2H_2O$ the spin z axis corresponds to the crystallographic b axis. The strong ferromagnetic J_z couples spins along the c axis. A laser beam is shown propagating at normal incidence to the b-c plane with magnetic-field polarization in the b direction.

than obtained in Ref. 7 as we consider the size oscillations of a single domain having two domain walls, while they considered the motion of a single domain wall.

In order to populate the excited levels at very low temperatures, thus producing BOs, we propose here to use a laser with a wavelength in the far infrared. The Co electrons causing the magnetism are d-shell electrons thus having no electric dipole moment.[17] We therefore model the laser as an extra time-dependent magnetic field which couples to the spins as

$$H_{\rm ext} = -B_0^z \cos(\omega t) \sum_i S_i^z, \qquad (4)$$

where ω is the laser frequency and B_0^z is the laser magnetic-field amplitude. We have here assumed a linearly polarized laser beam such that the magnetic field is along the Ising direction. This corresponds to the crystallographic b direction in $CoCl_2 \cdot 2H_2O$. Such a setup can be made by cleaving the crystals in the b-c plane and directing the laser at normal incidence to this surface polarizing the laser beam such that the magnetic field points along the b direction; see Fig. 1. We have assumed the laser beam to be coherent along its front, and also through the crystal. The laser considered here has a wavelength of about 0.3 mm thus for this approximation to be good the crystal should be thinner than this. For thicker crystals there will be an additional phase shift associated with the depth.

The time-dependent Hamiltonian $H + H_{\rm ext}$ can be treated numerically for large system sizes when restricting to states where $N_{dw} \leqslant 2$. This restriction implies that the energy gap between the ground state and any excited state will depend on the system size N. This can be understood by considering the perturbative energy correction from virtual processes involving the creation and destruction of an additional domain. As there are roughly N places to insert the new domain, the energy correction will be proportional to N. When restricting to $N_{dw} \leqslant 2$ the ferromagnetic state receives this correction, but not the states having one domain, as their corrections come from the excluded $N_{dw} \geqslant 4$ sector. In order to make the energy gap intensive we redefine the coupling between the ferromagnetic and the $l = 2$, $N_{dw} = 2$ state in the Hamiltonian by dividing it by a factor $\sqrt{N}$.[10] This effectively makes the correction to the ferromagnetic state independent of system size.

Starting in the ground state of H, the time-dependent Schrödinger equation is solved iteratively numerically with the laser field $H_{\rm ext}$ present. In the iterations we keep the 300 lowest energy states of H with zero momentum and $N_{dw} \leqslant 2$. The laser frequency ω is tuned such that $\omega = (E_n - E_0)/\hbar$ where n corresponds to an energy level in the region where the spectrum is approximately equidistant. We choose $n = 12$ corresponding to $E_{12} - E_0 \approx 1.6 J_z$ for a static magnetic field $h_z = 0.05 J_z$. With this we find essentially Rabi oscillations between the ground state and the $n = 12$ excited level with a Rabi frequency $\omega_R = |B_0^z \alpha_{12}|/\hbar$, where α_{12} is the matrix element of $\sum_i S_i^z$ between the ground state and the $n = 12$ excited state. Exciting the level $n = 12$ alone does not give Bloch oscillations as one also needs to populate the levels with $n + 2$ (or $n - 2$); see Eq. (3). This can be achieved by using a large laser amplitude which causes off-resonant tunneling between the n and the $n \pm 2$ levels. However, in order to get a sizable population of the $n \pm 2$ levels we have to use a laser amplitude as big as $B_0^z = 0.2 J_z$, which, with a g factor of 6.8,[11] corresponds to an electric-field amplitude of approximately 500 MV/m. Experimentally this is too large as the dielectric breakdown field strength of most insulators is an order of magnitude less than this.

To achieve population of nearby levels with a smaller laser amplitude we propose instead to use *two* lasers, each in resonance with one of the two nearby levels. Specifically we use $B_{01}^z = 0.01 J_z$, $\omega_1 = (E_{12} - E_0)/\hbar$, and $B_{02}^z = 0.03 J_z$, $\omega_2 = (E_{14} - E_0)/\hbar$ in our simulation. The population of the different levels as a function of time after the lasers are turned on is shown in Fig. 2. Only even n states are excited because the S^z terms do not flip any spins. The black dot-dashed curve in Fig. 2 shows how the ground state is depleted. The minimum of the ground-state population coincides with the maxima of the population of levels $n = 12$ and $n = 14$, and occurs roughly at a time $2 \times 10^4 \hbar/J_z$ for the parameters used here. Using smaller laser amplitudes this time gets larger proportional to the inverse laser amplitude.

We turn off $H_{\rm ext}$ at the first maximum of the population curves, $\tau = 20\,440 \hbar/J_z$. As the sum $\sum_n a_n^* a_{n+2}$ is dominated by the term $n = 12$, the amplitude of the BO will be proportional to $|a_{12}^* a_{14}|$ which is shown in the lower inset of Fig. 2. It shows a beating pattern corresponding to the two frequencies ω_1 and ω_2. It may be difficult to turn off the laser when this quantity is maximal. However, this is not a major concern as the variation is small. The time-averaged value is approximately 0.48.

Letting the system evolve further in time without $H_{\rm ext}$ produces the BOs shown in Fig. 3. As our simulation only allows single domain excitations we have plotted the relative size of the domain, measured by the expectation value of the number of spins opposing the field $N_{1\downarrow}(t) = M_z(t) - N/2$ divided by its time average $\bar{N}_{1\downarrow}$. $\bar{N}_{1\downarrow} \approx n$ for excitation E_n. We see that the relative size of the domain oscillates between 0.7 and 1.3 corresponding to a size between 9.1 and 16.9 for $\bar{N}_{1\downarrow} \approx (12 + 14)/2 = 13$. Thus the amplitude is 3.9 which is close to the expected value $4 J_a/h_z \times 0.48 = 4.0$ from Eq. (3). Allowing a finite density ρ of coherently oscillating domain states, the relative size of a single domain state

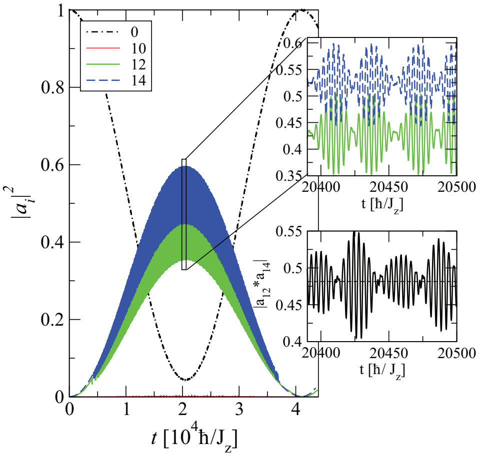

FIG. 2. (Color online) Population $|a_i|^2$ of selected energy levels i, indicated in the legend, as a function of time after turning on the two lasers. The laser frequencies and amplitudes are $\omega_1 = (E_{12} - E_0)/\hbar$, $B^z_{01} = 0.01 J_z$, and $\omega_2 = (E_{14} - E_0)/\hbar$, $B^z_{02} = 0.03 J_z$. The upper-right panel shows a zoom in the boxed time region. The lower-right panel shows the time dependence of $|a^*_{12}a_{14}|$. The time-averaged value is shown as the horizontal dashed line. The time scale $\hbar/J_z$ is 0.2×10^{-12} s for $\mathrm{CoCl_2 \cdot 2H_2O}$.

shown in Fig. 3 will be proportional to the experimentally relevant quantity, the time-dependent relative magnetization: $[M_z(t) - \bar{M}]\,/\,\bar{M} = \rho\bar{N}_{1\downarrow}\,/\,(1/2 - \rho\bar{N}_{1\downarrow})[N_{1\downarrow}(t)\,/\,\bar{N}_{1\downarrow} - 1]$. Assuming noninteracting domains we estimate that the density of domains per unit length is $\rho = c(1 - |a_0|^2)/\bar{N}_{1\downarrow}$, where c is a constant of the order unity. The lower panel of Fig. 3 shows the power spectrum of the BOs which reveals a single peak very close to $\omega_B = 2h_z/\hbar$. The small deviation reflects the fact that the spectrum is not exactly the WZL at low energies.[10]

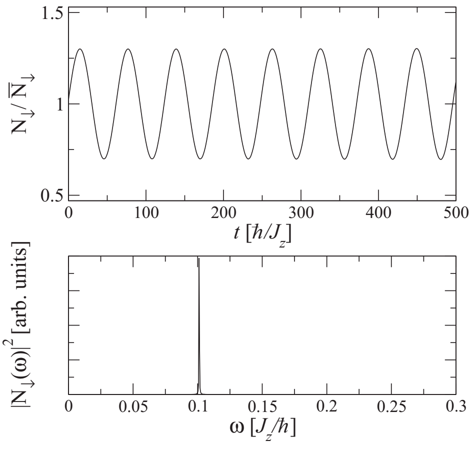

FIG. 3. Size oscillations of a domain excitation, measured as the number of down spins $N_{1\downarrow}/\bar{N}_{1\downarrow}$ vs time after the laser is switched off (upper panel), and its Fourier spectrum (lower panel).

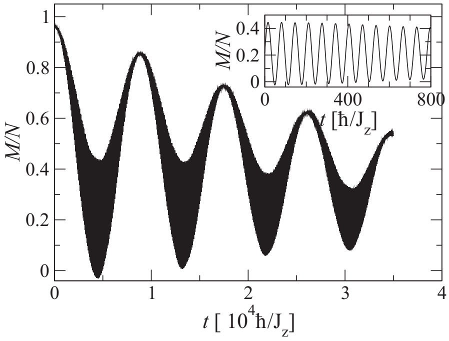

FIG. 4. Magnetization per site vs time for an interacting system in the presence of two laser beams, having amplitudes and frequencies as in Fig. 2 for $N = 32$ and $N_{dw} \leqslant 6$. The inset shows the magnetization vs time after the two lasers have been switched off at $\tau = 4420\hbar/J_z$.

One can also change the laser polarization to have a component along the spin-x direction. This will induce transitions between the even and odd n states. Our simulations show BOs also in this case, but with $\omega_B = h_z/\hbar$, which corresponds to the energy spacing between adjacent even and odd levels.

The restriction to $N_{dw} \leqslant 2$ and the associated redefinition of the coupling to the ferromagnetic state can raise doubts about the validity of the matrix elements calculation, also it does not allow for any discussion of interactions between domains. We have therefore numerically investigated cases where we allow more domains without any redefinition of couplings. Computer performance restrictions let us consider $N_{dw} \leqslant 6$ for $N \leqslant 34$.

In order to address the effects of interactions between domains we do a time-dependent simulation of the magnetization of a $N = 32$ system with $N_{dw} \leqslant 6$ in the presence of the two lasers. Figure 4 shows that the magnetization is rapidly varying, and has large-scale weakly damped oscillating behavior due to dephasing coming from populating other levels. We estimate the damping time scale to be roughly $5 \times 10^4\hbar/J_z$. We expect this time scale to decrease as the system size is increased. The time at which the magnetization envelope reaches its first minimum, $t_m = 4420\hbar/J_z$, is shorter than the time of maximal population in Fig. 2, $\tau = 20\,440\hbar/J_z$, by a factor $k = t_m/\tau = 1/4.6$. This is a reflection of the $\sqrt{N}$ in the matrix element connecting the ferromagnetic state to the single domain states, together with the near blocking by interactions and finite-size effects of states with more than one domain.[18,19] For larger system sizes we expect that k turns into $k = 1/\sqrt{R}$ where R is the distance, in units of the lattice spacing, between domains beyond which the domain-domain interaction energy is smaller than $B^z_{01}\alpha_{12} \approx B^z_{02}\alpha_{14}$. This energy scale is $\sim 10^{-4} J_z$ for the parameters in Fig. 4. When domains are closer than this the excitation of the second domain will be blocked by the presence of the first domain and will not participate in the resonance. On turning off the lasers at $t_m = 4420\hbar/J_z$ the magnetization oscillates at the Bloch frequency, shown in the inset of Fig. 4.

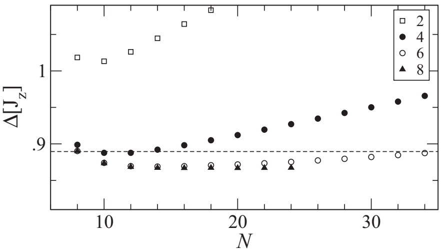

FIG. 5. Energy gap Δ to the first excited state vs system size N for different N_{dw}. The legend specifies the maximum N_{dw} included in the diagonalization. The dashed line shows the energy gap for $N_{dw} \leqslant 2$ with the $1/\sqrt{N}$ redefinition of the coupling to the ferromagnetic state.

To see how energies are affected by allowing more domains we have plotted in Fig. 5 the N dependence of the energy gap Δ to the first excited state. This decreases as higher domain-wall sectors are included. For comparison the $N_{dw} \leqslant 2$ result with redefined coupling to the ferromagnetic state is shown as the dashed line.

In order to identify the elementary domain excitations and the associated transition matrix elements, for the interacting system, we construct the approximate single domain creation operator[10]

$$a^{\dagger}_{p,n} = \sum_{l,j} \frac{e^{-ip(r_j+l/2)}}{\sqrt{N}} J_{(l-\mu_n)/2}\,(x_0 \cos p)\, \Pi_{k=j}^{j+l-1} S_k^{+} \tag{5}$$

with momentum $p = 0$ and let it act on the ferromagnetic state. The sum is restricted to even values of l, and $J_m(x)$ is the Bessel function of the first kind of order m with argument x. We then compute the overlap of this with the exact eigenstates of the $N_{dw} \leqslant 6$ system. For each value of n we pick the state with maximum overlap. Figure 6(a) shows the energies of these states. We see that for high enough n the energies become equidistant and agree well with what we found for $N_{dw} \leqslant 2$. The laser transition matrix element between these states and the ground state behaves as $\sqrt{N}\alpha_n$. The coefficients α_n are very close to those we found for $N_{dw} \leqslant 2$; see Fig. 6(a). Note that α_n drops very fast with increasing n.

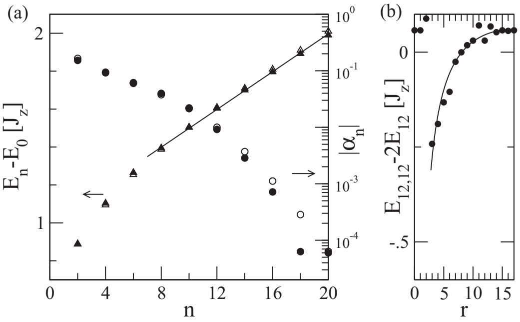

FIG. 6. (a) Excitation energy of elementary domain states vs n (triangles). Also shown is $|\alpha_n|$ vs n (circles) on a semilog scale. Filled symbols refer to $N_{dw} \leqslant 6$ and $N = 34$, while open symbols are for $N_{dw} \leqslant 2$ with redefined coupling to the ferromagnetic state. (b) Interaction energy of two $n = 12$ excitations vs separation distance r for $N_{dw} \leqslant 6$ and $N = 34$.

Further insights about interactions can be gotten by identifying two-domain excitations. We construct approximate two-domain states as pairs with total momentum zero of two $n = 12$ single domain states separated by a distance r, with creation operator $b^{\dagger}_{r,n} = \sum_p a^{\dagger}_{p,n} a^{\dagger}_{-p,n} e^{-ipr}$. We let this act on the ferromagnetic state, retain only the terms having four domain walls, and compute its overlap with the exact eigenstates of the $N_{dw} \leqslant 6$ system. The energy of the states with maximum overlap minus two times the single-particle excitation energy E_{12} is shown in Fig. 6(b) as a function of r. We interpret this as the interaction energy of domains separated by r lattice spacings. We find that the functional form $a - b[1/r + 1/(N-r)]$ fits the results reasonably with $a = 0.22J_z$ and $b = 1.37J_z$. The positive a is caused by the restriction on N_{dw} which tends to overestimate energies in higher domain-wall sectors relative to those in lower sectors. This interaction energy causes an inhomogeneous broadening of the resonance frequency, and can lead to an upper limit on the density of domains excited by the laser together with an increased oscillation frequency due to interaction blocking effects, as seen in Fig. 4.

We conclude that it should be possible to excite magnetic BOs in $CoCl_2 \cdot 2H_2O$ using two resonant lasers at low temperatures in a static magnetic field. On turning off the lasers after an excitation time τ the magnetization of $CoCl_2 \cdot 2H_2O$ will oscillate at the Bloch frequency which is proportional to the static magnetic field and is 500 GHz for $CoCl_2 \cdot 2H_2O$ in a 0.4 T field. In order to generate the BOs one needs to populate at least two nearby levels in the WZL. Due to the relatively small laser transition matrix elements connecting the ground state to these levels we propose to use two large amplitude resonant lasers. It should be possible to use also resonant lasers with smaller amplitudes at the expense of longer excitation times, limited by the coherence time of the system. Collisions between domains can lead to dephasing behavior and associated decoherence. The domain excitations are heavy due to their flat dispersion, so we expect a significant effect only at a high density of excitations when neighboring domains are close together. We have performed a simulation taking into account the interaction between domains for a system of size $N = 32$. From this we conclude that the interactions cause a blocking effect which speeds up the excitation process and that the dephasing time scale due to interactions is long compared with the excitation time for the parameters considered. Other effects might contribute to dephasing such as static impurities and interactions between chains. We have not studied these, but given the fact that the oscillations considered here are localized within a region of roughly 20 sites, we expect that the effects of static impurities are small for an impurity concentration of less than a few percent. In addition to $CoCl_2 \cdot 2H_2O$ our simulations using the Hamiltonian and parameters from Ref. 20 also indicate that BOs in $CoNb_2O_6$ may be excited in a similar way.

[1] F. Bloch, Z. Phys. **52**, 555 (1929).

[2] C. Zener, Proc. R. Soc. London, Ser. A **145**, 523 (1934).

[3] E. E. Mendez, F. Agullo-Rueda, and J. M. Hong, Phys. Rev. Lett. **60**, 2426 (1988).

[4] M. Ben Dahan, E. Peik, J. Reichel, Y. Castin, and C. Salomon, Phys. Rev. Lett. **76**, 4508 (1996).

[5] R. Sapienza, P. Costantino, D. Wiersma, M. Ghulinyan, C. J. Oton, and L. Pavesi, Phys. Rev. Lett. **91**, 263902 (2003).

[6] H. Sanchis-Alepuz, Y. A. Kosevich, and J. Sánchez-Dehesa, Phys. Rev. Lett. **98**, 134301 (2007).

[7] J. Kyriakidis and D. Loss, Phys. Rev. B **58**, 5568 (1998).

[8] N. B. Christensen, K. Lefmann, I. Johannsen, and O. Jørgensen, Physica B **276**, 784 (2000).

[9] W. Montfrooij, G. E. Granroth, D. G. Mandrus, and S. E. Nagler, Phys. Rev. B **64**, 134426 (2001).

[10] S. Shinkevich and O. F. Syljuåsen, Phys. Rev. B **85**, 104408 (2012).

[11] J. B. Torrance Jr. and M. Tinkham, Phys. Rev. **187**, 587 (1969); **187**, 595 (1969).

[12] D. F. Nicoli and M. Tinkham, Phys. Rev. B **9**, 3126 (1974).

[13] H. C. Fogedby, Phys. Rev. B **5**, 1941 (1972).

[14] H. C. Fogedby, Phys. Rev. B **10**, 4000 (1974).

[15] S. B. Rutkevich, J. Stat. Mech. (2010) P07015.

[16] G. Wannier, Phys. Rev. **117**, 432 (1960).

[17] W. J. L. Buyers, T. M. Holden, E. C. Svensson, R. A. Cowley, and M. T. Hutchings, J. Phys. C **4**, 2139 (1971).

[18] M. D. Lukin, M. Fleischhauer, R. Cote, L. M. Duan, D. Jaksch, J. I. Cirac, and P. Zoller, Phys. Rev. Lett. **87**, 037901 (2001).

[19] E. Urban, T. A. Johnson, T. Henage, L. Isenhower, D. D. Yavuz, T. G. Walker, and M. Saffman, Nat. Phys. **5**, 110 (2009).

[20] J. A. Kjäll, F. Pollmann, and J. E. Moore, Phys. Rev. B **83**, 020407(R) (2011).

PHYSICAL REVIEW B **83**, 054423 (2011)

Spin-wave calculation of the field-dependent magnetization pattern around an impurity in Heisenberg antiferromagnets

Sergey Shinkevich,[1] Olav F. Syljuåsen,[1] and Sebastian Eggert[2]

[1]*Department of Physics, University of Oslo, P.O. Box 1048 Blindern, N-0316 Oslo, Norway*

[2]*Department of Physics and Research Center OPTIMAS, University of Kaiserslautern, D-67663 Kaiserslautern, Germany*

(Received 4 November 2010; published 22 February 2011)

We consider the magnetic-field-dependent spatial magnetization pattern around a general impurity embedded in a Heisenberg antiferromagnet using both an analytical and a numerical spin-wave approach. The results are compared to quantum Monte Carlo simulations. The decay of the magnetization pattern away from the impurity follows a universal form which reflects the properties of the pure antiferromagnetic Heisenberg model. Only the overall magnitude of the induced magnetization depends also on the size of the impurity spin and the impurity coupling.

DOI: 10.1103/PhysRevB.83.054423 PACS number(s): 75.10.Jm, 75.25.−j, 75.20.Hr, 75.40.Mg

I. INTRODUCTION

The local magnetization around impurities in antiferromagnets has already been studied by nuclear magnetic resonance (NMR) experiments since the early 1970s.[1,2] The analysis of local Knight shifts has been expanded after the discovery of high-temperature superconductivity.[3] Typically, the strongly correlated state is reflected by the observation of large alternating magnetic moments around static impurities,[3] which become especially strong in one dimension.[4] Another remarkable experimental tool is given by scanning tunneling microscopy (STM),[5] which offers the unique possibility of studying materials directly on the atomic scale. In particular, by coating the STM tips with different magnetic materials,[6] so-called spin-polarized scanning tunneling microscopy (SP-STM) has made it possible to study the magnetization of individual atoms.[7]

From the theoretical point of view, antiferromagnets are often represented by the isotropic Heisenberg model with static impurities. In this case the pinning of the order is a result of an interplay of the applied uniform magnetic field with impurities. The first theoretical studies of impurities in an antiferromagnet date back to the 1960s.[8,9] More recent research has made much progress in the understanding of the impurity behavior in one-dimensional[4,10,11] and two-dimensional[12–14] Heisenberg antiferromagnets. In particular, the magnetic response around a vacancy in an isotropic antiferromagnet was studied in Ref. 15 using a hydrodynamic approach. In this work, we now extend those studies by considering the local magnetization using spin-wave theory for a more general impurity type, which is given by a spin S_0 coupled to the host antiferromagnet with a general coupling J_0. One main result is that the decay constant of the magnetization is to leading order governed by properties of the host magnet, while the overall magnitude is governed by properties of the impurity and its coupling to the host antiferromagnet. We complement our analytical spin-wave analysis with quantum Monte Carlo (QMC) simulations as well as a numerical spin-wave approach for the case of calculating the magnetization on and close to the impurity site.

II. HAMILTONIAN

We consider the following Hamiltonian of a Heisenberg-type magnet in a magnetic field

$$H = \sum_{\langle i,j \rangle} J_{ij} \vec{S}_i \cdot \vec{S}_j - \sum_i B_i S_i^z \tag{1}$$

on a hypercubic lattice where each site has Z nearest neighbors. We will start out with general site-dependent couplings J_{ij} and magnetic fields B_i and later specialize to the case of a single impurity in an otherwise uniform antiferromagnet in a homogeneous field.

In order to treat the nonhomogeneous Hamiltonian in Eq. (1) with spin-wave theory, let us first review in detail how to derive the expansion in fluctuations about an ordered classical state. The classical state of an antiferromagnet in a magnetic field is that of canted spins pointing partly along the z axis (see Fig. 1). In order to parametrize this state we introduce rotated spins $\vec{S}'$ so that $S_i'^z$ points along a direction parametrized by the angles θ_i and ϕ_i (see Fig. 1).

The rotated spin components $\vec{S}'$ are related to the spin components in Eq. (1) as

$$\begin{aligned} S_i^x &= \left(S_i'^x \sin\theta_i - S_i'^z \cos\theta_i\right)\cos\phi_i - S_i'^y \sin\phi_i, \\ S_i^y &= \left(S_i'^x \sin\theta_i - S_i'^z \cos\theta_i\right)\sin\phi_i - S_i'^y \cos\phi_i, \\ S_i^z &= S_i'^x \cos\theta_i + S_i'^z \sin\theta_i. \end{aligned} \tag{2}$$

Inserting these into Eq. (1) we get the Hamiltonian expressed in terms of rotated spins for arbitrary angles, which will be determined later. In order to express the fluctuations about the ordered state we use the Holstein-Primakoff transformation[16] on the rotated spins into bosonic operators

$$\begin{aligned} S_i'^z &= S_i - a_i^\dagger a_i, \\ S_i'^+ &= \sqrt{2S_i}\sqrt{1-\frac{a_i^\dagger a_i}{2s}}\,a_i, \\ S_i'^- &= \sqrt{2S_i}\,a_i^\dagger\sqrt{1-\frac{a_i^\dagger a_i}{2s}}, \end{aligned} \tag{3}$$

1098-0121/2011/83(5)/054423(10)

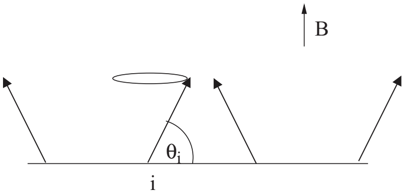

FIG. 1. The canted spin state for classical spins. $\theta_i \in [0,\pi/2]$ is the angle between the spin i and a line drawn perpendicular to the applied magnetic field B. The angle $\phi_i \in [0,2\pi]$ parametrizes how much the spin i is rotated (a full rotation is indicated by the ellipse) about the applied magnetic field.

where expanding the square roots and using $S_i'^{\pm} = S'^x \pm i S'^y$ yields

$$\begin{aligned} S_i'^x &= \sqrt{\frac{S_i}{2}}\left[a_i + a_i^\dagger - \frac{1}{4s}(a_i^\dagger a_i a_i + a_i^\dagger a_i^\dagger a_i) + \cdots\right], \\ S_i'^y &= -i\sqrt{\frac{S_i}{2}}\left[a_i - a_i^\dagger - \frac{1}{4s}(a_i^\dagger a_i a_i - a_i^\dagger a_i^\dagger a_i) + \cdots\right]. \end{aligned} \tag{4}$$

By inserting these expressions for $\vec{S}'$ into the Hamiltonian (1) we get terms H_n with different powers n of bosonic operators.

The zeroth-order term in boson operators corresponds to the energy of classical spins oriented along the S'^z axes. This is so because in the classical limit $S_i \to \infty$ the S'^x and S'^y components are overwhelmed by the S'^z component which is proportional to S. The zeroth-order terms read

$$\begin{aligned} H_0 = &\sum_{\langle ij\rangle} J_{ij} S_i S_j (\cos\theta_i \cos\theta_j \cos(\phi_{ij}) + \sin\theta_i \sin\theta_j) \\ &- \sum_i B_i S_i \sin\theta_i, \end{aligned} \tag{5}$$

where $\phi_{ij} = \phi_i - \phi_j$. Because of the $U(1)$ symmetry of spin rotations about the magnetic field axis H_0 depends on the relative angles ϕ_{ij}. Minimizing with respect to ϕ_{ij} gives the condition

$$-J_{ij} S_i S_j \cos\theta_i \cos\theta_j \sin(\phi_{ij}) = 0, \tag{6}$$

meaning that $\phi_{ij} = 0$ or π. For this to be a *minimum* of the energy one needs $-J_{ij}\cos(\phi_{ij}) > 0$, which means that $\phi_{ij} = \pi$ for an antiferromagnetic coupling and 0 for a ferromagnetic one. Equivalently, $-\cos(\phi_{ij}) = J_{ij}/|J_{ij}| \equiv \nu_{ij}$. In the following we will select the rotation angle ϕ_0 so that it is either 0 or π. With this choice, and the minimization condition $\phi_{ij} = 0$ or π, all terms with $\sin\phi_i$ will be zero. Then the Hamiltonian can be written

$$\begin{aligned} H = &\sum_{\langle ij\rangle} J_{ij}\big[\cos(\theta_i + \nu_{ij}\theta_j)\big(S_i'^x S_j'^x - \nu_{ij} S_i'^z S_j'^z\big) \\ &- \nu_{ij} S_i'^y S_j'^y + \sin(\theta_i + \nu_{ij}\theta_j)\big(\nu_{ij} S_i'^x S_j'^z + S_i'^z S_j'^x\big)\big] \\ &- \sum_i B_i \left(S_i'^x \cos\theta_i + S_i'^z \sin\theta_i\right). \end{aligned} \tag{7}$$

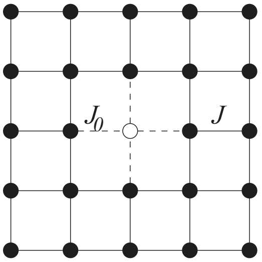

FIG. 2. Couplings. Dashed lines indicate the coupling J_0 to the impurity site (empty circle) while solid lines indicate J.

We will now specialize to the case of a single impurity embedded in an otherwise uniform antiferromagnet of spin-S spins. We label the impurity site $i = 0$ and allow for an impurity spin S_0 which, in general, can be different from S. We take all bonds not connected to the impurity to be antiferromagnetic with a magnitude J. The bonds connected to the impurity are also equal, but of a different magnitude J_0 and can be either ferromagnetic or antiferromagnetic (see Fig. 2); ν_0 denotes the sign of J_0. This antiferromagnet is placed in a magnetic field oriented along the z direction with magnitude B. We have absorbed the Zeeman coupling into the magnitude of the magnetic field. In order to allow for a different gyromagnetic factor of the impurity spin and thus a different Zeeman coupling, we label the magnitude of the effective magnetic field on the impurity site B_0 which, in general, can be different from B.

In order to simplify Eq. (7) we use an initial rotated frame that is given by a site-independent value of $\theta_i = \theta$ for all sites i away from the impurity site to zeroth order. We will later allow for a site-dependent shift of θ in order to calculate the nontrivial local variation of the magnetization. For the impurity site $i = 0$ we keep a separate angle θ_0. Performing this ansatz the zeroth-order term in boson operators takes the form

$$\begin{aligned} H_0 = &-NS\left(\frac{JSZ}{2}\cos 2\theta + B\sin\theta\right) \\ &+ ZS(JS\cos 2\theta - |J_0| S_0 \cos(\theta + \nu_0\theta_0)) \\ &+ BS\sin\theta - B_0 S_0 \sin\theta_0. \end{aligned} \tag{8}$$

Minimizing this with respect to θ and θ_0 in the thermodynamic limit, $N \to \infty$, determines the angles θ and θ_0,

$$\sin\theta = \frac{B}{2SZJ} \tag{9}$$

and

$$\tan\theta_0 = \frac{B_0}{|J_0| SZ\cos\theta} - \nu_0 \tan\theta. \tag{10}$$

The zeroth-order condition on θ is identical to the one found for a uniform antiferromagnet in a homogeneous field and does not depend on the impurity. This is a natural consequence of taking a site-independent ansatz in the thermodynamic limit.

When using the value of θ obtained from Eq. (9) the terms that are of linear order in boson operators connected to the bulk behavior vanish. After also using the condition (10) only linear terms of bosons around the impurity are left:

$$H_1 = \frac{C}{Z}\sum_{\langle 0j\rangle}(a_j + a_j^\dagger), \tag{11}$$

where the sum is restricted to run over the nearest neighbors of the impurity spin. This expression can be interpreted as a local effective field in the rotated frame acting on the spins that are coupled to the impurity spin, which will cause a shift of the angles θ over an extended range as we will see later.

The constant C is given by

$$C = J_0 S_0 Z\sqrt{\frac{S}{2}}\nu_0 \sin(\nu_0\theta_0 + \theta) - JSZ\sqrt{\frac{S}{2}} \sin 2\theta \tag{12}$$

or equivalently when we use the minimization conditions

$$C = \sqrt{\frac{S}{2}}\left(\frac{S_0}{S}\nu_0 B_0 \cos\theta_0 - B\cos\theta\right). \tag{13}$$

The linear terms can also be written in terms of Fourier transforms

$$a_i = \frac{1}{\sqrt{N}}\sum_{\vec{k}} a_{\vec{k}} e^{i\vec{k}\cdot\vec{r}_i} \tag{14}$$

as

$$H_1 = \frac{C}{\sqrt{N}}\sum_{\vec{k}} \gamma_{\vec{k}}(a_{\vec{k}} + a_{\vec{k}}^\dagger), \tag{15}$$

where we have defined $\gamma_k = 2(\cos k_x + \cos k_y + \cdots)/Z$, where the k's are given in units of the inverse lattice spacing and the dots indicate the remaining directions on the hypercubic lattice.

For the quadratic terms we will as a first approximation keep only the terms that are leading order in N. Therefore, the quadratic terms are identical to those in the absence of an impurity

$$H_2^{\text{bulk}} = \frac{1}{2}\sum_{\vec{k}}\{A_{\vec{k}} a_{\vec{k}}^\dagger a_{\vec{k}} + B_{\vec{k}} a_{\vec{k}} a_{-\vec{k}} + \text{H.c.}\}, \tag{16}$$

where $A_{\vec{k}} = JSZ(\cos 2\theta - \gamma_{\vec{k}} \sin^2\theta) + B\sin\theta = JSZ(1 - \gamma_{\vec{k}}\sin^2\theta)$ and $B_{\vec{k}} = JSZ\cos^2\theta\gamma_{\vec{k}}$ which are also known from standard spin-wave theory.[17] The neglected quadratic impurity terms can, in principle, lead to a renormalization of the overall magnitude in the local order around the impurity. However, this effect is known to be surprisingly small from numerical studies,[18] so that we can omit those terms for now in order to calculate the magnetization around the impurity. We will include them later when considering the magnetization of the impurity spin itself.

The quadratic term can be diagonalized by the canonical transformation

$$a_{\vec{k}} = u_{\vec{k}} b_{\vec{k}} + v_{\vec{k}} b_{-\vec{k}}^\dagger, \tag{17}$$

which results in the quadratic Hamiltonian

$$H_2^{\text{bulk}} = \sum_{\vec{k}}\omega_{\vec{k}} b_{\vec{k}}^\dagger b_{\vec{k}} + \frac{1}{2}\sum_{\vec{k}}(\omega_{\vec{k}} - A_{\vec{k}}), \tag{18}$$

where $\omega_{\vec{k}} = \sqrt{A_{\vec{k}}^2 - B_{\vec{k}}^2}$ which becomes

$$\omega_{\vec{k}} = JSZ\sqrt{(1-\gamma_{\vec{k}})(1+\cos 2\theta\gamma_{\vec{k}})}. \tag{19}$$

The transformation coefficients obey $u_{\vec{k}}^2 - v_{\vec{k}}^2 = 1$, $u_{\vec{k}}^2 + v_{\vec{k}}^2 = A_{\vec{k}}/\omega_{\vec{k}}$, and $2u_{\vec{k}}v_{\vec{k}} = -B_{\vec{k}}/\omega_{\vec{k}}$.

Using the quadratic bulk Hamiltonian we can calculate the following expectation values:

$$\begin{aligned}
\delta &= \langle a_i a_i\rangle = \frac{1}{N}\sum_{\vec{k}} u_{\vec{k}} v_{\vec{k}},\\
\Delta &= \langle a_i a_j\rangle = \frac{1}{N}\sum_{\vec{k}} \gamma_{\vec{k}} u_{\vec{k}} v_{\vec{k}},\\
m &= \langle a_i^\dagger a_j\rangle = \frac{1}{N}\sum_{\vec{k}} \gamma_{\vec{k}} v_{\vec{k}}^2,\\
n &= \langle a_i^\dagger a_i\rangle = \frac{1}{N}\sum_{\vec{k}} v_{\vec{k}}^2
\end{aligned} \tag{20}$$

for nearest-neighbor sites i and j. Note that the bulk nature of the quadratic term dictates that these expressions do not depend on i and j. At this stage we truncate higher-order terms in the Hamiltonian. Therefore we have reduced the problem to a solvable bulk Hamiltonian in Eq. (16) together with an impurity term in Eq. (15).

III. MAGNETIZATION AWAY FROM THE IMPURITY

The magnetization in the direction of the field $M_i^z = \langle S_i^z\rangle$ is

$$M_i^z = \langle S_i^{\prime x}\rangle \cos\theta_i + \langle S_i^{\prime z}\rangle \sin\theta_i. \tag{21}$$

Expressed in terms of bosons the above expression is up to quadratic order

$$M_i^z \approx \sin\theta_i(S_i - \langle a_i^\dagger a_i\rangle) + \cos\theta_i\sqrt{\frac{S_i}{2}}(\langle a_i^\dagger\rangle + \langle a_i\rangle). \tag{22}$$

To calculate these expectation values in the presence of the impurity we perform a shift of the boson operators

$$a_i \to a_i + \alpha_i \tag{23}$$

so as to get rid of the remaining linear terms in the Hamiltonian in Eq. (15). This is equivalent to a site-dependent variation of the angle θ_i. The impurity-induced shift is given by

$$\alpha_i = -\frac{C}{N}\sum_{\vec{k}}\frac{\gamma_{\vec{k}}}{A_{\vec{k}} + B_{\vec{k}}} e^{i\vec{k}\cdot\vec{r}_i}. \tag{24}$$

For future convenience we parametrize

$$A_{\vec{k}} + B_{\vec{k}} = f(1 + g\gamma_{\vec{k}}) \tag{25}$$

in terms of constants f and g which to leading order in $1/S$ are obtained from Eq. (16); $f = JSZ$ and $g = \cos 2\theta$.

Shifting the boson operators gives the following expression for the magnetization:

$$M_i^z \approx \sin\theta_i(S_i - |\alpha_i|^2 - \langle a_i^\dagger a_i\rangle) + \sqrt{\frac{S_i}{2}}\cos\theta_i(\alpha_i^* + \alpha_i). \tag{26}$$

Since the shift of the boson operators has eliminated the linear terms, we can now use the usual bulk theory to calculate the corresponding expectation value $n = \langle a_i^\dagger a_i \rangle$ in Eq. (20). Thus the magnetization takes the form

$$M_i^z \approx \sin\theta(S - |\alpha_i|^2 - n) + \sqrt{\frac{S}{2}}\cos\theta(\alpha_i^* + \alpha_i), \quad i \neq 0. \tag{27}$$

As is shown in the Appendix, α_i is real and changes sign depending on which sublattice i belongs with $e^{i\vec{Q}\cdot\vec{r}} = (-1)^{x_i+y_i+z_i}$, where $\vec{Q} = (\pi,\pi,\pi)$ is the antiferromagnetic wave vector. Here we have specialized to the cubic lattice. The case of the quadratic lattice can be obtained by setting $z_i = 0$ and $\vec{Q} = (\pi,\pi)$. With this oscillating behavior it is convenient to write $\alpha_i = (-1)^{x_i+y_i+z_i}\tilde{\alpha}_i$ and to divide the magnetization into an alternating and a nonalternating part. Using the assumption that $\tilde{\alpha}_i$ does not vary rapidly, the alternating (nonalternating) magnetization on site i is obtained by taking half of the magnetization on an odd sublattice site i and subtract (add) half of the magnetization on the neighboring even sublattice sites surrounding site i. Therefore, the nonalternating part takes the form

$$M_{\mathrm{nalt},i}^z = \sin\theta\left(S - n - \tilde{\alpha}_i^2\right), \tag{28}$$

which will decay rapidly to its uniform bulk value. This nonalternating part is not our primary focus here. Instead we will focus on the alternating part which does not decay as rapidly. To leading order the alternating magnetization is

$$M_{\mathrm{alt},i}^z = -\sqrt{2S}\cos\theta\tilde{\alpha}_i, \tag{29}$$

thus $\tilde{\alpha}_i$ dictates its behavior. The sum in Eq. (24) can be carried out by expanding the integrand about the minimum of the denominator which is at the antiferromagnetic point $\vec{Q}$, as shown in the Appendix. Carrying out this expansion for the case $i \neq 0$, we get in $D = 2$ and $D = 3$ dimensions.

$$\tilde{\alpha}_i \approx \frac{CZ}{2\pi f g^2}\begin{cases} K_0(r_i/d), & D = 2 \\ e^{-r_i/d}/(2r_i), & D = 3 \end{cases}, \quad i \neq 0, \tag{30}$$

where $r_i = \sqrt{x_i^2 + y_i^2 + z_i^2}$ is the distance from the impurity in units of the lattice spacing and K_0 is the zeroth-order modified Bessel function of the second kind which decays as $e^{-r_i/d}/\sqrt{r_i}$ for large arguments. The characteristic decay scale is

$$d = \sqrt{\frac{g}{Z(1-g)}} \tag{31}$$

in both cases. The result in Eq. (30) is the main result of this section for the induced magnetization by the general impurity model, which will be compared to Monte Carlo results in the following. Note that the shape and the decay scale d are universal and only depend on properties of the host magnet in the bulk. Only the constant prefactor C in Eq. (13) depends on impurity properties S_0, J_0, and B_0. With the expression $g = \cos 2\theta$, the decay constant is $d = [\cos 2\theta/(2Z\sin^2\theta)]^{1/2}$.

In Fig. 3 we have plotted a comparison of M_{alt}^z calculated using the expressions in Eqs. (29) and (30) and results from a QMC simulation. The QMC simulations were carried out using the stochastic series expansion technique[19] using directed-loop updates[20] at a low temperature $T/J = 0.05$ on a 128×128 square lattice. As can be seen from Fig. 3 , the leading-order analytical result decays faster than the QMC result. However, the decay d depends crucially on the exact expression for $A_{\vec{k}} + B_{\vec{k}}$ which we have approximated with its leading-order value $d = [\cos 2\theta/(2Z\sin^2\theta)]^{1/2}$. In fact, we can do better by including $1/S$ corrections. Taking into account $1/S$ corrections to $A_{\vec{k}} + B_{\vec{k}}$ and to the angle $\sin\theta$, we get

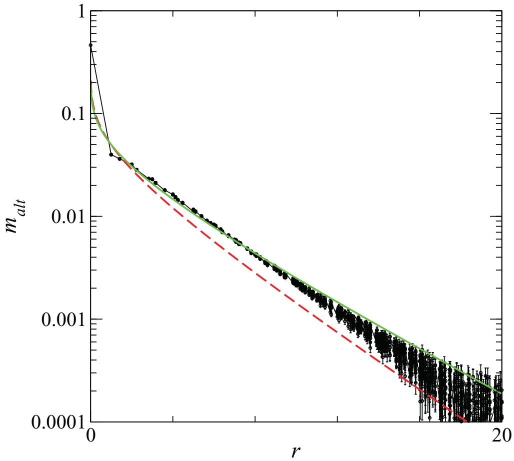

FIG. 3. (Color online) M_{alt}^z vs distance from the impurity r on the square lattice. The circles are quantum Monte Carlo data, while the dashed line (red) is a plot of the analytic result (29) using $g = \cos 2\theta$. The result where we have taken into account $1/S$ corrections for $A_{\vec{k}} + B_{\vec{k}}$ is shown as the solid line (green). Here $S = S_0 = 1/2$, $Z = 4$, $B = B_0 = 0.4J$, and $J_0 = 0.1J$.

$$\begin{aligned} A_{\vec{k}} + B_{\vec{k}} = JSZ\Bigg[1 - \frac{2n + 2\Delta + m}{2S} - \sin^2\theta\frac{m + \Delta}{2S} \\ + \gamma_{\vec{k}}\Bigg(\cos 2\theta - \frac{2n + 2m + 2\Delta + \delta}{2S} \\ - \sin^2\theta\frac{2n + 2m + 2\Delta - \delta}{S}\Bigg)\Bigg]. \end{aligned} \tag{32}$$

This result can also be inferred from Ref. 17. The $1/S$ corrections give modified expressions for the constants f and g, which lead to better agreement with the $S = 1/2$ Monte Carlo data in Fig. 3 . For higher spin S of the embedding lattice we expect that the $1/S$ corrections become less important, and the decay $d\sqrt{Z}$ will depend only on the scaling variable B/SZJ. By also allowing another classical angle θ_1 for the impurity nearest-neighbor spins the agreement with QMC close to the impurity site can be improved at the expense of having more complicated analytic expressions. To connect our result in Eqs. (29) and (30) to that obtained in Ref. 15 for the induced magnetization around a vacancy ($J_0 = 0$) we observe that for $\vec{k}$ close to $\vec{Q}$ but $|\vec{k} - \vec{Q}| > [8\sin^2\theta/\cos 2\theta]^{1/2}$ the dispersion equation (19) is linear with a spin-wave velocity $c = 2JS\sqrt{2}\cos 2\theta$. In the limit $B \rightarrow 0$ this becomes the well-known leading-order spin-wave theory result for the spin-wave velocity of an antiferromagnet. Combining this with

Eq. (9) we see that the decay constant of Ref. 15 becomes $c/B = [\cos 2\theta/(8 \sin^2 \theta)]^{1/2}$, which equals the leading-order result for the decay constant d. Similarly, we can compare the factor multiplying the Bessel function K_0. In the case of a vacancy $J_0 = 0$ our expression for $C = -(S/2)^{1/2} B \cos\theta$ so that the prefactor becomes

$$-\sqrt{2S}\,\cos\theta\,\frac{C}{2\pi f g^2} \approx \frac{B}{2\pi J}, \tag{33}$$

where we have used $f = JSZ$ and $g = \cos 2\theta$ and approximated $\cos\theta \approx 1$ which is valid for low magnetic fields. This is to be compared to the expression $m_{\max} SB/(2\pi\rho_s)$ obtained in Ref. 15. When inserting the leading-order expressions $m_{\max} = S$, $\rho_s = JS^2$ we see that the two results become equal.

For larger fields the use of the renormalized zero-field spin-wave velocity c in Ref. 15 is not so natural, however. As the decay depends heavily on the behavior of $A_{\vec{k}} + B_{\vec{k}}$ around $\vec{k} = \vec{Q}$, where the dispersion is quadratic in a finite field, it is more natural to relate the decay constant to the effective mass of this minimum. For finite but not too large fields the dispersion around $\vec{Q}$ can be written $\omega_{\vec{k}} = B + \frac{\vec{k}^2}{2m}$, where the effective mass is $m = \frac{2Z \sin^2\theta}{B \cos 2\theta}$. It is then straightforward to see that the leading-order decay constant can also be written $d = 1/\sqrt{Bm}$.

While the decay of the induced alternating magnetization pattern is governed by the properties of the uniform magnet, the *magnitude* of the alternating magnetization is given in terms of the prefactor C in Eq. (13), which depends on impurity properties, as shown in Figs. 4 and 5. For impurity spin $S_0 = 1/2$ and coupling $0 < J_0 < 1$, the prefactor C is negative and rather small. For $J_0 = J$ it vanishes completely because it corresponds to the uniform case. For ferromagnetic couplings $J_0 < 0$, $|C|$ gets larger with increasing magnetic field B/J. Thus we expect a substantial induced alternating magnetization pattern for ferromagnetically coupled impurities. Note, however, that when the field gets larger the magnetization pattern decays faster with distance from the impurity. For an $S_0 = 1$ impurity, $|C|$ is no longer necessarily small for antiferromagnetic couplings and it changes sign at a small positive value of J_0/J. The sign change signals a sublattice change in the magnetization pattern as indicated in Fig. 6, where for a ferromagnetic impurity the magnetization follows the pattern shown in Fig. 6(a). This pattern extends also to weak antiferromagnetic couplings up to a critical value of J_0 that depends on the magnetic field where it becomes favorable to interchange the orientation of magnetization on the two sublattices while keeping the impurity spin oriented along the field. This results in the pattern shown in Fig. 6(b). For large values of B/J and for all couplings except large antiferromagnetic ones, $|C|$ increases linearly with field strength B/J, as shown in Fig. 5. For $S_0 = 1$ and a small antiferromagnetic coupling J_0, C changes sign as the magnetic field is increased (see second curve from the top in Fig. 5). Thus a change in the sublattice rearrangement in Fig. 6 can also happen for a fixed J_0 as the magnetic field is varied. The exact point where C reverses sign is special, because when $C = 0$ the spin-1 impurity appears to have no effect on the host spins of the surrounding antiferromagnet. Therefore, the field and/or the coupling can be tuned in such a way that the impurity becomes almost invisible to the bulk, i.e., very little scattering occurs.

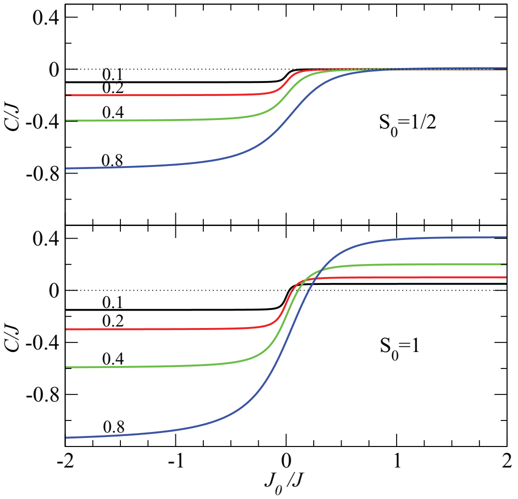

FIG. 4. (Color online) C/J vs impurity coupling J_0 for impurity spin $S_0 = 1/2$ (upper panel) and $S_0 = 1$ (lower panel) for different values of the magnetic field B/J indicated by the numbers above each curve on the left side. Here $S = 1/2$, $Z = 4$, and $B_0 = B$.

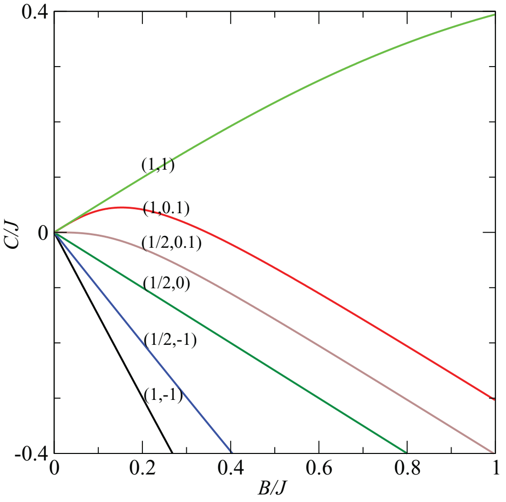

FIG. 5. (Color online) C/J vs magnetic field B/J for different values of the impurity spin and coupling denoted by (S_0, J_0). Here $B_0 = B$, $S = 1/2$, and $Z = 4$.

For high spin S of the embedding lattice and not too large magnetic field, the prefactor of the alternating magnetization becomes

$$-\sqrt{2S}\,\cos\theta\,\frac{CZ}{2\pi f g^2} \approx \frac{BS - B_0 S_0 \nu_0}{2\pi J S} + \mathcal{O}(S^{-2}), \tag{34}$$

thus it approaches a constant as $S \to \infty$.

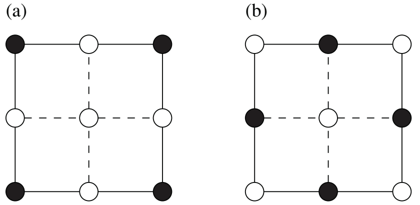

FIG. 6. Orientations of the magnetization close to the impurity. The impurity spin is the middle circle. Open circles indicate that the magnetization is pointing along the applied magnetic field, while filled circles indicate the opposite orientation. (a) $C < 0$ and (b) $C > 0$.

IV. MAGNETIZATION OF THE IMPURITY SPIN

At the impurity site the leading-order magnetization is obtained by the classical expression

$$M_0^z = S_0 \sin\theta_0. \tag{35}$$

For $S_0 = 1/2$ and $J_0 > 0$ this gives reasonable agreement with the QMC data, as is seen in Fig. 7. However, for other spins and ferromagnetic couplings $J_0 < 0$, the result is rather far from that of the QMC result. Thus it is necessary to also take into account the quantum corrections to Eq. (35). However, these quantum corrections are difficult to calculate analytically. This is because for the impurity itself it is necessary to include explicitly the bilinear terms connecting the impurity site to its neighbors, in addition to the quadratic bulk part in Eq. (18). These impurity terms induce nonlocal interactions in k space, thus an analytic diagonalization becomes difficult. In order to solve this we will instead numerically diagonalize the quadratic boson Hamiltonian as described below, which gives much better results, as shown in Fig. 7. As this method is numerical there is no need for the restriction of keeping only two angles θ_0 and θ. Thus we will instead keep track of all the angles θ_i. This has the consequence that all linear boson terms vanish when using the values of the angles obtained from minimizing the zeroth-order term, as will be shown below.

As a function of all angles θ_i, the zeroth-order term is

$$H_0 = \sum_{\langle ij\rangle} -|J_{ij}| S_i S_j \cos(\theta_i + \nu_{ij}\theta_j) - \sum_i B_i S_i \sin\theta_i, \tag{36}$$

where we have used the minimization condition for the ϕ's. Minimizing H_0 with respect to θ_i, we find

$$\sum_{j=e_i} |J_{ij}| S_j \sin(\theta_i + \nu_{ij}\theta_j) - B_i \cos\theta_i = 0, \tag{37}$$

where the sum is restricted to run over the nearest neighbors e_i of site i. This condition is equivalent to the equation

$$\tan\theta_i = \frac{B_i - \sum_{j=e_i} J_{ij} S_j \sin\theta_j}{\sum_{j=e_i} |J_{ij}| S_j \cos\theta_j}. \tag{38}$$

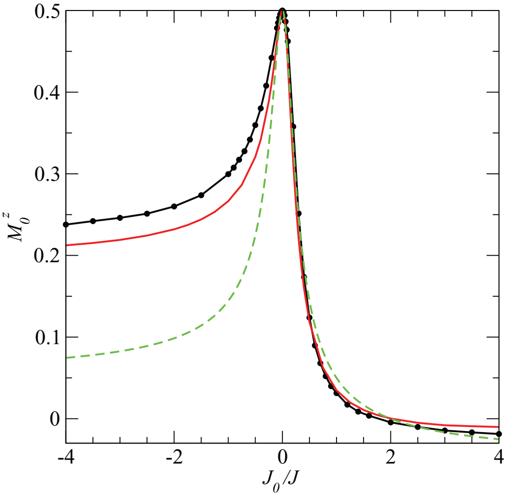

FIG. 7. (Color online) Magnetization at the impurity site for a spin-1/2 impurity coupled to a bulk spin-1/2 antiferromagnet by a coupling J_0. The filled black circles are results from quantum Monte Carlo simulations. The dashed line (green) is the classical result coming from Eq. (35), and the solid line (red) is the numerical spin-wave result.

The operators $S_i^{\prime x} S_j^{\prime z}$, $S_i^{\prime z} S_j^{\prime x}$, and the magnetic field term in Eq. (7) give the linear terms of the Hamiltonian,

$$\begin{aligned} H_1 &= \sum_{\langle ij\rangle} \left(|J_{ij}| \sqrt{\frac{S_i}{2}} S_j \sin(\theta_i + \nu_{ij}\theta_j)(a_i + a_i^\dagger) + (i \leftrightarrow j) \right) \\ &\quad - \sum_i B_i \sqrt{\frac{S_i}{2}} \cos\theta_i (a_i + a_i^\dagger) \\ &= \sum_i \sqrt{\frac{S_i}{2}} (a_i + a_i^\dagger) \\ &\quad \times \left(\sum_{j=e_i} |J_{ij}| S_j \sin(\theta_i + \nu_{ij}\theta_j) - B_i \cos\theta_i \right). \end{aligned} \tag{39}$$

By comparing this to Eq. (37) we see that the minimization of the constant terms leads to the vanishing of the linear terms.

The quadratic terms are

$$\begin{aligned} H_2 &= \sum_{\langle ij\rangle} J_{ij} \sqrt{\frac{S_i S_j}{4}} [\cos(\theta_i + \nu_{ij}\theta_j) - \nu_{ij}](a_i^\dagger a_j + a_j^\dagger a_i) \\ &\quad + J_{ij} \nu_{ij} \cos(\theta_i + \nu_{ij}\theta_j)(S_j a_i^\dagger a_i + S_i a_j^\dagger a_j) \\ &\quad + J_{ij} \sqrt{\frac{S_i S_j}{4}} [\cos(\theta_i + \nu_{ij}\theta_j) + \nu_{ij}](a_i a_j + a_i^\dagger a_j^\dagger) \\ &\quad + \sum_i B_i \sin\theta_i a_i^\dagger a_i, \end{aligned} \tag{40}$$

which can be written in the form

$$H_2 = \sum_{ij} (a_i^\dagger A_{ij} a_j + a_i A_{ij}^* a_j^\dagger + a_i^\dagger B_{ij} a_j^\dagger + a_i B_{ij}^* a_j) + G, \tag{41}$$

where the constants are

$$G = -\sum_i \left(\frac{B_i}{2} \sin\theta_i + \sum_{j=e_i} \frac{J_{ij}}{2} \nu_{ij} \cos(\theta_i + \nu_{ij}\theta_j) S_j \right), \tag{42}$$

$$\begin{aligned} A_{ij} = {} & J_{ij} \frac{\sqrt{S_i S_j}}{4} [\cos(\theta_i + \nu_{ij}\theta_j) - \nu_{ij}] \delta_{\langle ij \rangle} \\ & + \left(\frac{B_i}{2} \sin\theta_i + \sum_{k=e_i} \frac{J_{ik}}{2} \nu_{ik} S_k \cos(\theta_i + \nu_{ik}\theta_j) \right) \delta_{ij}, \end{aligned} \tag{43}$$

and

$$B_{ij} = J_{ij} \frac{\sqrt{S_i S_j}}{4} [\cos(\theta_i + \nu_{ij}\theta_j) + \nu_{ij}] \delta_{\langle ij \rangle}, \tag{44}$$

where $\delta_{\langle ij \rangle}$ is 1 when i and j are nearest neighbors and zero otherwise.

In order to numerically diagonalize Eq. (41) we will first find the numerical values of the θ_i's by solving Eq. (38). This is achieved by the relaxation method where the boundary condition is specified as $\sin\theta_{\text{boundary}} = B/2SZJ$ and an initial guess for the angles on other sites is made as indicated in Fig. 8. Then the lattice is traversed site by site and new angles are computed using Eq. (38). This step is repeated until convergence. It is known that this procedure converges slowly. However, for typical lattice sizes (28 × 28) used here this is not an issue of practical importance. Having determined the angles numerically we proceed to diagonalize the quadratic Hamiltonian.

We begin by forming the $2N$ column vector $\mathfrak{a} = (a_1, a_2, \ldots, a_N, a_1^\dagger, a_2^\dagger, \ldots, a_N^\dagger)^T$, where we have numbered the lattice sites in a consecutive fashion from 1 through N. The components of $\mathfrak{a}$ obey the commutation relation $[\mathfrak{a}_i, \mathfrak{a}_j^\dagger] = \eta_{ij}$, where $\eta = \begin{pmatrix} 1_{N\times N} & 0 \\ 0 & -1_{N\times N} \end{pmatrix}$. With this notation the quadratic Hamiltonian takes the form

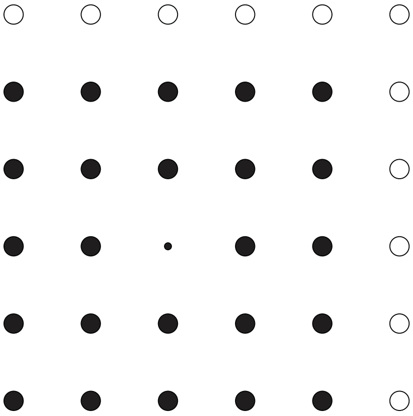

FIG. 8. Geometry of a 6 × 6 lattice. The open circles mark sites where the boundary condition is imposed. The filled circles are sites where the angles are being calculated. The small circle is the impurity site. Periodic boundary conditions are used.

$$H = \mathfrak{a}^\dagger \mathfrak{D} \mathfrak{a}, \tag{45}$$

where $\mathfrak{D}$ is the $2N \times 2N$ matrix with entries from the quadratic part of the Hamiltonian

$$\mathfrak{D} = \begin{pmatrix} A & B \\ B^* & A^* \end{pmatrix}. \tag{46}$$

We seek a $2N \times 2N$ Bogoliubov transformation matrix $\mathfrak{t}$ that transforms $\mathfrak{a}$ into new bosonic operators $\mathfrak{b}$: $\mathfrak{a} = \mathfrak{t}\mathfrak{b}$. In order for the entries of $\mathfrak{b}$ to obey bosonic commutation rules the matrix $\mathfrak{t}$ must obey

$$\eta = \mathfrak{t}\eta\mathfrak{t}^\dagger. \tag{47}$$

Inserting $\mathfrak{a} = \mathfrak{t}\mathfrak{b}$ into the Hamiltonian (45) we seek a $\mathfrak{t}$ that fulfills the commutation condition (47) and that makes $\mathfrak{t}^\dagger \mathfrak{D} \mathfrak{t} = \mathfrak{E}$ where $\mathfrak{E}$ is diagonal. However, it is not always possible to find such a diagonal matrix. When the Hamiltonian contains zero modes associated with a continuous spectrum one will never be able to write the free-particle operator p^2 as a $b^\dagger b$ term alone. However, such a term can always be written as $b^\dagger b + bb^\dagger - bb - b^\dagger b^\dagger$ with the proper rescaling of operators. Thus we will seek a matrix $\mathfrak{E}$ that is almost diagonal in the sense that for massive modes it only has entries along the diagonal, while the continuous parts of the spectrum are represented by $1s$ or $-1s$ in appropriate places. More specifically, we are seeking a matrix $\mathfrak{t}$ that makes $\mathfrak{t}^\dagger \mathfrak{D} \mathfrak{t}$ into a $2N \times 2N$ matrix $\mathfrak{E}$ of the form

$$\mathfrak{E} = \begin{pmatrix} E_e & & & & & \\ & 0_{\bar{z}} & & & 0_{\bar{z}} & \\ & & I_z & & & J_z \\ & & & E_e & & \\ & 0_{\bar{z}} & & & 0_{\bar{z}} & \\ & & J_z & & & I_z \end{pmatrix}, \tag{48}$$

where E_e is a diagonal $e \times e$ matrix of positive energies which represents the discrete harmonic oscillator energies associated with e gapped modes. Here $0_{\bar{z}}$ is a $\bar{z} \times \bar{z}$ matrix of zeros that represents $\bar{z}$ proper zero modes where the harmonic oscillator energy is zero, I_z and J_z are describing the z improper zero modes associated with a continuous free-particle spectrum, I_z is a $z \times z$ diagonal unit matrix, and J_z is a $z \times z$ diagonal matrix with diagonal entries either +1 or −1. The sign distinguishes between operators of the type x^2 and p^2. Empty entries indicate zeros. The procedure of finding such a $\mathfrak{t}$ is outlined in detail in Ref. 21. We have implemented this on a computer and find that the procedure works very well.

In the absence of linear terms the magnetization is given to quadratic order by

$$\langle S_i^z \rangle = \sin\theta_i (S_i - \langle a_i^\dagger a_i \rangle). \tag{49}$$

The value of $\sin\theta_i$ is known from the minimization of the classical term, and $\langle a_i^\dagger a_i \rangle$ can be obtained from the transformation matrix $\mathfrak{t}$. Without loss of generality the matrix $\mathfrak{t}$ can be written

$$\mathfrak{t} = \begin{pmatrix} U & V^* \\ V & U^* \end{pmatrix}, \tag{50}$$

where U and V are $N \times N$ matrices. Then the expectation value $\langle a_i^\dagger a_i \rangle$ is

$$\langle a_i^\dagger a_i \rangle = \sum_{jk} (U_{ij}^* U_{ik} \langle b_j^\dagger b_k \rangle + V_{ij} V_{ik}^* \langle b_j b_k^\dagger \rangle + U_{ij}^* V_{ik}^* \langle b_j^\dagger b_k^\dagger \rangle + V_{ij} U_{ik} \langle b_j b_k \rangle). \tag{51}$$

We will compute the expectation value in a state with low energy. For massive modes we pick the ground state to be the vacuum state and then only the second term contributes $\langle b_j b_k^\dagger \rangle = \delta_{jk}$. The situation is not so simple for the improper zero modes. An improper zero mode $b^\dagger b + b b^\dagger \pm b b \pm b^\dagger b^\dagger$ can be written as the momentum-squared operator $2p^2$ (the minus sign) or the position-squared operator $2x^2$ (the plus sign) using $b = \frac{1}{\sqrt{2}}(x + ip)$ and $b^\dagger = \frac{1}{\sqrt{2}}(x - ip)$. Thus it is clear that its spectrum is continuous.

For each improper zero mode we choose instead to compute the expectation value in a Gaussian state[22] characterized by a width w. Specifically,

$$\psi(x) = \left(\frac{1}{\pi w^2} \right)^{1/4} e^{-1/2(x/w)^2}. \tag{52}$$

In this state the expectation values of the energies are

$$\langle p^2 \rangle = \tfrac{1}{2} w^{-2}, \tag{53}$$

$$\langle x^2 \rangle = \tfrac{1}{2} w^2, \tag{54}$$

while the expectation values of the operators needed in $\langle a_i^\dagger a_i \rangle$ are

$$\langle b^\dagger b \rangle = (w^2 + w^{-2} - 2)/4, \tag{55}$$

$$\langle b b^\dagger \rangle = (w^2 + w^{-2} + 2)/4, \tag{56}$$

$$\langle b^\dagger b^\dagger \rangle = \langle b b \rangle = (w^2 - w^{-2})/4. \tag{57}$$

Using this the expectation value $\langle a_i^\dagger a_i \rangle$ takes the form

$$\langle a_i^\dagger a_i \rangle = \sum_{j \in e} |V_{ij}|^2 + \sum_{j \in z} \frac{1}{4} \left(w_j^2 |U_{ij}^* + V_{ij}|^2 + \frac{1}{w_j^2} |U_{ij}^* - V_{ij}|^2 - 2 \left(|U_{ij}|^2 - |V_{ij}|^2 \right) \right). \tag{58}$$

We will refer to the last sum in the above as the zero mode(s) contribution, and we have allowed for a separate width w_j for each improper zero mode. We will choose values of w_j so that the total energy of the improper zero modes is equal to that of the lowest finite-energy mode. This choice is made to avoid divergences and at the same time still justify calling them zero-energy modes. In our case, in the presence of a magnetic field, there is only one improper zero mode, and it turns out that the precise value of the w is not important quantitatively for the z-axis magnetization. In all cases we have looked at here, the zero mode contribution is negligible and we might as well neglect it completely. This is in contrast to the one-dimensional case, where the zero modes dominate and are responsible for the divergences of spin-wave theory in the infinite volume limit.

The results from this numerical diagonalization on a 28×28 lattice are shown in Fig. 7 for $S_0 = 1/2$ alongside the classical result and results from QMC simulations for the square lattice at a fixed value of the magnetic field $B/J = 0.4$. Figure 9 is similar but for $S_0 = 1$.

The numerical diagonalization restricts the system size $L \lesssim 28$. One may ask whether this is adequate to represent the infinite size behavior. We expect that it is as long as the decay length of the alternating magnetization $d \ll L$. For the magnetic field $B = 0.4J$, $d = 3.5$. Thus we expect that $L = 28$ is large enough to essentially capture the infinite size limit. We have checked this by performing QMC simulations of the magnetization for different system sizes ranging from $L = 4$ to $L = 96$ using the magnetic field $B = 0.4J$. We find that the magnetization depends roughly linearly on L for $L \lesssim 12$ at which it saturates rapidly. At $L = 28$ the values of the magnetization differ by the extrapolated infinite size values by roughly 1%.

From Fig. 7 one can see that the numerical diagonalization procedure compares much more favorably to the QMC data than the classical result does. Especially for antiferromagnetic J_0, the agreement is very good. For large ferromagnetic J_0 the agreement is worse, which we believe is related to the truncation of the Hamiltonian at quadratic order in boson operators. The main feature of the curves is a maximum at $J_0 = 0$ which reflects the trivial fact that an uncoupled (isolated) impurity will point along the magnetic field. In fact, the impurity spin will point along the field for most couplings except very large antiferromagnetic J_0 for $S_0 = 1/2$.

For sites in the neighborhood of the impurity we can also compare the analytic and the numerical spin-wave calculations

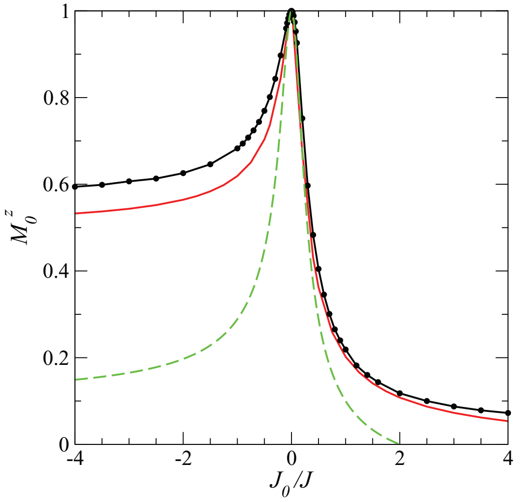

FIG. 9. (Color online) Magnetization at the impurity site for a spin-1 impurity coupled to a bulk spin-1/2 antiferromagnet by a coupling J_0. The filled black circles are results from quantum Monte Carlo simulations. The dashed line (green) is the classical result coming from Eq. (35), and the solid line (red) is the numerical spin-wave result.

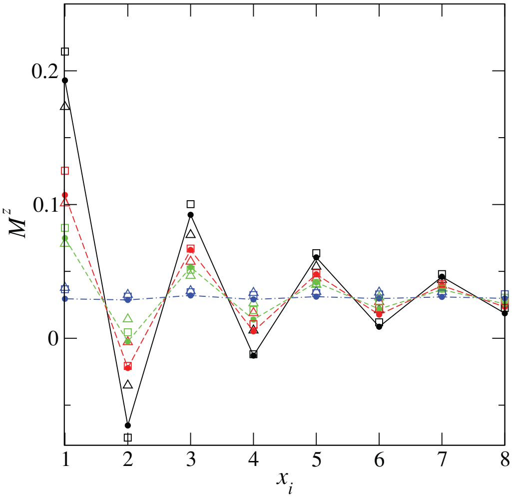

FIG. 10. (Color online) Magnetization as a function of horizontal distance x_i from the impurity site as calculated by QMC (solid circles), numerical spin waves (triangles), and the analytic spin-wave theory (squares). $S_0 = 1/2$, $S = 1/2$, and $B = B_0 = 0.4J$. The colors are for different values of $J_0/J = -2$ [solid (black)], 0 [long dashed (red)], 0.1 [dashed (green)], and 0.5 [dot-dashed (blue)]. QMC error bars are smaller than the size of the solid circles, and both the QMC and the numerical spin-wave calculations are carried out on a 28 × 28 lattice.

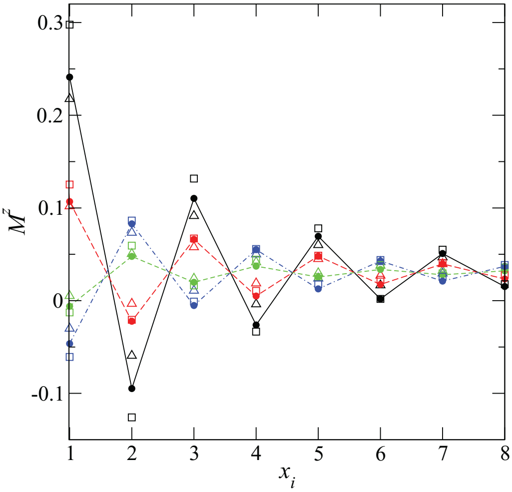

FIG. 11. (Color online) Magnetization as a function of horizontal distance x_i from the impurity site as calculated by QMC (solid circles), numerical spin waves (triangles), and the analytic spin-wave theory (squares). $S_0 = 1$, $S = 1/2$, and $B = B_0 = 0.4J$. The colors are for different values of $J_0/J = -1$ [solid (black)], 0 [long dashed (red)], 0.2 [dashed (green)], and 1 [dot-dashed (blue)]. QMC error bars are smaller than the size of the solid circles, and both the QMC and the numerical spin-wave calculations are carried out on a 28 × 28 lattice.

to the QMC results. In Fig. 10 we show the magnetization for an $S_0 = 1/2$ impurity at different positions $(x_i, y_i = 0)$ close to the impurity. The different lines are for the various values of the impurity coupling J_0 and the different symbols indicate the method used. In comparing the methods we see that the analytic result lies reasonably close to the QMC data except for the nearest-neighbor point where the numerical spin-wave calculation gives a better approximation to the QMC data. For a fixed value of J_0 one can see that the magnetization exhibits a predominantly alternating pattern with a magnitude that is largest for ferromagnetic couplings $J_0 < 0$, as predicted in Fig. 4. As the ferromagnetic coupling J_0 becomes smaller, the magnetization of the impurity spin increases (Fig. 7), while the surrounding pattern is not much affected. On the antiferromagnetic side, $J_0 > 0$, the magnetization of the impurity spin decreases accompanied also by a decrease in the amplitude of the magnetization oscillation away from the impurity. At $J_0 = J$ the oscillation pattern vanishes completely. For strong antiferromagnetic couplings $J_0 > J$ there is almost no induced magnetization on the sites surrounding the impurity, but the magnetization of the impurity spin becomes smaller than the average magnetization and can even become negative for strong enough J_0.

For the $S_0 = 1$ impurity the magnetization pattern around the impurity is shown in Fig. 11. Again the oscillations are large for ferromagnetic J_0. As $J_0 \to 0$ the magnetization of the impurity spin increases, while the oscillating pattern around it decreases. Then as J_0 becomes antiferromagnetic the magnetization oscillations increase again, but now the sublattice pattern has changed to the pattern in Fig. 6(b), consistent with the fact that C changes sign in Fig. 4. The amplitude of the oscillations saturates as J_0 becomes even stronger.

V. DISCUSSION

We have presented results for the magnetization around a general impurity in a Heisenberg spin-S antiferromagnet in a magnetic field. Away from the impurity we find that the induced magnetization is dominantly a staggered magnetization in the field direction. We have calculated this alternating magnetization, and our results are in reasonable agreement with extensive QMC simulations that we have also carried out. One important feature of the spin-wave result is that the parameters of the impurity model only affect the overall prefactor C of the magnetization, while the scale and shape of the decay are universal and only reflect the properties of the host magnet and the applied field. We have analyzed how the prefactor C depends on impurity properties and found that the effect on the alternating magnetization is largest for ferromagnetically coupled impurities and generally increases with magnetic field. In order to calculate the magnetization at the impurity site we have described in detail how to diagonalize the quadratic spin-wave Hamiltonian numerically. This approach agrees well with the QMC calculations and we have outlined how the magnetization of the impurity spin depends on the coupling strength of the impurity to its neighbors.

In summary, the results can be used to predict the detailed local magnetization pattern around general magnetic and nonmagnetic impurities in isotropic antiferromagnets, e.g., from doping Zn, Co, and Ni in copper-oxide antiferromagnets. In most real materials the effects from crystal fields and other anisotropies are also important, but our calculations provide the first step, before other possible terms in the Hamiltonian are taken into account.

ACKNOWLEDGMENTS

The QMC calculations were carried out on CPUs provided by the Notur project. Financial support by the DFG via the research initiative SFB-TR49 and the Graduate School of Excellence MAINZ/MATCOR is gratefully acknowledged.

APPENDIX: SUM

The sum

$$I = \frac{1}{N}\sum_{\vec{k}} \frac{\gamma_{\vec{k}}}{1+g\gamma_{\vec{k}}} e^{i\vec{k}\cdot\vec{r}} \tag{A1}$$

for $\vec{r} \neq 0$ can be written

$$I = \frac{1}{gN}\sum_{\vec{k}} \frac{1+g\gamma_{\vec{k}}-1}{1+g\gamma_{\vec{k}}} e^{i\vec{k}\cdot\vec{r}} = -\frac{1}{gN}\sum_{\vec{k}} \frac{1}{1+g\gamma_{\vec{k}}} e^{i\vec{k}\cdot\vec{r}}. \tag{A2}$$

This sum can be calculated by expanding the denominator about the antiferromagnetic point $\vec{Q} = (\pi,\pi,\pi)$. Shifting the $\vec{k}$ summation $\vec{k} \rightarrow \vec{k} + \vec{Q}$ and expanding the denominator to order $\vec{k}^2$ we get

$$I \approx -\frac{e^{i\vec{Q}\cdot\vec{r}}}{g}\frac{1}{N}\sum_{\vec{k}} \frac{e^{i\vec{k}\cdot\vec{r}}}{1-g+g\vec{k}^2/Z}, \tag{A3}$$

where Z is the coordination number of the lattice. This can also be written

$$I \approx -\frac{Zd^2 e^{i\vec{Q}\cdot\vec{r}}}{g^2}\frac{1}{N}\sum_{\vec{k}} \frac{e^{i\vec{k}\cdot\vec{r}}}{1+d^2\vec{k}^2}, \tag{A4}$$

where $d = \sqrt{\frac{g}{Z(1-g)}}$. The sum is calculated by transforming it into an integral and using polar coordinates

$$\frac{1}{N}\sum_{\vec{k}} \frac{e^{i\vec{k}\cdot\vec{r}}}{1+d^2\vec{k}^2} = \frac{1}{2\pi d^2}\begin{cases} K_0(r/d), & D=2 \\ e^{-r/d}/(2r), & D=3, \end{cases} \tag{A5}$$

where K_0 is the zeroth-order modified Bessel function of the second kind. Putting this together we get

$$I \approx -\frac{Ze^{i\vec{Q}\cdot\vec{r}}}{2\pi g^2}\begin{cases} K_0(r/d), & D=2 \\ e^{-r/d}/(2r), & D=3, \end{cases} \tag{A6}$$

where $e^{i\vec{Q}\cdot\vec{r}} = (-1)^{x_i+y_i+z_i}$.

---

[1] M. Butler, V. Jaccarino, N. Kaplan, and H. J. Guggenheim, Phys. Rev. B **1**, 3058 (1970).

[2] J. A. van Luijk, A. F. M. Arts, and H. W. de Wijn, Phys. Rev. B **21**, 1963 (1980).

[3] For a review, see H. Alloul, J. Bobroff, M. Gabay, and P. J. Hirschfeld, Rev. Mod. Phys. **81**, 45 (2009).

[4] S. Eggert and I. Affleck, Phys. Rev. Lett. **75**, 934 (1995); G. B. Martins, M. Laukamp, J. Riera, and E. Dagotto, *ibid.* **78**, 3563 (1997); M. Takigawa, N. Motoyama, H. Eisaki, and S. Uchida, Phys. Rev. B **55**, 14129 (1997); S. Eggert and S. Rommer, Phys. Rev. Lett. **81**, 1690 (1998); S. Rommer and S. Eggert, Phys. Rev. B **62**, 4370 (2000).

[5] For a review, see G. Binnig and H. Rohrer, Rev. Mod. Phys. **59**, 615 (1987).

[6] S. Heinze *et al.*, Science **288**, 1805 (2000); A. Kubetzka, M. Bode, O. Pietzsch, and R. Wiesendanger, Phys. Rev. Lett. **88**, 057201 (2002).

[7] See, for instance, S. Meckler, N. Mikuszeit, A. Pressler, E. Y. Vedmedenko, O. Pietzsch, and R. Wiesendanger, Phys. Rev. Lett. **103**, 157201 (2009).

[8] S. W. Lovesey, J. Phys. C **1**, 102 (1968).

[9] T. Tonegawa, Prog. Theor. Phys. **40**, 1195 (1968).

[10] S. Eggert and I. Affleck, Phys. Rev. B **46**, 10866 (1992).

[11] S. Fujimoto and S. Eggert, Phys. Rev. Lett. **92**, 037206 (2004); A. Furusaki and T. Hikihara, Phys. Rev. B **69**, 094429 (2004); J. Sirker, N. Laflorencie, S. Fujimoto, S. Eggert, and I. Affleck, Phys. Rev. Lett. **98**, 137205 (2007); J. Stat. Mech.: Theory Exp. (**2008**) P02015.

[12] S. Sachdev, C. Buragohain, and M. Vojta, Science **286**, 2479 (1999).

[13] K. H. Höglund and A. W. Sandvik, Phys. Rev. Lett. **91**, 077204 (2003); Phys. Rev. B **70**, 024406 (2004); **79**, 020405 (2009).

[14] F. Anfuso and S. Eggert, Phys. Rev. Lett. **96**, 017204 (2006); K. H. Höglund and A. W. Sandvik, Europhys. Lett. **73**, 271 (2006).

[15] S. Eggert, O. F. Syljuåsen, F. Anfuso, and M. Andres, Phys. Rev. Lett. **99**, 097204 (2007).

[16] T. Holstein and H. Primakoff, Phys. Rev. **58**, 1908 (1940).

[17] M. E. Zhitomirsky and A. L. Chernyshev, Phys. Rev. Lett. **82**, 4536 (1999).

[18] N. Bulut, D. Hone, D. J. Scalapino, and E. Y. Loh, Phys. Rev. Lett. **62**, 2192 (1989).

[19] A. W. Sandvik and J. Kurkijärvi, Phys. Rev. B **43**, 5950 (1991).

[20] O. F. Syljuåsen and A. W. Sandvik, Phys. Rev. E **66**, 046701 (2002).

[21] J. H. P. Colpa, Physica A **134**, 377 (1986).

[22] P. W. Anderson, Phys. Rev. **86**, 694 (1952).